# APPLIED COMPUTATIONAL ELECTROMAGNETICS SOCIETY JOURNAL

February 2023
Vol. 38 No. 2
ISSN 1054-4887

**The ACES Journal is abstracted in INSPEC, in Engineering Index, DTIC, Science Citation Index Expanded, the Research Alert, and to Current Contents/Engineering, Computing & Technology.**

The illustrations on the front cover have been obtained from the ARC research group at the Department of Electrical Engineering, Colorado School of Mines

Published, sold and distributed by: River Publishers, Alsbjergvej 10, 9260 Gistrup, Denmark

## FEBRUARY 2023 REVIEWERS

**Huseyin Aniktar**
**Sami Barmada**
**Thippesha D.**
**Arkaprovo Das**
**Zahid Hasan**
**Mustafa Kara**
**Ashutosh Kedar**
**Mehmet Onur Kok**
**Wang-Sang Lee**
**Xiaobo Liu**
**Matteo Bruno Lodi**
**Asmaa Majeed**
**Antonio Orlandi**
**Fan Peng**
**D. Prabhakar**
**Jun Qiu**
**Mohammed Salim**
**Michael Saville**
**Sayidmarie**
**Ye Tian**
**Gaobiao Xiao**
**Salah I. Yahya**
**Abubakar Yakubu**
**Wentao Yuan**

THE APPLIED COMPUTATIONAL ELECTROMAGNETICS SOCIETY JOURNAL

Vol. 38 No. 2 February 2023

## TABLE OF CONTENTS

# Antenna Synthesis by Levin's Method using a Novel Optimization Algorithm for Knot Placement

**Goker Sener**

Department of Electrical-Electronics Engineering
Cankaya University, Ankara, 06790, Turkey
sener@cankaya.edu.tr

***Abstract –*** Antenna synthesis refers to determining the antenna current distribution by evaluating the inverse Fourier integral of its radiation pattern. Since this integral is highly oscillatory, Levin's method can be used for the solution, providing high accuracy. In Levin's method, the integration domain is divided into equally spaced sub-intervals, and the integrals are solved by transferring them into differential equations. This article uses a new optimization algorithm to determine the location of these interval points (knots) to improve the method's accuracy. Two different antenna design examples are presented to validate the accuracy and efficiency of the proposed method for antenna synthesis applications.

***Index Terms –*** antenna synthesis, fourier integral, highly oscillatory integrals knot placement, Levin's method.

## I. INTRODUCTION

Antenna synthesis aims to find the current distribution by evaluating the inverse Fourier integral of the antenna radiation pattern. [1, 2]. Since this integral is highly oscillatory, a proper solution algorithm must be employed [3, 4].

Levin's method is a numerical technique widely used for solving highly oscillatory integrals, and it gives accurate results, especially with complex phase functions [4–7]. In this method, the integral domain is divided into equally spaced sub-intervals, and the integrals of these sub-intervals are evaluated by transferring them into differential equations. These equations are then solved by converting the problem into a linear equation system by the collocation method. Lastly, the results of the sub-integrals are added to obtain the final solution.

The collocation approximation is the finite sum of some linearly independent basis functions with unknown coefficients. Therefore, selecting the basis functions is highly important regarding the method's accuracy. In [8], Levin's method is used with "reproducing kernel functions", giving better accuracy and stability than the other well-known basis functions.

In this paper, the Levin's method is improved by using a new optimization algorithm to determine the locations of the integration sub-interval points (knots). This algorithm was first introduced by Yeh et al. in [9] as a knot placement method for the B-spline curve fitting. Here, it is used in the Levin's method to obtain higher accuracy. To the author's knowledge, this is the first time the Levin's method is used with this new knot optimization technique in an antenna synthesis application.

Two examples are presented to validate the accuracy and efficiency of the proposed method. In the first example, the radiation pattern of a log-periodic antenna, 4030/LP/10, is used to obtain the equivalent current distribution on a linear conductor. In the second example, an array antenna with a narrow beamwidth is considered. The error and stability analyses are carried out by comparing the original radiation patterns with the ones obtained by the proposed solution. The results show that the proposed method provides more accuracy than the standard equal-distance knot placement integration technique, particularly for narrow beam radiation.

The remaining of this paper is arranged as follows: In sections II and III, the Levin's method and reproducing kernel functions are explained, respectively. In section IV, the novel knot placement method is explained. In section V, the antenna synthesis examples are presented. In section VI, conclusions are made based on the error and stability analysis results.

## II. LEVIN'S METHOD

Levin's method is a numerical technique to solve highly oscillatory integrals in the form:

$$I = \int_a^b f(x)e^{iq(x)}dx, \tag{1}$$

where $f(x)$ is a slowly varying function, and $q(x)$ is a highly oscillatory function. Since $q(x)$ is oscillatory, it can be written that $|q'(x)| \gg (b-a)^{-1}$.

In Levin's method, the integral in (1) is transformed into the following differential equation:

$$f(x) = iq'(x)p(x) + p'(x) = L^{(1)}p(x). \tag{2}$$

*Submitted On: September 25, 2022*
*Accepted On: February 20, 2023*

https://doi.org/10.13052/2023.ACES.J.380201

Substituting (2) in (1) yields:

$$\begin{aligned} I &= \int_a^b \left(iq'(x)p(x)+p'(x)\right)e^{iq(x)}dx \\ &= \int_a^b \frac{d}{dx}\left(p(x)e^{iq(x)}\right)dx \\ &= p(b)e^{iq(b)} - p(a)e^{iq(a)}. \end{aligned} \tag{3}$$

Thus, the solution of the integral in (1) requires the solution of $p(a)$ and $p(b)$ only. By the collocation approximation, $p(x)$ can be written as:

$$p_n(x) = \sum_{k=1}^{n} \alpha_k u_k(x), \tag{4}$$

where $\{u_k(x)\}_{k=1}^n$ are some linearly independent basis functions, and $\alpha_k$'s are the coefficients to be determined by the n collocation points as:

$$L^{(1)}p_n(x_j) = f(x_j),\ j = 1,2,3,...,n. \tag{5}$$

The integral in (3) can be re-written in terms of (4) as

$$I = p_n(b)e^{iq(b)} - p_n(a)e^{iq(a)}. \tag{6}$$

Substituting (4) into (2) and using (5) gives the following linear equation system:

$$\begin{gathered} \sum_{k=1}^{n} \alpha_k u_k'(x_j) + iq'(x_j)\sum_{k=1}^{n}\alpha_k u_k(x_j) = f(x_j), \\ j = 1,2,3,...,n, \end{gathered} \tag{7}$$

where $\{\alpha_k\}_{k=1}^n$'s are the unknown coefficients that can be solved. Thereupon, (4) and (6) can be used to find the solution to (1).

In attempt to increase the accuracy of the method, instead of increasing the number of collocation nodes, $n$, which causes the solution matrix to be ill-conditioned and the method to become unstable, the integration domain is divided into more intervals. Thus, the selection of the basis function set is a highly important for the accuracy and stability of the Levin's method.

## III. REPRODUCING KERNEL FUNCTIONS

The basis function $\{u_k(x)\}_{k=1}^n$ to be used in the Levin's method is given as follows:

$$u_k(x) = \lambda_{k,y}K^m(x,y), \tag{8}$$

where $K^m(x,y)$ is the reproducing kernel function, defined in [8] as:

$$K^m(x,y) = \begin{cases} \xi(x,y),\ y \le x \\ \xi(y,x),\ y > x \end{cases}, \tag{9}$$

where $m = 1,2,...$ gives a set of reproducing kernel functions. Also,

$$\xi(x,y) = \sum_{i=0}^{m-1}\left(\frac{y^i}{i!} + (-1)^{m-1-1}\frac{y^{2m-1-i}}{(2m-1-1)!}\right)\frac{x^i}{i!}, \tag{10}$$

and $\lambda_k = \delta_{x_k}$, $k = 1,2,...,n$, is the evaluation functional and $\lambda_{k,y}$ is $\lambda_k$ acting on the function of $y$. The reproducing kernel function $K^m(x,y) \in H^m[a,b]$, where $H^m[a,b]$ is the reproducing kernel Hilbert space with $m > 1$.

Hilbert space H is a function space defined on domain E. The reproducing kernel Hilbert space (RKHS) is defined as for each $x \in E$, the function $K : E \times E \to R$ is known as the RKF of the Hilbert function space H if

$$K(\cdot,x) \in H\ for\ all\ x \in \Omega, \tag{11}$$

and

$$p(x) = \langle p(\cdot), K(\cdot,x)\rangle, \tag{12}$$

where the inner product defines the reproducing property of the Hilbert space. For further information on RKHS, the reader can refer to [10, 11].

## IV. KNOT PLACEMENT METHOD

This method was introduced in [9] to optimize the placement of knots for a B-spline curve fitting.

The methodology follows that for an $m$-point dataset, the location of the sample points are defined as $U = \{u_i : u_i \in R, u_i < u_{i+1}\}_{i=1}^m$, and the data points corresponding to these locations are $Q = \left\{q_i : q_i \in R^d\right\}_{i=1}^m$ where $d$ is the dimension of the problem. For 1D problems, $d = 1$ and $q_i = y_i$, and for 2D problems, $d = 2$ and $q_i = (x_i, y_i)$, etc. Also, $Q^{(k)} = \left\{q_j^{(k)} \in R\right\}_{j=1}^{m-k}$ is the set for $k$'th derivatives of this dataset.

For $Q^{(0)} = Q$ and $U^{(0)} = U$, the derivatives are calculated for $k > 0$ using the central difference formula:

$$q_j^{(k+1)} = \frac{q_{j+1}^{(k)} - q_j^{(k)}}{u_{j+1}^{(k)} - u_j^{(k)}}, \tag{13}$$

with parameter

$$u_j^{(k+1)} = \frac{1}{2}\left(u_j^{(k)} + u_{j+1}^{(k)}\right). \tag{14}$$

The "feature function", $f(u)$, is defined using a set of "feature points", $f_i$, as to measure the amount of detail in the input data. Furthermore, the feature points, $f_i$, are defined at a set of point locations $\bar{u}_i$ as:

$$(\bar{u}_i, f_i) = \begin{cases} (u_1, 0), & i = 0 \\ \left(u_i^{(p)}, \left(\|q_i^{(p)}\|_2\right)^{1/p}\right), & 1 \le i \le m-p \\ (u_m, 0), & i = m-p+1 \end{cases}, \tag{15}$$

where $p$ is the order of the polynomial approximation. For a B-spline approximation with polynomial order $p$, the highest degree is $(p-1)$. Also, $\ell^2$-norm defines the magnitude of the derivatives with respect to the problem's dimensionality.

The feature function, $f(u)$, is given as:

$$f(u) = \frac{u - \bar{u}_{i+1}}{\bar{u}_i - \bar{u}_{i+1}}f_i + \frac{u - \bar{u}_i}{\bar{u}_{i+1} - \bar{u}_i}f_{i+1}, \tag{16}$$

where $0 \le i \le m-p+1$, and $\bar{u}_i < u < \bar{u}_{i+1}$.

In order to determine the knot locations, the cumulative distribution function (CDF), $F(u)$, of the feature function is defined as:

$$F(u) = \int_{-\infty}^{u} f(v)dv. \tag{17}$$

Then the location of r distinct knots, $\{k_1, k_2, ..., k_r\}$, are given in terms of this CDF as:

$$k_i = F^{-1}\left((i-1)\delta F\right),\ i = 1, 2, ..., r, \tag{18}$$

where the boundary values $k_1 = u_1$ and $k_r = u_m$. Furthermore, the inverse CDF, $F^{-1}$, is defined as:

$$F^{-1}(q) = u \ \Leftrightarrow\ F(u) = q. \tag{19}$$

Also, the progressive feature increment value, $\delta F$, is described by:

$$\delta F = \frac{F_{max} - F_{min}}{r-1}. \tag{20}$$

The increment value, $\delta F$, determines the number of knots, as well as the accuracy of the approximation. The smaller $\delta F$ refers to more knots with greater accuracy. However, the knot intervals must not be less than the data intervals, so this puts a limit on the number of nodes that can be used in a given dataset.

## V. ANTENNA DESIGN EXAMPLES

### A. Example 1

A rotatable log-periodic antenna, 4030/LP/10, is used in an antenna synthesis application to verify the effectiveness of the proposed method. The radiation pattern (space factor for the electric field) of the antenna is obtained from the antenna's spec sheet, and it is imported into MATLAB using a B-spline interpolation at 91 points. The resulting pattern is shown in Fig. 1.

The equivalent current distribution on a linear conductor, which would create this radiation pattern, is calculated by solving the following inverse Fourier integral [2]:

$$I(z') = \frac{1}{2\pi}\int_{-\infty}^{\infty} f(\theta) e^{-jz'\xi} d\xi, \tag{21}$$

where $f(\theta)$ is the radiation pattern, and the variable $\xi = kcos\theta$, and where $k = 2\pi/\lambda$ is the wavenumber and $\lambda$ is the wavelength. Furthermore, the antenna is assumed

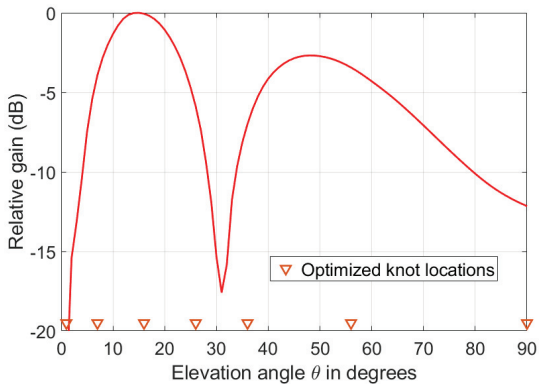


Fig. 1. Normalized radiation pattern, $f(\theta)$, of the log-periodic antenna, 4030/LP/10.

to be located along the vertical $z'$ axis, where the prime notation is used to designate the source coordinates.

The knot placement method is applied using $r = 7$ distinct knots ($\ell = 6$ intervals) and the increment value $\delta F = 1.29$. The optimized knot locations are evaluated at $\theta_i = \{0, 7, 16, 26, 36, 56, 90\}$ degrees for $i = 1, 2, ..., 7$. The CDF, $F(\theta)$, is shown in Fig. 2.

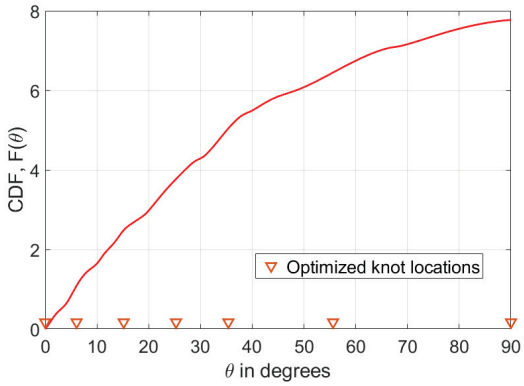


Fig. 2. Cumulative distribution function.

The Levin's method is used to solve the integral in (21) using the optimized knot locations using $n = 6$ collocation points for each interval and $m = 3$ for the reproducing kernel function as the basis in the collocation formulation. The limits of the integral in (21) are truncated to $\theta \in [90^0, 0^0]$ or $\xi \in [0, k]$. Thus, the integrals for each sub-interval become:

$$I_j(z') = \frac{1}{2\pi}\int_{kcos\theta_j}^{kcos\theta_{j+1}} \dot{f}(\theta) e^{-jz'\xi} d\xi,\ j = 1, 2, ..., \ell, \tag{22}$$

where $\dot{f}(\theta)$ is the part of the radiation pattern in the given interval. Due to the linearity, the total current can be written as:

$$I(z') = \sum_{j=1}^{\ell} I_j(z'),\ j = 1, 2, ..., \ell. \tag{23}$$

The resulting current distribution is shown in Fig. 3.

In order to analyze the accuracy of the proposed method, the radiation pattern created by this current distribution must be obtained. This is accomplished by solving the following Fourier integral:

$$f(\theta) = \int_{-l/2}^{l/2} I(z') e^{j\xi z'} dz' = \int_{-15\lambda}^{15\lambda} I(z') e^{jkcos(\theta)z'} dz'. \tag{24}$$

The Levin's method is re-used to solve this integral with $r = 91$ knots ($\ell = 90$ intervals) and 3 evaluation points ($n = 3$) for each sub-interval for the purpose of obtaining higher accuracy.

The radiation patterns for the optimized knot placement and the equally spaced knot placement methods are compared with the original pattern. The results are

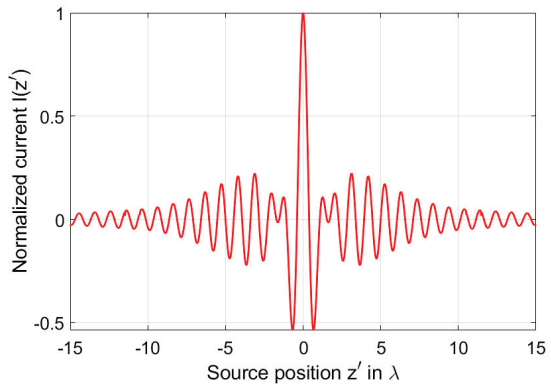


Fig. 3. Current distribution along the $z'$ axis in terms of the wavelength.

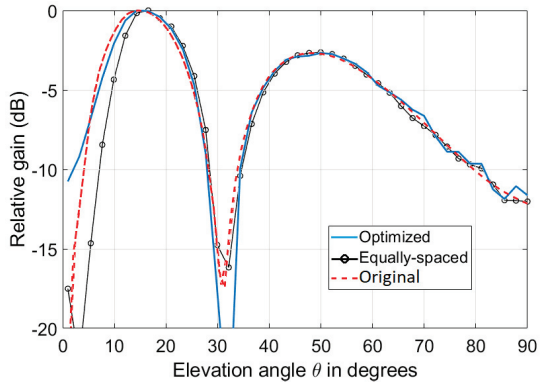


Fig. 4. Comparison of the radiation patterns for the knot optimized and the equally spaced Levin's method ($\ell = 6$, $n = 6$).

Table 1: Error and stability analysis in terms of the absolute errors and the matrix condition numbers for the standard (Std.) and the optimized (Opt.) methods

| $\ell$ | **n** | m (RKF) | **Error (Std.)** | **Error (Opt.)** | **Cond. Num. (Std.)** | **Cond. Num. (Opt.)** |
|---|---|---|---|---|---|---|
| 3 | 3 | 3 | 3.00 | 3.80 | 2e03 | 3e07 |
| 3 | 6 | 3 | 3.78 | 2.60 | 2e06 | 3e10 |
| 3 | 11 | 3 | 3.46 | 2.70 | 2e10 | 2e12 |
| 6 | 3 | 3 | 1.97 | 1.13 | 5e07 | 4e11 |
| 6 | 6 | 3 | 1.88 | 1.01 | 4e10 | 8e13 |
| 6 | 11 | 3 | 1.69 | 1.36 | 4e12 | 6e14 |
| 12 | 3 | 2 | 0.90 | 0.64 | 7e05 | 6e06 |
| 12 | 6 | 2 | 0.50 | 0.46 | 5e07 | 4e08 |
| 12 | 11 | 2 | 0.50 | 0.47 | 6e09 | 4e09 |

shown in Fig. 4. It can be observed that the absolute error is minimized for the proposed optimized knot placement method to be 1.01, whereas for the same settings ($\ell = 6$, $n = 6$, $m = 3$), the absolute error is 1.88 for the equally spaced knot placement method.

The error and stability analysis results are listed in terms of the absolute errors and the condition numbers of the solution matrices in Table 1 for different $\ell$ and $n$ values. In a linear equation system, the matrix condition number measures how sensitive the output vector is against the changes in the input vector. These results show that the optimized knot placement method yields more accuracy and slightly less stability than the standard method (equally spaced knot placement) for every $m$ value of the reproducing kernel function.

### B. Example 2

In this example, an array antenna is used with a narrow beam radiation at $\theta = 30^\circ$ on the elevation plane (E-plane). The radiation data is transferred into Matlab using B-spline interpolation at 91 points as before, and the resulting pattern function is shown in Fig. 5.

The knot optimization algorithm is carried out for $r = 4$ knots ($\ell = 3$ intervals), and the knot locations are obtained at $\theta_i = \{27, 29, 32, 34\}$ degrees for $i = 1, 2, ..., 4$. The cumulative distribution function corresponding to the antenna radiation pattern, $F(\theta)$, is shown in Fig. 6.

Equivalent current distribution on a linear conductor is obtained by using the Levin's method with optimized knot locations. The resulting current distribution is shown in Fig. 7. The comparison results of the radiation patterns for the knot optimized and the standard methods are shown in Fig. 8. It is observed that the absolute error for the proposed method is 0.16, whereas for the same settings ($\ell = 3$, $n = 3$, $m = 3$), the absolute error is 2.7 for the equally spaced knot placement method.

The error and stability analysis results are listed for the standard and the optimized methods in Table 2. The results show that the proposed method provides even more significant error reduction.

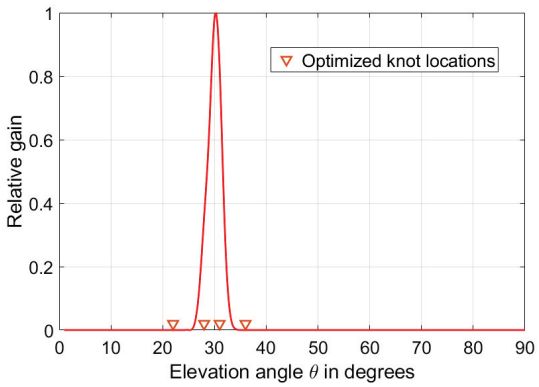


Fig. 5. Normalized radiation pattern of the array antenna.

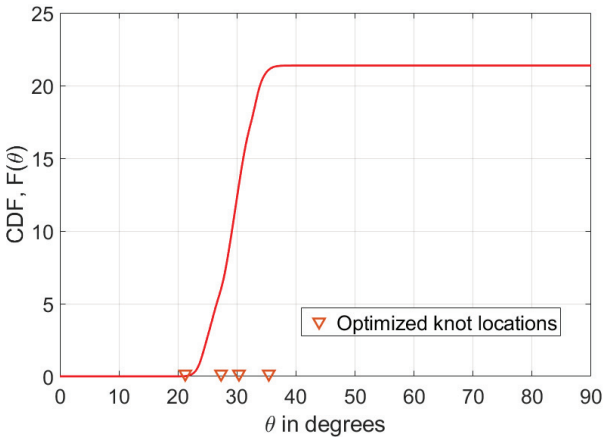


Fig. 6. Cumulative distribution function.

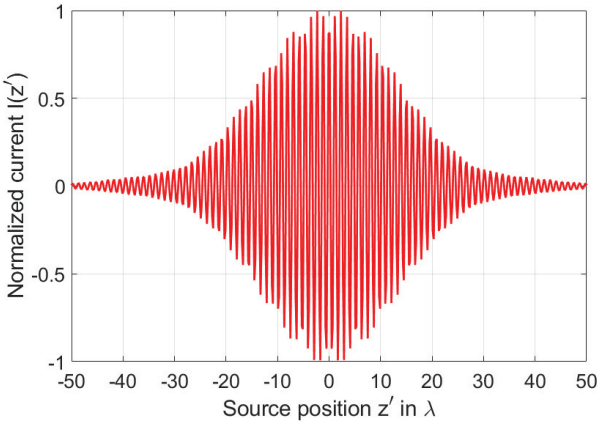


Fig. 7. Current distribution along the $z'$ axis in terms of the wavelength.

Table 2: Error and stability analysis in terms of the absolute errors and the matrix condition numbers for the standard (Std.) and the optimized (Opt.) methods

| $\ell$ | **n** | m (RKF) | **Error (Std.)** | **Error (Opt.)** | **Cond. Num. (Std.)** | **Cond. Num. (Opt.)** |
|---|---|---|---|---|---|---|
| 3 | 3 | 3 | 2.70 | 0.16 | 3e04 | 3e07 |
| 3 | 6 | 3 | 1.50 | 0.29 | 3e09 | 7e11 |
| 3 | 11 | 3 | 1.00 | 1.50 | 3e11 | 9e13 |
| 6 | 3 | 3 | 4.50 | 0.46 | 1e06 | 1e06 |
| 6 | 6 | 3 | 1.38 | 0.10 | 2e08 | 2e08 |
| 6 | 11 | 3 | 0.98 | 0.06 | 3e09 | 3e09 |
| 12 | 3 | 2 | 6.20 | 0.15 | 3e04 | 6e06 |
| 12 | 6 | 2 | 5.00 | 0.06 | 3e06 | 8e08 |
| 12 | 11 | 2 | 5.97 | 0.01 | 6e07 | 2e10 |

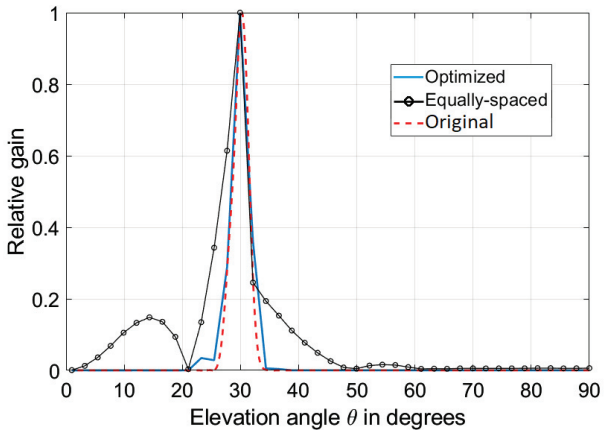


Fig. 8. Comparison of the radiation patterns for the knot optimized and the equally spaced Levin's methods using $\ell = 3$ intervals and $n = 3$ collocation points.

## VI. CONCLUSION

Based on the simulation results, the Levin's method gives more accurate results when combined with the knot optimization algorithm for antenna synthesis applications. This accuracy improvement can be observed from Table 1 and Table 2, where the error is reduced for the increasing number of intervals ($\ell$) independent of the number of collocation points ($n$) used for each interval.

The proposed method is particularly advantageous for radiation patterns with small beam widths, as this requires a large number of intervals for the standard technique. This result can be seen from the error analysis between the standard and the proposed techniques in Table 2.

In both examples, the optimized method gives the most accurate result for $m = 2$ of the reproducing kernel function, especially with an increase in intervals. For the other $m$ values not listed in Tables 1 and 2, the error is almost the same for different values of m for $n = 3$ and degrades significantly for $n > 3$, independent of the number of intervals $\ell$ for both the standard and the optimized methods. Also, the matrix condition number increases with increasing m regardless of the values for $n$ and $\ell$.

The only drawback of the proposed method is the increased condition number of the solution matrix, which implies that the method's stability decreases slightly compared to the equal-interval integration technique.

## REFERENCES

[1] C. A. Balanis, *Antenna Theory, Analysis and Design*, New York, John Wiley and Sons, 1997.

[2] W. L. Stutzman and A. T. Gary, *Antenna Theory and Design*, New Jersey, John Wiley and Sons, 2013.

[3] S. Khan, S. Zaman, A. Arama, and M. Arshad, "On the evaluation of highly oscillatory integrals

with high frequency," *Engineering Analysis with Boundary Elements*, vol. 121, pp. 116-125, 2020.

[4] D. Levin, "Procedures for computing one and two dimensional integrals of functions with rapid irregular oscillations," *Mathematics of Computation*, vol. 38, no. 158, pp. 531-538, 1982.

[5] S. Khan, S. Zaman, M. Arshad, H. Kang, H. H. Shah, and A. Issakhov, "A well-conditioned and efficient Levin method for highly oscillatory integrals with compactly supported radial basis functions," *Engineering Analysis with Boundary Elements*, vol. 131, pp. 51-63, 2021.

[6] S. Xiang, "On the Filon and Levin methods for highly oscillatory integral," *Journal of Computational and Applied Mathematics*, vol. 208, pp. 434-439, 2007.

[7] A. Molabahrami, "Galerkin–Levin method for highly oscillatory integrals," *Journal of Computational and Applied Mathematics*, vol. 397, pp. 499-507, 2017.

[8] F. Z. Geng and X. Y. Wu, "Reproducing kernel function-based Filon and Levin methods for solving highly oscillatory integral," *Applied Mathematics and Computation*, vol. 397, pp. 125980, 2021.

[9] R. Yeh, Y. S. G. Nashed, T. Peterka, and X. Tricoche, "Fast automatic knot placement method for accurate B-spline curve fitting," *Computer-Aided Design*, vol. 128, Art no. 102905, 2020.

[10] L. Wasserman, *Function Spaces, Lecture Notes*, Department of Statistics and Data Science, Carnegie Mellon University.

[11] O. Baver, *Reproducing Kernel Hilbert Spaces*, M. S. dissertation, Bilkent University, 2005.

**Goker Sener** was born in 1973. He completed his B.S. degree in Electrical Engineering in 1995 at the Wright State University, Dayton, OH. He completed his M.S. and Ph.D. degrees in Electrical and Electronics Engineering in 2004 and 2011 at Middle East Technical University, Ankara, Turkey. He is currently an Assistant Professor in Cankaya University Electrical-Electronics Engineering department, Ankara, Turkey. His fields of interest are electromagnetic theory and antennas.

# Analyze the Crosstalk of Multi-core Twisted Wires and the Effect of Non-matched Impedance Based on BSAS-BPNN Algorithm

**Fubin Pang[1], Jianfei Ji[1], Jiafei Ding[2], Wu Zhang[2], Dong Xu[2], and Mengxia Zhou[2]***

[1]State Grid Jiangsu Electric Power Co., Ltd. Research Institute, Nanjing 211103, China
pangfubin2006@163.com, 15105175122@163.com

[2]School of Electrical & Automation Engineering, Nanjing Normal University, Nanjing 210046, China
2269533002@qq.com, m13571872250@163.com, xd2636864610@outlook.com
*Corresponding author: 61239@njnu.edu.cn

***Abstract –*** In this paper, a multi-core twisted wire model with random non-uniform twists is established. The random combination of complete and non-complete pitch sections is used to accurately simulate the randomness of actual multi-core twisted wires. On the basis of the model, the cross section of the cascaded MTL is obtained, and a neural network algorithm is used to describe the complex relationship between the arbitrary position of the multi-core twisted wires and the unit length parameters. The unit length parameters at any position are obtained by cross section rotational transformation and random transposition transformation between conductors. Finally, the crosstalk in electromagnetic compatibility performance is calculated, and different termination impedances are analyzed. The results show that the crosstalk of multi-core twisted wires is susceptible to the effects of twisting and termination impedance at high frequencies, and the reliability of the proposed method is verified by comparison with full-wave simulation.

***Index Terms –*** BSAS, chain parameters, crosstalk, electromagnetic compatibility (EMC), multi-core twisted wire, non-uniform twisting, neural network algorithm.

## I. INTRODUCTION

Multi-core twisted wires, which often transmit high-speed data between different electronic devices, have the characteristics of low loss, low cost, and small coupling [1–3]. They are widely used in many electrical and electronic systems and other industrial equipment, but they are susceptible to unintentional and intentional electromagnetic interference, where crosstalk becomes important noise in multi-core twisted wires [4, 5], which may lead to electromagnetic compatibility (EMC) problems.

The traditional modeling method is the transmission line model (TLM). In 1980, Taylor and Spadacini et al. initially studied the field-to-line coupling model of twisted wire pair (TWP) placed in the reference plane [6–8] and free space [9]. In [10], the crosstalk between multi-core twisted wires with equal and unequal twist rate was compared, and [11] proposed a multiconductor TLM for analyzing crosstalk of shielded random twisted pair bundles. In addition to crosstalk, [12] studied the influence of non-uniform twist-pitch on the radiated susceptibility of a TWP, and [13] studied the random response of non-uniform multi-strand twisted pairs (MTB-TWP) excited by random plane waves.

In addition to the difference in the model and EMC response of the multi-core twisted wire, there are also differences in the solution method. Based on the TLM method proposed in [5], a closed-form analytical approximation of plane wave coupling is proposed. For non-uniform multiconductor transmission lines, [14, 15] proposed a method for predicting the response of a single TWP and TWP bundles when there is a ground plane illuminated by a plane wave electromagnetic field. In addition, researchers have focused on its statistical characteristics. In [16], a Monte Carlo algorithm was introduced to statistically represent the randomness of manually assembled cables. Furthermore, the random midpoint displacement algorithm [17, 18] and the random displacement spline interpolation method [12] are used to model the randomness of cables. Reference [19] uses cubic Hermite interpolation polynomial to ensure the continuity of the wire. Reference [13] uses the polynomial chaotic random Galerkin method (PC-SGM) to respond under random plane waves.

In this paper, a cross-sectional model of uniform twisted wire is established, and based on this, a cross-sectional model of non-uniform twisted wire is obtained by a neural network method and matrix transposition. The relationship between the unit length parameter matrix at different positions and the degree of twisting and cross section are successfully described

*Submitted On: April 15, 2022*
*Accepted On: November 7, 2022*



https://doi.org/10.13052/2023.ACES.J.380202

mathematically. Using the chain parameter model, near-end crosstalk (NEXT) and far-end crosstalk (FEXT) are given, and numerical experiment results verify the effectiveness of the method. Through a numerical calculation, the terminal crosstalk response of the line can be obtained.

This paper is organized as follows. In Section II, the geometric model and circuit model of multi-core twisted wires with uniform twist and non-uniform twist are established. In Section III, the PUL parameter at any position is obtained through the neural network algorithm and matrix transposition. Secondly, the crosstalk is calculated based on the chain parameter theory of the cascade method. The comparison verification by the numerical simulation technology of the method of moment (MOM) is given in Section IV, and the results of crosstalk and different terminal loads are analyzed. In Section V, conclusions are given.

## II. MULTI-CORE TWISTED WIRE MODEL

### A. Geometric model

In the ideal case, the four core twisted wire is uniformly twisted and has a uniform fixed pitch $p$, as shown in Fig. 1. However, in common engineering practice, multi-core twisted wires will have random non-uniform twists due to artificial and environmental influences. It is a model under the common combination of different complete pitch segments (a certain cable length $l_i$ is an integral multiple of the corresponding pitch $p_i$) and different incomplete pitch segments (a certain cable length $l_i$ is a non-integral multiple of the corresponding pitch $p_i$ at that location). This non-uniform twisting model is shown in Fig. 2, which is essentially a non-uniform transmission line.

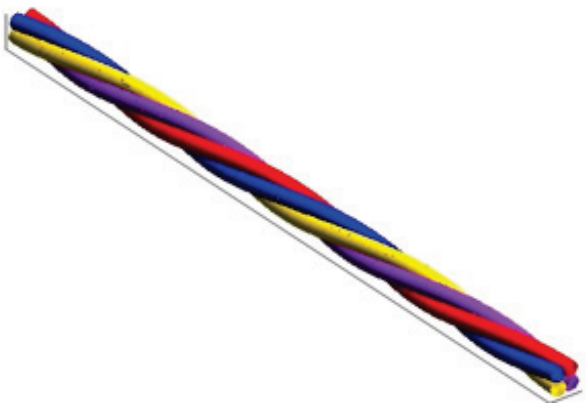

Fig. 1. Uniform twisting model.

The conductor is cylindrical conductor with insulation layer, the radius of conductor is $r$, the height of the center of twist is $h$, and the length of multi-core twisted wire is $L$. The wires are twisted along the $z$-axis. Taking a four core conductor as an example, the central point position of the four conductors is $\vec{l}_{red}\vec{l}_{blue},\vec{l}_{yellow},\vec{l}_{purple}$, under the same abscissa $z$, it can be expressed as follows:

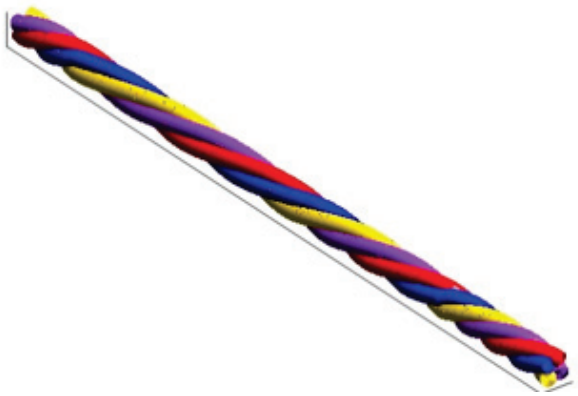

Fig. 2. Non-uniform twisting model.

$$\begin{cases} \vec{l}_r(x_1,y_1,z) = \sqrt{2}r\cos(\theta+\frac{\pi}{4})\vec{a}_x \\ +(h+\sqrt{2}r\sin(\theta+\frac{\pi}{4}))\vec{a}_y + z\vec{a}_z \\ \vec{l}_b(x_2,y_2,z) = \sqrt{2}r\cos(\theta+\frac{3\pi}{4})\vec{a}_x \\ +(h+\sqrt{2}r\sin(\theta+\frac{3\pi}{4}))\vec{a}_y + z\vec{a}_z \\ \vec{l}_y(x_3,y_3,z) = \sqrt{2}r\cos(\theta+\frac{5\pi}{4})\vec{a}_x \\ +(h+\sqrt{2}r\sin(\theta+\frac{7\pi}{4}))\vec{a}_y + z\vec{a}_z \\ \vec{l}_p(x_4,y_4,z) = \sqrt{2}r\cos(\theta+\frac{7\pi}{4})\vec{a}_x \\ +(h+\sqrt{2}r\sin(\theta+\frac{7\pi}{4}))\vec{a}_y + z\vec{a}_z \end{cases}, \quad (1)$$

where $\vec{a}_x\vec{a}_y\vec{a}_z$ are the unit vectors of the $xyz$ axis respectively. $\theta$ is the rotation angle of the section at each position $z$.

Fig. 3 shows the transposition of the wires corresponding to the twisting of the four core twisted wire in a pitch $p$. It can be seen that the cross-sectional rotation angle $\theta$ relative to the initial position and the position $z$ satisfy the functional relationship:

$$\theta = \mathrm{z}(z). \quad (2)$$

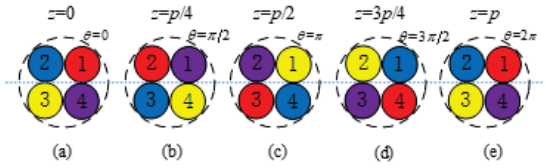


Fig. 3. Sections and rotation angles corresponding to different $z$ values.

Considering the establishment process of the non-uniform model, the cross section and rotation angle of each $z$ value are obtained by changing the pitch length and the transmission line length under the corresponding pitch type. Take $L_i$ as the set of $z$ values in a certain section of the twisted wire, $p_i$ is the pitch length of the

complete and uniform twist at that place, and $l_i$ is the length of the corresponding section along the axial direction (may be an incomplete twist). Then the rotation angle of the section in each section of $L_i$ is:

$$\theta = \begin{cases} \frac{2\pi z}{p_1} & i = 1, z \in L_1 \\ \sum_{j=1}^{i-1} \frac{2\pi l_j}{p_j} + \frac{2\pi(z - \sum_{j=1}^{i-1} l_j)}{p_i} & i \geq 2, z \in L_i \end{cases} . \quad (3)$$

The case of $i$ = 1 corresponds to the case of uniform twisting, and the number of pitch types of general non-uniform twisting is greater than or equal to 2.

### B. Circuit model

The large electromagnetic noise interference caused by multi-core twisted wire is mainly expressed by the crosstalk of the line to the line. Figure 4 shows the terminal conditions at both ends of the multi-core twisted wire model and the equivalent circuit per unit length of the multi-core twisted wire.

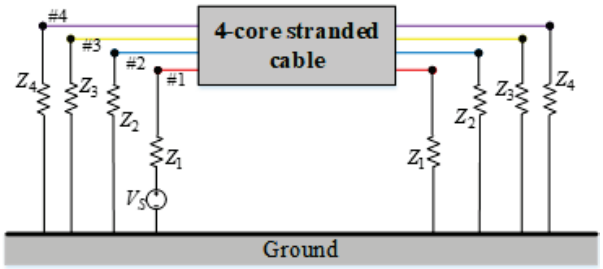


(a)

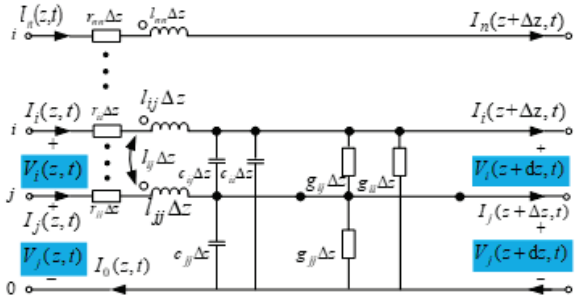

(b)

Fig. 4. Terminal conditions and equivalent circuit: (a) Termination impedance and power supply. (b) The equivalent circuit per unit length of the multi-core twisted wire.

The voltage and current of the transmission line satisfy the following equation:

$$\begin{cases} \frac{d}{dz}\mathbf{V}(z) = -\mathbf{Z}(z)\mathbf{I}(z) \\ \frac{d}{dz}\mathbf{I}(z) = -\mathbf{Y}(z)\mathbf{V}(z) \end{cases}, \quad (4)$$

where $\mathbf{V}(z)$ and $\mathbf{I}(z)$ represent the voltage and current vectors at different positions. $\mathbf{Z}(z)$ and $\mathbf{Y}(z)$ represent the corresponding impedance and admittance at different positions, which can be expressed as:

$$\begin{cases} \mathbf{Z}(z) = \mathbf{R}(z) + jw\mathbf{L}(z) \\ \mathbf{Y}(z) = \mathbf{G}(z) + jw\mathbf{C}(z) \end{cases}, \quad (5)$$

where $\mathbf{R}(z)$, $\mathbf{L}(z)$, $\mathbf{C}(z)$, $\mathbf{G}(z)$ respectively represent the resistance, inductance, capacitance, and conductance matrix of the corresponding cross section at different positions, namely the per unit length (PUL) parameter matrix. They are all symmetric matrices of order n×n. $w$ is the angular frequency of the signal source.

For the convenience of modeling and the unity of description, the four parameter matrices are represented by X. In the model of four core twisted wire with uniform twist, because the rotation of twisted wire is uniform, the parameter matrix X of uniform cross section model in $0^o \sim 90^o$, $90^o \sim 180^o$, $180^o \sim 270^o$, $270^o \sim 360^o$ is the same, but the position is different, so long as the corresponding transformation is carried out:

$$\mathbf{X}(\theta') = \begin{cases} \mathbf{P}\mathbf{X}(\theta)\mathbf{P}^T, & \theta' \in [90°, 180°) \\ \mathbf{P}^2\mathbf{X}(\theta)(\mathbf{P}^T)^2, & \theta' \in [180°, 270°) \\ \mathbf{P}^3\mathbf{X}(\theta)(\mathbf{P}^T)^3, & \theta' \in [270°, 360°) \end{cases}, \quad (6)$$

where $\theta \in [0°, 90°)$, P is the rotation matrix, in the model of this paper:

$$\mathbf{P} = \begin{bmatrix} 0 & 0 & 0 & 1 \\ 1 & 0 & 0 & 0 \\ 0 & 1 & 0 & 0 \\ 0 & 0 & 1 & 0 \end{bmatrix} . \quad (7)$$

In the ideal conductor, in some cases, if the harness of the transmission line has strong conductivity and good insulation performance, it can be regarded as a lossless ideal conductor, that is, $\mathbf{R}(z) = \mathbf{G}(z) = \mathbf{0}$. The corresponding line to line coupling equations for multiconductor transmission lines degenerate into:

$$\begin{cases} \frac{d}{dz}\mathbf{V}(z) = -jw\mathbf{L}(z)\mathbf{I}(z) \\ \frac{d}{dz}\mathbf{I}(z) = -jw\mathbf{C}(z)\mathbf{V}(z) \end{cases} . \quad (8)$$

## III. SOLUTION OF PUL PARAMETERS AND CROSSTALK RESULTS

### A. Acquisition of PUL parameters

Since the RLCG parameter matrices at different positions are different, but due to the geometric characteristics of the multi-core stranded wire, only the RLCG parameters of $0^o \sim 90^o$ are needed to obtain.

However, different positions $z$ correspond to different parameter matrices, and it is difficult to obtain a parameter matrix of any angle in the traditional way. Any certain rotation angle of the cross section has its unique corresponding parameter matrix, and there is a nonlinear mapping relationship between the rotation angle and the parameter matrix. The transformations of the four parameter matrices are all the same. For simple descrip-

tion, the PUL parameter matrix can be expressed as:

$$\mathbf{X}(z)=\begin{bmatrix} x_{11} & x_{12} & \cdots & x_{1n} \\ & x_{22} & \cdots & x_{2n} \\ & & \ddots & \vdots \\ & & & x_{nn} \end{bmatrix}, \tag{9}$$

where $x_{ij}$ represents the specific resistance value $r_{ij}$, inductance value $l_{ij}$, capacitance value $c_{ij}$ and conductance value $g_{ij}$ corresponding to different parameter matrices. There is a complicated mathematical relationship between it and the angle. Therefore, a neural network optimized by the BSAS method can be used to describe this complex mapping relationship. The network topology is shown in Fig. 5.

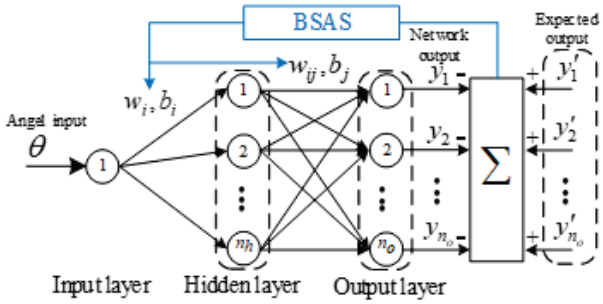


Fig. 5. BSAS-BP neural network topology.

The network is that the number of input layers is 1, that is, the input is the cross-sectional rotation angle $\theta$, the number of hidden layers is $n_h$, and the number of output layers is $n_o$, that is, the output is a column vector composed of the upper triangular elements of the parameter matrix in Equation (4):

$$Y=[x_{11},x_{12},\cdots,x_{nn}]^T. \tag{10}$$

The weights $w_i, b_i$ and thresholds $w_{ij}, b_j$ are optimized using the BSAS optimization algorithm. The specific steps are as follows:

(1) Determine the optimized objective function

The output value of the network is:

$$y_j=\sum_{i=1}^{n_h}\frac{w_{ij}}{1+e^{-w_i\theta+b_j}}+b_j. \tag{11}$$

Arrange all the weights and thresholds to indicate the position of the longhorn beetle in the high-dimensional space:

$$w=\left[w_1,\cdots,w_i,\cdots,w_{ij},\cdots,b_1,\cdots,b_i,\cdots,b_j,\cdots\right]^T. \tag{12}$$

For N groups of data, the mean square deviation between the network output value and the actual value is:

$$f(w)=Ew_{1i},w_{ij}=\frac{1}{2N}\sum_{i=1}^{N}\sum_{j=1}^{n_o}\left(y_j-y_j'\right)^2, \tag{13}$$

where $y_j'$ is the actual given parameter matrix data value, $f(w)$ is the optimized objective function.

(2) Initialize the beetle position vector w and the optimal value of the objective function $f_{best}$

$$w^0=rands\,(k,1), \tag{14}$$

where $w$ represents the initial position of the longhorn beetle in the high-dimensional data space. k represents the dimension of the weight vector, and *rands* represents a row vector that obeys a uniform distribution.

(3) Randomly generate the search direction and location of M groups of longhorn beetles:

$$\begin{cases} dir_n^t=\frac{rands(k,1)}{\|rands(k,1)\|_2} \\ w_n^t=w^t+dir_n^t \end{cases}, \tag{15}$$

where $dir_n^t$ represents the $n$th direction in the $t$th iteration process, $t$ = 0,1,2,. . . .,$n$ = 1,2,. . . ,M.

(4) Obtain the optimal objective function value

Calculate the position of left and right whiskers of longicorn beetles:

$$\begin{cases} w_n^t(r)=w_n^t+\frac{d^t}{2}*dir_n^t \\ w_n^t(l)=w_n^t-\frac{d^t}{2}*dir_n^t \end{cases}, \tag{16}$$

where $d$ is the distance between the left and right whiskers of longicorn beetles, and the sensory intensity of left and right whiskers of longicorn beetles is calculated:

$$\begin{cases} f_n^r=f_n(w_n^t(r)) \\ f_n^l=f_n(w_n^t(l)) \end{cases}. \tag{17}$$

(5) Update longicorn position:

$$w^t=\frac{\arg(\min(f_n^r))+\arg(\min(f_n^l))}{2}, \tag{18}$$

$$w^{t+1}=w^t-\delta^t*dir_n^t*sign(\min(f_n^r)-\min(f_n^l)), \tag{19}$$

where $\delta$is the longhorn beetle step size, the general initial step size is $\delta=\sqrt{k}$, *sign* is the sign function, and the output result is plus or minus 1.

(6) Update the step length and the distance between left and right whiskers of longicorn beetles:

$$\begin{cases} d^{t+1}=0.95d^t+0.01 \\ \delta^{t+1}=0.95\delta^t \end{cases}. \tag{20}$$

For the new one $w^{t+1}$, the position of longicorn in each search direction can be obtained and the next iteration can be carried out. Until the iteration reaches the maximum iteration or the minimum error value is satisfied, the iteration is stopped to obtain the global minimum of the average error.

The PUL parameter matrix of any rotation angle can be predicted by the network trained by the pre-extracted data. Considering the symmetry of TWP cross section and periodicity of rotation angle, the angle of training network only needs to be $0^o\sim90^o$.

Considering the situation of non-uniform twisting, random transposition between wires will occur, as shown in Fig. 6.

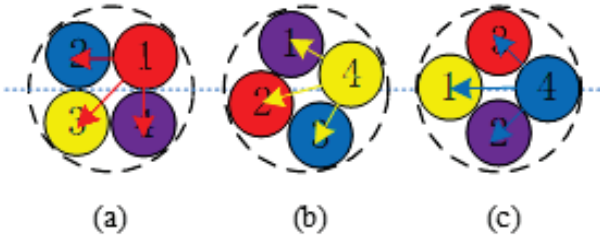


Fig. 6. Random transposition occurs.

First consider that only two conductors are transposed, that is, the *i*th conductor and the *j*th conductor are interchanged. The unit PUL parameter matrix X' after transposition can be expressed as:

$$\mathbf{X}'=\begin{bmatrix} x_{11} & x_{12} & \cdots & x_{1j} & \cdots & x_{1i} & \cdots & x_{1n} \\ & x_{22} & \cdots & x_{2j} & \cdots & x_{2i} & \cdots & x_{2n} \\ & & \ddots & \vdots & \vdots & \vdots & \vdots & \vdots \\ & & & x_{jj} & \cdots & x_{ji} & \cdots & x_{jn} \\ & & & & \ddots & \vdots & \vdots & \vdots \\ & & & & & x_{ii} & \cdots & x_{in} \\ & & & & & & \ddots & \vdots \\ & & & & & & & x_{nn} \end{bmatrix}. \tag{21}$$

The transformation matrix $\mathrm{T}_{ij}$ can be used to represent the transformation of the PUL parameter matrix before and after transposition:

$$\mathbf{X}'=\mathbf{T}_{ij}\mathbf{X}\mathbf{T}_{ij}, \tag{22}$$

where the transformation matrix is:

$$\mathbf{T}_{ij}=\begin{bmatrix} 1 & 0 & \cdots & 0 & \cdots & 0 & \cdots & 0 \\ 0 & 1 & \cdots & 0 & \cdots & 0 & \cdots & 0 \\ \vdots & \vdots & \ddots & \vdots & \vdots & \vdots & \vdots & \vdots \\ 0 & 0 & \cdots & 0 & \cdots & 1 & \cdots & 0 \\ \vdots & \vdots & \vdots & \vdots & \ddots & \vdots & \vdots & \vdots \\ 0 & 0 & \cdots & 1 & \cdots & 0 & \cdots & 0 \\ \vdots & \vdots & \vdots & \vdots & \vdots & \vdots & \ddots & \vdots \\ 0 & 0 & \cdots & 0 & \cdots & 0 & \cdots & 1 \end{bmatrix}. \tag{23}$$

When multiple wires are randomly transposed in the wiring harness, the corresponding parameter matrix can be expressed as:

$$\mathbf{X}=\mathbf{T}_k\cdots\mathbf{T}_1\mathbf{X}\mathbf{T}_1\cdots\mathbf{T}_k, \tag{24}$$

where $\mathrm{T}_k$ is the *k*th transposition, that is, the matrix corresponding to the transposition between certain two conductors, and satisfies $1 \le k \le$ n-1, and n is the number of the cores.

### B. Solving crosstalk with chain parameters

As discussed in the previous section, different positions z and the rotation angle $\theta$ of the cross section can be transformed into each other. In the uniformly twisted multi-core twisted wire model, the PUL within $0^o\sim90^o$ can be obtained through BSAS-BPNN. The PUL within $90^o\sim180^o$,$180^o\sim270^o$,$270^o\sim360^o$ can be obtained by transforming the rotation matrix P. In the non-uniform twisted multi-core twisted wire model, the PUL within $0^o\sim90^o$ can still be obtained by BSAS-BPNN, but the random transposition of the conductor caused by the non-uniform twist can be obtained by the transposition matrix $\mathrm{T}_{ij}$ transformation.

Considering the terminal impedance and power supply in Fig. 4, the transmission line equation can be converted to:

$$\begin{cases} \mathbf{V}(z)=\mathbf{T}_V(z)\mathbf{V}_m(z) \\ \mathbf{I}(z)=\mathbf{T}_I(z)\mathbf{I}_m(z) \end{cases}. \tag{25}$$

The original equation can be reduced to:

$$\begin{cases} \frac{d^2}{dz^2}\mathbf{V}_m(z)=\mathbf{T}_V^{-1}(z)\mathbf{Z}(z)\mathbf{Y}(z)\mathbf{T}_V(z)\mathbf{V}_m(z) \\ \quad =r^2\mathbf{V}_m(z) \\ \frac{d^2}{dz^2}\mathbf{I}_m(z)=\mathbf{T}_I^{-1}(z)\mathbf{Y}(z)\mathbf{Z}(z)\mathbf{T}_I(z)\mathbf{I}_m(z) \\ \quad =r^2\mathbf{I}_m(z) \end{cases}, \tag{26}$$

where $r^2$ is a diagonal matrix of $n\times n$, and $\mathbf{T}_V^T=\mathbf{T}_I^{-1}$.

Considering Equation (4), the relationship between voltage and current is characterized by port. As shown in Fig. 7, it is the chain parameter port based on the cascade idea.

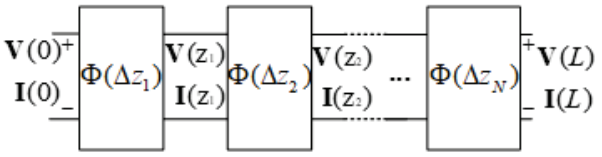


Fig. 7. Transmission line chain parameter model.

Therefore, the voltage and current across each port satisfy:

$$\begin{bmatrix} \mathbf{V}(\Delta z_k) \\ \mathbf{I}(\Delta z_k) \end{bmatrix}=\mathbf{\Phi}(\Delta z_k)\begin{bmatrix} \mathbf{V}(\Delta z_{k-1}) \\ \mathbf{I}(\Delta z_{k-1}) \end{bmatrix}. \tag{27}$$

As shown in Fig. 7, get different chain parameter matrix:

$$\mathbf{\Phi}(\Delta z_k)=\begin{bmatrix} \phi_{11}(\Delta z_k) & \phi_{12}(\Delta z_k) \\ \phi_{21}(\Delta z_k) & \phi_{22}(\Delta z_k) \end{bmatrix}, \tag{28}$$

where $\phi_{11}(\Delta z_k)$, $\phi_{12}(\Delta z_k)$, $\phi_{21}(\Delta z_k)$, $\phi_{22}(\Delta z_k)$ are the chain parameter subarrays, they are:

$$\begin{cases} \phi_{11}(\Delta z_k)=\frac{1}{2}\mathbf{Y}^{-1}\mathbf{T}_I\left(e^{r\Delta z_k}+e^{-r\Delta z_k}\right)\mathbf{T}_I^{-1}\mathbf{Y} \\ \phi_{12}(\Delta z_k)=-\frac{1}{2}\mathbf{Y}^{-1}\mathbf{T}_I\left(e^{r\Delta z}-e^{-r\Delta z_k}\right)\mathbf{T}_I^{-1} \\ \phi_{21}(\Delta z_k)=-\frac{1}{2}\mathbf{T}_I\left(e^{r\Delta z_k}-e^{-r\Delta z_k}\right)r^{-1}\mathbf{T}_I^{-1}\mathbf{Y} \\ \phi_{22}(\Delta z_k)=\frac{1}{2}\mathbf{T}_I\left(e^{r\Delta z_k}+e^{-r\Delta z_k}\right)\mathbf{T}_I^{-1} \end{cases}. \tag{29}$$

Combining the BSAS-BPNN algorithm to obtain the PUL at any position $z$, all the chain parameters $\mathbf{\Phi}(z)$ can be obtained by using Equation (29).

The chain parameters of the transmission line are:

$$\mathbf{\Phi}(L)=\prod_{k=1}^{N}\mathbf{\Phi}_{N-k+1}(\Delta z_{N-k+1}), \tag{30}$$

where N is the divided length of the transmission line, then the voltage and current between the near-end (z = 0) and the far-end (z = L) of the transmission line are:

$$\begin{bmatrix} \mathbf{V}(L) \\ \mathbf{I}(L) \end{bmatrix} = \mathbf{\Phi}(L) \begin{bmatrix} \mathbf{V}(0) \\ \mathbf{I}(0) \end{bmatrix}. \quad (31)$$

The terminal constraints are:

$$\begin{cases} \mathbf{V}(0) = \mathbf{V}_S - \mathbf{Z}_S\mathbf{I}(0) \\ \mathbf{V}(L) = \mathbf{V}_L + \mathbf{Z}_L\mathbf{I}(L) \end{cases}, \quad (32)$$

where $\mathbf{V}_S = [V_S;0;0;0]^T$ is the near-end termination voltage source, and $\mathbf{Z}_S$ is the near-end termination impedance. $\mathbf{V}_L = [0;0;0;0]^T$ is the far-end termination voltage source, and $\mathbf{Z}_L$ is the far-end termination impedance.

Solve for near-end crosstalk (NEXT) and far-end crosstalk (FEXT) as:

$$\begin{cases} \text{NEXT} = 20\log_{10}(\mathbf{V}(0)/V_s) \\ \text{FEXT} = 20\log_{10}(\mathbf{V}(L)/V_s) \end{cases}. \quad (33)$$

## IV. NUMERICAL EXPERIMENT VERIFICATION AND ANALYSIS

### A. Validation of the proposed method

The wire used in this article is a copper core wire, the outer insulating material is PVC, and its thickness is 0.655 mm. In the transmission line, the conductor radius r = 0.335 mm, the ground height h = 15 mm, the transmission line length L = 1 m, which is divided into N = 2000 sections. A small number of PUL parameter matrices are obtained through the finite element method for network training.

In a uniform stranded wire, the method in this paper is used to apply a voltage source to the No. 1 conductor, with the frequency of the power supply range from 0.1 MHz to 1 GHz. The crosstalk results of the Nos. 2, 3 and 4 conductors are calculated and compared with the one based on MOM. As shown in Figs. 8, 9 and 10, it can be seen that there is a high degree of agreement. The effect in the low frequency band ($f$<100 MHz) is better than that in the high frequency band ($f$>500 MHz), and the trend of change the peak and the valleys of the graph are very similar, which can prove the reliability of the method in this paper.

It can be seen that the NEXT and FEXT of No. 2 conductor and No. 4 conductor are very close. This is because the power is applied to No. 1 conductor and the disturbed conductor No. 2 and No. 4 are symmetrically distributed with each other, so the crosstalk magnitudes are so close. In addition, the NEXT of the three conductors has a large change in the high frequency range, while the FEXT has a small change in the high frequency range. This may be because the NEXT is closer to the power supply and is affected more.

Tables 1 and 2 are the average error of NEXT and FEXT between the proposed method and MOM. The average error of both is less than 1 dB in 0.1∼100 MHz,

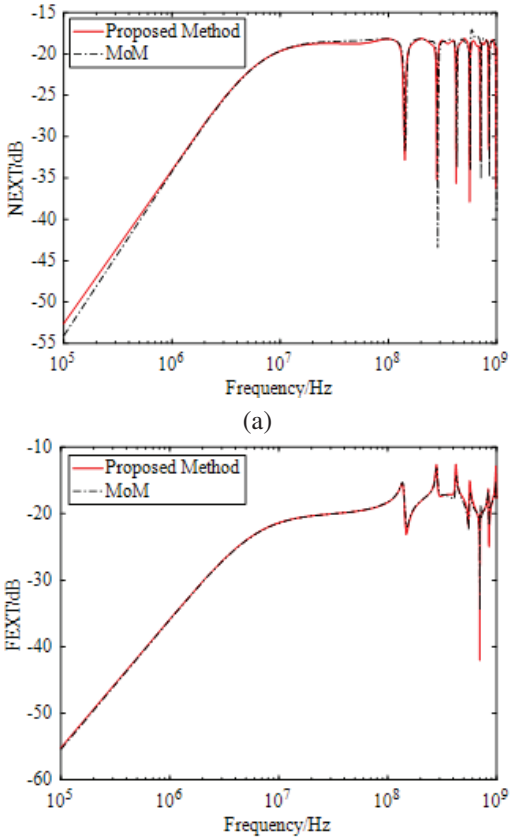


Fig. 8. Crosstalk of No. 2 conductor in uniform stranded wire (a) NEXT, and (b) FEXT.

Table 1: Average error of NEXT (dB)

| Conductor | 0.0001-0.1GHz | 0.1-0.5GHz | 0.5-1GHz |
|---|---|---|---|
| No. 2 | 0.21 | 1.11 | 1.82 |
| No. 3 | 0.30 | 1.51 | 2.12 |
| No. 4 | 0.21 | 1.25 | 2.01 |

2 dB in 0.1∼0.5 GHz, and 3 dB in 0.5∼1 GHz. Compared with NEXT, the average error of FEXT has a smaller difference. Therefore, from the average error point of view, the method in this paper is more accurate in the low frequency and mid–high frequency range. This result further proves that the crosstalk of the uniformly twisted multi-core stranded wire in this paper has a relatively accurate predictive ability.

### B. Crosstalk of non-uniform model

The crosstalk results of non-uniform twisting are shown in Fig. 11. Figures 11 (a) and (b) are NEXT and FEXT, respectively. It calculates 600 sets of models, corresponding to 1800 NEXT and FEXT curves

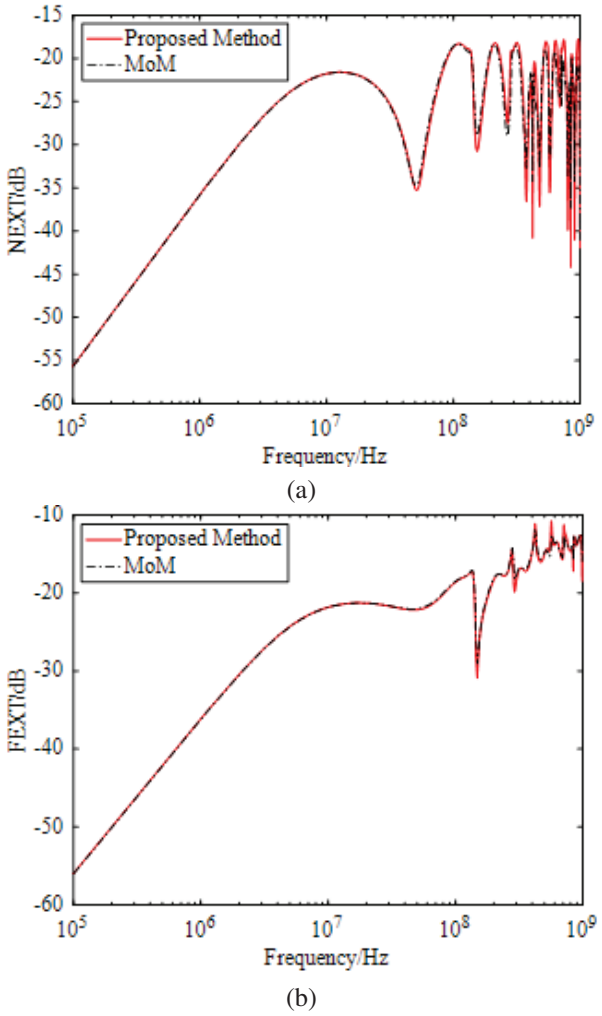


Fig. 9. Crosstalk of No. 3 conductor in uniform stranded wire (a) NEXT, and (b) FEXT.

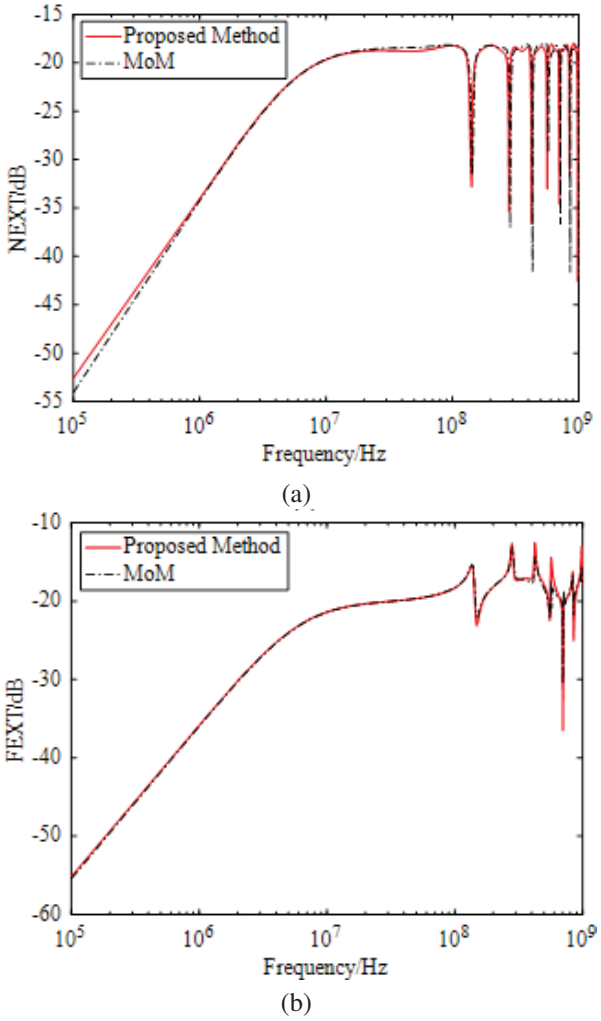


Fig. 10. Crosstalk of No. 4 conductor in uniform stranded wire (a) NEXT, and (b) FEXT.

Table 2: Average error of FEXT (dB)

| Conductor | 0.0001-0.1GHz | 0.1-0.5GHz | 0.5-1GHz |
|---|---|---|---|
| No. 2 | 0.03 | 0.34 | 0.73 |
| No. 3 | 0.10 | 0.34 | 0.50 |
| No. 4 | 0.03 | 0.31 | 0.81 |

each, which more accurately describes the range of non-uniform twisted wire crosstalk. The green dashed line represents the upper envelope value and lower envelope value of the crosstalk, which represent the crosstalk amplitude boundary under the "worst case".

It can be seen that both NEXT and FEXT are very close in the low frequency, while NEXT fluctuates larger in the high frequency, and FEXT fluctuates less. The frequency points of the peak and the valleys are very consistent, but NEXT has more valley frequency points, and FEXT has less valley frequency points.

The maximum value of the upper and lower envelope width of NEXT is 60.534 dB, which is much higher than the maximum value of FEXT's upper and lower envelope width (22.983 dB), and the corresponding frequency of the maximum width is in the high frequency range. Within 0.1 MHz–100 MHz, the average width of the upper and lower envelopes of the NEXT is 1.322 dB greater than the average width of the upper and lower envelopes of the FEXT (0.428 dB). It can be seen that NEXT is easily affected by high frequency signals, which has limited impact on FEXT. Additionally, NEXT is easily affected by the twisting of multi-core twisted wires, while the change of twisting has low influence on FEXT. As the complexity of twisting increases, the curves of NEXT and FEXT will gradually become similar.

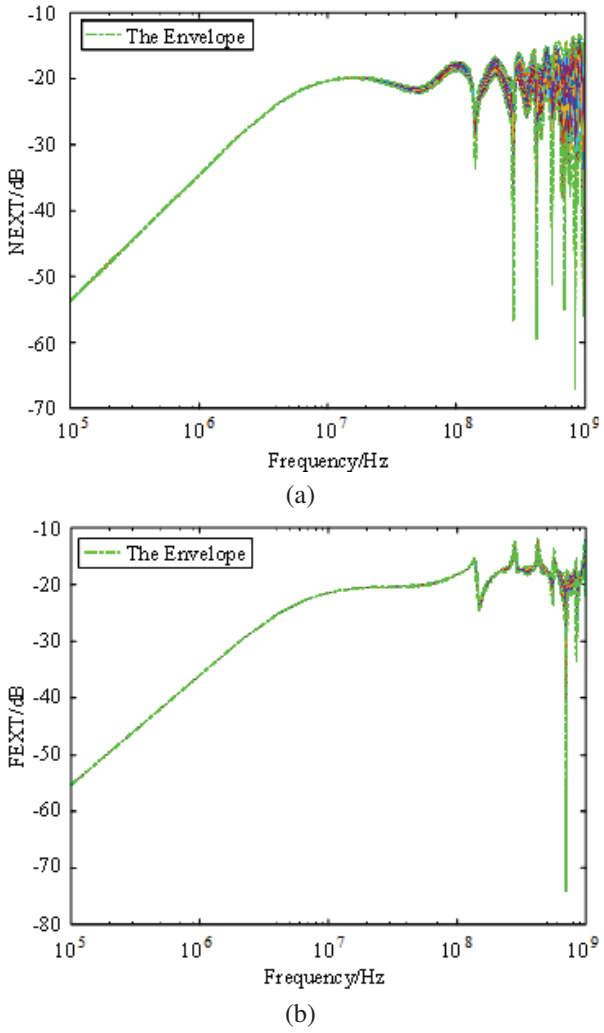


Fig. 11. Crosstalk of non-uniform twisted wires (a) NEXT, and (b) FEXT.

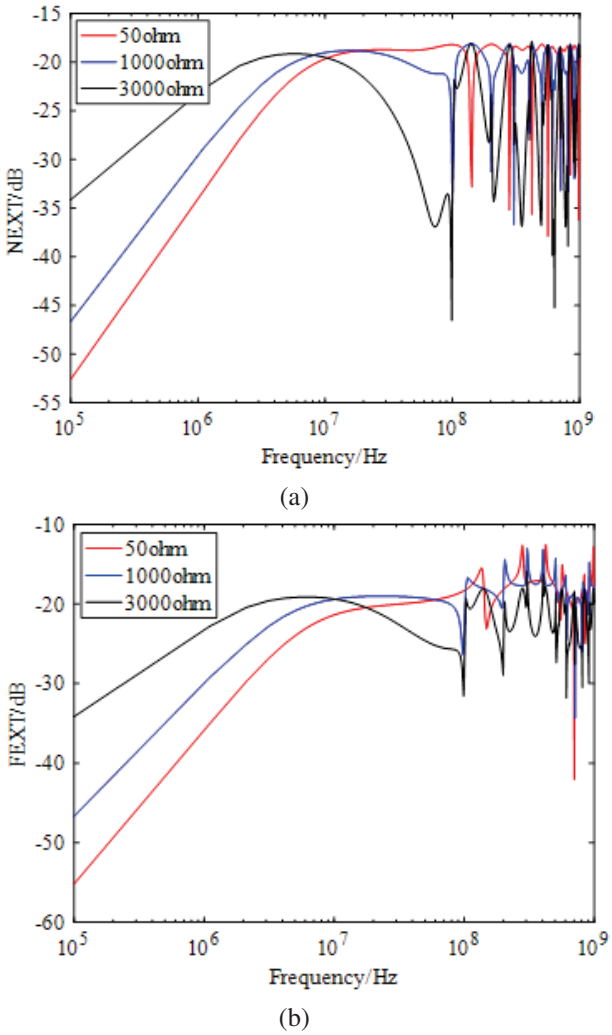


Fig. 12. The crosstalk of terminating different impedances (a) NEXT, and (b) FEXT.

**C. The crosstalk of terminating different impedances**

The crosstalk of terminating different impedances is shown in Fig. 12. Figures 12 (a) and (b) are the NEXT and FEXT curves of terminal matching impedance 50ohm, non-matching resistance 1000 ohm and 3000 ohm. It can be seen that in the low frequency range, both the sizes of NEXT and FEXT are increasing with the increase of load impedance. In the vicinity of 100 MHz, its size decreases as the load impedance increases. In the high frequency range, its changes are more complicated but the trend of changes will basically not change. The maximum amplitude of NEXT has not changed significantly. No matter how the load impedance changes, its value is stable on the same horizontal line, while the maximum value of FEXT decreases as the load impedance increases.

The crosstalk of terminating arbitrary impedance is shown in Fig. 13. Figures 13 (a) and (b) are NEXT and FEXT. A total of 600 sets of terminal loads have been calculated, from 50 ohm to 5000 ohm, corresponding to 1800 NEXT and FEXT curves each, which more accurately describes the impact of different terminal impedances on crosstalk.

It can be seen that NEXT and FEXT curves have opposite trends with impedance on both sides of 106 Hz. And it will cause the original resonance frequency point (108 Hz) of the 50 ohm matching impedance to move forward to 108 Hz after the termination impedance changes. In addition, at certain frequency points, as the termination impedance changes, the peaks and valleys of the original crosstalk curve will be interchanged. However, with the increase and change of the termination

impedance, some common resonance frequency points are more clearly displayed, which will have a guiding role for subsequent EMC applications.

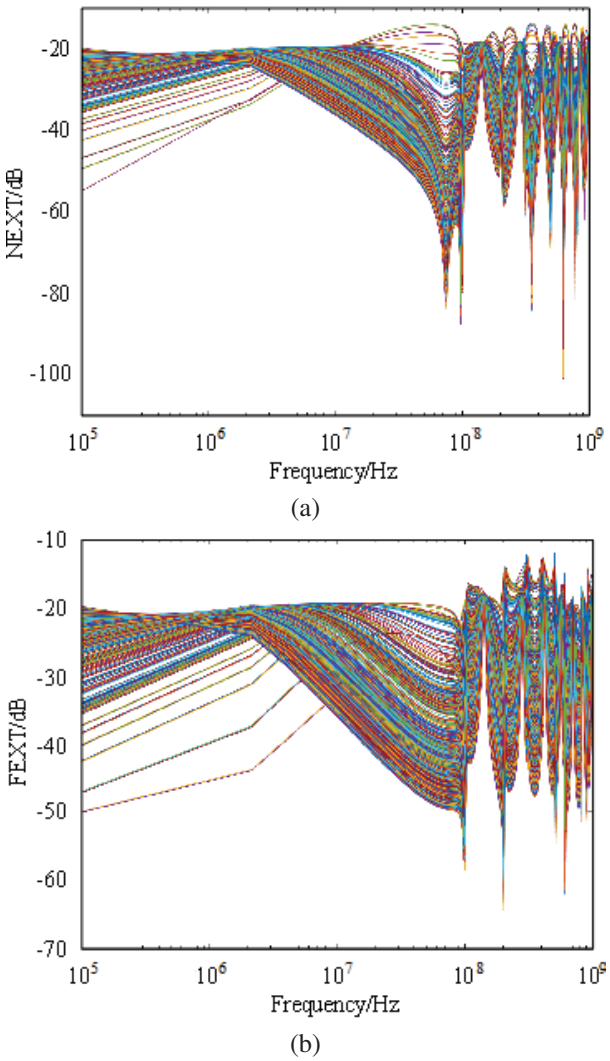


Fig. 13. The crosstalk of terminating arbitrary impedance (a) NEXT, and (b) FEXT.

## V. CONCLUSION

In this article, a model of multi-core stranded wire is proposed. This model includes both uniform twisting and non-uniform twisting, which overcomes the randomness problem in the multi-core stranded wire model.

In addition, the PUL parameter matrix within the rotation angle of the cross section is obtained through a neural network algorithm. The PUL parameter matrix under arbitrary position and non-uniform twisting is extracted. The crosstalk is solved by the chain parameter method with the cascade thought. When compared with the reference method based on MOM, it is shown that the method proposed in this paper has high reliability.

In the crosstalk results, NEXT is easily affected by high frequency signals, and NEXT and FEXT are less affected in the low frequency range. And as the complexity of twisting increases, the curves of NEXT and FEXT will gradually become similar. In the termination of different load impedances, the curves of NEXT and FEXT at about 106 Hz have opposite trends with impedance, which will cause the initial resonance frequency point to shift. With the increase and change of the termination impedance, a more obvious common resonance frequency point can be obtained. These influencing factors and results will have important reference significance in subsequent research and engineering applications.

## ACKNOWLEDGMENT

This paper is supported by Science and Technology Project of State Grid Jiangsu Electric Power Co., Ltd. (J2022121).

## REFERENCES

[1] C. Jullien, P. Besnier, M. Dunand, and I. Junqua, "Advanced modeling of crosstalk between an unshielded twisted pair cable and an unshielded wire above a ground plane," *IEEE Trans. Electromagn. Compat.*, vol. 55, no. 1, pp. 183-194, Feb. 2013.

[2] C. D. Taylor and J. P. Castillo, "On the response of a terminated twisted-wire cable excited by a plane-wave electromagnetic field," *IEEE Trans. Electromagn. Compat.*, vol. 22, no. 1, pp. 16-19, Feb. 1980.

[3] F. Grassi and S. A. Pignari, "Immunity to conducted noise of data transmission along dc power lines involving twisted-wire pairs above ground," *IEEE Trans. Electromagn. Compat.*, vol. 55, no. 1, pp. 195-207, Feb. 2013.

[4] A. Shoory, M. Rubinstein, A. Rubinstein, C. Romero, N. Mora, and F. Rachidi, "Application of the cascaded transmission line theory of Paul and McKnight to the evaluation of NEXT and FEXT in twisted wire pair bundles," *IEEE Trans. Electromagn. Compat.*, vo1.55, no. A, pp.648-656, Aug. 2013.

[5] G. Spadacini, F. Grassi, F. Marliani, and S. A. Pignari, "Transmission-line model for field-to-wire coupling in bundles of twisted-wire pairs above ground," *IEEE Trans. Electromagn. Compat.*, vol. 56, no. 6, pp. 1682-1690, Dec. 2014.

[6] R. Stolle, "Electromagnetic coupling of twisted pair cables," *IEEE J. Sel. Areas Comm.*, vol. 20, no. 5, pp. 883-892, Jun. 2002.

[7] G. Spadacini and S. A. Pignari, "Numerical assessment of radiated susceptibility of twisted-wire pairs

with random nonuniform twisting," *IEEE Trans. Electromagn. Compat.*, vol. 55, no. 5, pp. 956-964, Oct. 2013.

[8] S. A. Pignari and G. Spadacini, "Plane-wave coupling to a twisted-wire pair above ground," *IEEE Trans. Electromagn. Compat.*, vol. 53, no. 2, pp. 508-523, May 2011.

[9] G. Spadacini and S. A. Pignari, "Radiated susceptibility of a twisted-wire pair illuminated by a random plane-wave spectrum," *IEICE Trans. Commun.*, vol. E93-B, no. 7, pp. 1781-1787, Jul. 2010.

[10] J. H. G. J. L. Rotgerink and J. Verpoorte, "Low-frequency closed-form expressions for crosstalk between twisted wire pairs," *2016 ESA Workshop Aeros. EMC*, pp. 1-6, 2016.

[11] X. Song, J. Wang, and B. Li, "Crosstalk model for shielded bundles of random twisted-wire pairs," *IEEE Asia-Pac. Int. Symp. Electromagn. Compat.*, Shenzhen, China, 2016.

[12] A. Tatematsu, F. Rachidi, and M. Rubinstein, "A technique for calculating voltages induced on twisted-wire pairs using the FDTD method," *IEEE Trans. Electromagn. Compat.*, vol. 59, no. 1, pp. 301-304, Feb. 2017.

[13] O. Gassab, S. Bouguerra, and L. Zhou, "Stochastic analysis of multitwisted cables with random parameters excited by random plane-wave fields," *IEEE Trans on Electromagn Compat.*, vol. 62, no. 5, pp. 2084-2095, Oct. 2020.

[14] Y. Yan, L. Meng, X. Liu, T. Jiang, J. Chen, and G. Zhang, "An FDTD method for the transient terminal response of twisted-wire pairs illuminated by an external electromagnetic field," *IEEE Trans. Electromagn. Compat.*, vol. 60, no. 2, pp. 435-443, Apr. 2018.

[15] S. Chabane, P. Besnier, and M. Klingler, "A modified enhanced transmission line theory applied to multiconductor transmission lines," *IEEE Trans. Electromagn. Compat.*, vol. 59, no. 2, pp. 518-528, Apr. 2017.

[16] S. Shiran, B. Reiser, and H. Cory, "A probabilistic model for the evaluation of coupling between transmission lines," *IEEE Trans. Electromagn. Compat.*, vol. 35, no. 3, pp. 387-393, Aug. 1993.

[17] D. Weiner and G. Capraro, "A statistical approach to EMI theory and experiment, part 2," presented at the *1987 Zurich Symp. Electromagn. Compat.*, Zurich, Switzerland, 1987.

[18] S. Salio, F. Canavero, D. Lecointe, and W. Tabbara, "Crosstalk prediction on wire bundles by Kriging approach," *Proc. IEEE Int. Symp. Electromagn. Compat.*, vol. 1, pp. 197-202, Aug. 2000.

[19] S. Sun, G. Liu, J. L. Drewniak, and D. J. Pommerenke, "Hand-assembled cable bundle modeling for crosstalk and common-mode radiation prediction," *IEEE Trans. Electromagn. Compat.*, vol. 49, no. 3, pp. 708-718, Aug. 2007.

**Fubin Pang** (1987), male, senior engineer, mainly engaged in electromagnetic environment simulation of power systems, relay protection of power system, electronic transformer test technology, etc.

**Jianfei Ji** received his Ph.D. degree in Engineering from Harbin Engineering University, entered the postdoctoral workstation of electrical engineering discipline of Jiangsu Electric Power Company and Southeast University in December 2012, and joined the State Grid Jiangsu Electric Power Co., Ltd. Research Institute in 2015.

**Jiafei Ding** graduated from Nanjing Normal University with a bachelor's degree in 2019 and is currently studying for a master's degree at Nanjing Normal University. His main research interests are signal integrity and electromagnetic compatibility of power systems.

**Wu Zhang** received the B.S degree in Electrical Engineering and Automation from Xi'an University of Technology, Xi'an, China, in 2020. He is currently working toward the master's degree at Nanjing Normal University. His main research interests include multiconductor transmission lines and EMC.

**Dong Xu** received his bachelor's degree in Engineering from the School of Electrical Engineering and Automation, Jiangsu University of Science and Technology in 2020. He is currently pursuing a master's degree in electrical engineering at Nanjing Normal University. He is mainly engaged in EMC.

**Mengxia Zhou** obtained a PhD in Physics and Electronics and an M.S. in Electrical Engineering from Nanjing Normal University in 2021 and 2018. His main research interests include electromagnetic compatibility, electromagnetic environment effects and high frequency device modeling.

# Study of High Frequency Characteristics Modeling and EMI Suppression of Common Mode Chokes

**Yakang Pei, Wei Yan, Hao Ma, Mengxia Zhou, and Jian Yang**

School of Electrical and Automation Engineering
Nanjing Normal University, Nanjing 210023, China
eaepyk@nnu.edu.cn, 61197@njnu.edu.cn, mahaonnu@qq.com, 61239@njnu.edu.cn, 1721317641@qq.com
Corresponding author: Mengxia Zhou, 61239@njnu.edu.cn

***Abstract* –** This paper proposes a method for building a high-frequency model of common-mode chokes in the frequency range of 9kHz to 200MHz. The method only needs to measure the common mode and differential mode impedance data of the common mode choke, and then use the differential evolution algorithm to process the impedance data to complete its high-frequency modeling. Comparison with the high-frequency model obtained by using a genetic algorithm shows that the method has high accuracy. After the high frequency modeling of the common mode chokes, the high frequency modeling of the X and Y capacitors is performed using the differential evolution algorithm, and the high frequency model of the EMI filter is obtained by combining it with the established high frequency model of common mode chokes. By comparing the measured and simulated conducted interference noise suppression effect of the EMI filter, the high frequency model of the common mode chokes is verified to suppress the conducted interference, and the effectiveness of the common mode choke high frequency modeling method is determined.

***Index Terms* –** common mode chokes, electromagnetic compatibility, electromagnetic interference, EMI filters and differential evolution algorithm

## I. INTRODUCTION

With the development of the power electronics industry and the gradual application of new materials such as gallium nitride (GaN) and silicon carbide (SiC), the switching frequency and power density of power electronics devices are increasing, and the resulting electromagnetic interference (EMI) is becoming more and more serious. EMI not only reduces the reliability of the power electronic equipment itself, but also pollutes the power grid, and can even lead to the failure of equipment in the grid [1]. Therefore, all electronic equipment must be rectified for its electromagnetic compatibility (EMC) characteristics before production and use. The EMI filter is a low-pass filter whose main function is to transmit the power of DC, 50Hz or 400Hz, to the equipment without attenuation, greatly attenuate the EMI signal introduced by the power supply, and protect the equipment from damage. At the same time, the filter can effectively suppress the EMI signal generated by the equipment itself from entering the power grid, polluting the electromagnetic environment and endangering other equipment. Therefore, EMI filters are indispensable devices to help electromagnetic equipment and systems meet relevant EMC standards, such as IEC, FCC, VDE, MIL-STD-461, and other EMC standards.

A common mode choke (CMC) is a key component of an EMI filter, and its volume generally accounts for 40% of the volume of an EMI filter, which is the cornerstone of EMI filter design. However, due to the parasitic parameters of the CMC in the EMI filter and the frequency characteristics of the magnetic core material, the performance of the EMI filter will decrease above a certain frequency, resulting in unexpected EMI suppression effects. Therefore, the study of the high-frequency characteristics of CMC is conducive to better suppression of conducted interference, thereby helping to improve the performance of EMI filters. The CMC core material is usually Mn–Zn ferrite, nanocrystalline and other magnetic materials [2]. Due to the common influence of the frequency characteristics of CMC core materials, parasitic capacitance, and winding leakage inductance, the frequency characteristics of a CMC are significantly different from the ideal value, which also brings challenges to the research of CMCs.

In recent years, there have been much research on CMC modeling methods at home and abroad; for example, the common mode and differential mode S parameters of a CMC have been obtained through three measurement methods, and then its passive equivalent circuit model established, the parasitic inductive coupling parameters extracted through network gain measurement, and the performance of EMI filter analyzed. The parameters in the CMC high-frequency model have been extracted by impedance measurement and combined with an iterative rational function approximation fitting algorithm. There have been studies on identifying and

*Submitted On: September 22, 2022*
*Accepted On: January 18, 2023*
https://doi.org/10.13052/2023.ACES.J.380203

quantifying the physical mechanisms leading to changes in the attenuation of CMCs and EMI filters by analyzing the effect of conductive strips placed close to the CMC on the attenuation provided by CMC-mounted EMI filters [3–17].

However, there are still deficiencies in previous research, specifically: although the literature [18] initially gave a modeling method for CMC based on impedance measurement, the influence of the decrease of the common mode inductance value with the increase of the frequency has been ignored and the effects of factors such as leakage capacitance have not been considered. Therefore, the proposed modeling method is not perfect. In the literature [19], Henglin Chen improved the CMC high-frequency modeling method based on impedance measurement implementation and established a more accurate CMC high-frequency model. However, the impedance extraction of this method is based on the impedance analyzer, while the vector network analyzer (VNA) and the optimization algorithm used in this paper provide another reference for the high frequency modeling of CMCs. In addition, Stevanovic I [20] made common mode (CM) and differential mode (DM) circuits connected together by adding mutual inductance to the inductor in the CMC equivalent circuit, which avoided studying the CM and DM parts of the CMC separately. Although Stevanovic I used a genetic algorithm (GA) in high-frequency modeling, the algorithm was proposed earlier and converged slowly when the impedance formula was more complex, which was not favorable for the extraction of *RLC* values.

The second part of this paper introduces the application of a differential evolution algorithm (DE) algorithm in CMC high-frequency modeling; the third part establishes the CMC high-frequency modeling by using a DE algorithm and the method of split-band fitting, and compares the impedance curves of the high-frequency model established by the GA algorithm and DE algorithm, after which the X-capacitor and Y-capacitor high-frequency models are also established; the fourth part verifies the suppression effect of the CMC high-frequency model that has been established in this paper on the conducted interference noise, and verifies the effectiveness of this high-frequency modeling method.

## II. DE ALGORITHM IN THE EMI FILTER HIGH FREQUENCY MODELING

### A. DE algorithm principles

The DE algorithm is a parallel direct search algorithm that performs random operations on candidate populations. The steps are mainly to initialize the randomly selected population and initialize the parameters of the DE algorithm, and then determine whether the termination conditions are satisfied. At this point, if the termination condition is not satisfied, the mutation operation, crossover operation, and selection operation will be performed, followed by an iterative loop, and then the above steps will be performed once more until the termination condition is satisfied; the flow chart is shown in Fig. 1.

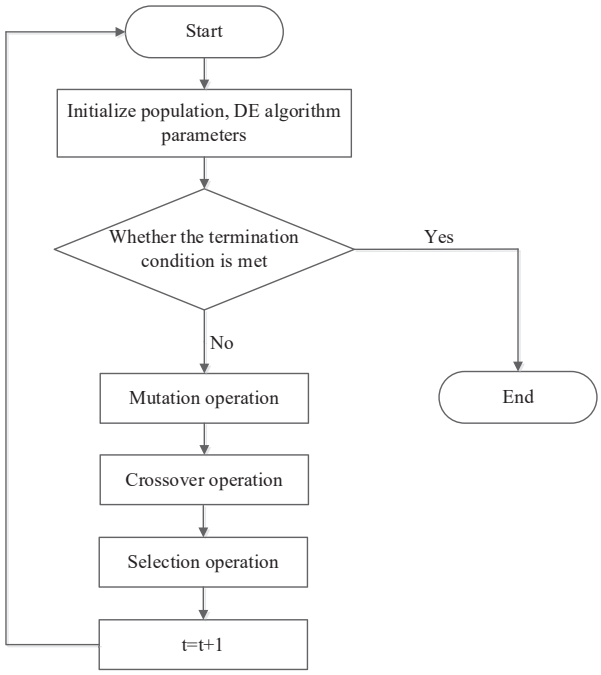


Fig. 1. DE algorithm flow chart.

### B. Application of the DE algorithm in CMC high frequency modeling

The DE algorithm is used for high frequency modeling of the CMC, in essence, the impedance measurement data of the CMC is processed using the DE algorithm to solve the relevant *RLC* parameters in its equivalent circuit in order to obtain the optimal solution of the above parameters. The specific steps of the DE algorithm to process the impedance data of CMC are as follows [21].

Step 1: Propose the equivalent circuit topology of the CMC and obtain the expressions of its CM and DM impedances.

In this paper this is the CM impedance expression $Z_{CM}$ and the DM impedance expression $Z_{DM}$.

Step 2: Extraction of device impedance information.

The CMC equivalent circuit modeling based on the DE algorithm needs to solve the expression about the impedance $Z$ derived from its equivalent circuit model according to the impedance information of the CMC, so as to obtain its optimal equivalent model *RLC* parameters.

Step 3: Optimal parameter problem transformation.

The impedance expression obtained from the CMC equivalent circuit topology is transformed into an expression for the impedance amplitude $Z_x$, and then $Z_x$ is used as the original function of the *RLC* parameters to be optimized, and the measured impedance data $Z_m$ is the sample. Let the expression of the CM or DM impedance $Z_x$ of the CMC equivalent circuit model be:

$$\begin{aligned} &Z_x=\varphi(f;x_1,x_2,x_3,...,x_D) \\ &s.t \quad x_j^L \le x_j \le x_j^U \quad j=1,2,3,...,D, \end{aligned} \tag{1}$$

where $D$ is the spatial dimension, $D \subset R^n$, $x_j^L$ and $x_j^U$ denote the maximum and minimum values of the $j$th component $x_j$, respectively, $f$ is an independent variable, $Z_x$ is a dependent variable, and $x_1,x_2,x_3,...,x_D$ are the parameters to be determined, which are the *RLC* parameters of the CM (DM) impedance equivalent model in this paper. The DE algorithm is applied to the *RLC* parameter extraction of the CM (DM) equivalent impedance, and its optimization criterion function can be established by the least-square sum of the residuals of the system model as follows:

$$\min Q = \sum_{i=1}^{N} \left| \varphi(f_i) - \varphi(f_i)' \right|^2. \tag{2}$$

Step 4: Initialize the parameters.

For the initial populations $\left\{ x_i(0) x_{j,i}^L \le x_{j,i}(0) \le x_{j,i}^U, i=1,2,3,\ldots,N_P; j=1,2,3,...,D \right\}$ randomly generated,

$$x_{j,i}(0) = x_{j,i}^L + \text{rand}(0,1) \cdot \left( x_{j,i}^U - x_{j,i}^L \right), \tag{3}$$

where $N_P$ is the population size, $x_i(0)$ refers to the $i$th individual of generation 0 in the overall population, and $x_{j,i}(0)$ refers to the $j$th gene of the $i$th individual of generation 0. rand(0,1) denotes the number of random distributions between 0 and 1.

Step 5: Variation operation.

The DE algorithm takes the actual value parameter vector as the population of each generation and the weighted difference of two individuals in the population as the intermediate individual, i.e., the difference vector. The difference vector is then added to the third individual to generate mutations as follows:

$$v_i(g+1) = x_{r1}(g) + F\left( x_{r2}(g) - x_{r3}(g) \right), \tag{4}$$

where $F$ is the mutagenic factor and $x_i(g)$ is the $i$th individual of the $g$-generation population.

Step 6: Crossover operation.

The crossover operation refers to the exchange of some components of individuals in the current population with the corresponding components of mutant individuals according to certain rules to produce a crossover population. $g$-generation population $|x_i(g)|$ and its variant $\{v_i(g+1)\}$ are crossed over as follows:

$$u_i(g+1) = \begin{cases} v_{j,i}(g+1), & \text{if and } (0,1) \le C_R \\ x_{j,i}, & \text{otherwise} \end{cases}, \tag{5}$$

where $j_{rand}$ is a random integer in [1,2,3,...,$D$] and $C_R$ is the crossover probability.

Step 7: Selection operation.

If the objective function of the next generation individual is smaller than that of the current individual, the next generation individual will replace the current individual:

$$x_i(g+1) = \begin{cases} u_i(g+1), & \text{if } f(u_i(g+1)) \le f(x_i(g)) \\ x_i(g), & \text{otherwise} \end{cases}. \tag{6}$$

Step 8: Convergence discriminant operation.

Let the optimal individual in $x(g+1)$ be $x_{best}(g+1)$. The operation can be finished when DE runs to a predetermined number of times or the objective function value $Q$ reaches the set accuracy, and the predicted result is the optimal value of *RLC* parameters. If there is no convergence, the operation returns to the second step and performs variation, crossover, and selection again.

## III. CMC AND CAPACITOR HIGH FREQUENCY MODELING

The physical and circuit topology of the EMI filter used in this paper is shown in Fig. 2, followed by modeling of the high frequency characteristics of the CMC, X capacitor and Y capacitor, respectively.

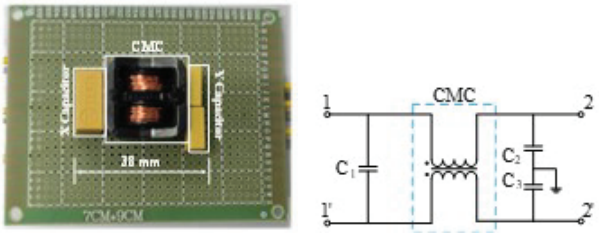


(a) EMI filters (b) Circuit topology

Fig. 2. EMI filter physical and circuit topology.

### A. CMC high frequency modeling

The equivalent model of the CMC is shown in Fig. 3. The model consists of multiple CM and DM resonant stages corresponding to resonances that may appear in the measured CMC impedance waveform, and also to improve high-frequency model accuracy. Each resonant stage consists of a pair of coupled inductors, where the coupling coefficient $k_C$ = 1 between the upper and lower inductors of the resonant stage in the common mode part and $k_D$ = −1 between the upper and lower inductors of the resonant stage in the differential mode part. The introduction of the mutual inductance factor ensures that, ideally, the differential mode path is shorted when the circuit flows common mode current and the common mode path is shorted when the differential mode current

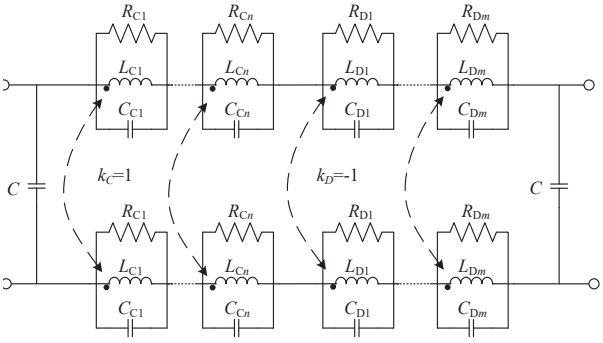


Fig. 3. CMC high frequency equivalent circuit.

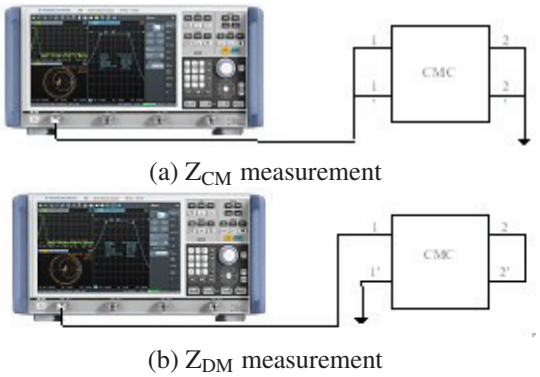


(a) $Z_{CM}$ measurement

(b) $Z_{DM}$ measurement

Fig. 4. CMC impedance measurement.

flows [20]. $R_{Ci}$ and $R_{Di}$ represent the core resistance, reflecting the energy loss in the ferrite core due to hysteresis and eddy currents energy loss of the ferrite core; $C_{Ci}$ and $C_{Di}$ represent the intra-winding capacitance; $C$ is the inter-winding capacitance.

Since the two windings of the CMC are completely symmetrical in practice, to reduce CM EMI noise, an attempt is made to ensure that the line impedance where the two windings are located is balanced, so the effect of $C$ on the CM path can be disregarded. Therefore, in the CM path, the CMC equivalent circuit can be viewed as a circuit with complete symmetry between the upper and lower components [19]. In the DM path, because $C$ is tolerant when the frequency is very low, therefore, when performing data fitting, the value of $C$ is only obtained from the starting frequency point to the first valley frequency range of the measured impedance value, and the value of other frequency bands is the same.

After determining the circuit topology of the CMC, the next step is to measure the impedance of the CMC. In this paper, we use a VNA to measure the impedance of CMC. When measuring the CM impedance of the CM path $Z_{CM}$, ports 1 and 2 are shorted and then connected to the VNA, as shown in Fig. 4 (a), the expression of the CM path impedance relative to it is

$$Z_{\mathrm{CM}} = \frac{\mathrm{j}\omega R_{\mathrm{C}i} L_{\mathrm{C}i}}{R_{\mathrm{C}i} + 2\mathrm{j}\omega L_{\mathrm{C}i} - 2\omega^2 R_{\mathrm{C}i} L_{\mathrm{C}i} C_{\mathrm{C}i}}. \tag{7}$$

When measuring the DM impedance $Z_{DM}$ of the DM path, the two ports of the CMC are short-circuited, as shown in Fig. 4 (b), and the expression of the differential mode path impedance relative to it is

$$Z_{\mathrm{DM}} = \left( \mathrm{j}\omega C + \left( \frac{4\mathrm{j}\omega R_{\mathrm{D}i} L_{\mathrm{D}i}}{R_{\mathrm{D}i} + 2\mathrm{j}\omega L_{\mathrm{D}i} - 2\omega^2 R_{\mathrm{D}i} L_{\mathrm{D}i} C_{\mathrm{D}i}} \right)^{-1} \right)^{-1}. \tag{8}$$

In order to obtain high accuracy *RLC* values on a computer with limited performance for high frequency modeling of CMC, this paper uses a segmented fitting method to process the measured impedance data, i.e., the first segment from the start frequency to the first trough of the impedance waveform, the second segment from the first trough to the second trough, and so on. In this method, even if a professional workstation computer is not used, a personal computer can be used to process the measured impedance data and obtain the *RLC* values with high accuracy.

Table 1: *RLC* values of CMC CM and DM

| CM | $i=1$ | $i=2$ | DM | $i=1$ | $i=2$ |
|---|---|---|---|---|---|
| $R_{Ci}$ | 19.9 kΩ | 0.16 kΩ | $R_{Di}$ | 17.4 kΩ | 0.42 kΩ |
| $L_{Ci}$ | 0.19 mH | 8.77 nH | $L_{Di}$ | 7.67 μH | 4.46 nH |
| $C_{Ci}$ | 7.20 pF | 19.60 pF | $C_{Di}$ | 2.39 pF | 41.8 pF |

The fitting process of the common-mode impedance can be seen from the description of the application of the DE algorithm in the high-frequency modeling above. We have completed the first and second steps, and then replaced Eq. (1) with Eq. (7), and the measured impedance data is the sample $Z_m$. We then wait for the algorithm to run and then extract the *RLC* value from the common-mode impedance data. The same is true for the fitting of the differential mode impedance, but it should be noted that the intergroup capacitance $C$ comes from the first frequency band. Therefore, we use the DE algorithm and Eq. (8) to extract the value of *RLC* and the value of the inter-winding capacitance $C$ in the first frequency band. In the frequency bands other than the first frequency band, we substitute the value of the inter-group capacitance $C$ into Eq. (8), and then use the newly obtained formula to extract the value of the *RLC* of the remaining frequency segments.

The values of *RLC* extracted by the DE algorithm are shown in Table 1, while the parasitic capacitance between windings $C$ = 3.56 pF. A comparison of the simulated and measured CMC CM and DM impedance

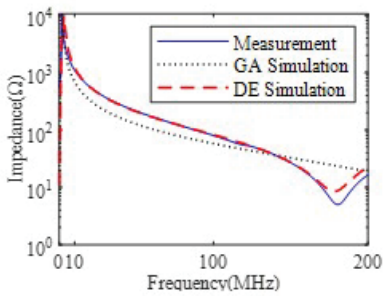


(a) Comparison between measured and simulated $Z_{CM}$

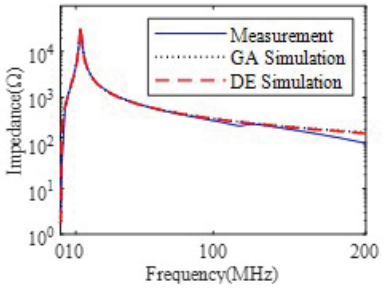


(b) Comparison between measured and simulated $Z_{DM}$

Fig. 5. Comparison between simulation and measurement of the CMC impedance waveform.

waveforms based on the GA and DE algorithms, respectively, is shown in Fig. 5. It can be seen from Fig. 5 that, in the low frequency band, the CM impedance and DM impedance curves of the CMC tend to match the measured ones regardless of the algorithm. In the high frequency section, the simulated and measured impedance curves show that the DE algorithm has better accuracy than the GA algorithm for the high frequency model in the CM path.

The reason for such different results is that although both the DE algorithm and the GA algorithm randomly generate the initial population, the fitness value of each individual in the population is the selection criterion, and the main process also includes three steps of mutation, crossover and selection. However, the GA algorithm is based on the fitness value to control the crossing of the parent generation. The probability value of the offspring generated after the mutation is selected. In the maximization problem, the individual with a large fitness value has a correspondingly higher probability of being selected. The DE algorithm mutation vector is generated by the difference vector of the parent generation, and crosses with the individual vector of the parent generation to generate a new individual vector, which is directly selected by means of the individual of the parent generation. Therefore, the approximation effect of the differential evolution algorithm is more significant than that of the genetic algorithm, which also makes the model established using the DE algorithm more accurate than the GA algorithm in this paper.

### B. High frequency modeling of capacitors

After the high-frequency characteristic modeling of the CMC is completed, the high-frequency characteristic modeling of the capacitor is carried out next. The X capacitance values used in this paper are $C_1$ = 4.7 $\mu$F and Y capacitance $C_2$ = $C_3$ = 2200 pF. The high-frequency equivalent model of the capacitor is shown in Fig. 6.

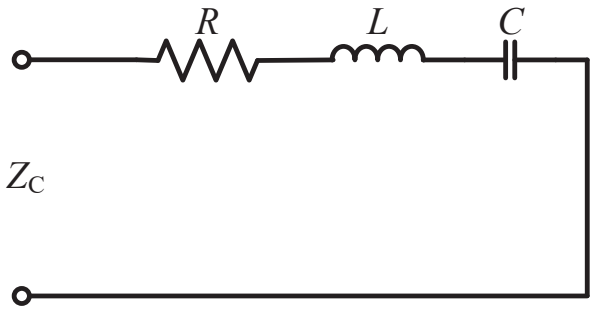


Fig. 6. High frequency model of capacitance.

The following is the same as the CMC high-frequency modeling method. First, the impedance data of the capacitor at different frequencies are measured using the VNA. Then, impedance data is processed using the DE algorithm. Finally, the *RLC* value of the high-frequency equivalent model of the capacitor is shown in Table 2, and the impedance comparison between measured and simulated data is shown in Fig. 7. It can be seen from Fig. 7 that, regardless of high frequency or low frequency, the DE algorithm can extract the relevant parameters of the capacitor very well.

Table 2: Capacitor high frequency equivalent model *RLC*

| | $C_1$ | $C_2$, $C_3$ |
|---|---|---|
| *R* | 0.19 Ω | 0.18 Ω |
| *L* | 26.2 nH | 28.3 nH |
| *C* | 0.48 uF | 2.85 nF |

## IV. CMC CONDUCTED INTERFERENCE SUPPRESSION ANALYSIS

In the above we have finalized the EMI filter components of the high-frequency model, according to its topology, in order to assemble the EMI filter to complete the establishment of a high-frequency model. In order to analyze the suppression effect of the high-frequency equivalent model of the EMI filter on the conduction

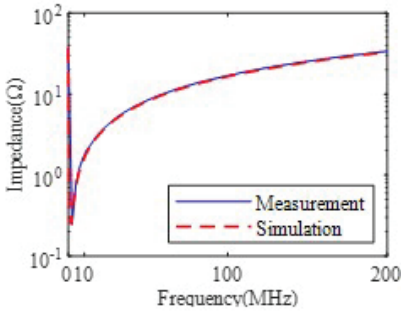


(a) $C_1$ impedance measurement and simulation comparison

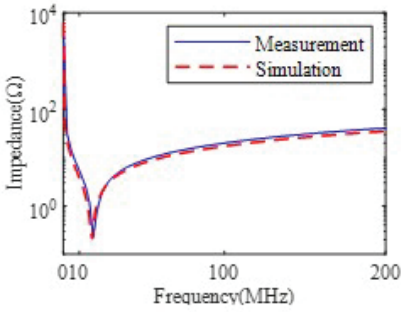


(b) $C_2$, $C_3$ impedance measurement and simulation comparison

Fig. 7. Comparison of the capacitive impedance simulation and actual measurement.

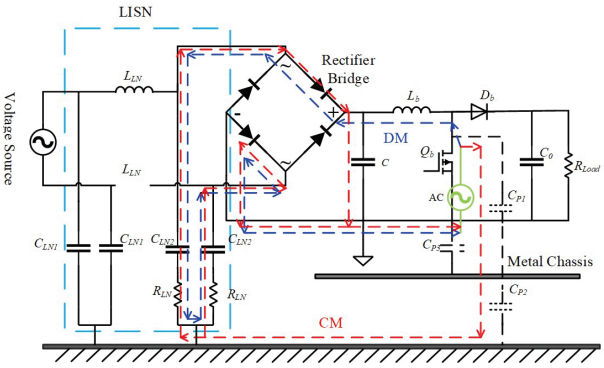


Fig. 8. Boost PFC circuit interference propagation path.

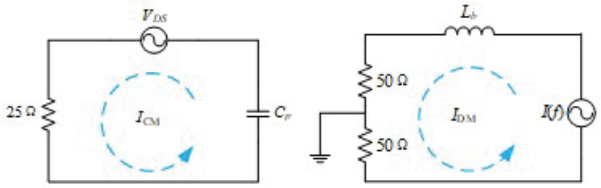

(a) Conductive CM path equivalence diagram

(b) Conductive DM pathequivalence diagram

Fig. 9. Conducted interference path equivalence diagram.

interference, this paper selects a switching power supply with an output of 24 V/2 A, 48 W to do the actual measurement and comparison of the interference. The switching power supply is a Boost PFC circuit, and the two diodes of the rectifier bridge are forward-biased conducting; the interference propagation path is shown in Fig. 8 [22], in which MOSFET $Q_b$ is the main noise source.

In the analysis of the conducted interference, in order to simplify the analysis, in the CM path when only the MOSFET drain voltage $V_{DS}$ as a CM conducted interference noise source, the line impedance stabilization network (LISN) structure is simplified to two 50 Ω parallel test impedances in a simplified circuit, as shown in Fig. 9 (a). DM interference is caused by high-frequency interference currents in the loop, while the PFC circuit DM conducted EMI interference is usually considered to be caused by the ripple of the inductor current $i_b$. This current is the DM current driven by the MOSFET drain voltage $V_{DS}$ along the loop, as shown in Fig. 8, this loop consists mainly of a MOSFET, a rectifier bridge, and a LISN test resistor. For the differential mode current, the series connection of the L and N two-wire test impedance of the LISN can be equivalent to a 100 Ω resistance, as shown in Fig. 9 (b).

In this paper, because the high-frequency model of the CMC introduced the mutual inductance coefficient, the conducted interference simulation does not have to be divided into CM and DM paths. In the conducted interference simulation modeling, the output of a square wave voltage source is a noise source, so as to verify the EMI high-frequency model of the conducted interference noise suppression capability. The conducted interference simulation is built in PSpice, a simulation schematic of which is shown in Fig. 10 (a). The $V_s$ consists of a square wave voltage source with a frequency of 20 kHz, a voltage of 0.05 V and a resistor of 50 Ω. The circuit topology is shown in Fig. 11. $V_1$ is a DM interference source, $V_2$ and $V_3$ together form a CM interference source to simulate the noise source of the conducted EMI generated by the boost circuit during operation. The conducted interference noise test apparatus of the switching power supply is arranged as shown in Fig. 10 (b). Simulation of the conducted interference waveform, as well as the EMI filter to suppress the interference waveform, is shown in Fig. 12 (a); measured with and without EMI filter conducted interference waveform. The results are shown in Fig. 12 (b).

From Fig. 12, it can be found that the EMI filter in the real test has a good suppression of conducted interference, and the EMI filter high-frequency equivalent model also reflects this suppression ability. Since

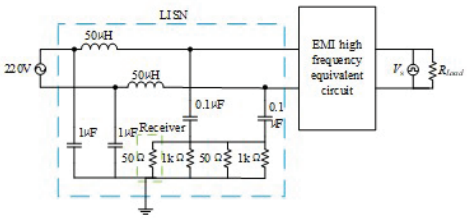


(a) Conducted interference simulation schematic

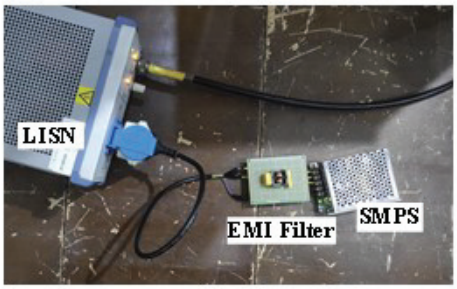


(b) Conducted disturbance actual measurement layout

Fig. 10. Conducted interference noise simulation and actual measurement chart.

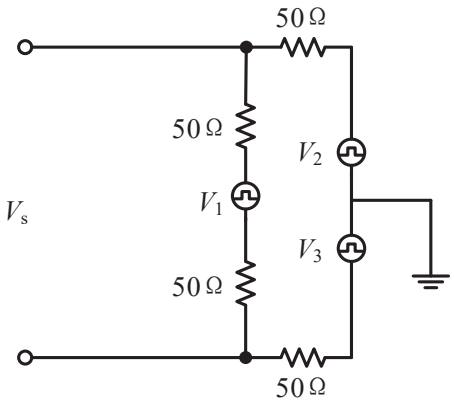


Fig. 11. Interference source circuit topology.

the noise source in the simulation is ideal and only simulates the switching frequency in the actual operation of the switching power supply, it does not fully reflect the real noise of the switching power supply used in the actual test. However, by comparing the measured and simulated, EMI filter suppression of the conducted interference can be found. The EMI filter high-frequency model can reflect the conductive interference suppression ability of the filter, but also proves that the modeling method of this paper works.

## V. CONCLUSION

This paper proposes a method for modeling the CMC high frequency model in the frequency range from

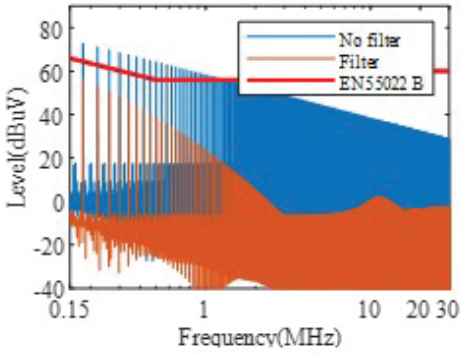


(a) Simulation

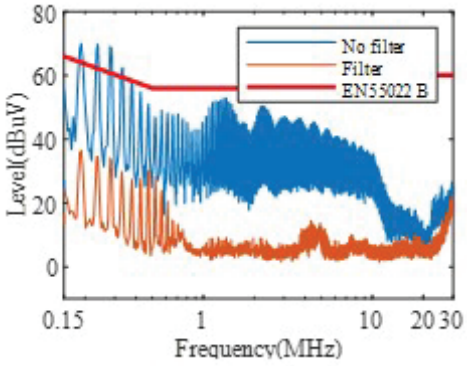


(b) Measurement

Fig. 12. Conducted interference noise waveform diagram.

9 kHz to 200 MHz. The method only requires measuring the CM and DM impedance data and extracting the *RLC* value from the impedance data by using the DE algorithm in separate frequency bands to complete the CMC high frequency modeling. Then, based on the built CMC high-frequency model, a high-frequency model of the EMI filter is further established. This high-frequency model does not need to be divided into CM and DM channels when performing conduction interference simulation. Finally, the EMI filter high frequency equivalent model is used to build a simulation test model of conducted interference noise, which verifies the suppression capability of the CMC high-frequency equivalent model for conducted interference noise and radiated interference noise.

In addition, this modeling method adopts the fitting method of sub-frequency bands, so the establishment of high-frequency models can be completed on personal computers without professional workstations. The use of the DE algorithm in extracting the *RLC* value in the impedance data can complete the establishment of the CMC high-frequency model in the frequency range

9 kHz to 200 MHz while maintaining high accuracy. In addition, because the high-frequency model of the EMI filter in the frequency range 9 kHz to 200 MHz can be obtained by using this modeling method, the model can also provide a reference for the radiation interference suppression of the switching power supply.

## ACKNOWLEDGMENT

This paper is supported by National Natural Science Foundation of China (52107005).

## REFERENCES

[1] C. R. Paul, *Introduction to Electromagnetic Compatibility*, 2nd edn., John Wiley & Sons, New York, pp. 414-426, 2005.

[2] H. Chen, Y. Hu, and L. Wang, "EMI filter design based on high-frequency modeling of common-mode chokes," *IEEE 27th International Symposium on Industrial Electronics (ISIE)*, pp. 384-388, 2018.

[3] H. Hemphill and B. Wallertz, "Critical core parameters in the design of common mode suppression chokes," *International Conference on Electromagnetic Interference and Compatibility (INCEMIC)*, pp. 334-336, 1995.

[4] Z. Li, D. Pommerenke, and Y. Shimoshio, "Common-mode and differential-mode analysis of common-mode chokes," *IEEE Symposium on Electromagnetic Compatibility. Symposium Record (Cat. No.03CH37446)*, vol. 1, pp. 384-387, 2003.

[5] W. Shen, F. Wang, D. Boroyevich, V. Stefanovic, and M. Arpilliere, "Optimizing EMI filter design for motor drives considering filter component high-frequency characteristics and noise source impedance," *Nineteenth Annual IEEE Applied Power Electronics Conference and Exposition*, vol. 2, pp. 669-674, 2004.

[6] J. R. Regue, M. Ribo, D. Duran, D. Badia, and A. Perez, "Common and differential mode characterization of EMI power-line filters from S-parameters measurements," *International Symposium on Electromagnetic Compatibility (IEEE Cat. No.04CH37559)*, vol. 2, pp. 610-615, 2004.

[7] A. Roc'h and F. Leferink, "In situ performances of common mode chokes," *10th International Symposium on Electromagnetic Compatibility*, pp. 494-499, 2011.

[8] H. Chen and Z. Qian, "Modeling and characterization of parasitic inductive coupling effects on differential-mode EMI performance of a boost converter," *IEEE Transactions on Electromagnetic Compatibility*, vol. 53, pp. 1072-1080, 2011.

[9] J. Kotny, X. Margueron, and N. Idir, "High-frequency model of the coupled inductors used in EMI filters," *IEEE Transactions on Power Electronics*, vol. 27, pp. 2805-2812, 2012.

[10] W. Tan, C. Cuellar, X. Margueron, and N. Idir, "A high frequency equivalent circuit and parameter extraction procedure for common mode choke in the EMI filter," *IEEE Transactions on Power Electronics*, vol. 28, pp. 1157-1166, 2013.

[11] A. Asmanis, G. Asmanis, D. Stepins, and L. Ribicks, "High-frequency modelling of EMI filters considering parasitic mutual couplings," *ESA Workshop on Aerospace EMC (Aerospace EMC)*, pp. 1-6, 2016.

[12] F. Hami, H. Boulzazen, and M. Kadi, "High-frequency characterization and modeling of EMI filters under temperature variations," *IEEE Transactions on Electromagnetic Compatibility*, vol. 59, pp. 1906-1915, 2017.

[13] D. Xu, C. K. Lee, S. Kiratipongvoot, and W. M. Ng, "An active EMI choke for both common- and differential-mode noise suppression," *IEEE Transactions on Industrial Electronics*, vol. 65, pp. 4640-4649, 2018.

[14] C. Dominguez-Palacios, J. Bernal, and M. M. Prats, "Characterization of common mode chokes at high frequencies with simple measurements," *IEEE Transactions on Power Electronics*, vol. 33, pp. 3975-3987, 2018.

[15] H. Chen, J. Wu, and X. Zheng, "Elimination of common-mode choke saturation caused by self-resonance of the EMI filter in a variable-frequency drive system," *IEEE Transactions on Electromagnetic Compatibility*, vol. 61, pp. 1226-1233, 2019.

[16] C. Dominguez-Palacios, P. Gonzalez-Vizuete, M. A. Martin-Prats, and J. B. Mendez, "Smart shielding techniques for common mode chokes in EMI filters," *IEEE Transactions on Electromagnetic Compatibility*, vol. 61, pp. 1329-1336, 2019.

[17] R. He, Y. Xu, S. Walunj, S. Yong, V. Khilkevich, D. Pommerenke, H. L. Aichele, M. Boettcher, P. Hillenbrand, and A. Klaedtke, "Modeling strategy for EMI filters," *IEEE Transactions on Electromagnetic Compatibility*, pp. 1-10, 2020.

[18] D. Liu and X. Jiang, "High frequency model of common mode inductor for EMI analysis based on measurements," *3rd International Symposium on Electromagnetic Compatibility*, pp. 462-465, 2002.

[19] H. Chen, *High-frequency Modeling of EMI Filter: Research on Parasitic Effect*, Zhejiang University, pp. 26-37, 2007.

[20] I. Stevanovic, S. Skibin, M. Masti, and M. Laitinen, "Behavioral modeling of chokes for EMI simulations in power electronics," *IEEE Transac-*

*tions on Power Electronics*, vol. 28, no. 2, pp. 695-705, 2013.

[21] C.-L. Li, C.-H. Huang, C.-C. Chiu, and C.-H. Sun, "Comparison of dynamic differential evolution and asynchronous particle swarm optimization for inverse scattering of a two-dimensional perfectly conducting cylinder," *Applied Computation Electromagnetics Society (ACES) Journal*, vol. 27, no. 10, pp. 850-865, 2021.

[22] C. Y. Wu, H. Kim, J. Y. He, N. Erickson, S. Cho, D. Kim, Y. Hur, D. J. Pommerenke, and J. Fan, "Analysis and modeling of conducted EMI from an AC-DC power supply in LED TV up to 1 MHz," *IEEE Transactions on Electromagnetic Compatibility*, vol. 61, pp. 2050-2059, 2019.

**Yakang Pei** was born in China. He completed his studies in Electrical Engineering and its Automation at the Haibin College of Beijing Jiaotong University in Cangzhou, Hebei, China in 2019, and received his bachelor's degree in Engineering. He is a master student at Nanjing Normal University with research interests in electromagnetic compatibility and high frequency device modeling.

**Wei Yan** is an Associate Professor at Nanjing Normal University. He obtained his Physics and Electronics Ph.D. and Electrical Engineering M.Sc. from Nanjing Normal University in 2014 and 2011. He is the Senior Member of China Electrical Technology Association and the evaluation expert of the Electromagnetic Compatibility Calibration Specification of China.

**Hao Ma** was born in Yangzhou, China. He received his B.Sc. degree in Automation from Jiangsu Normal University, Xuzhou, China, in 2019. He is currently working in electromagnetic compatibility of power supply system with Nanjing Normal University. His research interests are in the areas of Electromagnetic Compatibility and Power Electronics.

**Mengxia Zhou** received his M.Sc. degree in Electrical Engineering and his Ph.D. degree in Physics and Electronics from Nanjing Normal University, in 2018 and 2021, respectively. His main research interests include electromagnetic compatibility, electromagnetic environment effects, and high frequency device modeling.

**Yang Jian** was born in China. In 2021, he graduated from Jiangsu Institute of Technology, Changzhou, Jiangsu Province, China, majoring in Electrical Engineering and automation, with a Bachelor of Engineering degree. He is a Master's student at Nanjing Normal University, majoring in electromagnetic compatibility.

# A Novel Ultra-Wideband Wide-angle Scanning Sparse Array Antenna using Genetic Algorithm

**Z. N. Jiang[1,2], Y. Zheng[1], X. F. Xuan[1], and N. Y. Nie[1]**

[1]School of Electronic Science and Applied Physics,
Hefei University of Technology, Hefei, China, 230009

[2]National Mobile Communications Research Laboratory,
Southeast University, Jiangsu, 210096
jiangzhaoneng@hfut.edu.cn

***Abstract* –** A single-element antenna is usually unable to meet the communication requirements of the wireless system and the main solution is to use an array antenna. The desire to reduce the weight and cost of the array antenna gave rise to the sparse array. A linearly polarized sparse array antenna with ultra-wideband wide-angle scanning characteristics based on a genetic algorithm (GA) is developed in this paper. The antenna array consists of 40 units, which are arranged by a rectangular array with a side length of 300 mm. Compared to the conventional periodic array, the proposed sparse array has reduced about 190 antenna elements. The sparse array can achieve S11 $< -10$ dB in the ultra-wideband of 2.7–12 GHz (120%). Experimental results for the proposed antenna exhibit an azimuth scanning angle of $\pm 45^{\circ}$, and a pitching scanning angle of $\pm 30^{\circ}$.

***Index Terms* –** genetic algorithm (GA), linearly polarized, sparse array, ultra-wideband, wide-angle scanning.

## I. INTRODUCTION

With the rapid development of modern communication technology, the antenna is indispensable as the carrier of electromagnetic waves and current conversion. In some specific engineering applications, the antenna is required to have high gain and strong directivity, or the antenna pattern can be scanned, then a single antenna is often not qualified. The main method to solve the problem is to adopt an array antenna.

Periodic arrays are widely used due to the convenience of mathematical treatment and assembly of the array structure. In general, the main lobe resolution of an array is inversely proportional to the aperture. If the periodic array is required to have high resolution, the aperture will be large, leading to an increase in the number of array elements and production costs [1]. On this basis, to reduce the cost and system complexity, it is generally expected to design the large array into a sparse array or sub-array form. The sparse array is used to randomly sparse on the same aperture as the full array [2]. The array element spacing is usually not fixed and can be any value. The sparse array can satisfy the required radiation characteristics with fewer array elements, which not only simplifies the antenna structure and feed network, reduces the overall weight of the system, but also greatly reduces the cost of the system [3]. In the optimized design of a sparse antenna array, unequally spaced array element positions lead to a complicated nonlinear optimization. To solve this problem, setting the element spaces as integer multiples of a suitably chosen basic spacing simplifies the design procedure. As GA possesses intrinsic flexibility to a nonlinear problem, it is mature in optimizing the unequally spaced arrays. In addition, some antennas based on GA are proposed [4–6].

Due to the above advantages of a sparse array, the United States carried out related research on the synthesis of sparse arrays in the 1960s and successfully applied the sparse array to HAPDAR radar [7]. The same beam width and side-lobe level can be achieved when the number of sparse array elements is 50% of the full array. With the rapid development of sparse array technology, it has been well applied in Cobra Dane [8], TechSat21 space-based radar [9], SIAR, Sea-based X-band radar (SBX), SKA giant Square Kilometer Array [10], and other systems. Some ultra-wideband phased array antennas have been proposed [11–13]. Compared with this literature, The paper has some advantages as shown in Table 2.

Referring to the literature, it can be seen that most of the researchers on sparse array focus on the optimization of the algorithm, which only focuses on the theoretical part and less on the practical part [14]. This paper focuses on the practical part, and a novel sparse array based on a genetic algorithm is systematically designed, optimized, and fabricated. Considering that the practice environment is a missile-borne antenna, how to

*Submitted On: October 24, 2022*
*Accepted On: January 2, 2023*



https://doi.org/10.13052/2023.ACES.J.380204

design an ultra-wideband array antenna with wide-angle scanning, lightweight and high integration are difficult. Through many experiments, the log periodic dipole antenna (LPDA) with an exponential shape is selected as the antenna element. The overall sparse array can operate from 2.7 to 12 GHz (120%) with 40 antenna elements. Simulation results show that the beam pointing accuracy is better than 10 degrees, the azimuth scanning angle is $\pm 45^{\circ}$, and the pitching scanning angle is $\pm 30^{\circ}$. It is shown that the proposed sparse array significantly reduces the number of antenna elements.

## II. DESIGN PROCESS

### A. Sparse configuration

In the case of random array element distribution, there are many resonant points of the array that are not at the center frequency, which will lead to impedance mismatch. When the spacing of array elements is too large, there will be a gate flap, which will affect the antenna array gain. Therefore, it is necessary to use a genetic algorithm to optimize the array layout to determine the physical layout of the antenna array under the given constraints and obtain the radiation direction graph that meets the desired performance index. In GA, the fitness function is used to evaluate the merits and demerits of each individual, which is usually constructed according to the optimization target requirements of specific problems. In this paper, the antenna position is taken as the decision variable and the sidelobe level of the sparse array is reduced as the optimization objective to construct the fitness function. The starting point of array antenna theory is the principle of superposition. The principle is applied to the far-region radiation field of the array antenna, which is the principle of direction graph multiplication. According to the principle of direction graph multiplication:

$$s = \mathrm{e}l\rho at \cdot AF(\emptyset), \tag{1}$$

where $\mathrm{e}l\rho at$ is the element factor. $AF(\emptyset)$ is the array factor, which is related to the position of the antenna element in the array. The flowchart of the adopted GA is shown in Fig. 2 (a), and the population size NP is 50 when the initial population is formed. Encoding using real number coding, each optimized variable as a basis to construct the dye body. To achieve the required beamwidth while controlling the gain, the fitness function (2) was constructed according to the maximum E-plane beamwidth:

$$fit = \frac{1}{a(G-GT)+b(BW-TBW)}, a+b=1, \tag{2}$$

where $G$ is the main lobe phase-to-gain, $GT$ is the target main lobe phase-to-gain; $BW$ is the beam width, and $TBW$ is the target beam width. By adjusting the weight system number a and b to adjust the weight balance and beam width, a=0.8 and b=0.2 were selected according to the root data. As the beam width and the gain increase, the fitness function approaches zero. In the selection process, the crossover probability is 0.8 and the mutation probability is 0.05. When the global optimal solution is obtained or the iteration limit is reached, the iteration is stopped and the optimization variable is output.

The number of sparse array units is necessary, which can reduce the cost. As shown in Fig. 1, it realizes the same characteristics as a full array with fewer units. In this paper, the scanning angle of the antenna array is different in azimuth and pitch direction. The azimuth needs to realize -45 to +45 degree scanning and the pitch needs to realize -30∼+30 degree scanning. If a rectangular grid is adopted, as shown in Fig. 2 (b), the final rectangle grid determined by antenna element spacing is dx= 0.014 m, dy=0.0156 m. The number of antenna elements required by the conventional rectangular raster antenna array is 230 and the spacing between elements is $0.5\lambda$. The final number of units is determined to be 40 shown in Fig. 2 (c) and the dimensions are 300 mm $\times$ 300 mm. The degree of sparsity reached 17% and the average inter-element spacing of the antenna is $0.2\lambda$ when working in the low-frequency band. Considering the physical size of actual antenna elements, the minimum spacing between adjacent elements is 30 mm. Through the random array optimization algorithm, no grating lobes appear in the visible area when the antenna array is scanned in the area of azimuth plane 45 degrees and pitch plane 30 degrees. The convergence accuracy reaches the ratio of main and side lobes no less than the target value of 10 dB and the beam width no more than $35^{\circ}$. Ideally, the scanning results of the designed sparse array at 12 GHz are shown in Fig. 3. It can be seen that the antenna can scan up to 45 degrees in the azimuth plane and 30 degrees in the pitching plane accurately.

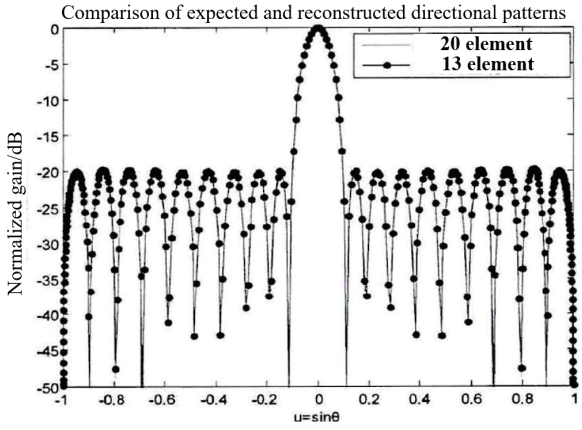


Fig. 1. Alignment of expected and reconstructed directional graphs.

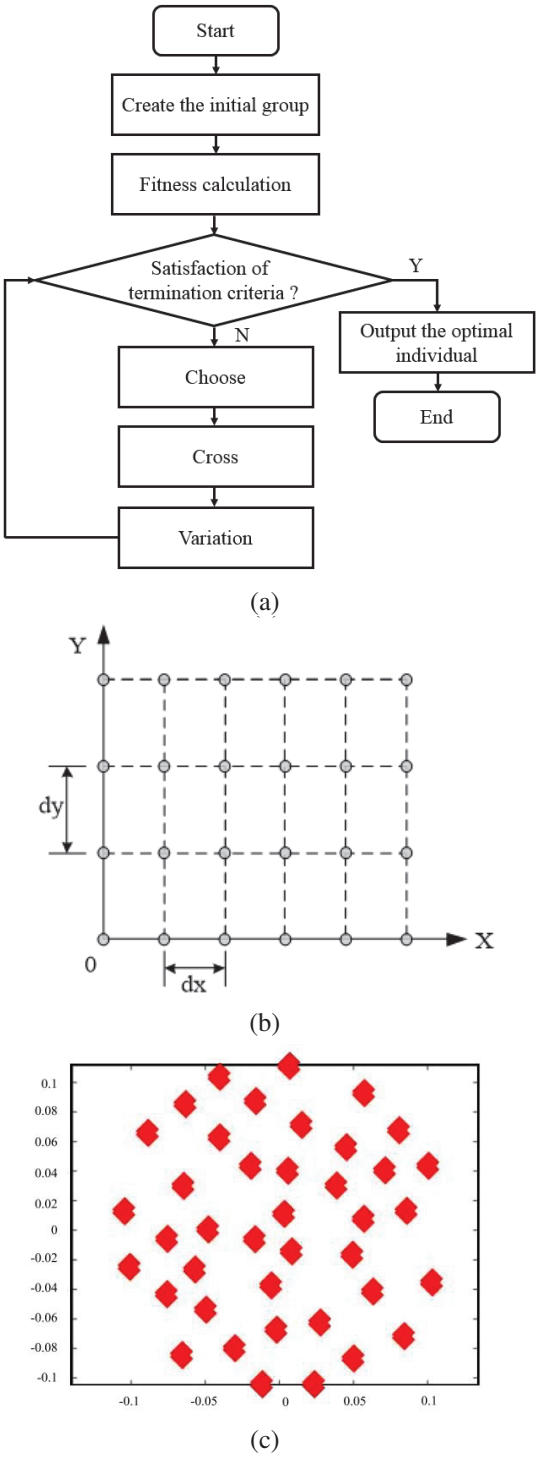


Fig. 2. Sparse layout: (a) Flowchart of genetic algorithm. (b) Rectangular grid. (c) Sparse layout.

### B. Design of the antenna unit

In the case that the theoretical design is finished, the next step is to verify whether the actual situation is realized. After the number and placement of array elements

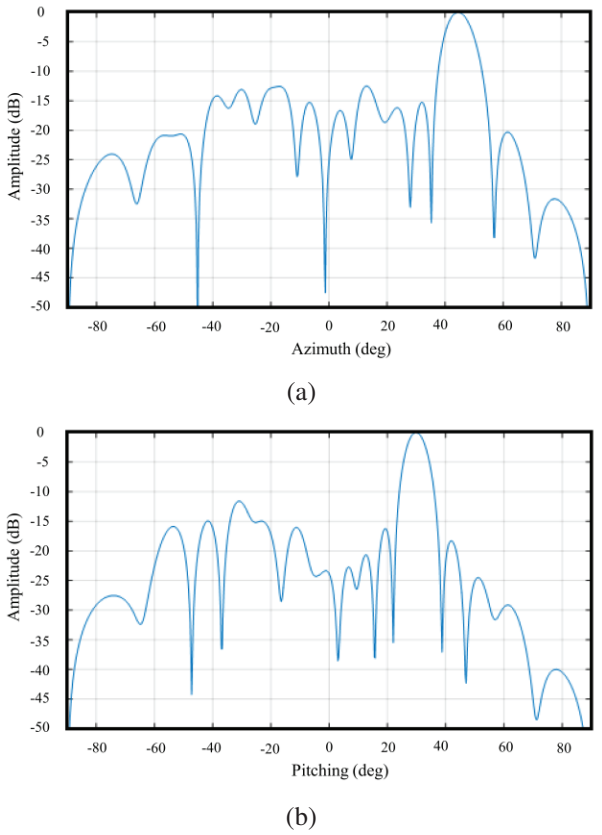


Fig. 3. Scanning results: (a) Azimuth plane with scanning at 45 degrees. (b) Pitching plane with scanning at 30 degrees.

are determined, the structure of array elements needs to be designed. To put 40 antenna units in a finite aperture, a variety of UWB antennas are compared such as a corrugated horn, ridged horn, a helical antenna, and so on [15]. To meet the index requirements of a sparse array, various LPDA models are simulated in the design process.

Figure 4 (a) shows the contour shape of LPDA with the director. The model can improve the antenna directivity greatly, but the impedance-matching effect is bad. Figure 4 (b) shows the LPDA with a dielectric lens. This structure is beneficial to improve the radiation efficiency of the antenna, but the cost of the lens is high. Figure 4 (c) shows the LPDA of the Koch fractal structure. Considering the performance of antenna elements and elements in the array, the printed LPDA is selected.

Figure 5 (a) shows the front view of improved LPDA, which is printed on a 1.016 mm dielectric substrate with a relative dielectric constant of 3.0 and a loss tangent of 0.002. To achieve miniaturization, unnecessary triangular areas are cut by the dielectric substrate.

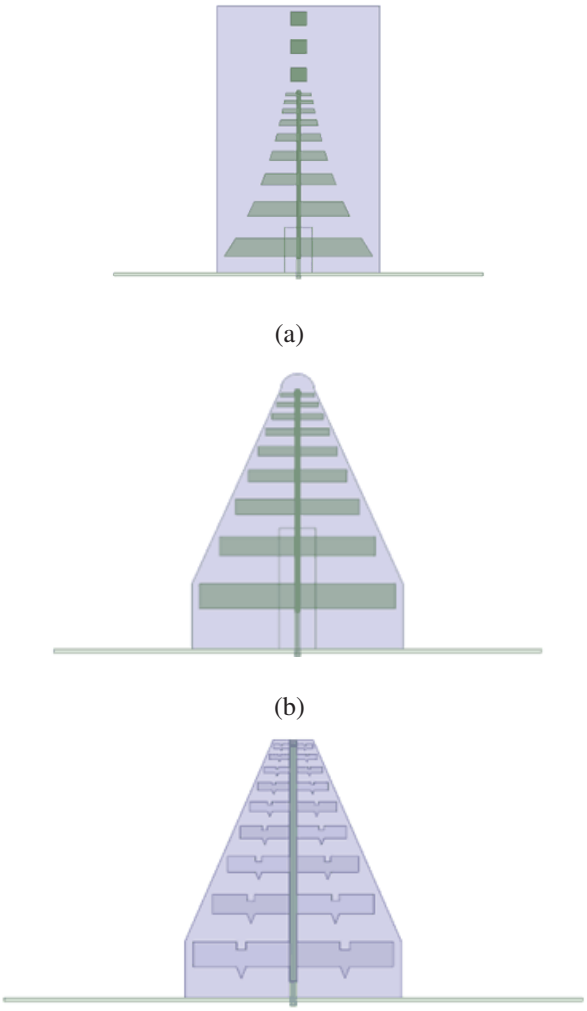

(a) (b) (c)

Fig. 4. Schemes: (a) The contour shape of LPDA with a director. (b) LPDA with a dielectric lens. (c) LPDA of Koch fractal structure.

For traditional LPDA, the dimensions and spacing of each oscillator are determined by the same scale factor $\tau$ [16]:

$$\tau = \frac{l_m}{l_{m+1}} = \frac{w_m}{w_{m+1}} = \frac{d_m}{d_{m+1}}, \tag{3}$$

where, $l_m$ and $w_m$ are the full length and width of the Mth symmetric bit. $d_m$ is the distance between the Mth symmetric bit and the Mth+1 bit. While keeping the length of the shortest and longest oscillator constant, the Vivaldi curve is adopted to cut the size of the remaining oscillators, which can not only reduce the transverse size to a certain extent but also improve the antenna gain in the operating frequency band [17]. The Vivaldi curve is expressed as follows:

$$y = c_1 e^{-Rz} + c_2, \tag{4}$$

$$c_1 = \frac{y_2 - y_1}{e^{-Rz_2} - e^{-Rz_1}}, \tag{5}$$

$$c_2 = \frac{y_1 e^{-Rz_2} - y_2 e^{-Rz_1}}{e^{-Rz_2} - e^{-Rz_1}}, \tag{6}$$

where (y1, z1), (y2, z2) are the coordinates of starting and ending points of the curve respectively, and R is the gradient rate. The contour shape of LPDA can be changed by adjusting R. Here, we choose R to be 21.4.

Figure 5 (b) shows the overall structure of improved LPDA and the feeding structure in detail. A pair of metal isolation plates with a distance of 4 mm is added to the front and back sides of each antenna element to avoid serious coupling in the subsequent sparse array design. Considering the processing feasibility, a metal rectangular plate is added between the isolation plate and the printed dielectric plate as support. The antenna is fed by a coaxial cable, which passes through the reflection plate and feeds from the bottom [18]. The outer conductor is welded directly to the antenna. The dielectric

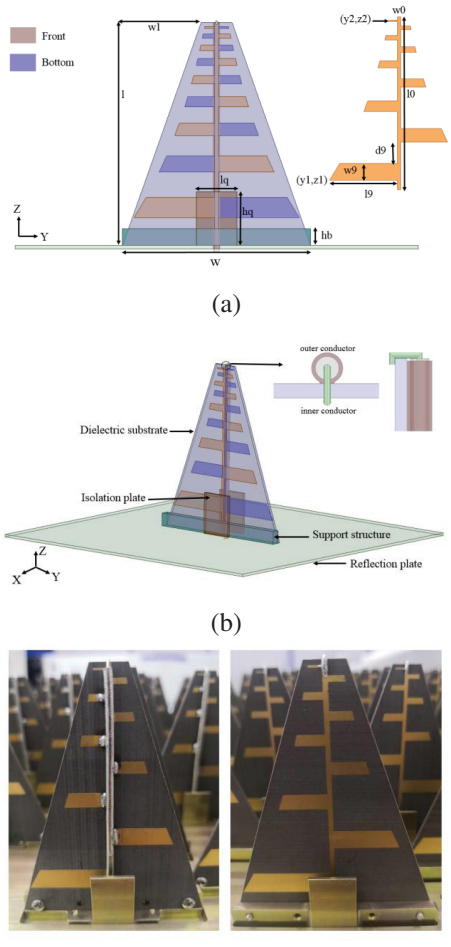


(a) (b) (c)

Fig. 5. The structure of LPDA antenna element: (a) Front view. (b) 3D view. (c) Fabricated antenna.

between the inner and outer conductor is higher than the outer conductor. The feeding structure plays a role of a broadband unbalanced-to-balanced converter without affecting the radiation of the antenna, making it easier to achieve impedance matching. The fabricated antenna is shown in Fig. 5 (c). The final dimensions of the proposed LPDA are shown in Table 1.

Table 1: Dimensions of the Proposed Antenna Element (unit: mm)

| Symbol | Value | Symbol | Value |
|---|---|---|---|
| *w* | 56 | *l9* | 24 |
| *l* | 64 | *d9* | 7.5 |
| *w0* | *1.2* | *lq* | *12* |
| *l0* | *61* | *hq* | *16* |
| *w1* | *23.4* | *hb* | *3* |
| *w9* | *6* | $\tau$ | *0.8* |

### C. Design of antenna array

After the unit design is completed, 40 antenna units are arranged according to the positions shown in Fig. 2. However, due to the idealization of the genetic algorithm, the position of some antenna elements needs to be further adjusted. The model of the sparse array after coordinate optimization is shown in Fig. 6.

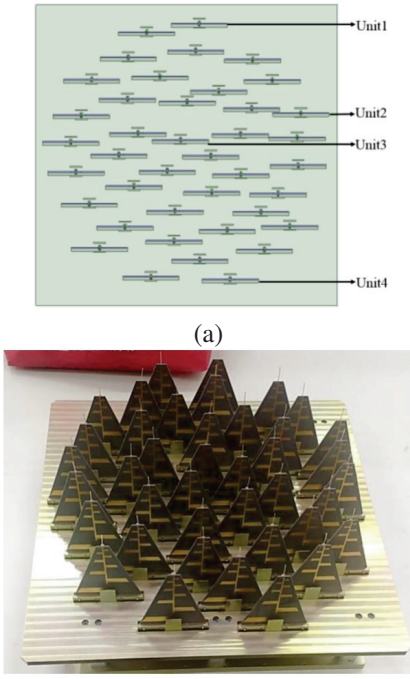


(a)

(b)

Fig. 6. The sparse array model: (a) Simulated sparse array. (b) Fabricated sparse array.

## III. SIMULATED AND MEASURED RESULTS

### A. Active standing wave ratio results

The simulated active VSWR $< 3$ bandwidth of the antenna is from 3 to 12 GHz (120%), as shown in Fig. 7. It can be seen that the active standing-wave ratio of individual units at individual frequency points exceeds 3. From Fig. 8, the results show the array antenna has a return loss of greater than 10 dB over an ultra-wide frequency band (approximately 5:1) for each unit. The operating frequency band of the array antenna is wider than that of the other antenna. However, when 40 units work simultaneously, individual units will not affect the array effect.

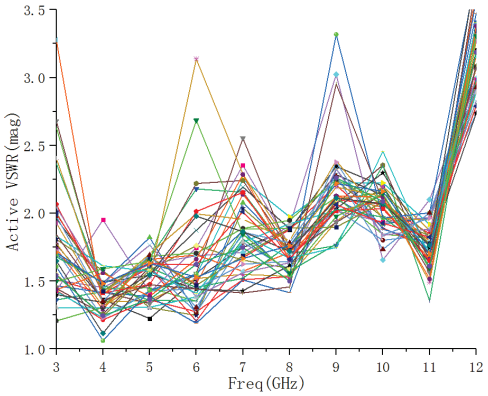


Fig. 7. Active VSWR simulated results.

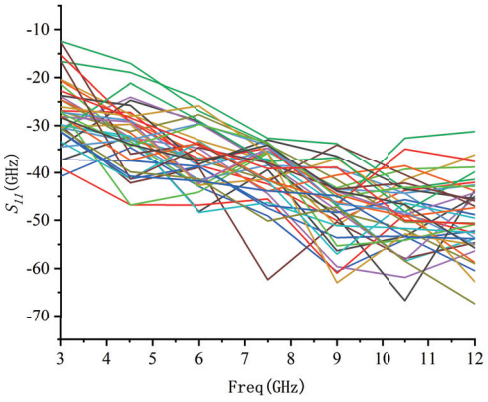


Fig. 8. S Parameter results.

Active VSWR of some units in the array environment was measured by Popular Portable Phasor Network Analyzer (PNA) as Fig. 9 shows. Due to the limited space in this paper, feeding measured results of four ports mentioned in Fig. 6 are given in Fig. 10. It can be seen that the active standing wave ratio of the antenna units is less than 3.

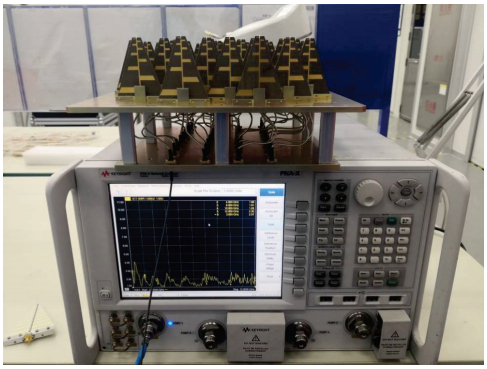

Fig. 9. Active VSWR test environment.

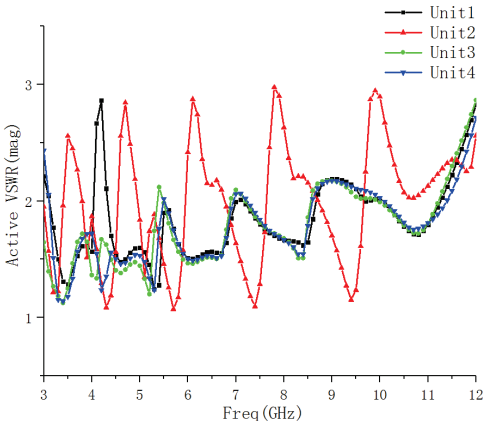


Fig. 10. Active VSWR measured results.

### B. Radiation pattern results

The radiation pattern was tested in the Microwave Anechoic Chamber using a planar near-field scanning technique as Fig. 11 shows. Figures 12 and 13 are the lobe diagrams at the azimuth plane with scanning 45 degrees and the pitching plane with scanning 30 degrees at 3.4 GHz, 6.5 GHz, and 11.5 GHz.

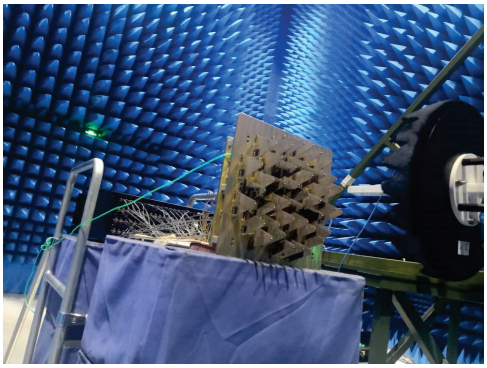

Fig. 11. Radiation pattern test environment.

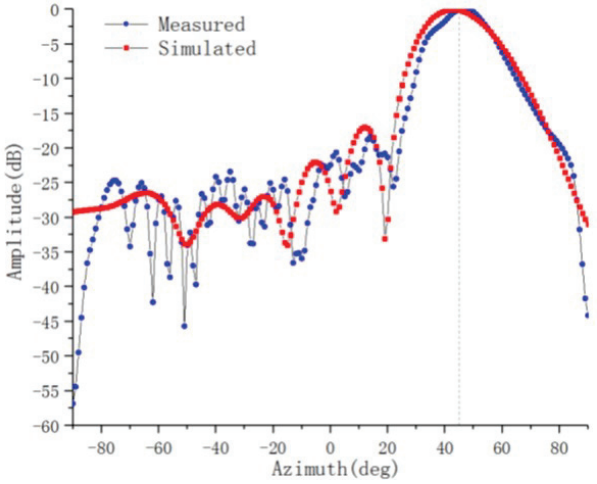


(a)

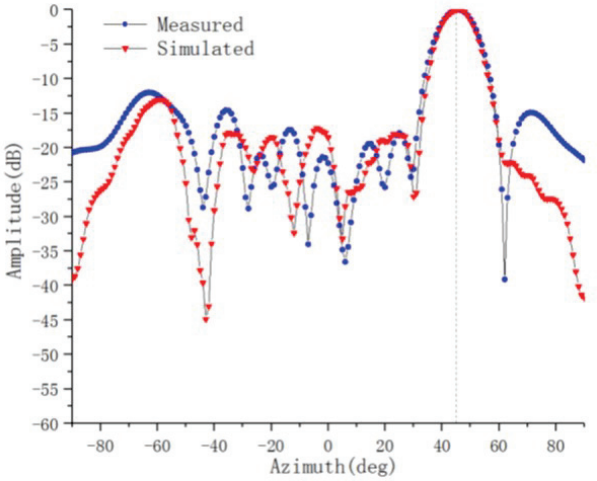


(b)

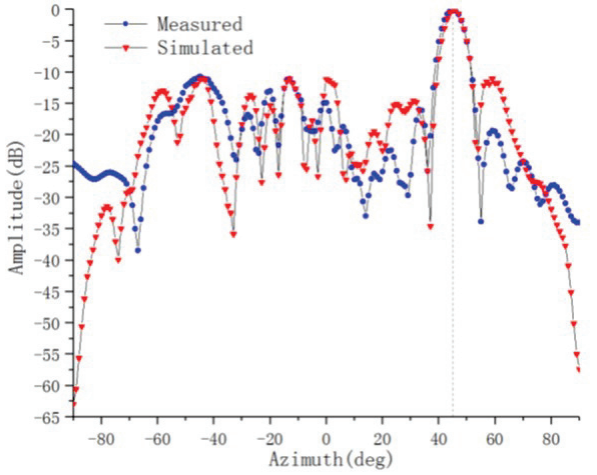


(c)

Fig. 12. Radiation pattern in azimuth plane with scanning 45 degrees: (a) 3.4 GHz, (b) 6.5 GHz, (c) 11.5 GHz.

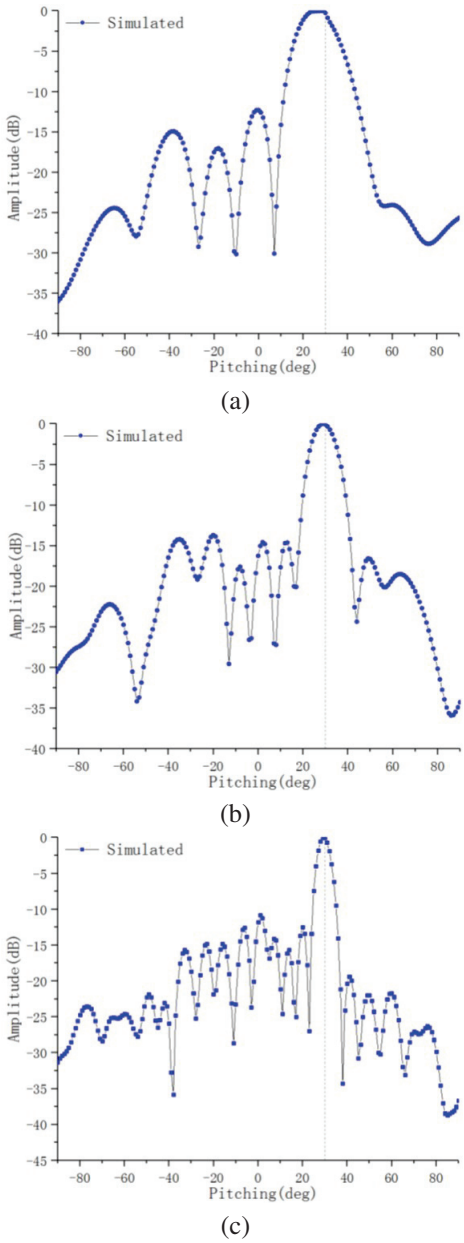


Fig. 13. Radiation pattern in pitching plane with scanning 30 degrees: (a) 3.4 GHz, (b) 6.5 GHz, and (c) 11.5 GHz.

Figure 14 shows the measured gain results. The gain of the proposed sparse array antenna is lower than that of the periodic array antenna with the same aperture. The decrease in gain is approximately proportional to the decrease in the number of active array elements, and the side-lobe is higher than that of the periodic array antenna with the same aperture. Therefore, when the gain and sidelobe requirement is not high, this sparse array can be used to achieve good performance with fewer antenna elements.

Table 2: Comparison with prior Literature

| Ref. | Units | BW | Scanning Angle |
|---|---|---|---|
| [11] | 256 | *3:1* | ±45° |
| [12] | 64 | *5:1* | ±45° |
| [13] | *64* | *3:1* | ±60° |
| *This Work* | *40* | *5:1* | ±45° |

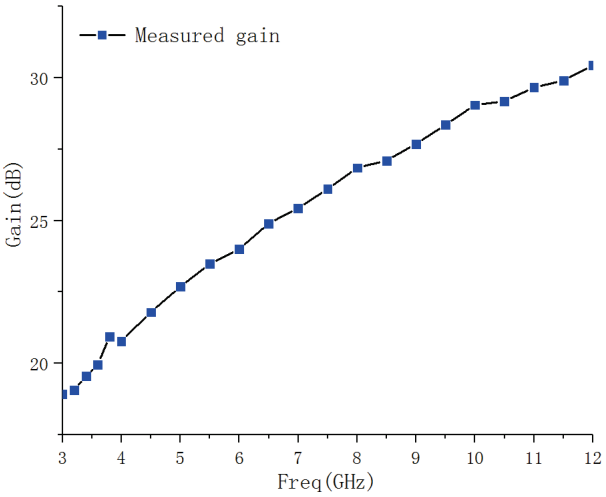


Fig. 14. Measured and simulated gain.

## IV. CONCLUSION

A new linearly polarized sparse array antenna with a small number of elements, well-controlled side-lobe levels, and wide-angle scanning is introduced. The sparse array is designed to replace the traditional periodic array to obtain better performance while reducing cost. The overall antenna has an impedance bandwidth of 120% for active VSWR $< 3$. The measured result overlapped frequency band covers the range of 2.7 – 12 GHz. The simulation and measurement results indicate that the sparse array antenna can scan up to $\pm 45^\circ$ in the azimuth plane, and up to $\pm 30^\circ$ in the pitching plane. The demonstrated sparse array is a good candidate for popular S-band, C-band, and X-band applications, such as satellite communications.

## ACKNOWLEDGMENT

We would like to thank the support of the open research fund of the National Mobile Communications Research Laboratory, Southeast University (No.2023D05), Anhui Natural Science Foundation (2208085MF161) Enterprise entrusted project (W2020JSKF0153, W2020JSFW0112), HeFei University of Technology teacher program (JZ2019HGTB0093).

## REFERENCES


[1] K. Chen, Y. Li, and J. Shi, "Optimization of sparse concentric ring arrays for low sidelobe," *International Journal of Antennas and Propagation*, vol. 2019, pp. 1485075, 2019.

[2] R. Z. Syeda, J. G. B. D. Vaate, and D. Prinsloo, "Regular and irregular-on-grid sparse array comparison of connected aperture arrays," *IEEE Antennas and Wireless Propagation Letters*, vol. 19, no. 4, pp. 586-590, 2020.

[3] P. Rocca, G. Oliveri, R. J. Mailloux, and A. Massa, "Unconventional phased array architectures and design methodologies—A review," *Proceedings of the IEEE*, vol. 104, no. 3, pp. 544-560, 2016.

[4] K. Kayalvizhi, and S. Ramesh, "Design and analysis of reactive load dipole antenna using genetic algorithm optimization," *American Computational Electromagnetics Society (ACES) Journal*, vol. 35, no. 3, pp. 279-287, 2020.

[5] J. Zolghadr, Y. Cai, and N. Ojaroudi, "UWB slot antenna with band-notched property with time domain modeling based on genetic algorithm optimization," *American Computational Electromagnetics Society (ACES) Journal*, vol. 31, no. 8, pp. 926-932, 2016.

[6] H.-T. Chou, C.-W. Liu, H.-H. Chou, and W.-J. Liao, "Optimum horn antenna design based on an integration of HFSS commercial code and genetic algorithms for the feed application of reflector antennas," *American Computational Electromagnetics Society (ACES) Journal*, vol. 25, no. 2, pp. 117-128, 2010.

[7] M. R. Stiglitz and C. Blanchard, *Practical Phased-Array Antenna Systems*, Artech House, Boston, USA, 1992.

[8] L. Xiaoming, and S. Xingrong, "Optimization design of sparse concentric ring arrays," *Tactical Missile Technology*, vol. 3, 2017.

[9] H. Steyskal, J. K. Schindler, P. Franchi, and R. J. Mailloux, "Pattern synthesis for TechSat21 - a distributed space-based radar system," *IEEE Antennas and Propagation Magazine*, vol. 45, no. 4, pp. 19-25, 2003.

[10] P. Bolli, et al., "Test-driven design of an active dual-polarized log-periodic antenna for the square kilometre array," *IEEE Open Journal of Antennas and Propagation*, vol. 1, pp. 253-263, 2020.

[11] S. S. Holland and M. N. Vouvakis, "The Planar Ultrawideband Modular Antenna (PUMA) Array," *IEEE Transactions on Antennas and Propagation*, vol. 60, no. 10, pp. 4589-4600, 2012.

[12] J. P. Doane, K. Sertel, and J. L. Volakis, "A wideband, wide scanning tightly coupled dipole array with integrated balun (TCDA-IB)," *IEEE Transactions on Antennas & Propagation*, vol. 61, no. 9, pp. 4538-4548, 2013.

[13] S. Xiao, S. Yang, H. Zhang, et al., "Practical implementation of wideband and wide-scanning cylindrically conformal phased array," *IEEE Transactions on Antennas and Propagation*, vol. 99, pp. 1-1, 2019.

[14] M. F. Raji, H. Zhao, and H. N. Monday, "Fast optimization of sparse antenna array using numerical Green's function and genetic algorithm," *International Journal Of Numerical Modelling: Electronic Networks, Devices and Fields*, vol. 33, no. 4, pp. e2544, 2020.

[15] J. Jose, T. Mathew, A. Thomas, N. Haripriya, M. Cherian, and D. D. Krishna, "A cost effective hybrid-log periodic dipole antenna (H-LPDA)," *2015 Fifth International Conference on Advances in Computing and Communications (ICACC)*, pp. 263-265, 2015.

[16] Z. Wang, X. Zhao, F. Ji, S. Huang, and Z. Jiang, "Ultra-wideband cylindrical conformal array antenna based on LPKDA," *2020 IEEE MTT-S International Conference on Numerical Electromagnetic and Multiphysics Modeling and Optimization (NEMO)*, pp. 1-4, 2020.

[17] Y. Hu, "Study on novel printed log periodic antennas," *Nanjing University of Posts and Telecommunications*, Nanjing, China, 2018.

[18] J. Fang, M. Jin, and X. Zhang, "An UWB printed log-periodic array antenna," *2018 International Workshop on Antenna Technology (iWAT)*, pp. 1-3, 2018.


**Z. N. Jiang** was born in Xuancheng, China. He received the Ph.D. degree from Nangjing University of Science And Technology, Nanjing, China, in 2012. Since 2013, he has worked on the numerical method of computational electromagnetism. He is currently a Professor with the Hefei University of Technology, Hefei, China. He has authored or coauthored more than 90 papers in refereed international conferences and journals and has served as Program Committee Member in several international conferences. Currently, he is focusing on antenna and microwave device. (Email: jiangzhaoneng@hfut.edu.cn)

**Y. Zheng** was born in Anhui, China, in 1998. He is currently working towards the M.E degree in Electronic Science & Applied Physics from Hefei University of Technology. He is currently focusing on antenna and microwave device design. (Email: 1597021984@qq.com)

**X. F. Xuan** was born in Anhui, China, in 1975. He received the M.S. degree from Nanjing University, China. He is focusing on numerical method of computational electromagnetism. (Email:941067868@qq.com)

**N. Y. Nie** (corresponding author) was born in Shandong, China, in 1990. She received the Ph.D. degree from University of Electronic Science and Technology of China. She is focusing on theory and design of microwave and millimeter wave antenna.(Email: liyingnie@sina.com)

# Research on the Model and Transient Characteristics of the Pantograph-Catenary Arc in Different Sections of Power Supply Lines

**Yutao Tang[1], Fei Li[2], Chao Zhou[1], Yulin Wang[2], and Feng Zhu[3]**

[1]Institute of Electronic and Electrical Engineering
Civil Aviation Flight University of China, Guanghan, 618307, China
835578907@qq.com, zc_cafuc@163.com

[2]Sichuan Province Engineering Technology Research Center of General Aircraft Maintenance
Civil Aviation Flight University of China, Guanghan, 618307, China
88604045@qq.com, minest@aliyun.com

[3]School of Electrical Engineering
Southwest Jiaotong University, Chengdu, 610031, China
zhufeng@swjtu.edu.cn

***Abstract –*** During the operation of high-speed trains, the pantograph will inevitably have occasional and instantaneous separations from the power supply line, resulting in the pantograph catenary arc (PCA). The diverse states of PCA generated in different sections of the power supply line will lead to various electromagnetic interference (EMI). To study the transient characteristics of PCA, firstly, the voltage and the dissipative power of PCA at the common and neutral sections of the power supply line are analyzed and calculated respectively. Secondly, two PCA models that describe the different PCA states are established based on the improved Habedank arc model. Finally, the high-frequency transient voltage and current of the PCA when high-speed trains pass through the common and neutral sections at different speeds are obtained by simulation. In this paper, we comprehensively study the model and the transient characteristics of PCA, which provides a theoretical basis and relevant data for further study of its EMI.

***Index Terms –*** arc model, dissipative power of arc, electromagnetic interference, pantograph-catenary arc.

## I. INTRODUCTION

The electromagnetic interference (EMI) produced by the pantograph catenary arc (PCA) of high-speed trains not only affects the surrounding electromagnetic signal, such as communication and navigation signals of airports [1–3] but also impacts the electronic equipment of high-speed trains, such as speed sensors [4–6]. Therefore, it is significant to study the characteristics of PCA. However, the existing research on the model and the characteristics of PCA is not comprehensive.

Some researchers proposed an aerial catenary nonuniform transmission line model to predict the longitudinal propagation characteristic of PCA [7]. The characteristics of the instantaneous voltage and current of PCA were studied based on the improved Habedank arc model in Ref. [8, 9]. The electromagnetic radiation (EMR) from the PCA of the subway has been measured and analyzed in [10]. Scholars further analyzed the relationship between the EMI of PCA and train speed [11]. Furthermore, S. Barmada and his research team have conducted in-depth research on arc detection in real-time Railway applications. They proposed an arc detection method based on a support vector machine, which can detect and locate the arc with great accuracy and obtain useful information on the pantograph/catenary state [12–14]. Their research results can provide a reference for further study on the characteristics of PCA. However, in the existing research, many studies did not take into account the different locations and states of PCA.

As an extension of previous works, firstly, the different states of PCA generated at two typical positions of the power supply line–common and neutral sections are analyzed. Secondly, the voltages and the dissipative powers of PCA in two different states are calculated respectively, which are used to modify the Habedank arc model. Thirdly, the PCA models at the common and neutral sections are established respectively based on the improved Habedank arc model. Finally, the transient voltage and current of the two kinds of PCA are obtained by simulation, and their transient characteristics are analyzed. The research results of this paper can provide a theoretical basis for the comprehensive study of the EMI and EMR caused by PCA.

*Submitted On: April 20, 2022*
*Accepted On: July 9, 2022*



https://doi.org/10.13052/2023.ACES.J.380205

## II. ANALYSIS OF THE STATES OF PCA

### A. Formation process of the PCA

High-speed trains get electric power by connecting their pantograph to the power supply line. It can be seen from Fig. 1 that the pantograph has occasional and instantaneous separations from the power supply line during the running of a high-speed train. The high voltage between them is enough to spark the air in the gap, resulting in discharge. Besides, the arc root of the PCA moves forward with the train on the power supply line, which will lengthen the PCA, reduce its radius and increase its resistance. As the train continues to move forward, the length of PCA becomes longer. When the energy absorbed by the PCA cannot meet the energy consumed, the arc will be extinguished.

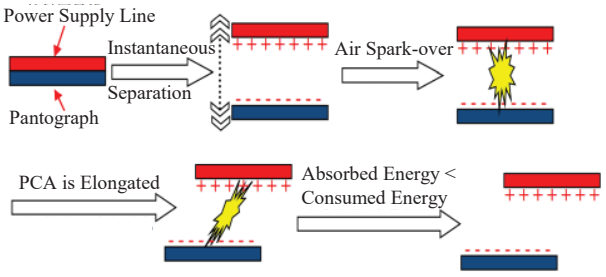


Fig. 1. Simplified process of the PCA formation.

### B. States of the PCA at the common and neutral sections

The reason for generating the PCA at the common sections is that there are some fixed hard points on the power supply line and the vibration of the pantograph. At this time, the separation distance between the pantograph and the power supply line is short. Therefore, it can be assumed that the PCA generated here is perpendicular to the horizontal plane of the train roof. Namely, the arc length of PCA at the common section ($L_{com}$) is approximately equal to the separation distance ($d_s$), as shown in Fig. 2.

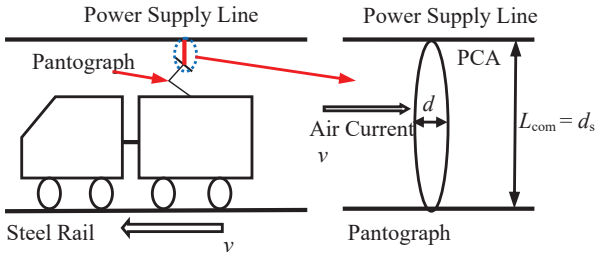


Fig. 2. Diagram of the PCA generated at the common section.

The reason for generating the PCA at the neutral sections is that the pantograph needs to be separated from the original power supply line and entered into the neutral line to realize the voltage phase conversion, as shown in Fig. 3.

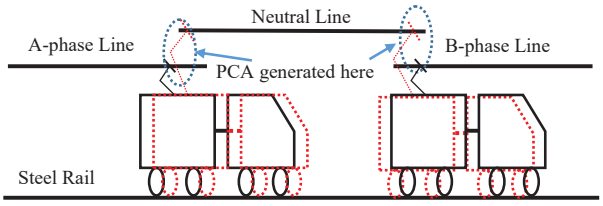


Fig. 3. Diagram of the train passing through the neutral section.

At this time, the ds is long and the angle between the PCA and the horizontal plane of the train roof cannot be ignored, as shown in Fig. 4.

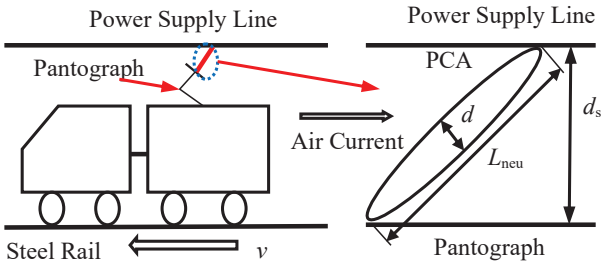


Fig. 4. Diagram of the PCA generated at the neutral section.

## III. CALCULATION OF THE ELECTRICAL PARAMETERS OF PCA

The characteristics of an arc are related to the length, diameter, voltage, current, and dissipative power of the arc. Among them, dissipative power includes three parts: conducted power, convective power, and radiated power. Because the PCA is affected by transverse or longitudinal arc blowing, it carries out convective heat dissipation. Therefore, the conducted power can be completely ignored. Besides, the convective power generally accounts for more than 80% of the dissipative power, which is the main way of PCA heat dissipation [15].

The convective power can be obtained by:

$$P_k = P_{kT} + p_{kL}, \tag{1}$$

where $P_k$ is the convective power, $P_{kT}$ and $P_{kL}$ are the convective power generated by the transverse arc blowing and the longitudinal arc blowing respectively.

Because the states of PCA generated at the common and neutral sections are different, the $P_k$ will be different at those two sections. Therefore, it needs to be studied separately.

### A. Electrical parameters of the PCA at the common section

The PCA at the common section is almost vertical, as shown in Fig. 2. Therefore, only convective power generated by transverse arc blowing exists. Refs. [16] and [17] give the calculation methods of the convective power per unit length generated by a transverse blowing arc ($P_{\mathrm{kT}'}$) and the diameter of arc ($d$). To facilitate the subsequent comparison with the measured data, the unit of speed is converted from m/s to km/h. So the $P_{\mathrm{kT}'}$ and d can be derived by:

$$P_{\mathrm{kT}}{}' = 0.1464d(v+36)^{1.5}, \tag{2}$$

$$d = 1.5369\sqrt{\frac{i_{\mathrm{arc}}}{v+36}}, \tag{3}$$

where $v$ is the moving speed of the arc, which unit is km/h; $i_{arc}$ is the current of PCA.

The $P_{\mathrm{kT}'}$ can be calculated by Eqs. (2) and (3):

$$P_{\mathrm{kT}}{}' = 0.225\sqrt{i_{\mathrm{arc}}}\,(v+36). \tag{4}$$

The separation distance between the pantograph and the power supply line can be got by [8]:

$$d_s = 4.571\times10^{-5}v^2 + 0.238v - 1.411, \tag{5}$$

where $ds$ is the separation distance, and which unit is mm.

As shown in Fig. 2, the arc length of PCA at the common section and $ds$ are equal. According to Eqs. (1), (4), (5), the convective power of PCA at the common sections $\left(P_{\mathrm{k(com)}}\right)$ can be obtained by :

$$P_{k(\,\mathrm{com}\,)} = \sqrt{i_{\mathrm{arc}}}\left(1.028\times10^{-5}v^3 + 0.053v^2 + 1.61v - 11.429\right). \tag{6}$$

Based on Eq. (6), it can be deduced that the dissipative power of PCA at the common section $(P_{loss(com)})$ is:

$$P_{loss(com)} = \frac{P_{k(com)}}{80\%} = \sqrt{i_{arc}}(1.285\times10^{-5}v^3 + 0.066v^2 + 2.013v - 14.286). \tag{7}$$

According to [8], when PCA is in a stable state, there is a 15 times relationship between its voltage and length. Thus, based on Eq. (5), the voltage of PCA at the common section can be expressed as:

$$E_{arc1} = 15L_{com} \approx 15d_s = 6.857\times10^{-4}v^2 + 3.57v - 21.165\ , \tag{8}$$

where $E_{arc1}$ and $L_{com}$ are the voltage and length of PCA at the common section respectively.

### B. Electrical parameters of the PCA at the neutral section

As for the PCA at the neutral section, $ds$ is longer and not equal to $L_{arc}$ of the PCA at the neutral section ($L_{neu}$). Thus, both $P_{kT}$ and $P_{kL}$ exist because the PCA has an angle with the horizontal plane as shown in Fig. 4. At this time, the $L_{arc}$ will be elongated because of the multiple external forces, and its stress diagram is shown in Fig. 5. Where $F_{wind}$ is the wind load force, and the direction is opposite to the running direction of the train; $F_{float}$ is the thermal buoyancy force, and the direction is vertical and upward; $F_m$ is the magnetic force, and the direction is related to the direction of the magnetic field.

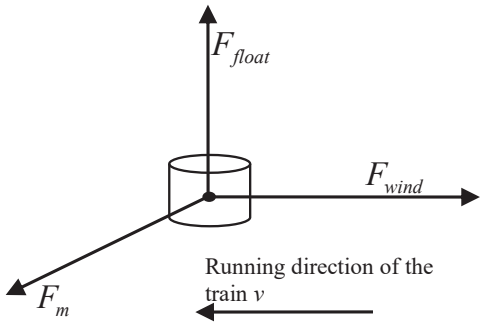


Fig. 5. Force diagram of the PCA under the multiple external forces.

It is assumed that the PCA moves at a uniform speed in a short time, and the mass density of the PCA is very small at high temperatures. So its mass can be ignored. Therefore, the resultant force on the PCA is:

$$\boldsymbol{F}_{wind} + \boldsymbol{F}_{float} + \boldsymbol{F}_m = 0, \tag{9}$$

where:

$$\begin{cases} F_{\mathrm{wind}} = 0.04\,(\mu_2\mu_s\gamma_{\mathrm{wind}})\cdot\rho_{\mathrm{air}}\,V_{\mathrm{wind}}{}^2\cdot\pi r_{\mathrm{arc}}\,l_{\mathrm{arc}} \\ F_{\mathrm{float}} = (\rho_{\mathrm{air}} - \rho_{\mathrm{arc}})\cdot g\pi r_{\mathrm{arc}}{}^2 l_{\mathrm{arc}} \\ F_m = l_{\mathrm{arc}}\,(I_{\mathrm{arc}}\times B) \end{cases}, \tag{10}$$

where $l_{\mathrm{arc}}$, $\boldsymbol{I}_{\mathrm{arc}}$, and $\boldsymbol{B}$ are the length, current vector, and magnetic induction intensity of the arc microelement.

The PCA can be regarded as a chain model connected by many cylindrical current elements. Therefore, $F_m$ can be refined into the magnetic field force on each current element. The model of the cylindrical current element is shown in Fig. 6.

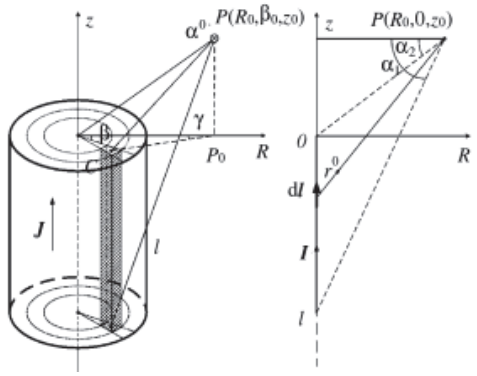


Fig. 6. Magnetic field calculation model of cylinder current element.

Based on the Biot-Savart Law, the magnetic induction intensity generated by current J in the current element at P is:

$$d\boldsymbol{B} = \frac{\mu_0}{4\pi}(\boldsymbol{J}\times\boldsymbol{r}^0)/r^2 \mathrm{d}V. \tag{11}$$

According to the arc chain model and Eq. (11), it can be deduced that the magnetic induction intensity generated by the cylindrical current element at P is:

$$\begin{aligned}\boldsymbol{B} &= \frac{\mu_0}{4\pi}\iiint_V \frac{\boldsymbol{J}(\rho)\times\boldsymbol{r}}{r^3}\,\mathrm{d}V \\ &= \alpha^0\frac{\mu_0}{4\pi}\int_0^{\pi}\int_0^{R}\frac{(\sin\alpha_1-\sin\alpha_2)\cos\gamma}{R_0}J(\rho)\rho\mathrm{d}\rho\mathrm{d}\varphi.\end{aligned} \tag{12}$$

The sum integral of the magnetic field generated by the current loop flowing through the arc is calculated by Eq. (12). Then, the comprehensive magnetic field at the gravity center of each arc current element can be obtained by coordinate transformation [18].

The values of other relevant parameters in Eq. (10) are shown in Table 1.

Table 1: Relevant parameters of the force calculation of arc microelement [19]

| | Name | Value | | Name | Value |
|---|---|---|---|---|---|
| $\mu_z$ | Coefficient of wind pressure height variation | 1.17 | $\rho_{arc}$ | Air density in high temperature of arc area | 1.295 $kg/m^3$ |
| $\mu_s$ | Coefficient of wind load shape | 0.76 | $\gamma_{arc}$ | Arc radius | 0.0013 mm |
| $\gamma_{\text{wind}}$ | Coefficient of uneven wind pressure | 0.67 | $v_{\text{wind}}$ | wind speed | Equal to the train speed |
| $\rho_{\text{air}}$ | Air density | 0.022 $kg/m^3$ | $g$ | Gravitational acceleration | 9.8 $m/s^2$ |

Assuming that $ds$ is 5 mm, the initial length of PCA is equal to $ds$. The length change of PCA caused by the external force can be obtained by simulation, as shown in Fig. 7.

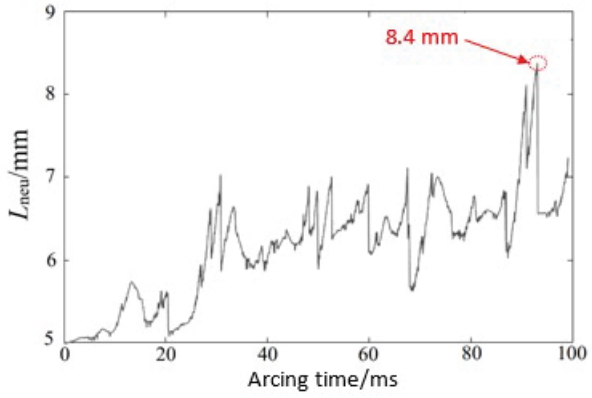


Fig. 7. Diagram of the $L_{neu}$ change caused by the external force.

The simulation results show that the length of PCA increases with the arcing time, and the maximum of $L_{neu}$ is about 8.4 mm. Therefore, $L_{neu}$ is about 1.68 times that of $d_s$. The $L_{neu}$ can be derived by Eq. (5):

$$L_{neu} \approx 1.68 d_s = 7.679\times10^{-5}v^2 + 0.4v - 2.37. \tag{13}$$

The $P_{kL}$ per unit length of the PCA ($P'_{\text{kL}}$) can be expressed as [16]:

$$P'_{\text{kL}} = 0.2182 d^2 v\int_{T_0}^{Tc} C dT, \tag{14}$$

where $P'_{\text{kL}}$ is produced by heating air from temperature $T_0$ to the average temperature of the arc $T_C$. $T_0$ and $T_C$ are 4000 K and 9500 K respectively. C is the heat capacity coefficient of air, and C is [20]:

$$C \approx \frac{0.41}{T}. \tag{15}$$

The $P'_{\text{kL}}$ can be derived by Eqs. (3), (14), and (15):

$$P'_{\text{kL}} = 0.18 i_{arc}\frac{v}{v+36}. \tag{16}$$

The convective power of the PCA at neutral sections ($P_{k(neu)}$) can be obtained by Eqs. (1), (4), (13), and (16):

$$\begin{aligned}P_{k(\text{ nen })} = &\left[0.225\sqrt{i_{\text{arc}}}(v+36)+0.18 i_{ar}\frac{v}{v+36}\right] \\ &\cdot\left(7.679\times10^{-5}v^2+0.4v-2.37\right).\end{aligned} \tag{17}$$

It is similar to the above, the dissipative power ($P_{loss(neu)}$) and the arc voltage ($E_{arc2}$) of the PCA at the neutral section is:

$$\begin{aligned}P_{\text{loss(neu)}} &= \frac{p_{k\,(\text{neu})}}{80\%} \\ &= \left[0.281\sqrt{i_{\text{arc}}}(v+36)+0.225 i_{\text{arc}}\frac{v}{v+36}\right] \\ &\cdot\left(7.679\times10^{-5}v^2+0.4v-2.37\right),\end{aligned} \tag{18}$$

and:

$$E_{\text{arc }2} = 1.152\times10^{-3}v^2 + 6v - 35.55. \tag{19}$$

## IV. MODELING AND SIMULATION OF THE PCA

### A. Establishment of the PCA model

The Habedank model is the classical arc model, and its equation is:

$$\begin{cases}\frac{dg_C}{dt} = \frac{1}{\tau_C}\left(\frac{{i_{\text{arc}}}^2}{E_0^2 g_C} - g_C\right) \\ \frac{dg_M}{dt} = \frac{1}{\tau_M}\left(\frac{i_{\text{arc}}^2}{P_0} - g_M\right) \\ \frac{1}{g} = \frac{1}{g_C} + \frac{1}{g_M}\end{cases}, \tag{20}$$

where $g_C/\tau_C$ and $g_M/\tau_M$ are the arc conductance/time constant of the Cassie and Mayr arc model respectively.

Besides, $E_0$ and $P_0$ are the voltage and the dissipative power of the arc, and they are assumed to be constants in this model.

However, it can be seen from the above research that $E_{arc}$ and $P_{loss}$ are not constants in practice. Therefore, it is necessary to modify the Habedank arc model to make it conform to the actual situation of PCA. Besides, it also needs to distinguish the different states of PCA at the common and neutral sections.

According to Eqs. (7), (8), and (18-20), the arc models of PCA generated by the high-speed train passing through common and neutral sections are:

$$\begin{cases} \dfrac{dg_C}{dt} = \dfrac{1}{\tau_C}\left[\dfrac{{i_{\text{arc}}}^2}{\left(6.857\times10^{-4}v^2+3.57v-21.165\right)^2 g_C} - g_C\right] \\ \dfrac{dg_M}{dt} = \dfrac{1}{\tau_M} \\ \quad \times\left[\dfrac{0.8{i_{\text{arc}}}^2}{\sqrt{i_{\text{arc}}}\left(1.028\times10^{-5}v^3+0.053v^2+1.61v-11.429\right)} - g_M\right] \\ \dfrac{1}{g} = \dfrac{1}{g_C} + \dfrac{1}{g_M} \end{cases}, \tag{21}$$

and:

$$\begin{cases} \dfrac{dg_c}{dt} = \dfrac{1}{\tau_0 g^\alpha}\left[\dfrac{i_{acc}^2}{\left(1.152\times10^{-3}v^2+6v-35.55\right)^2 g_c} - g_c\right] \\ \dfrac{dg_M}{dt} = \dfrac{1}{\tau_0 g^\alpha} \\ \left\{\dfrac{0.8i_{acc}^2}{\left[0.225\sqrt{i_{acc}}(v+36)+0.18i_{acc}\frac{v}{v+36}\right]\cdot\left(7.679\times10^{-5}v^2+0.4v-2.37\right)}\right. \cdot \\ \left. -g_M\right\}\cdot \\ \dfrac{1}{g} = \dfrac{1}{g_c} + \dfrac{1}{g_M} \end{cases}. \tag{22}$$

### B. Transient characteristics of the PCA

The transient voltage and current of PCA can be simulated and calculated by Eqs. (21) and (22).

Because the distance from the traction substation to the nearest neutral section is 25 km, it can be assumed that the PCA occurs in the middle of them. Namely, the distance between PCA and the traction substation is 12.5 km. The characteristic curves of the transient voltage and current of PCA when the train passes through this position at 80 km/h, 150 km/h, and 250 km/h are calculated by simulation, as shown in Fig. 8.

Similarly, the characteristic curves of the transient voltage and current of PCA when the train passes through the neutral section at 80 km/h, 150 km/h, and 250km/h are shown in Fig. 9.

As shown in Figs. 8 and 9, the EMI radiated by the PCA will produce strong voltage and current pulses. At the common section, the maximum transient voltage pulse is about 19000 V ($v$=250 km/h), and the maximum transient current pulse is nearly 170 A. At the neutral section, they are approximately 29000 V and 350 A respectively ($v$=250 km/h).

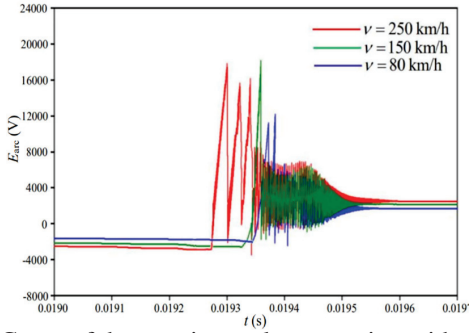


(a) Curve of the transient voltage varying with train speed at the common section

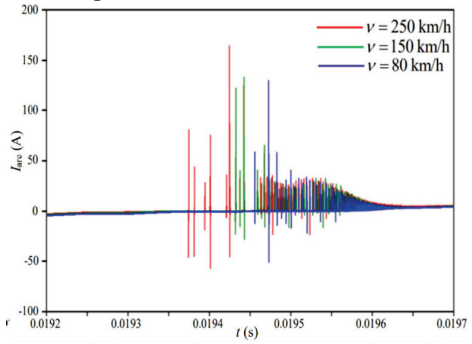


(b) Curve of the transient current varying with train speed at the common section

Fig. 8. Transient characteristic curve of the PCA at the common section.

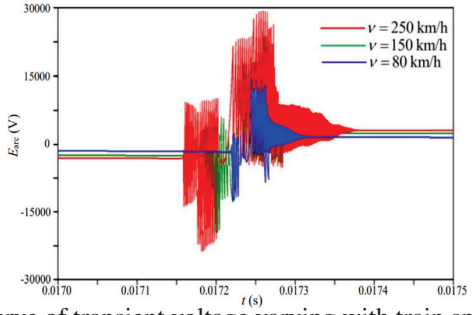


(a) Curve of transient voltage varying with train speed at the neutral section

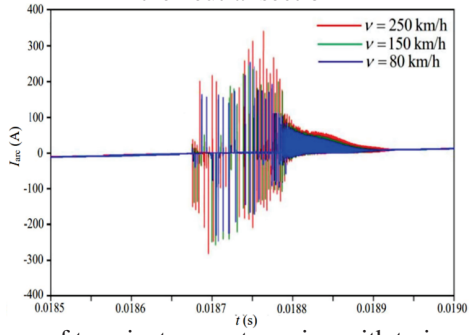


(b) Curve of transient current varying with train speed at the neutral section

Fig. 9. Transient characteristic curve of the PCA at the neutral section.

### C. Experimental validation

The PCA Test System is used to measure the electrical characteristics of PCA. It is composed of a PCA generator and test system, as shown in Fig. 10. Where the variable frequency motor is used to drive the wheel to rotate to simulate the mutual movement of the power supply line and the pantograph, and the arrow direction indicates the moving direction. Besides, the servo motor and roller screw drive are used to simulate the movement of the pantograph [21].

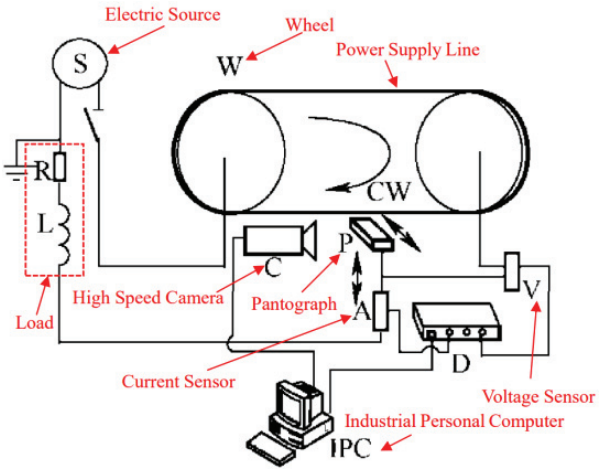


(a) Schematic diagram of the *PCA Test System*

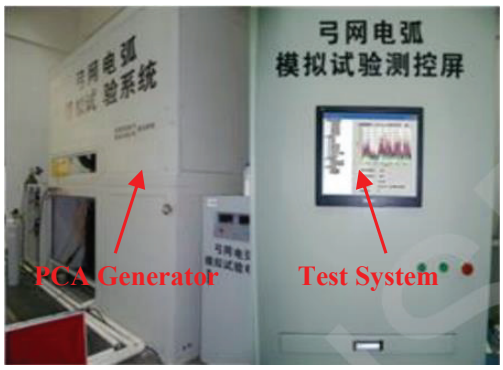


(b) Physical drawing of the *PCA Test System*

Fig. 10. The PCA Test System.

The voltage and current of PCA are measured by using the PCA Test System ($v$=250 km/h). Therefore, the wheel speed is set to 250 km/h, and the voltage and current of PCA are shown in Fig. 11.

The test results show that the maximum voltage is about 19.5 kV and the maximum current is nearly 185 A at the common section. While they are approximately 29.6 kV and 355 A respectively at the neutral section.

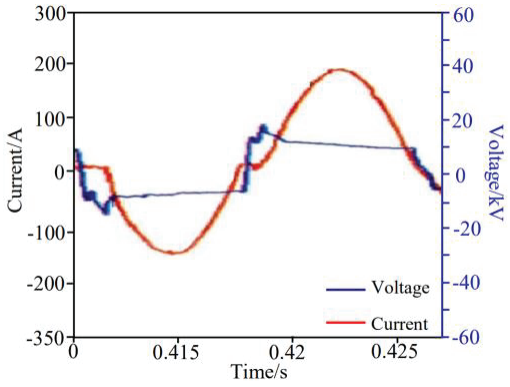


(a) Current and voltage of PCA at the common section

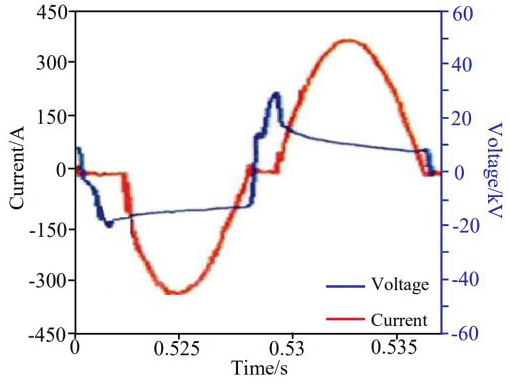


(b) Current and voltage of PCA at the neutral section

Fig. 11. Test results of electrical characteristics of PCA.

The test results are consistent with the simulation results, so the above PCA models are correct.

## V. CONCLUSION

The models and transient characteristics of PCA at the common and neutral sections are studied in this paper. The conclusions are as follows:

1) The PCA at common and neutral sections have different models because of their different states.
2) The EMI of PCA at the neutral section is more serious than that at the common section, which is reflected in the obvious increase of the peak value and high-frequency component of the transient voltage and current.
3) The peak and high-frequency component of the transient voltage and current will increase significantly with the train speed, which will increase the radiation intensity of PCA. Therefore, the faster the train speed, the more serious the EMI of PCA.
4) The main reason why the train speed affects the characteristics of PCA is that the speed will cause

the change of arc length, and then affect the voltage and the dissipative power of PCA.

To summarize, the EMI intensity of PCA will vary with the change of arc position and train speed, which can provide a research basis for the protection of the EMI of high-speed trains.

## ACKNOWLEDGMENT

The authors would like to thank the editors and anonymous reviewers for their insightful comments. This paper is supported by the National Key R&D Program of China (No. 2018YFC0809500), the Special Scientific Research Project of CAFUC (ZX2021-03), and the Independent Project of Key Laboratory of Civil Aviation Flight Technology and Safety (FZ2021ZZ03).

## REFERENCES

[1] Y. Tang, F. Zhu, and Y. Chen, "For more reliable aviation navigation: improving the existing assessment of airport electromagnetic environment," *IEEE Instrumentation & Measurement Magazine*, vol. 24, no. 4, pp. 104-112, 2021.

[2] F. Zhu, C. Gao, and Y. Tang, "Influence of pantograph-catenary arc on electromagnetic disturbance of airport terminal omnidirectional beacon," *China Railway Science*, vol. 39, no. 1, pp. 116-121, 2018.

[3] J. Gou, F. Zhu, J. Zou, J. Ye, H. Li, and Y. Wang, "Research on EMI of instrument landing system on aircraft caused by pantograph arc," *Journal of the China Railway Society*, vol. 40, no. 7, pp. 61-66, 2018.

[4] Y. Tang, F. Zhu, and Y. Chen, "For safer high-speed trains: a comprehensive research method of electromagnetic interference on speed sensors," *IEEE Instrumentation & Measurement Magazine*, vol. 24, no. 4, pp. 96-103, 2021.

[5] Y. Tang, F. Zhu, and Y. Chen, "Analysis of EMI from pantograph-catenary arc on speed sensor based on the high-speed train model," *Applied Computational Electromagnetics Society (ACES) Journal*, vol. 36, no. 2, pp. 205-212, 2021.

[6] F. Zhu, Y. Tang, and C. Gao, "Mechanism and suppression of electromagnetic interference of pantograph-catenary arc to speed sensor of CRH380BL electric multiple unit," *China Railway Science*, vol. 37, no. 6, pp. 69-74, 2016.

[7] X. Li, F. Zhu, H. Lu, R. Qiu, and Y. Tang, "Longitudinal propagation characteristic of pantograph arcing electromagnetic emission with high-speed train passing the articulated neutral section," *IEEE Trans. Electromagn. Compat.*, vol. 61, no. 2, pp. 319-326, 2018.

[8] Y. Wang, Z. Liu, X. Mu, K. Huang, H. Wang, and S. Gao, "An extended Habedank's equation-based emtp model of pantograph arcing considering pantograph-catenary interactions and train speeds," *IEEE Transactions on Power Delivery*, vol. 31, no. 3, pp. 1186-1194, 2016.

[9] F. Fan, "Study on separation between the pantograph and catenary based on improved habedank arc model," M.S. Thesis, Southwest Jiaotong University, Chengdu, China, 2011.

[10] X. Li, F. Zhu, R. Qiu, and Y. Tang, "Research on influence of metro pantograph arc on airport navigation system," *Journal of the China Railway Society*, vol. 40, no. 5, pp. 97-102, 2018.

[11] Y. Tang, F. Zhu, and Y. Chen, "Research on the influence of train speed change on the EMI of pantograph-catenary arc to main navigation stations," *Applied Computational Electromagnetics Society (ACES) Journal*, vol. 36, no. 4, pp. 450-457, 2021.

[12] I. Aydin, S. Celebi, S. Barmada, and M. Tucci, "Fuzzy integral-based multi-sensor fusion for arc detection in the pantograph-catenary system," Proceedings of the Institution of Mechanical Engineers Part F: *Journal of Rail & Rapid Transit*, vol. 232, no. 1, pp. 159-170, 2018.

[13] S. Barmada, M. Tucci, M. Menci, and F. Romano, "Clustering techniques applied to a high-speed train pantograph–catenary subsystem for electric arc detection and classification," Proceedings of the Institution of Mechanical Engineers Part F: *Journal of Rail & Rapid Transit*, vol. 230, no. 1, pp. 85-96, 2016.

[14] S. Barmada, M. Raugi, M. Tucci, and F. Romano, "Arc detection in pantograph-catenary systems by the use of support vector machines-based classification," *IET Electrical Systems in Transportation*, vol. 4, no. 2, pp. 45-52, 2014.

[15] S. Midya, D. Bormann, T. Schutte, and R. Thottappillil, "Pantograph arcing in electrified railways–mechanism and influence of various parameters–part II: with AC traction power supply," *IEEE Trans. on Power Del.*, vol. 24, no. 4, pp. 1940-1950, 2009.

[16] G. Gao, T. Zhang, W. Wei, Y. Hu, G. Wu, and N. Zhou, "A pantograph arcing model for electrified railways with different speeds," Proceedings of the Institution of Mechanical Engineers Part F: *Journal of Rail & Rapid Transit*, vol. 232, no. 6, pp. 1-10, 2018.

[17] Y. Liu, G. Chang, and H. Huang, "Mayr's equation-based model for pantograph arc of high-speed railway traction system," *IEEE Trans. on Power Del.*, vol. 25, no. 3, pp. 2025-2027, 2010.

[18] S. Gu, J. He, W. Chen, and G. Xu, "Magnetic force computation for the electric arc of parallel gap lightning protection device on overhead transmissionlines," *Proceedings of the CSEE*, vol. 26, no. 7, pp. 140-145, 2006.

[19] C. Chen, "Research on arc model of articulated phase insulator and laws of arc motion development in high speed railway," M.S. Thesis, Southwest Jiaotong University, Chengdu, China, 2016.

[20] S. Li, X. Jin, and H. Bi, "Numerical calculation on very fast transient overvoltage of UHV gas insulated substation by variable gap arc model," *High Voltage Engineering*, vol. 41, no. 4, pp. 1306-1312, 2015.

[21] W. Wang, G. Wu, G. Gao, B. Wang, Y. Cui, and D. Liu, "The pantograph-catenary arc test system for high-speed railways," *Journal of The China Railway Society*, vol. 34, no. 4, pp. 22-27, 2012.

**Yutao Tang** was born in Sichuan Province, China, in 1991. She received her B.S. degree in Automation from Southwest Science and Technology University, Mianyang, China, in 2013, and her Ph.D. degree in Electrical Engineering at Southwest Jiaotong University, Chengdu, China, in 2021.

She is currently a Lecturer at the Institute of Electronic and Electrical Engineering, Civil Aviation Flight University of China. Her research interests include electromagnetic environment testing and evaluation, and electromagnetic compatibility analysis and design.

**Fei Li** was born in Hubei Province, China, in 1983. He received a master's degree in Engineering Mechanics from Nanjing University of Aeronautics and Astronautics, China, in 2009. He is currently an engineer in the Aircraft Repair & Overhaul Plant Subsidiary of the Civil Aviation Flight University of China. His research fields include aircraft maintenance and airworthiness.

**Chao Zhou** was born in Anhui, Province, China, in 1980. He received his M.S. degree from South West Jiaotong University in 2002 and his Ph.D. degree from the University of Electronic Science and Technology of China in 2013, respectively.

He is working at the Civil Aviation Flight University of China, where he is currently a professor, deputy dean of the Institute of Electronic and Electrical Engineering, master tutor, and head of the UAV team. His current research interests include civil unmanned aerial vehicles and civil aviation electromagnetic environment effects.

**Yulin Wang** was born in Jiangxi Province, China, in 1986. He received a master's degree in Mechanical Design and Theory from Sichuan University, China, in 2011.

He is currently a senior engineer in the Aircraft Repair & Overhaul Plant Subsidiary of the Civil Aviation Flight University of China. His research fields include aircraft maintenance and airworthiness.

**Feng Zhu** was born in Anhui Province, China, in 1963. He received a B.S. degree in Physics from Huaibei Normal University, Huaibei, China, in 1984, an M.S. degree in Physics from Sichuan University, Chengdu, China, in 1987, and a Ph.D. degree in Electromagnetic Theory and Microwave Techniques from Southwest Jiaotong University, Chengdu, in 1997.

He is currently a Professor in the Department of Electrical Engineering, Southwest Jiaotong University. His research interests include electromagnetic environment test and evaluation, electromagnetic compatibility, and numerical electromagnetic methods.

# Resonant Frequency Analysis using Perturbation and Resonant Cavity Method in Printed Dual Band Antenna for WiMAX Application

**C. Mahendran[1] and M. Vijayaraj[2]**

[1]Department of Electronics and Communication Engineering
Alagappa Chettiar Government College of Engineering and Technology, Karaikudi-630003, Tamilnadu, India
mahendrangc@gmail.com

[2]Department of Electronics and Communication Engineering
Government College of Engineering, Tirunelveli-627007, Tamilnadu, India
mvijayaraj25567@gmail.com

***Abstract –*** A printed dual-band antenna is designed to resonate at 3.5 GHz with the measured gain of 6.38 dBi and at 5.5 GHz with that of 5.84 dBi for the WiMAX application. The bandwidth of this antenna at 3.5 GHz and 5.5 GHz is 8% and 5%, respectively. The radiation efficiency of 91.45% is obtained at 3.5 GHz and that of 89.56% at 5.5 GHz. A novel approach based on the perturbation technique is used to relate the resonant frequency to the electromagnetic energy stored and the volume of the proposed antenna's structure. The dual resonant length of this antenna is determined by a parameter named as the length reduction factor, which is computed by the curve fitting method. A polynomial equation connects the length reduction factor and resonance frequency. The resonant cavity model has been used to derive the resonant frequency equations for dual bands. The simulation and measured results are used to validate the analytically predicted resonant frequency caused by the structure perturbation and cavity technique and show good agreement. This antenna is fed by a balanced parallel plane, which conveniently facilitates the PCB's integration.

***Index Terms –*** curve fitting, electric and magnetic energy, perturbation technique, polynomial equation, printed antenna, resonant cavity, WiMAX band.

## I. INTRODUCTION

Around the world, every domestic and official activity has been computerized. As a result, high-speed internet access in emerging countries' rural areas is required. Orthogonal Frequency Division Multiplexing (OFDM) can be incorporated into WiMAX to provide a higher data rate without selective fading. A printed or microstrip antenna is the ideal tool for transmitting and receiving the WiMAX band of frequencies. It is affordable, lightweight, and takes up less space on mobile phones, laptops, and other electronic devices.

Numerous antennas for the WiMAX band that operate at 3.5 GHz and 5.5 GHz have been documented in the literature. These types include printed monopoles, ring-shaped patches, defective ground plane antennas, metamaterial loaded antennas, and MIMO antennas, according to Refs. [1–15]. In addition, coplanar waveguide-fed microstrips, Minkowski-Sierpinski carpet fractal constructed, complementary split-ring resonator-based, meander line slotted antennas, and Vicsek Fractal slotted antennas are reported in [16–26].

In order for a WiMAX signal to traverse a great distance, the antenna gain is critical. The gain of these reported antennas is lower. The antennas listed in the literature have either a full or partial ground plane, and most of them employ a microstrip line as a feeder, which necessitates the ground plane. Because the RF currents are carried via the pair of tracks on the printed circuit board (PCB), it is difficult to integrate the antenna with microwave or RF printed circuitry. This challenge is a result of the ground plane being a part of the antenna structure. The feeder lines in these reported antennas are unbalanced, although the tracks on the PCB are balanced. Consequently, compatibility issues exist between these antennas and the PCBs of high-frequency circuitry.

A novel mitigation strategy is proposed in this article to address these issues. A printed antenna is designed to radiate in the WiMAX band (3.5 GHz and 5.5 GHz) with a balanced line feeder. This proposed antenna does not require any full or partial ground plane as a part of the feeding structure, which facilitates the uniform field distribution. As a result, it is self-shielding to some extent. As it has a balanced line feeder, integrating this proposed printed antenna with the PCB of RF circuitry is very compatible. The gain of this proposed antenna is much better than that of those antennas reported in

*Submitted On: August 24, 2022*
*Accepted On: January 23, 2023*



https://doi.org/10.13052/2023.ACES.J.380206

the literature. The analytical expression for the resonant frequency of this proposed antenna is derived with the aid of perturbation and the resonant cavity method. This theoretical concept of perturbation is applied to the permittivity measurement of polystyrene mixed with carbon black fillers [27], and the computation of resonant frequency in a rectangular dielectric resonator antenna [28].

## II. ANTENNA DESIGN

The dimensions of the proposed dual-band printed antenna are 48.5 mm × 97 mm × 1.6 mm. The RT Duroid 5880 substrate was used to make this antenna, which has a relative permittivity of 2.2. A pair of balanced copper strip lines are printed to feed RF current into the radiating patch, with the appropriate length (Lf) and width (Wf) determined by the CST Studio Suite simulator to deliver the optimum signal level to the patch over the WiMAX band of frequency range.

This balanced line ensures a consistent electric field distribution between the strips. This mechanism ensures self-shielding, which reduces the undesired radiation from the feeder line. The proposed antenna's top and bottom views are depicted in Fig. 1, and its dimensions are provided in Table 1. To move the resonance from lower to higher frequency, the right-hand side edge of the top patch and the corresponding region on the bottom side are perturbed in this antenna. The unperturbed antenna resonates at a lower frequency. Resonant cavity modelling is used to calculate the length (Lr1, Lr2) and width (Wr) of the patch and ground plane. The width (Wx) is stretched along the Y-axis, whose dimension is determined by CST Studio Suite simulation, in order to enhance the gain.

Table 1: Dimensions of antenna

| **Parameter** | Lf | Wf | Lr1 | Lr2 | Wr | Wx |
|---|---|---|---|---|---|---|
| **Dimension (mm)** | 9 | 26 | 15.5 | 24 | 63 | 17 |

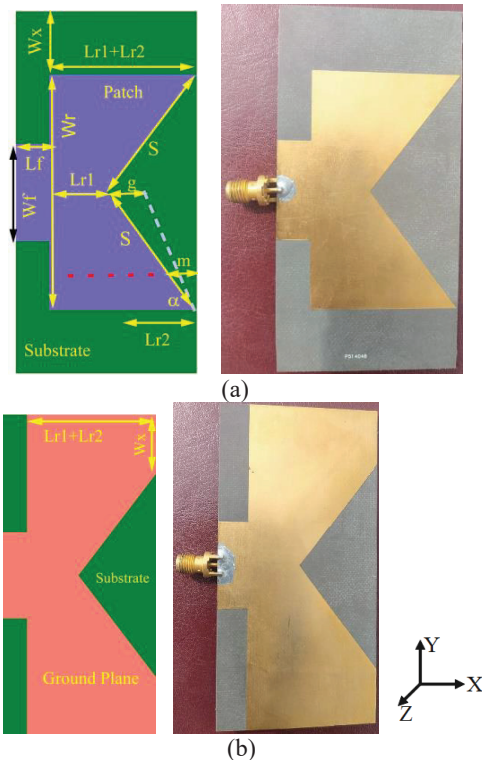


Fig. 1. Perturbed antenna. (a) Top view. (b) Bottom view. m = m1 at 3.5 GHz. m = m2 at 5.5 GHz.

## III. RESONANT FREQUENCY ANALYSIS

The resonant frequency of this proposed antenna is analyzed using the cavity model and perturbation technique. With CST simulation and measurement using Vector Network Analyzer, the expected resonant frequency derived from these two analytical techniques is validated. All these results are matched well, ensuring the accuracy of the analytical procedure.

## IV. RESONANT CAVITY METHOD

This proposed antenna forms a cavity filled with RT Duroid 5880 dielectric of a thickness (h) bounded by (Lr1+Lr2) × Wr × h $mm^3$. This resonant cavity supports two distinct resonant lengths, 3.5 GHz along Y-axis and 5.5 GHz along X-axis, as shown in Fig. 1 (a), causing a dual band of radiation. As there is no tapering along the Y-axis, the resonant length along this axis is constant, whereas the resonant length along the X-axis is variable due to tapering. The expression for the resonant frequency of these two bands is described in the following sections.

### A. WiMAX band of 3.5 GHz

Equation (1) states that for an antenna to resonant at 3.5 GHz, the resonant length along the Y-axis connecting the radiating slots should be one half of the guide wavelength ($\lambda_1$) at 3.5 GHz:

$$Wr + 2h = 0.5\lambda_1, \tag{1}$$

where electric field fringing at both ends along Y-axis is incorporated as '2h'. This fringing field should be taken into account due to the ground plane extension in the bottom side of antenna. For microstrip or printed antenna design, the resonant length extension can be approximated by $\frac{h}{\sqrt{\varepsilon_1}}$ for one radiating edge [29]. Here it is taken as 'h' approximately against the actual computed value of 0.7h. '$\lambda_1$' can be computed from Eqn. (1) as follows:

$$\lambda_1 = 132.4\ mm. \tag{2}$$

The length along the X-axis connecting the non-radiating slots is not constant due to the presence of

tapering and is represented by Eqn. (3). The effective length will be less than 'Lr2', which is represented by 'Lr2-m1', where 'm1' is length reduction factor. The value of 'm1' is 6.4mm, which is computed from MATLAB program:

$$Lr1 + Lr2 - m1 = 33.1\ mm = 0.3\lambda_1. \quad (3)$$

As there is no conductive plane extension at the ground plane, fringing field is neglected at both left and right edge of patch, compared to top and bottom edge.

Equation (4) represents the resonant frequency ($f_1$) corresponds to 3.5 GHz band [30]:

$$f_1 = \frac{150}{\sqrt{\varepsilon_1}}\sqrt{\left(\frac{P}{Lr1+Lr2-m1}\right)^2+\left(\frac{Q}{Wr+2h}\right)^2} \quad (4)$$
$$GHz = 3.497\ GHz,$$

where Lr1, Lr2, m1, Wr and h are in 'mm'.

'P' is an integer represents the half-cycle electric field variation along the X-axis and Q for Y-axis. For 3.5 GHz, P=1 and Q=1 from Eqn. (3) and Eqn. (1), respectively. As the 'P' has to be an integer to satisfy the boundary condition requirements, the nearest integer unity has been taken to satisfy the Eqn. (3). As the thickness 'h' is very small, the field variation along the Z-axis is negligible. The effective permittivity '$\varepsilon_1$' is given by Eqn. (5) [30]:

$$\varepsilon_1 = \frac{\varepsilon_r+1}{2}+\frac{\varepsilon_r-1}{2}\left[1+12\frac{h}{W}\right]^{-0.5} = 2.1. \quad (5)$$

W = W1= Lr1+Lr2-m1 at 3.5 GHz

W = W2= Wr + 2h at 5.5 GHz

The mode of operation at 3.5 GHz is Transverse Magnetic to Z-axis ($TM^Z{}_{110}$).

### B. WiMAX band of 5.5 GHz

The resonant length condition for 5.5 GHz band is given in Eqn. (6):

$$Lr1 + Lr2 - m2 = 0.5\ \lambda_2. \quad (6)$$

The length reduction factor 'm2' for this band is 16.9 mm, calculated from the MATLAB program. Equation (7) depicts the guide wavelength at 5.5 GHz.

$$\lambda_2 = 45.2\ mm. \quad (7)$$

The length which connects the non-radiating slots of this 5.5 GHz band is represented by the Eqn. (8):

$$Wr = 63\ mm = 1.39\ \lambda_2. \quad (8)$$

The nearest integers that satisfy the boundary condition of the cavity model are 'P' = 1 and 'Q' = 2. If 'Q' = 3 refers to the mode integer along the length linking the non-radiating slots, the length reduction factor 'm2' in the MATLAB program turns negative, ruling out the solution. The negative value of 'm2' refers to the length extension rather than the intended reduction. To make the 'm2' positive, the mode integer 'P' has to be increased, which does not mean full. 'P' should be '1' because it refers to the half-cycle field variation along the resonant length. Moreover, the length extension of '2h' due to the fringing field is insignificant for the non-radiating side of the patch as it regulates the impedance matching only at the band of interest. Hence 'Wr' is the most significant term for the integer value computation for 'Q' in Eqn. (8). The resonant frequency ($f_2$) expression for 5.5 GHz band is given by Eqn. (9):

$$f_2 = \frac{150}{\sqrt{\varepsilon_2}}\sqrt{\left(\frac{P}{Lr1+Lr2-m2}\right)^2+\left(\frac{Q}{Wr}\right)^2} \quad (9)$$
$$GHz = 5.58 GHz.$$

Equation (5) with the appropriate 'W' value is used to calculate the effective permittivity '$\varepsilon_2$'. The calculated value is 2.13, and the mode of operation is $TM^Z{}_{120}$.

### C. Length reduction factor computation

The length reduction factor plays a more vital role in the 5.5 GHz resonant band than in the 3.5 GHz band, as it appears in the resonant length expression of 5.5 GHz. The length along the X-axis varies almost linearly due to tapering. Therefore, numerous resonance lengths are feasible. One of these variable lengths has been set (activated) for 5.5 GHz resonance by matching the port impedance with the resonator exclusively for the 3.5 and 5.5 GHz bands, as depicted in Fig. 1 (a) as a red dashed line. Whereas, all other frequencies are not matched, hence those other resonant frequencies are not set. This is demonstrated in Figs. 8 (a), (b) and Figs. 6 (c) through (f). Therefore, 'm' specifies the length reduction necessary to activate the specified band. A MATLAB program is written to predict the 'm1' value for the 3.5 GHz band and the 'm2' value for the 5.5 GHz band. Angle '$\alpha$' can be varied by varying the parameter 'g' as shown in Fig. 1 (a), which alters the length of 'Lr2' to 'Lr3' as given by Eqn. (10):

$$Lr3 = Lr2 - g. \quad (10)$$

The '$\alpha$'and 'Lr3' can be related by the Eqns. (11a) or (11b):

$$\alpha = \tan^{-1}\left[\frac{Wr/2}{Lr3}\right] radian, \quad (11a)$$

$$\alpha = \frac{180}{\pi}\tan^{-1}\left[\frac{Wr/2}{Lr3}\right] degree. \quad (11b)$$

The 'm1' or 'm2' value also varied accordingly, influencing the resonant frequency in the 3.5 GHz or 5.5 GHz band. The resonant frequencies are noted from the simulator for each '$\alpha$' or 'g' value. The 'm1' or 'm2'

value depends on the effective electrical length along the X-axis. This is an unknown parameter. This 'm1' or 'm2' is predicted using the MATLAB program, whose algorithm is listed below:

Step 1: Keep all the parameters are constant except '$f_1$' ('$f_2$') and 'm1' ('m2') in Eqn. (4) (Eqn. (9)) for the 3.5 GHz (5.5 GHz) band.

Step 2: Vary the '$\alpha$' or 'g' values and note the resonant frequency in the CST Studio Suite simulator. Feed these simulated resonant frequencies '$f_1s$' ('$f_2s$') into MATLAB program.

Step 3: Arbitrarily vary the 'm1' ('m2') value with the step size of 0.001 mm and calculate the resonant frequency as '$f_1$m' ('$f_2$m') using MATLAB coding.

Step 4: Store the 'm1' ('m2') values when the deviation between '$f_1$m' ('$f_2$m') and '$f_1$s' ('$f_2$s') is less than 0.0001 GHz.

The expressions that relate the 'm1' ('m2') values with '$f_1$' ('$f_2$') are derived with the aid of curve fitting technique in MATLAB.

For 3.5 GHz Band, 3.044 GHz $\leq f_1 \leq$ 3.5 GHz,

$$m1 = -234.5{f_1}^{-1.904} + 28.03, \quad (12)$$

$$m1 = -6.425{f_1}^{2} + 56.42f_1 - 112.3. \quad (13)$$

For 5.5 GHz Band, 4.568GHz $\leq f_2 \leq$ 5.51 GHz,

$$m2 = -1503{f_2}^{-2.861} + 28.31, \quad (14)$$

$$m2 = 1.324{f_2}^{3} - 23.32{f_2}^{2} + 142.5f_2 - 281.5. \quad (15)$$

Equation (12) and Eqn. (14) represent the general power2 model. The linear polynomial of degree 2 and 3 models are represented by Eqn. (13) and Eqn. (15), respectively. Among these models, the general power2 model relates the 'm1' ('m2') with '$f_1$' ('$f_2$') better than the linear polynomial of degree 2 or degree 3 model. The R-square value is 1 for both models, which ensures the best goodness of fit. Figure 2 depicts this relationship. As the patch is perturbed, the resonant frequency is shifted from a lower to a higher value as shown in Fig. 3.

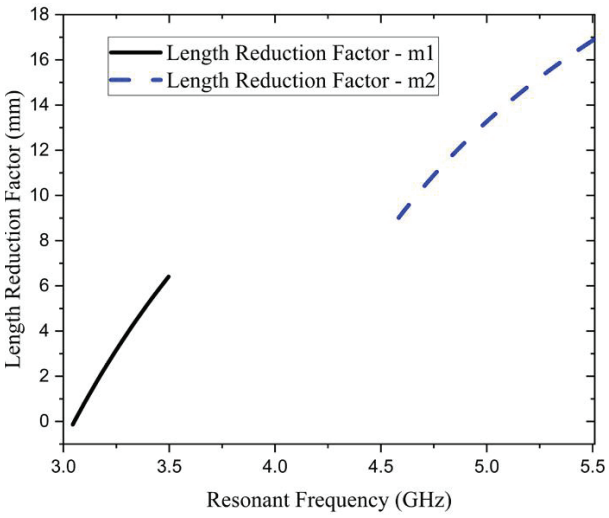


Fig. 2. Length reduction factor.

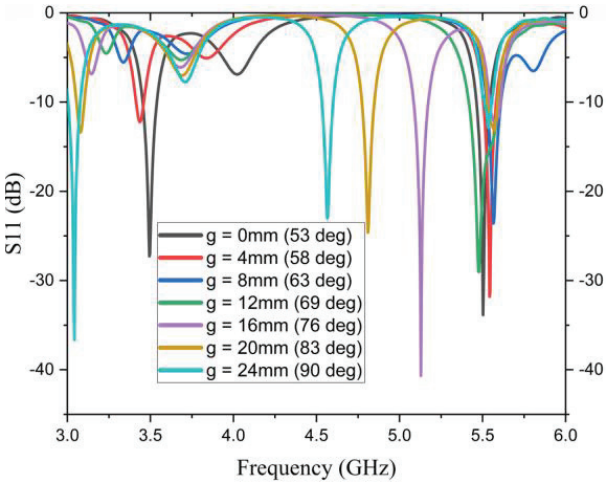


Fig. 3. Resonant frequency shifts due to perturbation.

## V. PERTURBATION TECHNIQUE

The solution of the homogeneous wave equation in terms of vector potential (Az) for this proposed antenna has been obtained using the differential equation method (separation of variables). Then the fields and the expression for resonant frequency are derived from 'Az'. This approach leads to an exact solution for this antenna that resembles an RT Duroid dielectric-loaded resonant cavity. However, many electromagnetic field problems such as microwave resonators, waveguides and antenna problems cannot be solved using the conventional differential equation method due to the mathematical complexity involved in the structural definition and boundary conditions. The perturbational method is an alternative approach for solving electromagnetic problems, including antenna analysis. The word 'perturb' means to disturb or to change slightly. The perturbational method is useful for calculating the shift in resonant frequency due to changes in the structure of the printed antenna. Two kinds of structures involved in this proposed printed antenna. One kind is the 'unperturbed' structure, for which the resonant frequency is known (3.04 GHz at 3.5 GHz band and 4.57 GHz at 5.5 GHz band), and the other is the 'perturbed' structure, which is different from the unperturbed one. The perturbed and unperturbed printed antennas are shown in Fig. 1 and Fig. 4, respectively. The electromagnetic energy is stored in the volume of 3981.6 mm$^3$ in the unperturbed antenna, bounded by

(Lr1+Lr2) × Wr × h mm$^3$. The right-hand side edge of the antenna is perturbed in both patch and ground plane, which reduces the conducting surface area in that region, which in turn removes the volume of 1209.6 mm$^3$.

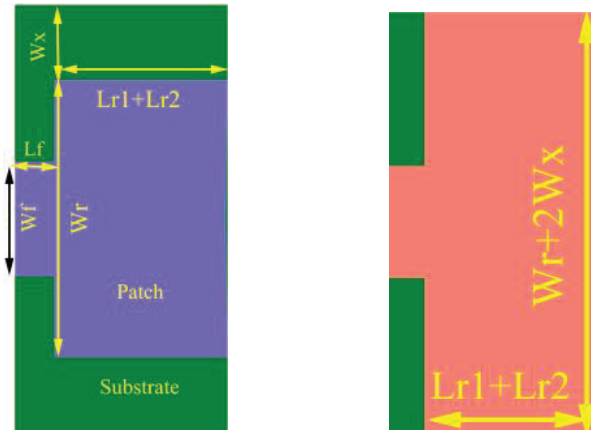


(a) (b)

Fig. 4. Unperturbed antenna. (a) Top view. (b) Bottom view.

Consequently, the stored energy is also removed in that volume governed by the removed surface area and the thickness of the substrate. Equation (16) relates the resonant frequency shift with the volume and energy stored in the resonant cavity [31]:

$$\frac{f_i - f_{0i}}{f_{0i}} = a_i = \frac{V_\alpha}{V} = \frac{W_{i\alpha}}{W_i}, \tag{16}$$

where, '$f_i$' is the shifted resonant frequency due to perturbation or resonant frequency of the perturbed antenna. '$f_{oi}$' is the resonant frequency of the unperturbed antenna. '$a_i$' is the parameter that depends on the antenna structure and the position of the perturbation. '$V_\alpha$' is the removed volume due to perturbation. 'V' is the volume of the unperturbed antenna. '$W_{i\alpha}$' is the removed energy due to perturbation or stored energy in the volume defined by the product of removed patch area and thickness of the antenna. '$W_i$' is the stored energy in the volume defined by the unperturbed antenna:

i = 1 for 3.5 GHz band

i = 2 for 5.5 GHz band

A change in the input power to the antenna will not affect the estimated frequency since the resonant frequency shift is proportional to the change in stored energy relative to the total energy stored in the unperturbed resonant cavity. For various input power levels, the stored and removed energy level will be proportionally varied. Consequently, the energy ratio will remain constant.

### A. WiMAX 3.5 GHz band

The resonant frequency of the unperturbed antenna '$f_{o1}$' is 3.04 GHz from Eqn. (4) with the effective value of 'm1' equals −0.133. The physical value of 'm1' equals zero also predicts the resonant frequency of the unperturbed antenna as 3.05 GHz, which is very close to 3.04 GHz. CST Studio Suite simulation demonstrating 3.04 GHz validates the calculated result. When it is perturbed at the right-hand edge, the frequency has shifted to 3.5 GHz. More perturbation is taking place at the position where its magnetic field is maximum.

The resonant frequency shift '$f_1$' caused by perturbation in the antenna's structure can be computed using Eqn. (16):

$$V = (Lr1 + Lr2) \times Wr \times h = 3981.6\ mm^3, \tag{17}$$

$$V\alpha = 0.5 \times Lr2 \times Wr \times h = 1209.6\ mm^3. \tag{18}$$

The electric and magnetic field expressions within the antenna structure (taken as cavity resonator) are given by Eqn. (19) to Eqn. (24) [30]:

$$\mathrm{E_x} = \frac{-\mathrm{jK_zK_x}}{\omega\mu\varepsilon} A_{pqr} \operatorname{Sin}(\mathrm{K_x x}) \operatorname{Cos}(\mathrm{K_y y}) \operatorname{Sin}(\mathrm{K_z z}), \tag{19}$$

$$\mathrm{E_y} = \frac{-\mathrm{jK_zK_y}}{\omega\mu\varepsilon} A_{pqr} \operatorname{Cos}(\mathrm{K_x} x) \operatorname{Sin}(\mathrm{K_y y}) \operatorname{Sin}(\mathrm{K_z z}), \tag{20}$$

$$\mathrm{E_z} = \frac{-\mathrm{j}(k_i^2 - K_z^2)}{\omega\mu\varepsilon} A_{pqr} \operatorname{Cos}(\mathrm{K_x} x) \operatorname{Cos}(\mathrm{K_y y}) \operatorname{Cos}(\mathrm{K_z z}), \tag{21}$$

$$\mathrm{H}_x = \frac{K_y}{\mu} A_{pqr} \operatorname{Cos}(\mathrm{K_x} x) \operatorname{Sin}(\mathrm{K_y y}) \operatorname{Cos}(\mathrm{K_z z}), \tag{22}$$

$$\mathrm{H_y} = \frac{-K_x}{\mu} A_{pqr} \operatorname{Sin}(\mathrm{K_x} x) \operatorname{Cos}(\mathrm{K_y y}) \operatorname{Cos}(\mathrm{K_z z}), \tag{23}$$

$$H_z = 0. \tag{24}$$

All of the above equations contain the mode-dependent amplitude coefficient 'Apqr', which scales the amplitude of all fields equally. As only TM$^z{}_{110}$ mode exists in this 3.5 GHz band, the 'Apqr' value will be the same for all fields. Therefore, its value is taken as unity. Moreover, all fields can be normalized by this coefficient to make its presence insignificant. The wavenumbers are expressed by the Eqn. (25) to Eqn. (28):

$$K_x = \frac{p\pi}{Lr1 + Lr2 - m1} = 95, \tag{25}$$

$$K_y = \frac{q\pi}{Wr + 2h} = 47.46, \tag{26}$$

$$K_z = \frac{r\pi}{h} = 0, \tag{27}$$

$$k_i = k_1 = \omega_1 \sqrt{\mu\varepsilon_1}. \tag{28}$$

The field variation along the Z-axis is negligible because the antenna's thickness is minimal to its operating wavelength. The denominator of Eqn. (25) determines the resonant length. The stored energy is computed for the band of interest, such as 3.5 and 5.5 GHz. Hence, the resonant length is the effective length along the X-axis, which is considered for stored energy calculation. The total energy stored in the electric field '$W_{e1}$' and

magnetic field '$W_{m1}$' at 3.5 GHz of an unperturbed antenna of volume 'V' is given by Eqn. (29) to Eqn. (32):

$$W_{e1} = \frac{\varepsilon_1}{2}\iiint |E_z|^2 dv = 4.947KJ, \tag{29}$$

with the integral limit for Eqn. (29), Eqn. (31) and Eqn. (32): x = 0 to Lr1+Lr2; y = 0 to Wr and z = 0 to h:

$$W_{m1} = W_{Hx} + W_{Hy} = 4.875KJ, \tag{30}$$

$$W_{Hx} = \frac{\mu}{2}\iiint |H_x|^2 dv = 1.054KJ, \tag{31}$$

$$W_{Hy} = \frac{\mu}{2}\iiint |H_y|^2 dv = 3.821KJ. \tag{32}$$

The energy stored in the electric and magnetic fields is almost the same at resonance. The perturbation technique is applied to predict the resonant frequency shift for two cases of energy perturbation.

Case 1: Electric energy perturbation

The part of the electric energy '$W_{1\alpha e}$' removed by the volume 'V$\alpha$' due to perturbation from the total stored energy is 1503 J. The ratio of removed energy to total stored energy in the electric field is given by the Eqn. (33):

$$\frac{W_{1\alpha e}}{W_1} = \frac{1503J}{2W_{e1}} = 0.153. \tag{33}$$

The shifted resonant frequency and parameter 'a1e' is predicted using the Eqn. (16) that relates the energy and volume ratio with the frequency ratio given by Eqn. (34) and Eqn. (35):

$$f_{1e} = 1.153 f_{01} = 3.505GHz, \tag{34}$$

$$a_{1e} = 0.5036. \tag{35}$$

Case 2: Magnetic energy perturbation

Magnetic energy of 1481J is removed by 'V$\alpha$' in this case. The magnetic energy ratio is given by Eqn. (36):

$$\frac{W_{1\alpha m}}{W_1} = \frac{1481J}{2W_{m1}} = 0.152. \tag{36}$$

The shift in resonant frequency and parameter 'a1m' is given by Eqn. (37) and Eqn. (38)

$$f_{1m1} = 1.152 f_{01} = 3.502GHz, \tag{37}$$

$$a_{1m1} = 0.5. \tag{38}$$

If 'W1' is the summation of energy stored in the electric and magnetic fields at the resonance, then Eqn. (39) and Eqn. (40) will result.

$$f_{1m2} = 1.151 f_{01} = 3.499GHz, \tag{39}$$

$$a_{1m2} = 0.497. \tag{40}$$

The same result is estimated for the resonant frequency shift resulting from perturbation from both electric and magnetic energy perturbation cases and is confirmed by simulation and measurement.

### B. WiMAX 5.5 GHz band

The resonant length in 3.5 GHz band is the length connecting the lower edge 'AB' to upper edge 'ED' as illustrated in Fig. (5) and is uniform. Whereas for 5.5 GHz band, the length connecting the left edge 'AE' to right edge 'BCD' is the resonant length and is not uniform due to the presence of perturbation. The 'm2' value corresponds to the effective length responsible for 5.5 GHz resonance is calculated using MATLAB program and simulation. The unperturbed antenna structure resonates at 4.57 GHz in the simulation, whereas, the Eqn. (9) predicts the resonance at 4.1 GHz. The simulated resonant frequency of 4.57 GHz is taken as the resonant frequency of the unperturbed antenna. For this 5.5 GHz band, the same procedure is followed as in section V. A for 3.5 GHz band to compute the resonant frequency shift using perturbation technique, and the results are furnished below:

Equation (41) to Eqn. (44) express the wavenumbers:

$$K_x = \frac{p\pi}{Lr1 + Lr2 - m2} = 139, \tag{41}$$

$$K_y = \frac{q\pi}{W_r} = 99.73, \tag{42}$$

$$K_z = \frac{r\pi}{h} = 0, \tag{43}$$

$$k_i = k_2 = \omega_2\sqrt{\mu\varepsilon_2}. \tag{44}$$

The field variation along the Z-axis is negligible because of the thin substrate compared to the operating wavelength. The total energy stored in the electric field ' $W_{e2}$' at 5.5 GHz of an unperturbed antenna of volume 'V' is expressed by Eqn. (45):

$$W_{e2} = \frac{\varepsilon_2}{2}\iiint |E_z|^2 dv = 10.187KJ, \tag{45}$$

with the integral limit for Eqn. (45): x = 0 to Lr1+Lr2; y = 0 to Wr and z = 0 to h. As the energy stored in the electric field will be the same as that in magnetic fields at resonance, the total energy stored in the antenna structure will be twice the energy stored in the E-field. This stored electric energy calculation is enough to predict the resonant frequency shift due to perturbation using the perturbation technique. Therefore, the energy stored in the H-field calculation is not necessary.

The part of the electric energy '$W_{2\alpha}$' of 3.1KJ is removed by the volume 'V$\alpha$' due to perturbation from the total stored energy. The ratio of removed energy to total stored energy in the electric field is illustrated by Eqn. (46):

$$\frac{W_{2\alpha}}{W_2} = \frac{3.1KJ}{2W_{e2}} = 0.152. \tag{46}$$

The shifted resonant frequency '$f_{2ea}$' and parameter 'a2ea' are predicted analytically using Eqn. (16) as illustrated by Eqn. (47) and Eqn. (48).

$$f_{2ea} = 1.152 f_{02} = 5.3GHz, \tag{47}$$

$$a_{2ea} = 0.5. \tag{48}$$

The ratio of the resonant frequency of a perturbed ($f_{2s}$) to an unperturbed ($f_{02}$) antenna from the simulation

is given by Eqn. (49):

$$\frac{f_{2s}}{f_{02}} = \frac{5.5GHz}{4.57GHz} = 1.2. \quad (49)$$

The ratio of the removed energy '$W_{2\alpha s}$' to total energy '$W_{2s}$' computed from Eqn. (16) corresponding to Eqn. (49) is illustrated by Eqn. (50):

$$\frac{W_{2\alpha s}}{W_{2s}} = 0.2. \quad (50)$$

The parameter 'a2s' corresponds to Eqn. (50) is calculated from Eqn. (16) and is given by Eqn. (51):

$$a_{2s} = 0.658. \quad (51)$$

The simulated resonant frequency shift due to perturbation is validated with the measured result using a vector network analyzer (ZNB20, Rohde & Schwarz) as shown in Fig. 8. Equation (52) depicts the deviation (d) between the measured frequency shift and that obtained from a calculation using the analytical method (resonant cavity method):

$$d = \left(\frac{f_{2s} - f_{2ea}}{f_{2s}}\right) \times 100 = 3.6\%. \quad (52)$$

It is observed from Eqn. (16) that the resonant frequency shift due to perturbation is determined by the energy removed in the perturbed volume. Equation (50) reveals that 20% of the total stored energy is removed due to perturbation, whereas Eqn. (46) predicts that 15.2% of that has been removed. A deviation of 4.8% exists between simulation and analytical computation based on the resonant cavity method. The removed energy predicted by the analytical method is lower than that of simulation, which eventually leads to the deviation in the resonant frequency shift, as notified by Eqn. (52). To validate this proposed perturbation technique, few antennas with slots and slits are selected from the literature [32–35]. In the aforementioned research, the shifted resonant frequencies are explored qualitatively rather than analytically. When the corners of a square patch are trimmed in Ref. [32], the patch's resonant frequency is shifted to 2.44 GHz from 2.4 GHz. The resonant frequency shift due to the addition of five slits on a radiating patch is reported in [33]. It is studied that the resonant frequency has shifted towards a higher value as the slits are added one by one from about 2.3 GHz to 7.5 GHz. Square-shaped slits and truncated corners are introduced on a patch fabricated using cotton and denim clothes as substrate [34]. The resonant frequency has shifted from 2.43 GHz to 2.53 GHz when the patch is perturbed. A square cavity formed by a substrate integrated waveguide, backed slot antenna is presented in [35]. An inward cut is made at the bottom right corner of the square cavity. As the size of the inward cut increases, the effective volume decreases. Eventually, the resonant frequency of the antenna increases. When these stated results are examined from the perspective of the perturbation approach, the energy removed from the volume corresponding to the region where the slits and truncations are taking place is what causes the resonant frequency shifting. In these described works [32–35], the eliminated energy causes the resonance to change from a lower to a higher value.

## VI. RESULTS AND DISCUSSION

The proposed printed antenna has two resonant lengths, responsible for 3.5 GHz along the Y-axis and 5.5 GHz along the X-axis, as shown in Fig. 1. The surface current density plot illustrated in Figs. 6 (a) and 6 (b) ensures that the current flows between the top and bottom edges for 3.5 GHz resonance, and for 5.5 GHz, it flows between left and right edges. The E-field contour plot shown in Fig. 6 (c) demonstrates the electric field variation along the X and Y axes. There is a null between the maximum field that occurs at either end. This scenario ensures the $TM^{Z}_{110}$ mode for 3.5 GHz resonance. In Fig. 6 (d), the horizontal white-coloured dashed line refers to the resonant path length responsible for the 5.5 GHz band. It is observed that a null occurs in between the two field maxima, and it refers to a one half-cycle variation along the X-axis. Three maximum field clusters with two nulls along the white-coloured vertical dotted line indicate the two half-cycle electric field variation along the Y-axis.

It dictates $TM^{Z}_{120}$ mode at 5.5 GHz resonance. Figures 6 (e) and (f) show the magnetic field contour with the most significant amplitude corresponding to the space where the E-field is least and vice versa.

The resonant frequency of the unperturbed antenna is 3.04 GHz and 4.57 GHz, which has shifted to 3.5 GHz and 5.5 GHz, respectively, when its right-side edge is perturbed. This perturbation is made by removing copper on both the top and the corresponding bottom side.

However, the RT Duroid substrate is left in place, as illustrated in Fig. 1. When the copper and substrate of the perturbed volume are fully removed as shown in Fig. 5, little more energy is lost than in the perturbed structure, which eventually shifts the resonance further as depicted in Fig. 7. The simulated and measured return loss of the perturbed antenna is plotted in Fig. 8 (a), which shows the impedance bandwidth of 8% (3.35–3.64 GHz) at the 3.5.

GHz band and 5% (5.36–5.65 GHz) at the 5.5 GHz WiMAX band. Figure 8 (b) depicts the input reactance of the antenna, which ensures zero reactance at the resonant frequencies. Figures 9 and 10 depict the co and cross-polarization pattern at 3.5 GHz for E- and H-planes, respectively. This antenna is a broadside radiator, and the maximum radiation is taking place towards the normal to the patch. The cross-pol level is less than

−50 dB in E-plane at the maximum radiation direction and −120 dB in the H-plane. The polarization pattern at 5.5 GHz for both E and H-plane is shown in Figs. 11 and 12, respectively. It is observed that the cross-pol level is about −90 dB in the E-plane and −70 dB in the H-plane. A sharp null exists in the normal direction to the plane of the patch, and the main beam is tilted to 18° from the normal in the H-plane, which looks like a split beam. This split is due to the cut at the right edge of the perturbed antenna.

The simulated and measured gain are illustrated in Fig. 13. The simulated gain is 6.62 dBi at 3.5 GHz, whereas measured gain is 6.38 dBi. The simulated and measured gain for 5.5 GHz are 6.07dBi and 5.84 dBi, respectively. The measured gain at 5.5 GHz is less than that of 3.5 GHz due to the tapering at the right edge of perturbed antenna shown in Fig. 5. The red line shown in Fig. 5 is the resonant length for 5.5 GHz. A small amount of the electric field around this line at the left side (AE) forms the radiating slot. The electric field marked as 'E2' at the right side (BCD) has normal and tangential components. The angle between 'AB' and 'BC' is 53°. The angle between the electric field vector 'E2' and the edge 'AB' or 'ED' is 37°. The 'E2' vector is resolved into normal and tangential components expressed by Eqn. (53).

$$\overline{E_2} = \hat{x}E_2 Cos37^\circ \pm \hat{y}E_2 Sin37^\circ = 0.799E_2\hat{x} \pm 0.602E_2\hat{y}. \quad (53)$$

Sign is positive for taper line 'BC' and negative for taper line 'CD'. The tangential component '0.799$E_2$' is constructively added with the corresponding E-field at the side 'AE', whereas the normal component '0.602$E_2$' is destructively added between 'BC' and 'CD'. About 20% of 'E2' field is lost due to tapering at the right side of the patch. This field loss reduces the field strength in the radiating slot, and the gain is also lowered accordingly. As there is no tapering in the resonant length for 3.5 GHz, its gain is not suffered.

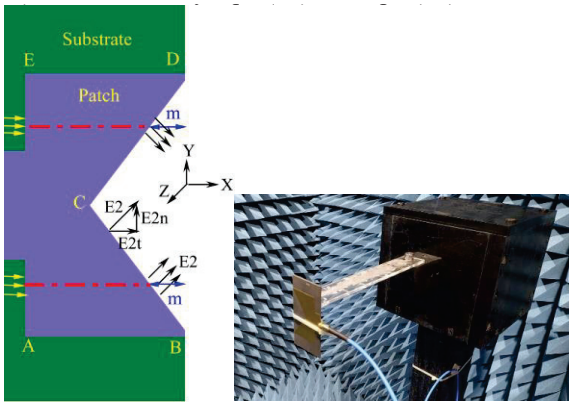


(a) (b)

Fig. 5. (a) Perturbed antenna with removed perturbed volume. m = m1 at 3.5 GHz. m = m2 at 5.5 GHz. (b) Antenna in an anechoic chamber for measurement.

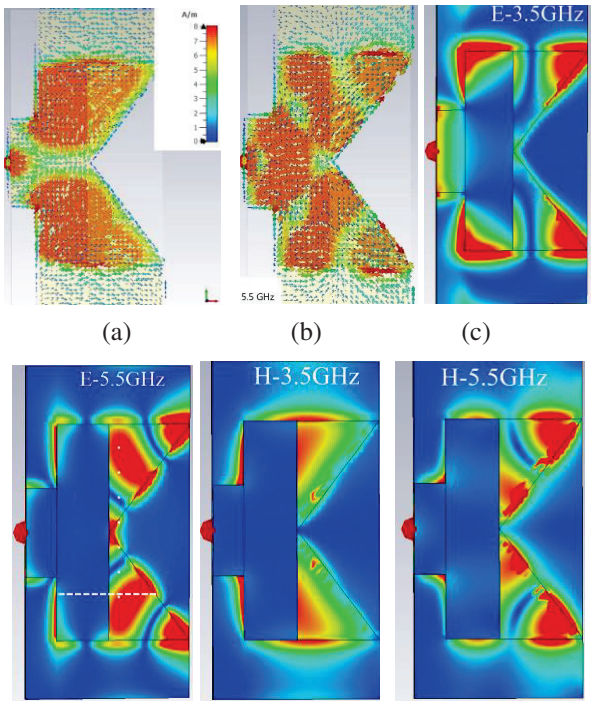


(a) (b) (c)

(d) (e) (f)

Fig. 6. Surface current density, E and H-field contour plot (a) Current at 3.5GHz. (b) Current at 5.5GHz. (c) E-Field at 3.5GHz. (d) E-Field at 5.5GHz. (e) H-Field at 3.5GHz. (f) H-Field at 5.5GHz.

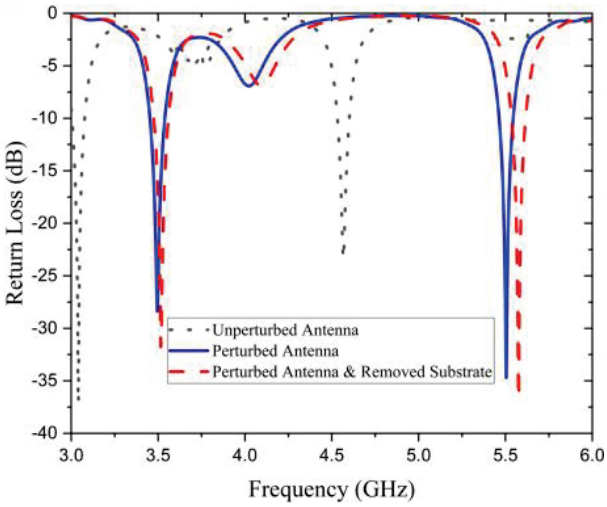


Fig. 7. Resonant frequency shift in three types of the antenna structure.

The simulated radiation efficiency is depicted in Fig. 14. The radiation efficiency is 91.45% at 3.5 GHz and 89.56% at 5.5 GHz.

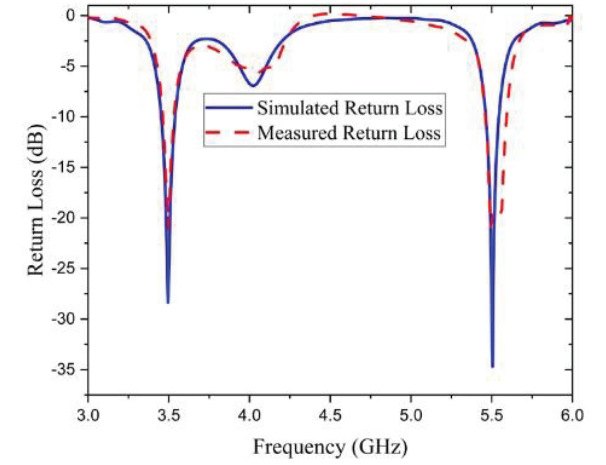


(a)

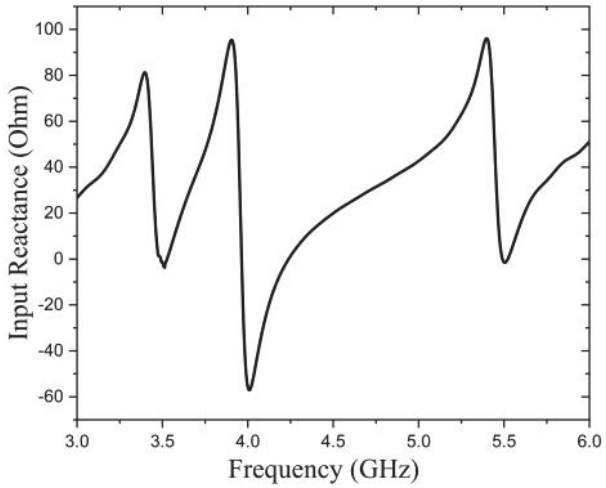


(b)

Fig. 8. (a) Return loss of perturbed antenna. (b) Input reactance.

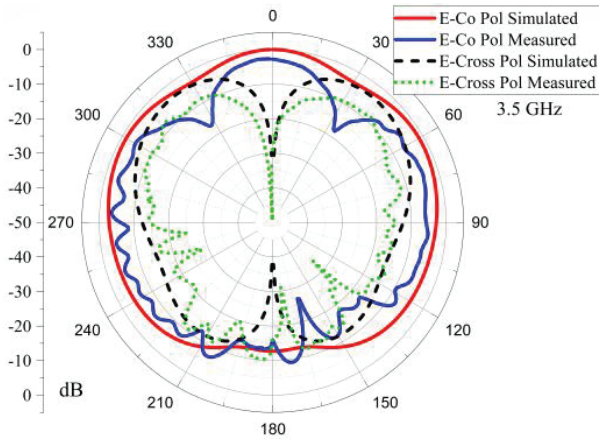


Fig. 9. Co and cross polarization at 3.5GHz for E-plane.

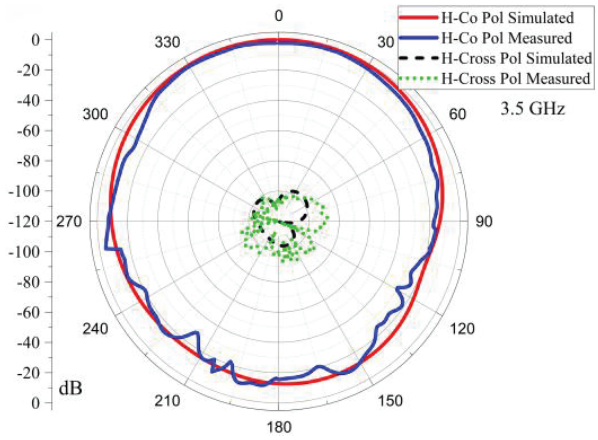


Fig. 10. Co and cross polarization at 3.5GHz for H-plane.

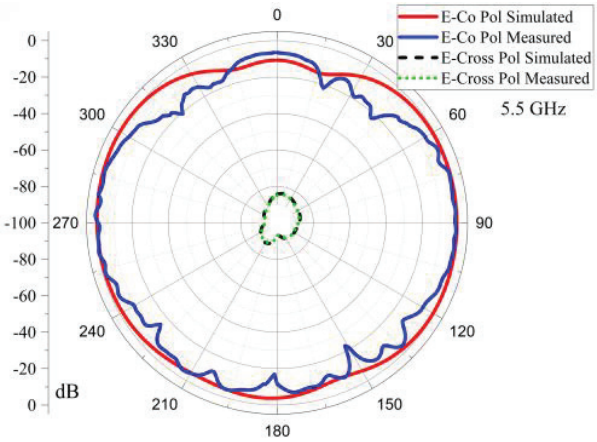


Fig. 11. Co and cross polarization at 5.5GHz for E-plane.

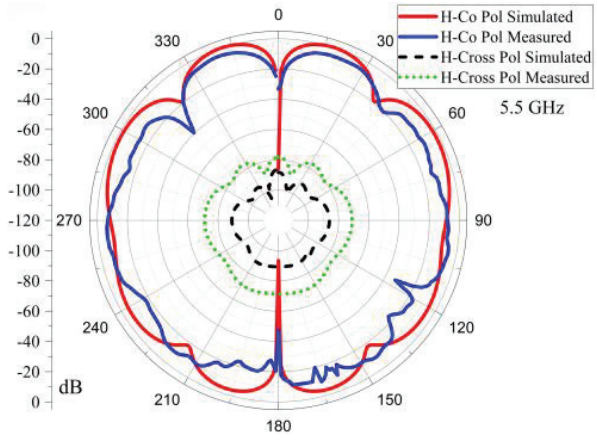


Fig. 12. Co and cross polarization at 5.5GHz for H-plane.

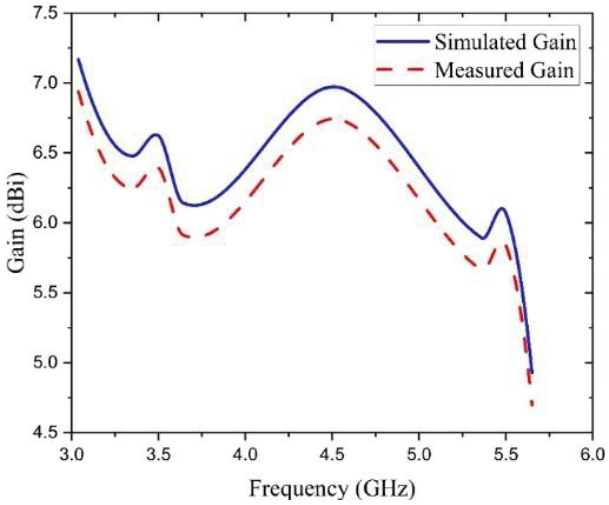


Fig. 13. Simulated and measured gain.

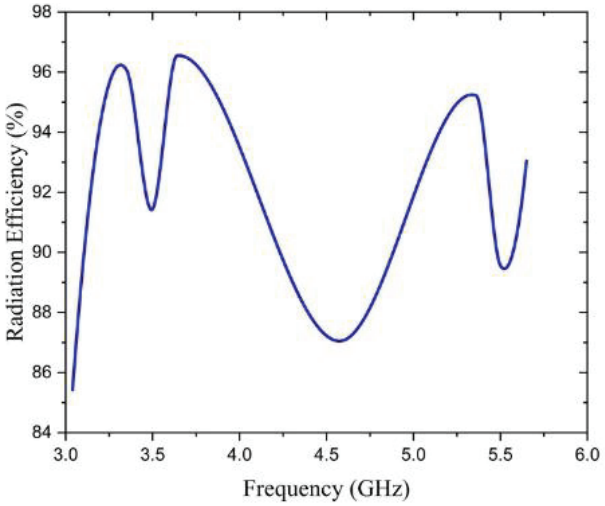


Fig. 14. Simulated Radiation efficiency.

## VII. CONCLUSION

A dual-band printed antenna has been designed for WiMAX application. The perturbation technique is applied to study the relationship between the resonant frequency and electromagnetic energy stored in the volume of antenna structure. The result obtained from this technique has been validated with simulation and measurement. The cross-pol level is well below the co-pol. As the structure of this proposed antenna is simple and conformal, it can be printed conveniently on electronic gadgets. The procedure discussed in this article for applying the perturbation technique can be adapted to predict the resonant frequency of any printed antenna loaded with slit or slot or similar patterns from the known resonant frequency of the undisturbed structure. In addition, to study the trend of frequency shift when the antenna's structure is perturbed, numerical methods can be used to compute the energy in the complicated or ununiformed perturbation.

## REFERENCES

[1] Z. J. Eleftheriades, "Dual-band metamaterial-inspired small monopole antenna for WiFi applications," *Electron. Lett.,* vol. 45, no. 22, 2009.

[2] X. S. Ren, Y. Z. Yin, W. Hu, and Y. Q. Wei, "Compact tri-band rectangular ring patch antenna with asymmetrical strips for WLAN/WiMax applications," *J. Electromagn. Waves Appl.,* vol. 24, pp. 1829-38, 2010.

[3] B. Yang, Y. Jiao, W. Zhang, H. Xie, and F. Zhang, "Dual-band ring-shaped antenna for WiMAX/WLAN applications," *IEEE Int. Conf. Microw. Technol. Comput. Electromagn.,* pp. 38-40, 2011.

[4] P. Jing, A. G. Wang, S. Gao, and W. Leng, "Miniaturized triple-band antenna with a defected ground plane for WLAN/WiMAX applications," *IEEE Antennas Wirel. Propag. Lett.,* vol. 10, pp. 298-301, 2011.

[5] B. Mazumdar, U. Chakraborty, A. Bhowmik, and S. K. Chowdhury, "Design of compact printed antenna for WiMAX & WLAN applications," *Procedia Technol.*, vol. 4, pp. 87-91, 2012.

[6] H. Zhai, Z. Ma, Y. Han, and C. Liang, "A compact printed antenna for triple-band WLAN/WiMAX applications," *IEEE Antennas Wirel. Propag. Lett.,* vol. 12, pp. 65-8, 2013.

[7] Y. Li and W. Yu, "A miniaturized triple band monopole antenna for WLAN and WiMAX applications," *Int. J. Antennas Propag.*, pp. 1-5, 2015.

[8] R. K. Saraswat and M. Kumar, "Miniaturized slotted ground UWB antenna loaded with metamaterial for WLAN and WiMax applications," *Prog. Electromagn. Res. B.,* vol. 65, pp. 65-80, 2016.

[9] F. Cirik and B. S. Yildirim, "Analysis and design of a 3.5-GHz patch antenna for WiMAX applications," *Int. J. Microw. Wirel. Technol.*, vol. 8, pp. 63-70, 2016.

[10] T. Ali, A. W. M. Saadh, R. C. Biradar, J. Anguera, and A. Andújar, "A miniaturized metamaterial slot antenna for wireless applications," *AEU - Int. J. Electron. Commun.,* vol. 82, pp. 368-82, 2017.

[11] M. Challal, F. Mouhouche, K. Djafri, and A. Boutejdar, "Quad-band microstrip patch antenna for WLAN/WIMAX/C/X applications," *5th Int. Conf. Electr. Eng.,* Boumerdies, Algeria, vol. 1, pp. 1-4, 2017.

[12] T. Ali and R. C. Biradar, "A compact multi-band antenna using $\lambda/4$ rectangular stub loaded with metamaterial for IEEE 802.11N and IEEE

802.16E," *Microw. Opt. Technol. Lett.*, vol. 59, pp. 1000-1006, 2017.

[13] D. Sipal, M. P. Abegaonkar, and S. K. Koul, "Compact planar 3.5/5.5 GHz dual band MIMO USB dongle antenna for WiMAX applications," *IEEE Indian Conf. Antennas Propogation.,* pp. 1-4, 2018.

[14] W. S. Chen, M. H. Liang, T. Y. Zhuo, J. H. Lin, and J. H. Hsu, " Dual-strip monopole antenna for USB dongle applications," *IEEE Int. Work. Electromagn. Student Innov. Compet.,* pp. 1-2, 2018.

[15] P. Osklang, C. Phongcharoenpanich, and P. Akkaraekthalin, "Triband compact printed antenna for 2.4/3.5/5 GHz WLAN/WiMAX applications," *Int. J. Antennas Propag.,* vol. 2019, pp. 1-13, 2019.

[16] N. Ferdous, G. Chin Hock, H. A. S. Hamid, M. N. A. Raman, T. S. Kiong, and M. Ismail, "Design of a small patch antenna at 3.5 GHz for 5G application," *IOP Conf. Ser. Earth Environ. Sci.*, pp. 268, 2019.

[17] X. Li, H. Zhu, and Z. Huang, "A CPW-fed miniaturized dual-band antenna for 5G applications," *IEEE MTT-S Int. Conf. Numer. Electromagn. Multiphysics Model. Optim.,* pp. 1-3, 2020.

[18] O. Benkhadda, S. Ahmad, M. Saih, K. Chaji, A. Reha, A. Ghaffar, S. Khan, M. Alibakhshikenari, and E. Limiti, "Compact broadband antenna with vicsek fractal slots for WLAN and WiMAX applications," *Appl. Sci.*, vol. 12, no. 3, 2022.

[19] S. Tyagi, S. Kanojia, and P. K. Chakarvarti, "Micro strip patch antenna for WLAN/WiMAX applications: a review," *SSRN. Electron. J.*, pp. 162-166, 2020.

[20] P. Sandhiyadevi, V. Baranidharan, G. K. Mohanapriya, J. R. Roy, and M. Nandhini, "Design of dual-band low profile rectangular microstrip patch antenna using FR4 substrate material for wireless applications," *Mater. Today Proc.,* vol. 45, pp. 3506-3511, 2021.

[21] P. Mathur, R. Augustine, M. Gopikrishna, and S. Raman, "Dual MIMO antenna system for 5G mobile phones, 5.2 GHz WLAN, 5.5 GHz WiMAX and 5.8/6 GHz WiFi applications," *IEEE Access.,* vol. 9, pp. 106734-106742, 2021.

[22] K. Mahendran, D. R. Gayathri, and H. Sudarsan, "Design of multi band triangular microstrip patch antenna with triangular split ring resonator for S band, C band and X band applications," *Microprocess Microsyst.,* vol. 80, pp. 103400, 2021.

[23] S. K. Ibrahim and Z. T. Jebur, "A high gain compact rectangular patch antenna for 5G applications," *Int. Conf. Commun. Inf. Technol.*, vol. 2021, pp. 156-160, 2021.

[24] R. Kumar, R. Sinha, A. Choubey, and S. K. Mahto, "A circular monopole antenna with uniquely packed quad T-shaped strips for WLAN/WiMAX application," *Frequenz.,* 2022. https://doi.org/10.1515/freq-2022-0017

[25] A. K. Vallappil, A. M. K. Rahim, A. B. Khawaja, M. N. Iqbal, N. A. Murad, M. M. Gajibo, L. O. Nur, and B. S. Nugroho, "Complementary split-ring resonator and strip-gap based metamaterial fractal antenna with miniature size and enhanced bandwidth for 5G applications," *J. Electromagn. Waves. Appl.,* vol. 36, pp. 787-803, 2022.

[26] S. L. Gunamony, S. Rekha, and B. P. Chandran, "Asymmetric microstrip fed meander line slot antenna for 5.6 GHz applications," *Mater. Today Proc.,* vol. 58, pp. 91-95, 2022.

[27] S. Sharma and D. Kaur, "Measurement of complex permittivity of polystyrene composite at 11.64 GHz using cavity perturbation technique," *Applied Computational Electromagnetics Society (ACES) Journal*, vol. 31, no. 1, pp. 92-97, 2016.

[28] S. Fakhte and H. Oraizi, "Derivation of the resonant frequency of rectangular dielectric resonator antenna by the perturbation theory," *Applied Computational Electromagnetics Society (ACES) Journal*, vol. 31, no. 8, pp. 894-900, 2016.

[29] G. Kumar and K. P. Ray, *Broadband Microstrip Antennas,* Artech House, Boston, London, pp. 33, 2003.

[30] C. A. Balanis, *Antenna Theory Analysis and Design,* 4th ed., John Wiley & Sons, New Jersey, 2016.

[31] R. F. Harrington, *Time-Harmonic Electromagnetic Fields,* 2nd ed., Wiley-IEEE Press, New Jersey, 2001.

[32] S. Pawar and S. Hake, "Effect of different symmetric slits on microstrip patch antenna," *Int. J. Microw. Eng.,* vol. 1, pp. 23-33, 2016.

[33] K. Mondal and P. P. Sarkar, "Gain and bandwidth enhancement of microstrip patch antenna for WiMAX and WLAN applications," *IETE J. Research.,* vol. 67, pp. 726-734, 2021.

[34] R. Sreemathy, S. Hake, S. Sulakhe, and S. Behera, "Slit loaded textile microstrip antennas," *IETE J. Research.,* pp. 1-9, 2020.

[35] E. Baghernia and M. H. Neshati, "Development of a broadband substrate integrated waveguide cavity backed slot antenna using perturbation technique," *Applied Computational Electromagnetics Society (ACES) Journal*, vol. 29, no. 11, pp. 847-855, 2014.

**C. Mahendran** received the B.E degree in 1997 from Government College of Engineering, Tirunelveli, India and M.E in 2002 from Alagappa Chettiar Government College of Engineering and Technology (ACGCET), Karaikudi, India. He is currently working as an Assistant Professor at ACGCET and is pursuing his Ph.D at Anna University, Chennai, India. He worked as a Scientist (Grade B) in the Broadcast and Communication Group, Centre for Development of Advanced Computing, Thiruvananthapuram, India. His research interests include printed antenna design and RF system design.

**M. Vijayaraj** received the B.E degree in 1988 from Thiagarajar College of Engineering, Madurai, India and M.E in 1997 from ACGCET, Karaikudi, India. He was awarded a Ph.D from Anna University, Chennai, India in 2010. He is currently working as a Professor in Government College of Engineering, Tirunelveli, India. His research interests include wireless communication and printed antenna design.

# Ultra-wideband Terahertz Absorber Based on E Shape Graphene Pattern

**Muhammad Sajjad[1], Xiangkun Kong[1], Shaobin Liu[1], Saeed Ur Rahman[2], Zakir Khan[3], and Owais[4]**

[1]Key Laboratory of Radar Imaging and Microwave Photonics
Ministry of Education, College of Electronic and Information Engineering
Nanjing University of Aeronautics and Astronautics (NUAA), Nanjing, 211106, China
sajjadwazir@nuaa.edu.cn, xkkong@nuaa.edu.cn, lsb@nuaa.edu.cn

[2]School of Electronic Engineering
Xidian University, Xi'an, China
saeed@xidian.edu.cn

[3]Department Micro-/Nano-Electronic System Integration Center
University of Science and Technology of China, Hefei 230027, China
zakirkhan@mail.ustc.edu.cn

[4]Department of Electrical and Computer Engineering
COMSATS University Islamabad, Abbottabad, 22060, Pakistan
mkowais@cuiatd.edu.pk

***Abstract –*** We present a tunable ultra-wideband (UWB) absorber based on a multilayer of "E" shaped graphene patterns. The numerically calculated results indicate that the absorption of the proposed design is above 95% in the range of 1.12 to 14.04 THz. By using the multiple layers of graphene, the relative bandwidth is 95% and reaches up to 170% of the central frequency. Furthermore, for transverse electric polarization mode at a resonating frequency of 1.68, 3.99, 7.51, 13.56, and 17.74 THz the absolute value exceeds 99.57, 99.37, 99.94, 99.86, and 99.09%, respectively. Also, owing to the structure's rotational symmetry, the absorber is insensitive to both transverse magnetic (TM) and transverse electric (TE) polarization. The absorption peaks and frequency band can be controlled effectively by altering the Fermi level of graphene without modifying the structure manually. Moreover, the absorber exhibits steady absorption over an incident angle of 0° to 60°, with just a minor decrease in bandwidth around 60°.

***Index Terms –*** absorber, broadband, graphene, tunable.

## I. INTRODUCTION

In recent years, the research interest toward terahertz (THz) (0.1-10) frequency has increased due to its great potential in the areas of modulators, security, medical imaging spectroscopy, and communication [1, 2]. The THz absorber is a vital section that can be considered to be the practical application in the fields discussed above [3, 4]. However, it is very difficult to distinguish THz electromagnetic waves through a natural element. To resolve this problem, recently an artificial electromagnetic material known as metamaterial absorber (MMA) has been proposed which shows some remarkable electronic and optical properties. Graphene is a newly discovered 2-D monolayer based on a carbon atom. It has been widely considered in view of its unique electrical and optical properties [5, 6]. Its most desirable characteristics are that the conductivity and permittivity of the graphene can be dynamically controlled, by adjusting the Fermi level by external bias voltage or chemical doping, to obtain dynamically tunable MMAs [7, 8]. Over the last decade, numerous graphene-based tunable devices have been introduced which include transistors [9-12] and polarization convertors [13, 14]. A large number of graphene-based THz MMAs with different structures have been designed and published, including square patches [15], disks and ribbons [16], stacks [17], cross-shaped arrays [18], and as well as the combination of graphene wire and gold cut wire [19] configurations.

However, in the scope of our knowledge, the majority of these MMAs still have certain disadvantages, including single or narrow band absorption, and limited tunable range and considerable polarization and incident angle dependency, and having complex structure designs, thus reducing their potential application. In this article the "E" shape structure is designed as a

*Submitted On: October 13, 2022*
*Accepted On: January 24, 2023*

https://doi.org/10.13052/2023.ACES.J.380207

basic absorber unit cell that is simple and reliable. It is found that an "E" shape has many resonance modes, which compete with each other and increase the frequency range. Additionally, the absorption is very consistent across a wide range of incident angles. The design method provides a new way of achieving the band, enhanced by using the C-4 symmetry of "E" shape graphene in multilayer. Due to C-4 symmetry, the proposed design is less sensitive to the incident angles.

We developed an ultra-wideband absorber with an absorption of more than 175% for the central frequency of 7.83 THz, which is considerably greater than the best previous work. To achieve wide bandwidth, multiple layers of "E" shaped graphene patterns are used. The calculated results indicate that absorption spectra greater than 90% from 0.97 to 14.70 THz has been achieved. An "E" shaped graphene pattern was evaluated numerically and results revealed that the efficiency and bandwidth of the absorber can be improved by using multiple layers of graphene, while also achieving dynamic tuning. Additionally, field distribution is examined in order to investigate the absorption mechanisms. Also, in order to minimize the reflection coefficient, the impedance of the designed device is adjusted to be approximately matched to the free-space impedance, further explained in the Results & Discussion section (III).

## II. DESIGN AND SIMULATION

Figure 1 schematically show the structure of the suggested proposed ultra-wideband THz absorber. The proposed design consists of four layers of graphene in the "E" shape format. As shown in Fig. 1, all the four layers have the same structure but with 90° rotation. The graphene layers were deposited on silicon dioxide layers. The Topas layer with permittivity of 1.53 is considered as a low loss substrate [20]. Gold is selected as a ground metal as described by the Drude model [21].

The other parameters are as follows: $w$=5 $\mu$m, $L_1$=40 $\mu$m, $L_2$=20 $\mu$m, $H_1$=8 $\mu$m, $H_2$=5 $\mu$m, $H_3$=5 $\mu$m, $H_4$=5 $\mu$m, $H_5$=1 $\mu$m and $tm$=0.1 $\mu$m. The measurement along the $x$ and $y$ direction is 40 $\mu$m. To determine the chemical potential of the ultra-wideband (UWB) absorber's first layer, such as the graphene Fermi velocity, the electron mobility of the graphene and the relaxation time can be calculated as follows. If we set $\mu = 0.15\ m^2/(V.s)$ [22]. $\mu_{C1} = \tau v_f{}^2/\mu$ [23], $v_f = 1.73(m/s)$, [24] and $\tau = 0.05(ps)$ the chemical potential can be adjusted to 0.97 eV. The suggested design was numerically investigated by applying the frequency domain approach using commercial CST microwave studio simulation tools. The conductivity of graphene is composed of two parts, namely intraband and interband electron transition derived from the Kobo formula ($\sigma_{gra} = \sigma_{intra} + \sigma_{inter}$) [25]. In the THz and mid-

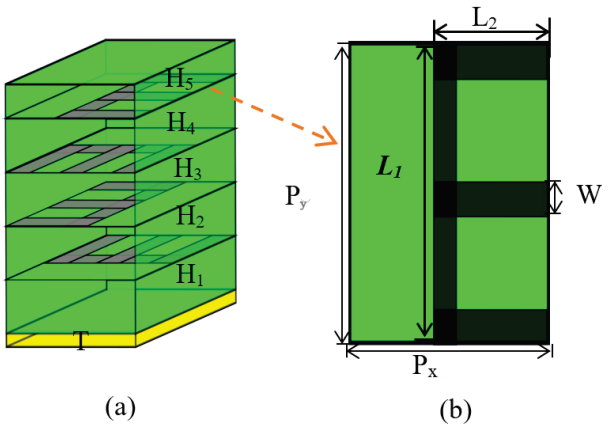


Fig. 1. (a) Schematic diagram of the proposed UWB-MMA unit cell, (b) top view of the "E" shape graphene layer.

infrared (MIR) wavelength ranges, the graphene intraband contribution is dominant because $E_F \gg \hbar\omega \gg K_B T$. So, in the view of the Puli exclusion principle for the THz frequency domain ($\hbar\omega \ll 2E_F$) at room temperature, the above expression is further simplified to the Drude model [26]:

$$\sigma_g = \frac{ie^2 E_F}{\pi\hbar^2(\omega + i\tau^{-1})}, \tag{1a}$$

where $\hbar$ represents reduced planks constant, $e$, $\tau$, and $\omega$ are electron charge, the relaxation time and angular frequency of the incident wave, respectively. The conductivity of the graphene at various Fermi levels is determined in Figs. 2 (a) and (b). When the Fermi level is fixed, it is shown that the real and imaginary parts of conductivity are proportional to the frequency. The amplitude modulation of the resonance is determined by the real component of the conductivity, while the resonance's spectral shift is controlled by the imaginary portion of the conductivity [27-29].

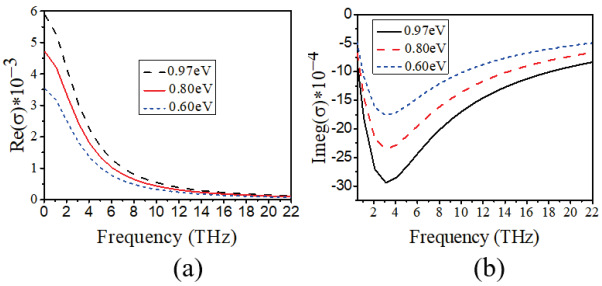


Fig. 2. Surface conductivity of the graphene with different chemical potential (a) Real part. (b) Imaginary part.

The theoretical relationship between $E_F$ and $V_g$ can be expressed as [30, 31]:

$$E_F = \mu_c \approx \hbar \upsilon_f \sqrt{\frac{\pi \varepsilon_r \varepsilon_\circ V_g}{eT_s}}, \quad (1b)$$

where, the Fermi velocity and external bias voltage are $\upsilon_f$ and $V_g$. The permittivity of substrate and vacuum is denoted by $e_r$ and $\varepsilon_0$. Equation [1b] indicates that carrier density can be modified by voltage or chemical doping due to the presence of the carrier density. By changing the bias voltage, graphene conductivity can be adjusted. The equivalent relative permittivity is then derived from the surface conductivity as follows [32]:

$$\varepsilon_g = 1 + \frac{i\sigma_g}{\varepsilon_o \omega t_g}, \quad (1c)$$

where $\sigma_g$ represents graphene surface conductivity, $\varepsilon_o$ and $t_g$ are vacuum permittivity and the thickness of the graphene layer. In equation (1c), the permittivity of the graphene can be found by measuring the conductivity of the graphene surface. The conductivity of the graphene surface can also be found by measuring the applied voltage. Thus, equations (1a-1c) show that the applied voltage may dynamically change the electromagnetic properties of graphene, implying that the structure absorption characteristics can likewise be dynamically adjusted. As a result, the absorbance may be varied by adjusting the Fermi level through applied voltage. The periodic boundary condition in the x-y plane is set in simulations and the incident THz wave will travel in the Z-direction as depicted in Fig. 1. Naturally, single-layer designs are simpler to produce than multilayer designs, but the use of multilayering is needed to enable high absorption rates and adjustable performance. The absorbance of the proposed design is computed/calculated as A=1-T-R=1-$|S_{21}(w)|^2$-$|S_{11}(w)|^2$, where T=$|S_{21}(w)|^2$ and R=$|S_{11}(w)|^2$, represent transmittance and reflectance respectively. The thickness of the gold ground is 0.5 $\mu$m, which is significantly higher than the skin depth, allowing $S_{21}$ to be technically reduced to zero.

## III. RESULT AND DISCUSSION

Firstly, to elevate the absorption efficiency of the proposed UWB-MMA. The unit cells are simulated under a normal THz incident wave. The calculated result is shown in Fig. 3. The TM incident wave is shown in Fig. 3 (a). The proposed UWB-MMA has a simulated reflective spectrum below 0.3 for 0.50 to 14.50 THz and has an absorption spectrum of more than 95% in the same range, as shown in Fig. 3 (a). For the TE incident wave the reflective spectrum is below 0.3 for 0.50 to 21.20 THz band, while the associated absorption is also higher than 95% within the 12.92 THz bandwidth as shown in Fig. 3 (b). The TM resonant frequencies in five distinct bands 3.94, 7.17, 14.05, 16.63, and 19.53 THz have 99.95, 99.65, 99.85, 99.54, and 99.70%, respectively, of the absorption spectrum.

These findings illustrate the almost symmetric pattern of the TM and TE polarization waves due to the almost symmetric structure of UWB-MMA as shown in Fig. 1. Furthermore, for TE polarization mode at resonating frequencies of 1.68, 3.99, 7.51, 13.56, and 17.74 THz the absolute value exceeds 99.57, 99.37, 99.94, 99.86, and 99.09%, respectively.

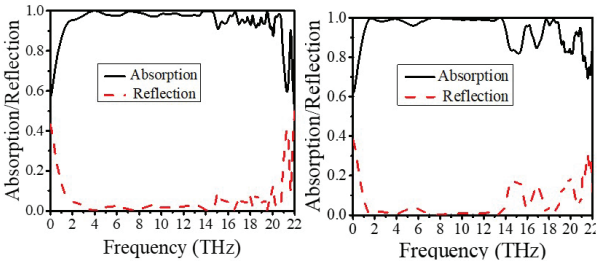


(a) (b)

Fig. 3. Absorption and reflection spectra of the proposed UWB-MMA (a) TM mode. (b) TE mode.

The characteristics of the complete absorption could be described using impedance matching theory. The absorber's effective impedance maybe represented as [33]:

$$Z_{eff} = \sqrt{\frac{\mu_{eff}}{\varepsilon_{eff}}} = \sqrt{\frac{(1+S_{11})^2 - S_{21}^2}{(1-S_{11})^2 - S_{21}^2}}, \quad (1)$$

where $\mu_{eff}$ and $\varepsilon_{eff}$ represent the effective permeability and permittivity, correspondingly. The S parameter is used to calculate the real and imaginary components of the impedance. If the device effective impedance approaches that of free space, significantly high absorption can be obtained. As shown in Fig. 4 (a), at a broad bandwidth the real component is near to 1 and imaginary part is close to 0, demonstrating that the effective impedance of the proposed device has equaled that of free space. This indicates that the absorber impedance steadily approaches that of empty space, which is characteristic of perfect absorber [34].

To describe the strong absorption in ultra-wideband bandwidth, the absorption spectrum is determined for each layer separately. When contrasting the effects of individual graphene layers with the whole system, the peaks of the whole system at 3.9, 4.6, 14.8, and 13.7 THz frequency band are led, respectively, by the fourth, third, second, and first layer, as shown in Fig. 4 (b). The UWB of the absorber is closely linked to each of these four peaks. The simulated field distribution demonstrated that UWB absorption of the proposed design can be considered as a superposition of these graphene layers. Absorption peaks at varying frequencies are close together and superimposed for UWB absorption. Then, to further explain the physical mechanism behind the

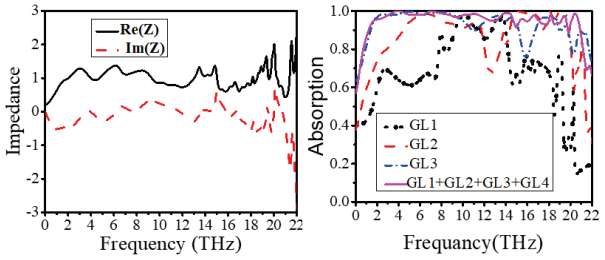


(a) (b)

Fig. 4. The relative input impedance and absorption spectrum of the proposed UWB-MMA, (a) input impedance (b) absorption spectrum.

UWB near-perfect absorption, we also provide a comprehensive analysis of electric field amplitude distributions at various frequencies under the setting of the Fermi level to 0.97 eV. Figure 5 illustrate electric field distributions of the unite cell at four distinct frequency bands under normal incidence TE wave. It may be noted that, as shown in Fig. 5, the suggested structure exhibited strong electric field confinement between the different layers of graphene and dielectric, leading to high absorption. This is the basic characteristic of the localized surface plasmonic. As depicted in Fig. 5 (a), from the simulated field distribution, it is evaluated that UWB absorption is achieved by the superposition of these graphene layers. As depicted in Fig. 5 (a), the top layer is largely attributed to the absorption peak around 3.9 THz. While the absorption peak at 4.6, 14.8, and 13.7 THz is primarily due to the third, second and first graphene layer respectively. Absorption peaks of various frequencies are closer to each other and superimpose to form an UWB absorption.

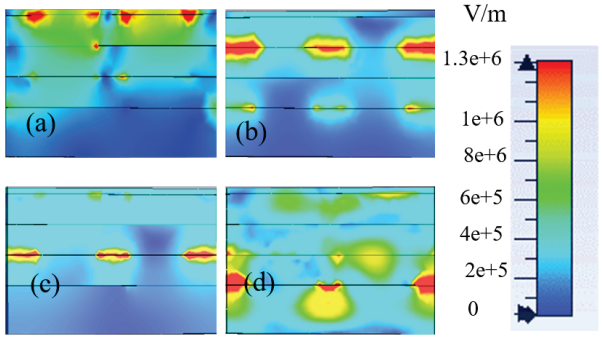


Fig. 5. Electric field distribution in TE polarization at XOZ plan at (a) 3.9 THz, (b) 4.6 THz, (c) 14.8 THz, and (d) 13.7 THz.

The absorption band is changed accordingly because graphene permittivity could be regulated by the chemical potential. The absorption changes to higher frequencies with increasing bandwidth and magnitude, as a result of increasing Fermi level. Figure 6 illustrate how the graphene Fermi level regulates the absorption spectrum with constant W and T. If the Fermi level increases, the graphene surface plasmon resonance increases and the structure absorption is higher with the $E_f$ =0.97 eV absorption band from 0.90 to 14.40 THz exceeds 90%. We have also investigated the influence of the permittivity and thickness of the substrate on the absorption property of the unit cell.

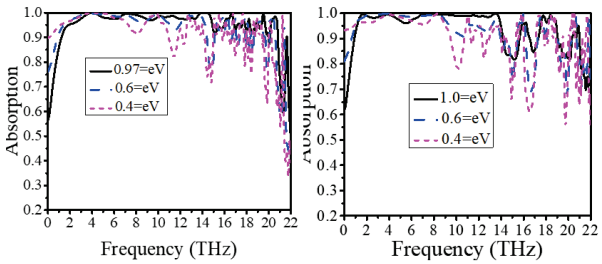


(a) (b)

Fig. 6. The absorption spectra of the proposed UWB-MMA under different Fermi levels (a) TM waves. (b) TE waves.

Figure 7 illustrate the influence of the dielectric thickness of the first and fifth layers ($H_1$ and $H_5$) over the absorption curve of the proposed absorber. When increasing the dielectric thickness value, the resonating frequencies are red-shifted. The high-frequency absorption curve shift to the left occurs, while the low-frequency band almost remains constant. When $H_1$ and $H_5$ are more than 8 $\mu$m and 1 $\mu$m the absorption rate at the center of the absorption band is less than 90%. The resonant coupling between the top and bottom layers of the graphene relies to a significant degree on their distance from one another. By increasing or reducing the coupling distance, near field coupling is reduced to a certain degree, resulting in a variation in absorption performance. Table 1 shows a comparison of our work with previously published works.

As shown in Fig. 8, the absorption spectrum's reliance on the dielectric substance is investigated in detail. The structure's whole set of parameters is stable and unaltered, and only the permittivity of the substrate is changed. As the permittivity decreased from 3.35 to 1.53, a minor change in the amplitude of absorption occurs while frequency shifts to the right.

Equation (3) shows the influence of the frequency shifts on the thickness and permittivity of the substrate. The $\phi_p$ and $\theta$ will be constant, as the plan wave will be transmitted on the homogenous medium layer at normal incidence.

Table 1: Performance comparison of the graphene bases UWB absorber with published work

| Ref. | Absorption Bandwidth (THz) | $F_o$ (THz) | Thickness ($\mu$m) | Angle | Fractional Bandwidth (%) | Absorptivity |
|---|---|---|---|---|---|---|
| [35] | 2.04-0.83 =1.21 | 1.435 | 0.07$\lambda$ | 0-50° | 84.3 | 90% |
| [36] | 7.85-2.05= 5.8 | 4.94 | 0.131$\lambda$ | 0-40° | 118 | 70% |
| [16] | 2.7-0.5=2.2 | 1.67 | 0.101 $\lambda$ | 0-30° | 131 | 90% |
| [37] | 2.67-0.65= 2.01 | 1.66 | 0.132 $\lambda$ | – | 121 | 90% |
| proposed | TE (14.70-0.97=13.73)<br>TM (14.96-0.70=14.26) | 7.85 | 0.083$\lambda$ | 0-45°<br>0-60° | 174 | 90% |

$\lambda$ is the wavelength of lowest frequency for each operating band, $F_o$ Central Frequency.

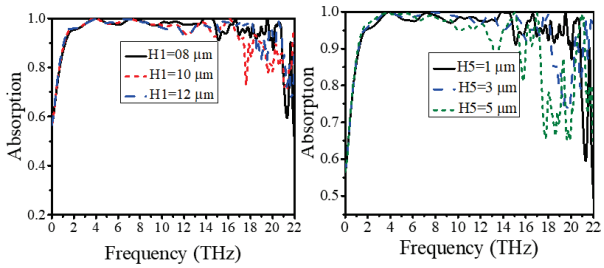


(a) (b)

Fig. 7. Absorption curve of the proposed absorber with different thicknesses of dielectric layer (a) first layer, and (b) fifth layer.

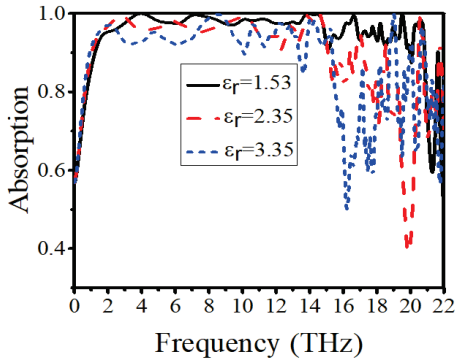


Fig. 8. Absorption curve of the proposed absorber with different permittivity of the dielectric substrate.

$$\phi_P = \frac{4d\sqrt{\varepsilon_r - \sin^2\theta}}{\lambda}, \quad (2)$$

where $d$ and $\phi_P$ represent substrate thickness and phase path of the incident EM wave.

Polarization insensitivity is useful for absorbers in practical applications. Therefore, the absorption under different polarized wave and incident angles is investigated. The absorption spectra of the proposed UWB-MMA are almost constant due to the symmetry of the rotation of the proposed configuration. As shown in Fig. 9. even when the polarization angle is between 0° and 45° for both TM and TE modes, the absorption spectra are still above 90% in the whole bandwidth. The UWB absorption efficiency will gradually decrease beyond 45° particularly for the lower frequency range for TE waves, as shown in Fig. 9 (b). That is why the magnetic flux between the ground plane and the graphene layer reduces as the angle of incidence TE waves increases [38]. Moreover, with the rise in the oblique incidence angle, the frequency spectrum of greater absorption has a small blue change.

The strong absorption of the UWB band frequency for TM waves can be sustained up to 60°, as seen in Fig. 9 (a). This means that at a higher incidence angle, the magnetic flux between the graphene layer and the ground layer is practically unchanged for the TM waves [38]. However, the absorption spectra for the proposed UWB-MMA also reveal a slight blue change with increasing angles of incidence for the TM wave. These findings demonstrate that both TE and TM waves can sustain absorption stability with varying polarization angles as well as large incident angles.

## IV. CONCLUSION

In this paper, we have proposed UWB tunable MMA based on the "E" shape graphene pattern on a gold layer separated by a dielectric substrate. Numerically calcu-

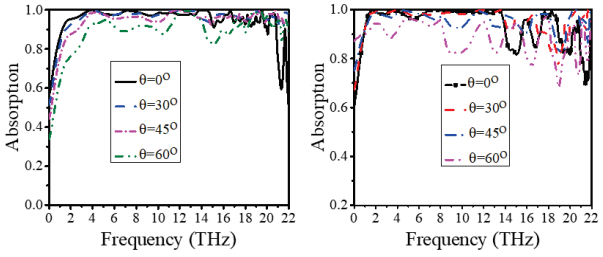


(a) (b)

Fig. 9. The absorption spectra of the proposed UWB-MMA under normal different incident angles (a) TM waves, and (b) TE waves.

lated results demonstrate that the suggested MMA attains higher absorption of over 95% in the frequency range of 1.12-14.04 THz, and the associated relative bandwidth is up to 170% to the central frequency. This UWB absorption is produced through localized surface plasmon and graphene surface plasmon stacking at various frequencies. To better understand the processes of absorption, we examined the electric field amplitude distribution at various frequencies. Thus, as the proposed structure is symmetrical, there is no significant difference between the TM and TE polarized waves it is not sensitive to wide angle of incidence wave. Furthermore, we have also discussed the influence of the permittivity and thickness of the substrate and Fermi energy level of the graphene over the absorption spectrum of the MMA.

## REFERENCES


[1] J. Federici and L. Moeller, "Review of terahertz and sub terahertz wireless communications," *Journal of Applied Physics*, vol. 107, no. 11, pp. 111101-111101-22, 2010.

[2] P. U. Jepsen, D. G. Cooke, M. Koch, and P. Reviews, "Terahertz spectroscopy and imaging–modern techniques and applications," *Laser & Photonics Reviews*, vol. 5, no. 1, pp. 124-166, 2011.

[3] M. Liu, X. Yin, E. Ulin-Avila, B. Geng, T. Zentgraf, L. Ju, F. Wang, and X. Zhang, "A graphene-based broadband optical modulator," *Nature,* vol. 474, no. 7349, pp. 64-67, 2011.

[4] H. Tao, N. I. Landy, C. M. Bingham, X. Zhang, R. D. Averitt, and W. Padilla, "A metamaterial absorber for the terahertz regime: design, fabrication and characterization," *Optics Express*, vol. 16, no. 10, pp. 7181-7188, 2008.

[5] X. Zhang, Y. Qi, P. Zhou, H. Gong, B. Hu, and C. J. P. S. Yan, "Refractive index sensor based on fano resonances in plasmonic waveguide with dual side-coupled ring resonators," *Photonic Sensors*, vol. 8, no. 4, pp. 367-374, 2018.

[6] H. Lin, X. Ye, X. Chen, Z. Zhou, Z. Yi, G. Niu, Y. Yi, Y. Hua, J. Hua, and S. Xiao, "Plasmonic absorption enhancement in graphene circular and elliptical disk arrays," *Materials Research Express,* vol. 6, no. 4, pp. 0-8, 2019.

[7] Z. Fang, S. Thongrattanasiri, A. Schlather, Z. Liu, L. Ma, Y. Wang, P. M. Ajayan, P. Nordlander, N. J. Halas, and F. J. García De Abajo, "Gated tunability and hybridization of localized plasmons in nanostructured graphene," *ACS Nano*, vol. 7, no. 3, pp. 2388-2395, 2013.

[8] S. Thongrattanasiri, F. H. Koppens, and F. J. García de Abajo, "Complete optical absorption in periodically patterned graphene," *Physical Review Letters,* vol. 108, no. 4, pp. 1-5, 2012.

[9] V. Kumar, "24 GHz graphene patch antenna array," *Applied Computational Electromagnetics Society (ACES) Journal,* vol. 34, no. 5, pp. 676-683, 2019.

[10] S.-L. Wang, J.-S. Hong, Y. Deng, and Z.-J. Chen, "A frequency reconfigurable antenna based on few layers graphene," *Applied Computational Electromagnetics Society (ACES) Journal,* vol. 36, no. 5, pp. 542-547, 2021.

[11] R. Bala, R. Singh, A. Marwaha, and S. Marwaha, "Wearable graphene based curved patch antenna for medical telemetry applications," *Applied Computational Electromagnetics Society (ACES) Journal,* vol. 31, no. 5, pp. 543-550, 2016.

[12] J. Huang, Y. Wu, B. Su, and J. Liu, "Preparation and electrical testing of double top gate graphene field-effect transistor," *Applied Computational Electromagnetics Society (ACES) Journal,* vol. 37, no. 7, pp. 774-781, 2022.

[13] M. Sajjad, X. Kong, S. Liu, S. U. Rahman, and J. Han, "Design of ultra-wideband tunable cross polarization converter based on a graphene," *International Applied Computational Electromagnetics Society (ACES) Symposium*, Nanjing, China, pp. 1-2, August 2019.

[14] L. Guo, S. Li, X. Jiang, X. Liao, and L. Peng, "Ultra-wideband transmissive linear polarization device based on graphene," *Applied Computational Electromagnetics Society (ACES) Journal,* vol. 36, no. 7, pp. 914-921, 2021.

[15] M. Huang, Y. Cheng, Z. Cheng, H. Chen, X. Mao, and R. Gong, "Based on graphene tunable dual-band terahertz metamaterial absorber with wide-angle," *Optics Communications*, vol. 415, pp. 194-201, 2018.

[16] S. Biabanifard, M. Biabanifard, S. Asgari, S. Asadi, and C. Mustapha, "Tunable ultra-wideband terahertz absorber based on graphene disks and ribbons," *Optics Communications*, vol. 427, pp. 418-425, 2018.

[17] Y. Dong, P. Liu, D. Yu, G. Li, L. J. I. A. Yang, and W. P. Letters, "A tunable ultrabroadband ultrathin terahertz absorber using graphene stacks," *IEEE Antennas and Wireless Propagation Letters*, vol. 16, pp. 1115-1118, 2016.

[18] B. Xiao, M. Gu, and S. Xiao, "Broadband, wide-angle and tunable terahertz absorber based on cross-shaped graphene arrays," *Applied Optics,* vol. 56, pp. 5458-5462, 2017.

[19] H. P. Xin, F. Liu, G. J. Ren, H. L. Zhao, and J. Q. Yao, "A liquid crystals modulated optical tunable filter based on Fano resonance of Au nanorod trimer," *Optics Express,* vol. 389, pp. 92-96, 2017.

[20] P. D. Cunningham, N. N. Valdes, F. A. Vallejo, L. M. Hayden, B. Polishak, X. H. Zhou, J. Luo, A. K. Y. Jen, J. C. Williams, and R. J. Twieg, "Broadband terahertz characterization of the refractive index and absorption of some important polymeric and organic electro-optic materials," *Journal of Applied Physics,* vol. 109, no. 4, pp. 043505-043505-5, 2011.

[21] N. Liu, L. Langguth, T. Weiss, J. Kästel, M. Fleischhauer, T. Pfau, and H. Giessen, "Induced transparency at the Drude damping limit," *Nature Materials*, vol. 8, pp. 758-763, 2009.

[22] C. R. Dean, A. F. Young, I. Meric, C. Lee, L. Wang, S. Sorgenfrei, K. Watanabe, T. Taniguchi, P. Kim, K. L. Shepard, and J. Hone, "Boron nitride substrates for high-quality graphene electronics," *Nature Nanotechnology,* vol. 5, no. 10, pp. 722-726, 2010.

[23] A. Khavasi, "Design of ultra-broadband graphene absorber using circuit theory," *Journal of the Optical Society of America B,* vol. 32, pp. 1941-1946, 2015.

[24] C. Hwang, D. A. Siegel, S. K. Mo, W. Regan, A. Ismach, Y. Zhang, A. Zettl, and A. Lanzara, "Fermi velocity engineering in graphene by substrate modification," *Scientific Reports,* vol. 2, pp. 1-4, 2012.

[25] G. W. Hanson, "Dyadic Green's functions and guided surface waves for a surface conductivity model of graphene," *Journal of Applied Physics*, vol. 103, no. 6, pp. 064302-064302-8, 2008.

[26] W. Gao, J. Shu, C. Qiu, and Q. Xu, "Excitation of plasmonic waves in graphene by guided-mode resonances," *ACS Nano,* vol. 6, no. 9, pp. 7806-7813, 2012.

[27] S. Ke, B. Wang, H. Huang, H. Long, K. Wang, and P. Lu, "Plasmonic absorption enhancement in periodic cross-shaped graphene arrays," *Optics Express,* vol. 23, no. 7, pp. 8888-8900, 2015.

[28] L. Ju, B. Geng, J. Horng, C. Girit, M. Martin, Z. Hao, H. A. Bechtel, X. Liang, A. Zettl, Y. R. Shen, and F. Wang, "Graphene plasmonics for tunable terahertz metamaterials," *Nature Nanotechnology,* vol. 6, no. 10, pp. 630-634, 2011.

[29] Y. J. Kim, Y. J. Yoo, K. W. Kim, J. Y. Rhee, Y. H. Kim, and Y. Lee, "Dual broadband metamaterial absorber," *Optics Express,* vol. 23, no. 4, pp. 3861-3868, 2015.

[30] M. L. Huang, Y. Z. Cheng, Z. Z. Cheng, H. R. Chen, X. S. Mao, and R. Z. Gong, "Design of a broadband tunable terahertz metamaterial absorber based on complementary structural graphene," *Materials*, vol. 11, no. 4, pp. 1-10, 2018.

[31] L. Ren, Q. Zhang, J. Yao, Z. Sun, R. Kaneko, Z. Yan, S. Nanot, Z. Jin, I. Kawayama, M. Tonouchi, J. M. Tour, and J. Kono, "Terahertz and infrared spectroscopy of gated large-area graphene," *Nano Letters,* vol. 12, no. 7, pp. 3711-3715, 2012.

[32] A. Vakil and N. Engheta, "Transformation optics using graphene," *Science,* vol. 332, no. 6035, pp. 1291-1294, 2011.

[33] D. Smith, S. Schultz, P. Markoš, and C. Soukoulis, "Determination of effective permittivity and permeability of metamaterials from reflection and transmission coefficients," *Physical Review,* vol. 65, no. 19, pp. 1-5, 2002.

[34] J. Huang, J. Li, Y. Yang, J. Li, Y. Zhang, and J. Yao, "Active controllable dual broadband terahertz absorber based on hybrid metamaterials with vanadium dioxide," *Optics Express,* vol. 28, no. 5, pp. 7018-7027, 2020.

[35] H. Shen, F. Liu, C. Liu, D. Zeng, B. Guo, Z. Wei, F. Wang, C. Tan, X. Huang, and H. Meng, "A polarization-insensitive and wide-angle terahertz absorber with ring-porous patterned graphene metasurface," *Nanomaterials,* vol. 10, no. 7, pp. 1-11, 2020,

[36] O. M. Daraei, K. Goudarzi, and M. J. O. Bemani, "A tunable ultra-broadband terahertz absorber based on two layers of graphene ribbons," *Optics & Laser Technology*, vol. 122, pp. 105853-105835-9, 2020.

[37] T. Aghaee and A. A. Orouji, "Circuit modeling of ultra-broadband terahertz absorber based on graphene array periodic disks," *International Journal of Numerical Modelling: Electronic Networks*, vol. 33, no. 3, pp. 1-13, 2020.

[38] Y. Cheng, H. Zou, J. Yang, X. Mao, and R. Gong, "Dual and broadband terahertz metamaterial absorber based on a compact resonator structure," *Optical Materials Express,* vol. 8, no. 10, pp. 3104-3114, 2018.

**Muhammad Sajjad** was born in 1990. He received the B.Sc. degree in Telecommunication from the University of Science and Technology, Bannu, Pakistan, in 2013, and the MSc. degree in Electrical Engineering from COMSAT University, Pakistan, in 2017. He is currently pursuing the Ph.D. degree with the Nanjing University of Aeronautics and Astronautics (NUAA), Nanjing, China. His research interests include electromagnetics and antennas especially metasurfaces, FSS, and polarization conversation.

**Xiangkun Kong** (Member, IEEE) received a Ph.D. degree in Communication and Information Systems from the Nanjing University of Aeronautics and Astronautics (NUAA), Nanjing, China, in 2015. He has been an Associate Professor with NUAA since his promotion in July 2015. He used to work at the University of St. Andrews, U.K., as an Academic Visitor supported by the China Scholarship Council. His main research interests include the electromagnetic properties of frequency selective surface, metamaterial and metasurface application, plasma photonic crystal, and computational electromagnetics. He has published more than 100 articles in different academic journals, including *Applied Physics Letters*, *Optics Express*, and *IEEE Transactions on Antennas and Propagation*, and has been cited 1600 times.

**Shaobin Liu** (Member, IEEE) received a Ph.D. in Electronics Science and Technology from the National University of Defense Technology, Changsha, China, in 2004. He is currently a Professor of Electromagnetic and Microwave Technology with the Nanjing University of Aeronautics and Astronautics, Nanjing, China. His current research interests include plasma stealthy antennas, microwave, radio frequency, and electromagnet incompatibility.

**Saeed Ur Rahman** is with school of Electronic Engineering, Xidian University, Xi'an, China. He has worked as a postdoctoral research fellow at Nanjing University of Aeronautics and Astronautics (NUAA), Nanjing China and also received his Ph.D. degree in information and communication engineering from NUAA. Currently he is an Associate Professor at Xidian University, Xi'an China.

**Zakir Khan** received his B.Sc. Engineering degree in Telecommunication Engineering from the University of Engineering and Technology, Peshawar, Pakistan, in 2013, the M.Sc. degrees in Electrical Engineering from COMSATS Institute of Information and Technology, Abbottabad, Pakistan in 2016 and the Ph.D. degree with Department of Electronics science and Technology, University of Science and Technology of China in 2022. His research interests include microwave and millimeter wave antenna design, microstrip patch antennas, miniaturized antennas, wide band antennas and multiband antennas.

**Owais** received the B.Eng. and M.Sc. degrees from the University of Engineering and Technology, Peshawar, Pakistan, in 1996 and 2000, respectively, and the Ph.D. degree in Communication Electronics from the Department of Science and Technology, Linköping University, Sweden. He is currently serving as an Associate Professor with the COMSATS University Islamabad, Abbottabad Campus, Pakistan. He has authored 40 international journal articles. His main research interests include the design of microstrip patch and dielectric resonator antennas, MIMO and reconfigurable DRAs, electromagnetic bandgap, and double-negative metamaterials; moreover, six-port front-end circuits for direct conversion transceiver design and high-speed data transmissions are also his area of interest.

# Wideband Iris-Fed Patch Antenna Under Operation of Dual-Resonance for X-band Applications: MOM-GEC Approach

**M. Abdi and T. Aguili**

Sys'Com Laboratory
National Engineering School of Tunis, Tunis El Manar University, BP 37, le Belvédère, Tunisia
mariemahmedabdi@gmail.com, taoufik.aguili@enit.utm.tn

***Abstract –*** In this paper, a microstrip patch antenna fed by a waveguide using an end-wall iris through ground plane has been modelled. The iris feed technique was proposed to overcome the narrow bandwidth problem of microstrip patch antenna. The iris is sized so that it is resonant and subsequently the antenna operates under the fusion of two modes relating to the iris and the patch, resulting in a wideband radiation characteristic with dual resonance. Measurement demonstrates the single bandwidth dual resonance type and the radiation bandwidth of (8 GHz-10.6 GHz). In order to show the impact of the iris feed technique on microstrip patch antenna's bandwidth, a comparison with some state-of-the-art works proposing various bandwidth enhancement techniques in the X-band is made. The proposed prototype, with a size of $1.76\lambda_0 \times 1.65\lambda_0 \times 1.29\lambda_0$, is more compact than several designs. It has a fractional bandwidth of 27.9%, thus it presents the prototype with the widest bandwidth with the simplest design fabrication. With regard to the electromagnetic modelling, this work is oriented towards the use of the hybrid MOM-GEC method in order to be able to perform a rigorous electromagnetic. It has been found that the MOM-GEC model is more efficient in terms of memory requirements and approximately four times faster than HFSS simulator software.

***Index Terms –*** bandwidth, dual-resonance, iris-fed patch antenna, MOM-GEC analysis, wideband, X-band.

## I. INTRODUCTION

Communication systems in the X-band require the design of antennas characterized by higher gains and wide bandwidths.

The microstrip patch antenna presents a good candidate for its low weight, its small size, the ease of its manufacture and its integration, etc. However, one of the major disadvantages is its low gain and its low bandwidth, which is of the order of a few percent (2% to 4%).

Multiple techniques have been used to widen the bandwidth of microstrip antennas, namely: the thick substrate, the partial substrate removal, the superstrate cover [1–2], the parasitic patches coupled to the main patch or stacked patches [3], the patch with metallic rings, the defected ground structure, the reflecting layer, the electromagnetic band gap as material [4], the merging of several antenna resonance modes [5–6], etc.

The microstrip patch antenna's type of alimentation has an impact on its bandwidth as well. The iris feed technique is used to increase the patch bandwidth in order to get over the issue of narrow bandwidth [7–8]. The iris-fed microstrip patch antenna is equivalent to an antenna having two patches, one of which radiates toward the open end of the rectangular waveguide and the other toward open air. Therefore, this structure combines appealing characteristics of a microstrip antenna, like low profile, light weight, compact size, and simple integration in electronic circuits, with those of a waveguide, like high power handling capacity and low losses (resistive) [9]. In this method, the waveguide's mouth is directly fitted with the microstrip antenna. As a result, the most energy is radiated.

Apart from the techniques for enlarging the bandwidth of the microstrip patch antenna, several antenna parameters intervene to achieve the maximum achievable bandwidth, namely: the height of the antenna cavity [10–11]., the thickness of the substrate or of the superstrate [12], the spacing between the main patch and the parasitic patches, etc.

From the above literature survey, this work proposes to model a microstrip patch antenna fed by a waveguide using an end-wall iris through ground plane since it has not been widely used in X-band. The iris is sized so that it is resonant and subsequently the antenna operates under the fusion of two modes relating to the iris and the patch [13], resulting in a wideband radiation characteristic with dual resonance.

Regarding the state-of-the-art works for the iris-fed patch antenna's electromagnetic modelling, it turns out that the current trend is to use simulation tools such as HFSS and CST which are essentially based on methods that require a 3D mesh [14]. Other works have been based on numerical models as in [7, 8] which

*Submitted On: September 20, 2022*
*Accepted On: February 24, 2023*



https://doi.org/10.13052/2023.ACES.J.380208

used the modal expansion model and the method of Moments respectively. These integral methods are best suited to perform an electromagnetic modelling of planar microwave structures. However, when the complexity of the structures increases, the resolution becomes complicated, and this requires more memory space and computation time.

Several research works [15, 16] have focused on the use of hybrid methods to improve the conventional methods. In fact, their major interest lies in the ability to solve complex structures whereas neither a single numerical method nor commercial software can model them correctly. In this context, this work is oriented towards modelling the proposed antenna based on MOM-GEC numerical technique. This latter handles complex electromagnetic structure as no mesh is required, thus, a gain is achieved in terms of computational time and memory storage.

This paper is divided as follows. Section II introduces the numerical technique formalism and the antenna description. The mathematical formulation based on the hybrid approach will be detailed in Section III. Section IV presents the validation of the antenna by full-wave simulations. To confirm the accuracy and the efficiency of the proposed numerical approach, a comparison with HFSS and with measurement is held. Finally, Section V concludes the work.

## II. THEORETICAL BACKGROUND

### A. MOM-GEC approach

In [17], Baudrand proposed the hybridization of the method of Moments (MOM) with the method of Generalized Equivalent Circuits (GEC) in order to be able to perform a rigorous electromagnetic calculation while minimizing the execution time and the required memory resources. The equivalent circuits were introduced in the development of the formulation of integral methods in an attempt to transpose field problems into equivalent circuit problems that are generally easier to deal with [18, 19].

The hybrid MOM-GEC is therefore considered to be a true electrical image of the structure to be studied since it faithfully describes the discontinuity as well as its environment:

- The wave which excites the surface of discontinuity is represented symbolically by a source (localized or modal) of field or current called real since it delivers power.
- At the level of the discontinuity, the electromagnetic state is described by generalized test functions which are modelled by virtual sources not storing energy. The virtual field source must be adjustable so as to cancel the dual magnitude (the transverse current of this source) and vice versa.
- The discontinuity environment is expressed by an impedance/admittance operator which represents the boundary conditions on either side of the discontinuity surface.
- The auxiliary sources (AS) make it possible to interconnect two distinct parts of a circuit when they are of different dimensions from each other [20, 21].

Once the equivalent circuit is extracted, the implementation of the proposed MOM-GEC steps is described in the flowchart as illustrated in Fig. 1.

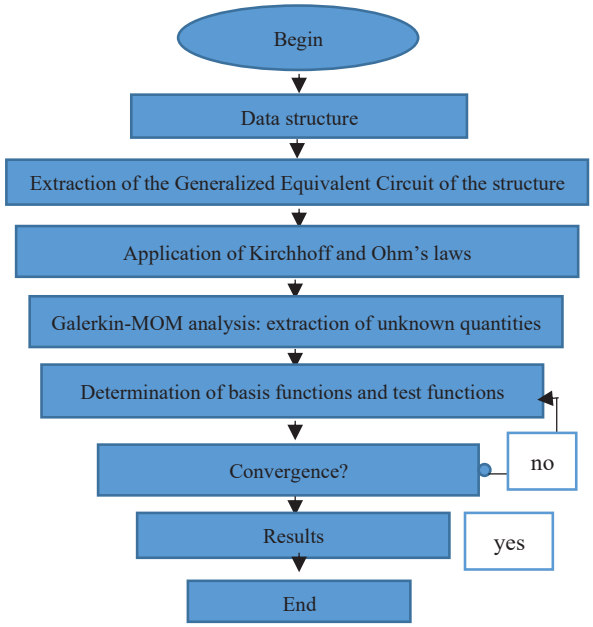


Fig. 1. Flowchart of the MOM-GEC method.

It should be noted that the computer code of the numerical method is translated with MATLAB and executed on an Intel Core i7 processor computer with a processing capacity of 2.7 GHz and 8 GB RAM.

The convergence study is essential in a first step for the validation of the numerical method MOM-GEC. It is carried out through the determination of the number of test functions and the number of basis functions which have to be fixed in such a way that the boundary conditions of the electromagnetic state of the antenna is verified. Once these parameters are found, they will be used in the rest of the calculation to extract the characteristics of the antenna. In fact, the exact solution is provided only at the convergent state of the structure's parameter that we can consider it as a steady state.

### B. Antenna description

The antenna illustrated in Fig. 2 is composed of a three-layer device which consists of a dielectric layer sandwiched between a radiating patch and a ground

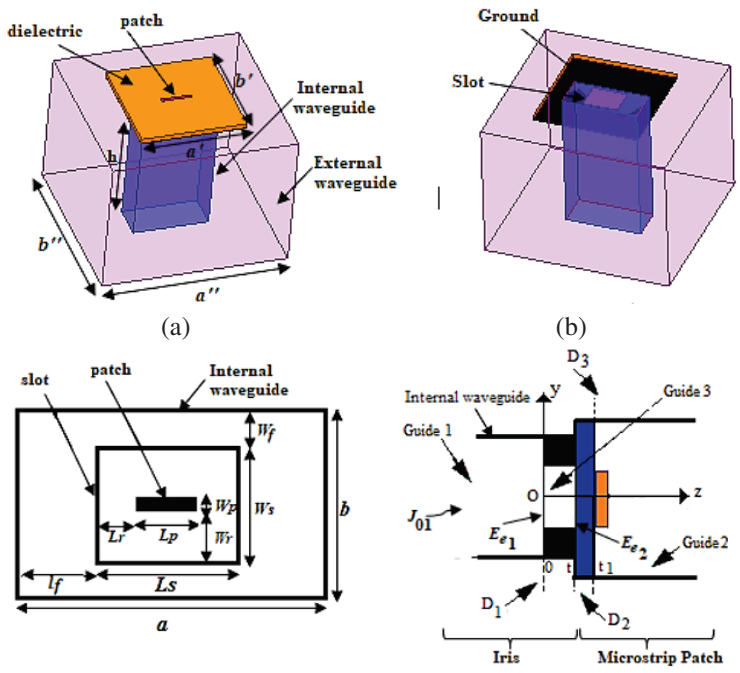


Fig. 2. (a) Iris-fed patch antenna. (b) Bottom view. (c) Top view. (d) Side view: a = 22.86, b = 10.16, h = 41.5, $a'' = 56.5$, $b'' = 53$, $a' = b' = 32$, $W_p = 0.93$, $L_p = 8$, $W_s = 8.28$, $L_s = 10.62$, $W_r = 3.675$, $L_r = 1.31$; $l_f = 6.12$; $W_f = 0.94$; $t_1$ (dielectric thickness)=1.6, t (ground and patch thickness) = 0.025, (all dimensions in millimeters), $Er_{(FR4)} = 4.4$.

plane. The structure is fed by an iris which is formed by an obstacle pierced with a rectangular coupling slot and terminating a rectangular waveguide. The presence of the conductive ground plane leads the electromagnetic radiation to be oriented from the exciter waveguide to the patch through the coupling slot. The feeder waveguide is excited by the fundamental mode $\boldsymbol{TE_{10}}$ and the microstrip patch antenna is excited by the quasi-TEM mode.

## III. MOM-GEC PROBLEM FORMULATION

### A. Generalized equivalent circuit

The antenna is composed of the iris and a microstrip patch interconnected through the auxiliary sources (AS), as illustrated in Fig. 3. Note that the external waveguide is not considered when modelling the structure since the excitation by the $TE_{10}$ mode is done through the internal waveguide.

The centered thick iris, as shown in Fig. 3 (a), is located between two virtual waveguides at (z=0), each of which is characterized by two electric side walls and two electric horizontal walls (which will be identified by EEEE for four times Electrical). These two waveguides are: the entry virtual waveguide (Guide 1) and the exit virtual waveguide (Guide 2), which do not have the same height.

The microstrip patch is placed in the cross section of a rectangular waveguide at (z=$D_2$) open to infinity. The boundary conditions are defined by perfect electrical walls on all sides as shown in Fig. 3 (b).

The whole structure represents three planes of discontinuity, respectively $D_1$ in z=0, $D_2$ in z=t, and $D_3$ in z=$t_1$, as illustrated in Fig. 2 (d). Each discontinuity includes two subdomains: the metal and the dielectric. By placing ourselves on the plane of discontinuity $D_1$, we solve the equivalent scheme GEC of Fig. 4.

On side (1), the real current source $J_{01}$ and the real field source $E_{01}$ are expressed respectively according the amplitude $I_{01}$ and $V_{01}$ and according the fundamental mode $f_0$ of the modal base function $f_{mn}$ [22]:

$$J_{01} = I_{01} f_0, \tag{1}$$

$$E_{01} = V_{01} f_0 + \sum_{m,n}^{N_b} V_{01} f_{mn}. \tag{2}$$

The auxiliary current source $J_{02}$ and the auxiliary field source $E_{02}$ are expressed respectively according the amplitude $I_{02}$ and $V_{02}$ and according the fundamental mode $f_0'$ of the modal base function $f_{mn}'$:

$$J_{02} = I_{02} f_0', \tag{3}$$

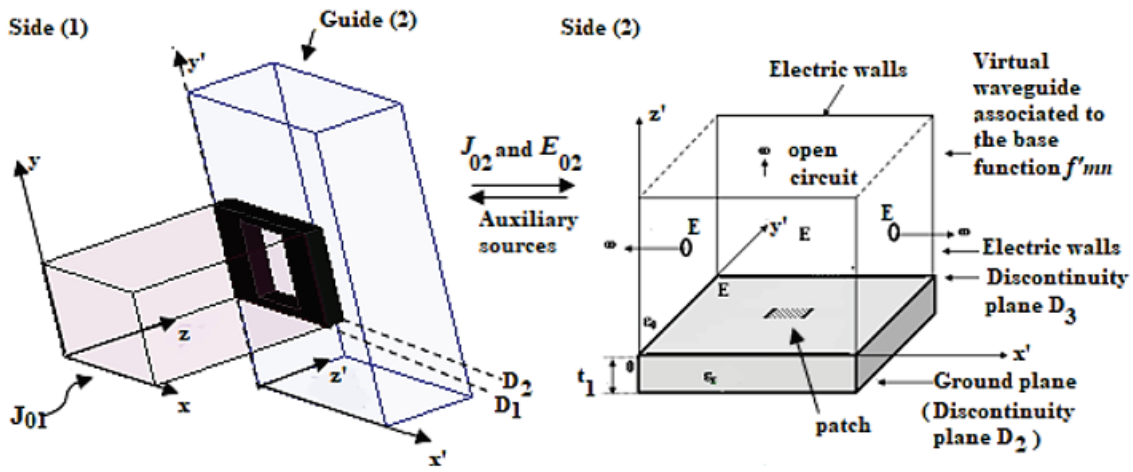


Fig. 3. (a) Iris located between two virtual waveguides at (z=0), each of which is characterized by perfect electrical walls (EEEE) on all faces. (b) Patch shielded in rectangular waveguide defined by perfect electrical walls (EEEE) on all faces.

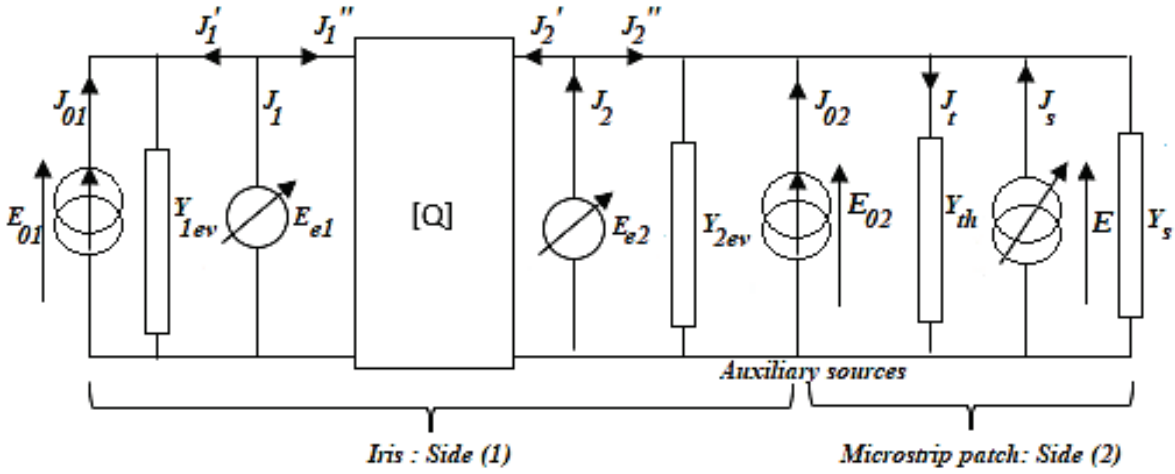


Fig. 4. GEC of the antenna using the MOM-GEC technique.

$$E_{02} = V_{02} f_0{}' + \sum_{m,n}^{N_b} V_{02} f'_{mn}. \tag{4}$$

Discontinuities $D_1$ and $D_2$ are identical so they have the same test function $(g_{1p})_{p=1,\ldots,N_{test}}$ which is similar to the fundamental mode in the iris. The virtual electric fields $E_{e_1}$ and $E_{e_2}$ are equals and expressed in terms of test function $(g_{1p})_{p=1,\ldots,N_{test}}$ and weighting coefficients $x_p$ [23]:

$$E_{e_1} = \sum_{p}^{N_{test}} x_p g_{1p}. \tag{5}$$

The thick rectangular iris between two guides of different heights can be subdivided into three guides [24] (see Fig. 2 (d)).

- Guide 1

The admittance of the modal source representing the evanescent modes at the level of discontinuity $D_1$ of the exciter waveguide which is associated with the modal base function $(f_{mn})_{(m,n)=\{1,\ldots,N_b{}^2\}}$ is expressed by [25]:

$$\hat{Y}_{ev_1} = \sum_{\substack{\alpha = TE,TM \\ out\,TE_{10}}} \left| \overset{\alpha}{f}_{mn} \right\rangle \overset{\alpha}{y}_{ev_1} \left\langle \overset{\alpha}{f}_{mn} \right|, \tag{6}$$

$$\begin{cases} y_{ev_1}{}^{TE} = \dfrac{\gamma_{mn_1}}{j\omega\mu_0} \\ y_{ev_1}{}^{TM} = \dfrac{j\omega\varepsilon_r\varepsilon_0}{\gamma_{mn_1}} \\ \gamma_{mn_1} = \sqrt{\left(\frac{m\pi}{a}\right)^2 + \left(\frac{n\pi}{b}\right)^2 - k_0{}^2} \end{cases}, \tag{7}$$

- Guide 2

The admittance of evanescent modes respectively related to the modal source at the level of discontinuity $D_2$ of the second waveguide which is associated with the modal base function $(f'_{mn})_{(m,n)=\{1,\ldots,N_b{}^2\}}$ is expressed by:

$$\hat{Y}_{ev_2} = \sum_{\alpha=TE,TM} \left| \overset{\alpha}{f'_{mn}} \right\rangle y^{\alpha}_{ev_2} \left\langle \overset{\alpha}{f'_{mn}} \right|, \tag{8}$$

$$\begin{cases} y_{ev_2}{}^{TE} = \frac{\gamma_{mn_2}}{j\omega\mu_0} \\ y_{ev_2}{}^{TM} = \frac{j\omega\varepsilon_r\varepsilon_0}{\gamma_{mn_2}} \\ \gamma_{mn_2} = \sqrt{\left(\frac{m\pi}{a'}\right)^2 + \left(\frac{n\pi}{b'}\right)^2 - k_0^2} \end{cases}. \tag{9}$$

- Guide 3

The line length between the two discontinuities $D_1$ and $D_2$ is represented by [26]:

$$[Q] = \begin{bmatrix} \hat{Y}_{11} & \hat{Y}_{12} \\ \hat{Y}_{12} & \hat{Y}_{11} \end{bmatrix}. \tag{10}$$

The input admittance $\widehat{Y_{11}}$ and the inverse transfer admittance $\widehat{Y_{12}}$ of quadrupole associated with the modal base function $(f'_{mn})_{(m,n)=\{1,\ldots,N_b{}^2\}}$ are respectively expressed by:

$$\hat{Y}_{11} = \sum_{\alpha=TE,TM} \left| \overset{\alpha}{f'_{mn}} \right\rangle y^{\alpha}_{11} \left\langle \overset{\alpha}{f'_{mn}} \right|, \tag{11}$$

$$\hat{Y}_{12} = \sum_{\alpha=TE,TM} \left| \overset{\alpha}{f'_{mn}} \right\rangle y^{\alpha}_{12} \left\langle \overset{\alpha}{f'_{mn}} \right|, \tag{12}$$

$$\begin{cases} y^{\alpha}_{11} = y^{\alpha}_{mn} \coth\left(\gamma_{mn_3} t\right) \\ y^{\alpha}_{12} = -\frac{y^{\alpha}_{mn}}{\sinh\left(\gamma_{mn_3}\right)} \\ \gamma_{mn_3} = \sqrt{\left(\frac{m\pi}{L_s}\right)^2 + \left(\frac{n\pi}{W_s}\right)^2 - k_0^2} \end{cases}. \tag{13}$$

On side (2), the virtual current distribution $J_s$ which is the dual of virtual electric field $E$, is expressed in terms of test function $(g_{2p})_{p=1,\ldots,Ntest}$ and weighting coefficients $x_p$:

$$J_s = \sum_{p}^{N_{test}} x_p g_{2p}. \tag{14}$$

The admittance of the dielectric layer is expressed by [27]:

$$\hat{Y}_{th} = \sum_{\alpha=TE,TM} \left| \overset{\alpha}{f'_{mn}} \right\rangle y^{\alpha}_{th} \coth(\gamma_{mn_4} t_1) \left\langle \overset{\alpha}{f'_{mn}} \right|. \tag{15}$$

The admittance from the vacuum brought to the surface of the dielectric $D_3$ is expressed by:

$$\hat{Y}_s = \sum_{\alpha=TE,TM} \left| \overset{\alpha}{f'_{mn}} \right\rangle y^{\alpha}_{s} \left\langle \overset{\alpha}{f'_{mn}} \right|, \tag{16}$$

$$\begin{cases} y^{TE}_s = y_{th}{}^{TE} = \frac{\gamma_{mn_4}}{j\omega\mu_0} \\ y_s{}^{TM} = y^{TM}_{th} = \frac{j\omega\varepsilon_r\varepsilon_0}{\gamma_{mn_4}} \\ \gamma_{mn_4} = \sqrt{\left(\frac{m\pi}{a'}\right)^2 + \left(\frac{n\pi}{b'}\right)^2 - k_0{}^2} \end{cases}. \tag{17}$$

**B. Kirchhoff and Ohm's laws**

On side (1), the application of Ohm's and Kirchhoff's law to the equivalent circuit leads to obtain the following equations given by:

$$E_{01} = E_{e1}, \tag{18}$$

$$E_{02} = E_{e2}, \tag{19}$$

therefore, the virtual current sources $J_1$ and $J_2$ are expressed as:

$$J_1 = -J_{01} + (\hat{Y}_{ev_1} + \hat{Y}_{11}) E_{ev_1} + \hat{Y}_{12} E_{ev2}, \tag{20}$$

$$J_2 = -J_{02} + (\hat{Y}_{ev_2} + \hat{Y}_{11}) E_{ev_2} + \hat{Y}_{12} E_{ev1}, \tag{21}$$

$$\begin{pmatrix} E_{01} \\ E_{02} \\ J_1 \\ J_2 \end{pmatrix} = \begin{pmatrix} 0 & 0 & 1 & 0 \\ 0 & 0 & 0 & 1 \\ -1 & 0 & (\hat{Y}_{ev_1} + \hat{Y}_{11}) & \hat{Y}_{12} \\ 0 & -1 & \hat{Y}_{12} & (\hat{Y}_{ev_2} + \hat{Y}_{11}) \end{pmatrix} \begin{pmatrix} J_{01} \\ J_{02} \\ E_{e_1} \\ E_{e_2} \end{pmatrix}. \tag{22}$$

On side (2), as the dielectric is thin, it is equivalent to a layer surface impedance. Then, by applying Ohm's and Kirchhoff's laws, the auxiliary electric field $E_{02}$ and the virtual electric source $E$ are given by:

$$E_{02} = \hat{Y}_{t_2}{}^{-1} \underbrace{(J_{02} + J_s)}_{J_t}, \tag{23}$$

$$E = \hat{Y}_{t_2}{}^{-1} (J_{02} + J_s). \tag{24}$$

The total admittance of the circuit $\widehat{Y_{t_2}}$ is the sum of $\widehat{Y_{th}}$.

**C. Application of Galerkin method**

The resolution of electromagnetic equations is provided by (V, I) physical scales instead of using (E, J) physical scales [28]. Therefore, Fig. 3 is presented as illustrated in Fig. 5.

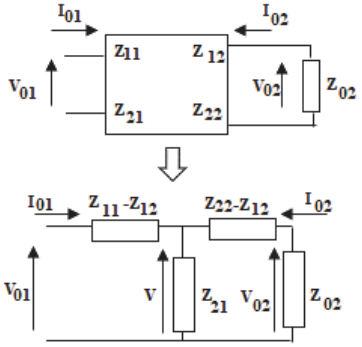


Fig. 5. GEC of the antenna using the MOM-GEC technique using (V, I) physical scales.

The projection of equations (18) and (19) on the test functions $(g_q)_{q=1,\ldots,N_{test}}$ with the cancellation of virtual current source $J_1$ and $J_2$ is solved by the method of

Galerkin as it is indicated in the matrix system (25):

$$\begin{pmatrix} V_{01} \\ V_{02} \end{pmatrix} = \begin{pmatrix} [A]^t[D_1]^{-1}[A] & [B]^t[C]^{-1}[A] \\ [A]^t[C]^{-1}[B] & [B]^t[D_2]^{-1}[B] \end{pmatrix} \begin{pmatrix} I_{01} \\ I_{02} \end{pmatrix}, \tag{25}$$

noting that $[X]$ is the vector ponderation expressed by $[X] = \sum_p^{N_{test}} x_p$, $[A]$ is the first excitation vector expressed by $[A] = \langle g_{1p}, f_0 \rangle$, $[B]$ is the second excitation vector expressed by $[B] = \langle g_{1p}, f_0' \rangle$, $[C]$ is the first impedance matrix expressed by $[C] = \langle g_{1p}, \hat{Y}_{12} g_{1q} \rangle$, $[D_1]$ is the second impedance matrix expressed by $[D_1] = \langle g_{1p}, (\hat{Y}_{ev_1} + \hat{Y}_{11}) g_{1q} \rangle$ and $[D_2]$ is the third impedance matrix expressed by $[D_2] = \langle g_{1p}, (\hat{Y}_{ev_2} + \hat{Y}_{11}) g_{1q} \rangle$.

Noting that:

$$\begin{cases} Z_{11} = [A]^t[D_1]^{-1}[A] \\ Z_{12} = [B]^t[C]^{-1}[A] \\ Z_{21} = [A]^t[C]^{-1}[B] \\ Z_{22} = [B]^t[D_2]^{-1}[B] \end{cases}, \tag{26}$$

the expression of the input impedance $Z_{in}$ (27) is deduced from (25):

$$Z_{in} = Z_{11} - \frac{Z_{21}.Z_{12}}{Z_{22} - Z_{12}}, \tag{27}$$

the magnitude in (dB) of the reflection coefficient is deduced from (27) as expressed in (28a):

$$S_{11} = \frac{Z_{in} - Z_0}{Z_{in} + Z_0}. \tag{28a}$$

The angle in (degree) of the reflection coefficient is deduced from (28a) as expressed in (28b):

$$S_{11_{(\varphi)}} = S_{11}.e^{-j2\varphi}, \tag{28b}$$

where $Z_0$ is the impedance of fundamental mode and $\varphi$ is the phase.

The projection of the equation (23) and (24) on the test functions $(g_{q_1})_{q_1=1,\ldots,N_{test}}$ with the cancellation of virtual current distribution $J_s$ is solved by the method of Galerkin as it is indicated in the matrix system (29):

$$\begin{pmatrix} V_{02} \\ [0] \end{pmatrix} = \begin{pmatrix} [A_0] & [A_1]^t \\ [A_1] & [C_1] \end{pmatrix} \begin{pmatrix} I_{02} \\ [X] \end{pmatrix}, \tag{29}$$

noting that $[A_0] = \langle f_0, \hat{Y}_{t_2}^{-1} f_0' \rangle$, $[A_1]$ is the excitation vector expressed by $[A_1] = \langle g_{2p}, \hat{Y}_{t_2} f_0' \rangle$, and $[C_1]$ is the impedance matrix which define the coupling between $p$ and $q$ dielectric elements and expressed by $[C_1] = y_{t_2}^{-1} \sum_{mn}^{N_b} \langle g_{2p}, f_{mn}' \rangle \langle f_{mn}', g_{2q} \rangle$.

From (29), the expression $Z_{02}$ of is deduced:

$$Z_{02} = [A_0] - \frac{[A_1]^t[A_1]}{[C_1]}. \tag{30}$$

The amplitude $V_{02}$ is expressed as:

$$V_{02} = \frac{Z_{02}}{Z_{02} + Z_{22} - Z_{12}} . \frac{Z_{eq}}{Z_{eq} + Z_{11} - Z_{12}} V_{01}, \tag{31}$$

$$Z_{eq} = \frac{(Z_{01} + Z_{22} - Z_{12}).Z_{21}}{(Z_{01} + Z_{22} - Z_{12}) + Z_{21}}. \tag{32}$$

## IV. COMPUTED RESULTS

### A. Convergence study

The convergence of the input impedance and the antenna current is established for the test function number $N_{test}$=11 and the number of modes $N_b$=300 as mentioned respectively in Fig. 6 and Fig. 7.

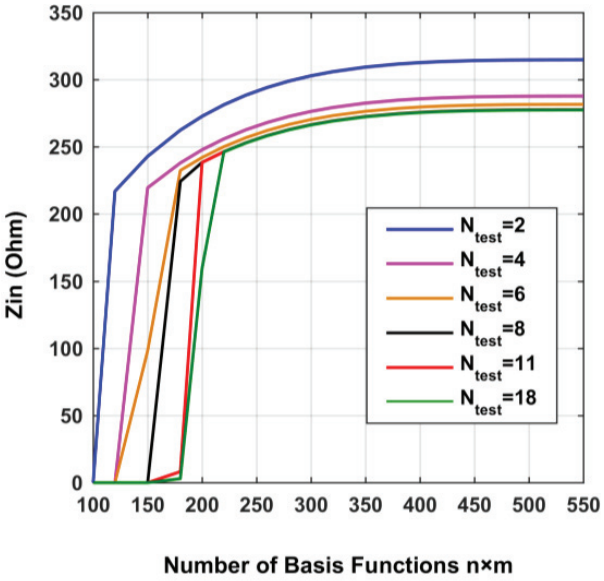


Fig. 6. Input impedance as a function of different number of $N_b$ and $N_{test}$.

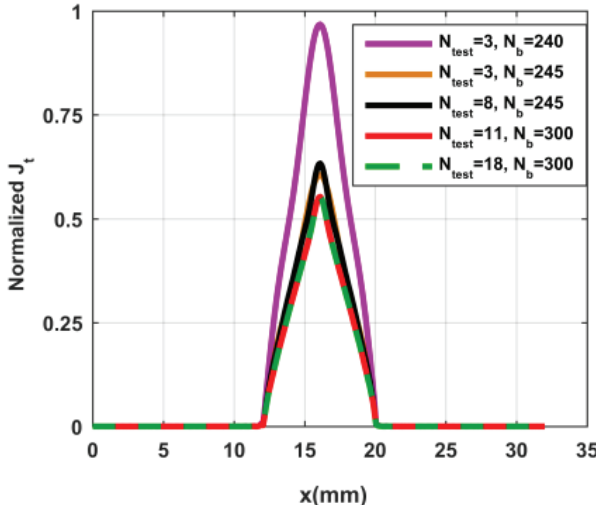


Fig. 7. Current distribution as a function of different number of $N_b$ and $N_{test}$.

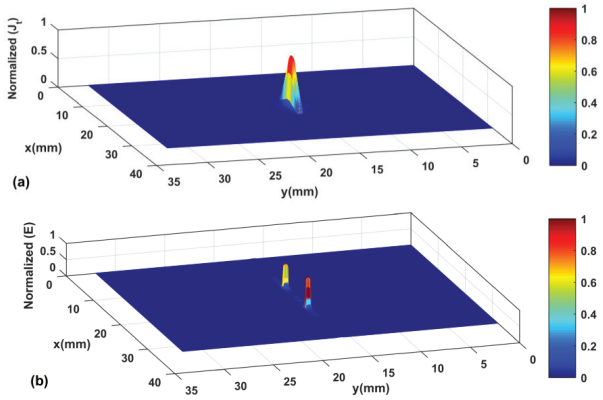


Fig. 8. (a) Normalized current distribution of the antenna. (b) Normalized electric field of antenna obtained at convergence.

### B. Boundary conditions verification

Figure 8 illustrates the current distribution and electric field of the antenna which are consistent with electromagnetic field theory. In Fig. 8 (a), the current density distribution is shown at the metallic patch. In Fig. 8 (b), the normalized electric field peak is at the edge of the patch in the x direction and the minimum values are at the dielectric.

### C. Antenna's characteristics

Figure 9 illustrates both the magnitude in dB and the angle in degree of reflection coefficient of the antenna. To confirm the accuracy and the efficiency of the proposed numerical approach, a comparison with HFSS is held. It shows a slight difference between results due to different numerical techniques used.

The simulated reflection coefficient of the proposed antenna has two resonance frequencies as illustrated in Fig. 9 (a); one appears at $f_{r1}$=8.7 GHz and the other appears at $f_{r2}$= 9.6 GHz, so the bandwidth is centered around $f_0$ = 9.15 GHz.

The frequency study on the phase of the reflection coefficient shows there are two modes whose resonance frequencies are $f_{r1}$ and $f_{r2}$ where the phase of the reflection coefficient is zero (see Fig. 9 (b). Note that each resonance is determined where the phase of the reflection coefficient is zero.

In order to identify each mode, a study was carried out on the reflection coefficient of the iris alone [24] and then on that of the total structure. As presented in Fig. 10, the iris alone presents a first resonance at 9.6 GHz. By adding the dielectric and the patch above the iris, a second resonance frequency at 8.7 GHz appears at a frequency lower than $f_0$. Due to the merging of the modes relating to the iris and the patch, a wideband radiation characteristic with dual-resonance is obtained.

In order to show the calculation efficiency of the proposed method, CPU time and storage memory

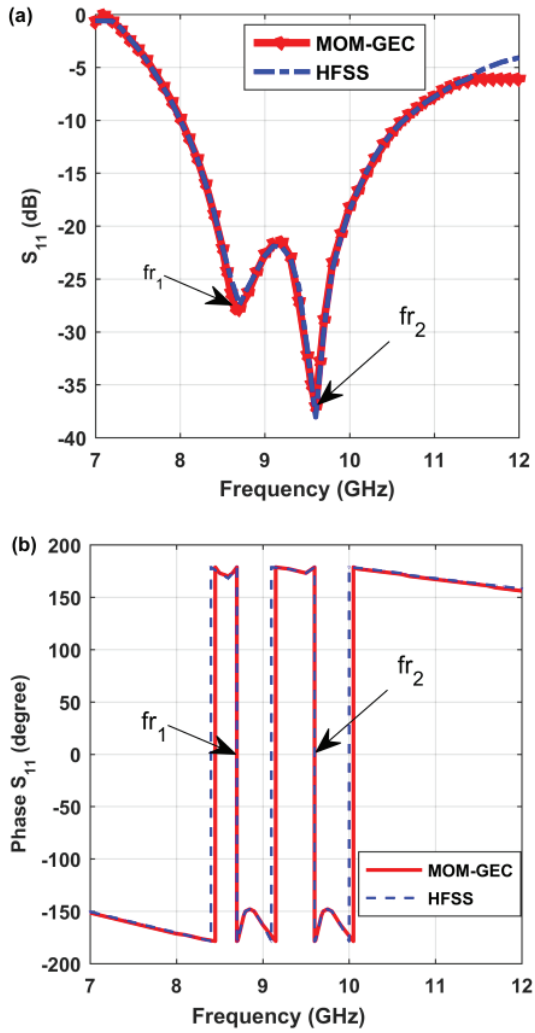


Fig. 9. (a) Magnitude in dB, and (b) the angle in degree of reflection coefficient of the antenna compared to HFSS.

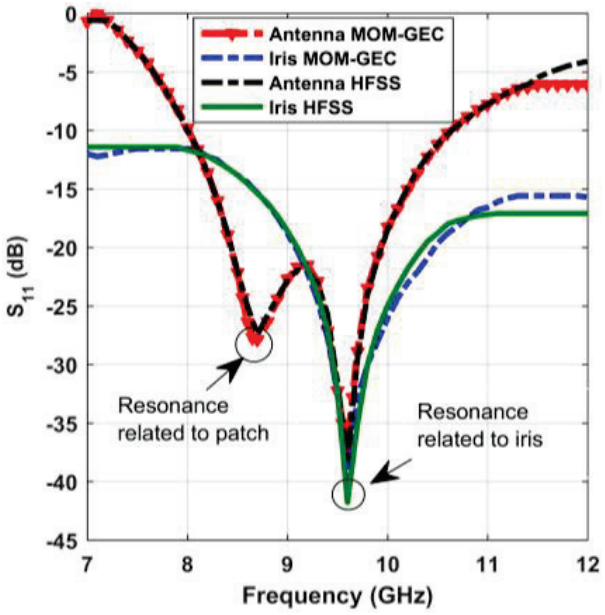


Fig. 10. Simulated reflection coefficients of the iris alone and the iris-fed antenna as a function of frequency.

Fig. 11. Photograph of the fabricated iris-fed microstrip patch antenna.

required by MOM-GEC and HFSS simulator have been reported in Table 1. It has been found that the MOM-GEC model is more efficient in terms of memory requirements and approximately four times faster than HFSS simulator software.

Table 1: Comparison of CPU time between the MOM-GEC method and the HFSS simulator (Intel Core i7 with a processing capacity of 2.7 GHz and 8 GB RAM)

| **CPU Time (in seconds)** | | **Memory Requirements (GB)** | |
|---|---|---|---|
| **HFSS** | **This Paper** | **HFSS** | **This Paper** |
| 1276 | 340 | 3.04 | 0.18 |

### D. Antenna fabrication and comparison with various X-band antennas

The prototype of the fabricated iris-fed patch antenna as shown in Fig. 11. The antenna is excited by a rectangular waveguide of the Oritel TGN R100/WR90 type with 22.86 mm $\times$ 10.16 mm $\times$ 41.5 mm dimension, also extended wall dimension is 56.5 mm $\times$53mm.

As illustrated in Fig. 12, the results are measured by an Agilent HP 8510C vector network analyzer (VNA) whose characteristics are described in [29].

Figure 13 illustrates both the magnitude in dB and the angle in degree of simulated and measured reflection coefficient of the antenna. Measurement demonstrates the single band with dual resonances type (8.7GHz

Fig. 12. Photograph of measurement set-up: Reflection coefficient measurement.

and 9.6GHz) and the radiation bandwidth of (8GHz-10.6GHz).

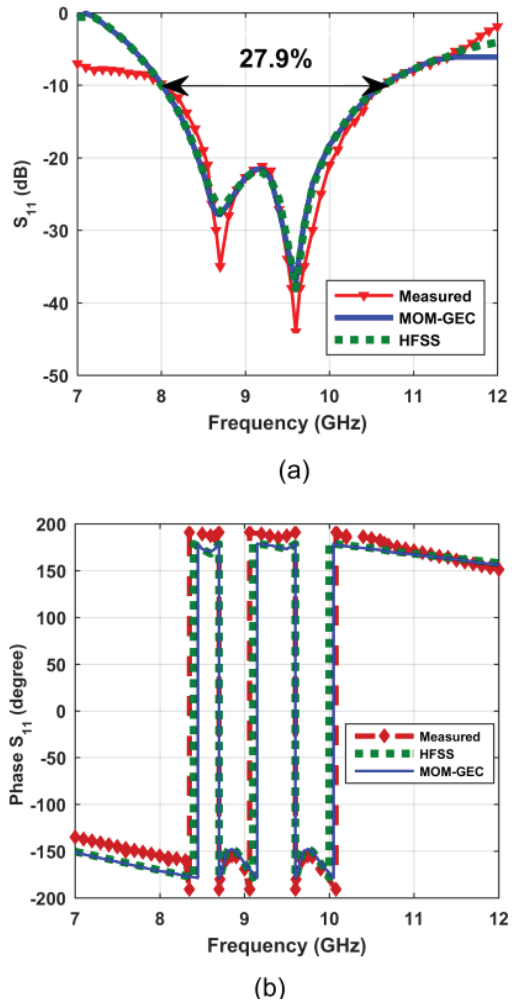


Fig. 13. (a) Magnitude in dB, and (b) the angle in degree of simulated and measured reflection coefficient of the antenna.

A slight difference between the simulated and measured results is marked especially between 7GHz and 8GHz. This may be due to the manufacturing tolerance and the effect of the connector which was not taken into account in the design with HFSS and when modelling with the numerical method. Integrating the connector into MOM-GEC modelling and in the HFSS design could be a solution to further minimize this difference.

A comparison of performance characteristics between the proposed antenna and the state-of-the-art works operating in the X-band is listed in Table 2.

Without the addition of superstrate cover, the antenna bandwidth is equal to 5.8% and 11.1% respectively in [30, 33]. Hence, the interest of adding superstrate cover as a bandwidth expansion technique. Indeed, the superstrate cover can be either dielectric, metallic, metamaterial, frequency selective surface. In [32], a stacked microstrip patch antenna has been presented. The addition of parasitic patch above foam compared to the main patch increased its bandwidth from 7.54% to 16.2%.

The proposed antenna has a smaller volume than [2, 30–33]. Moreover, it has the highest impedance bandwidth and the simplest design fabrication. Due to its high bandwidth, its simple fabrication, and its compactness, this antenna represents a promising candidate for X-band satellite communication, radar application, microwave power transmission, and wireless communication.

The state-of-the-art works mentioned in Table 2 have used simulation tools such as HFSS and CST which are essentially based on methods requiring a 3D mesh. This work is characterized by studying the antenna structure based on an analysis method, which makes it possible to convert a 3D investigation problem into a 2D investigation problem and, subsequently, to minimize the execution time and the memory resources required.

Table 2: Performances comparison of the proposed antenna with the state-of-the-art works operating in the X-band

| Ant | Bandwidth Enhancement Technique | Dimension $WL \times T$ in $\lambda_0^3$ | Band Type | -10 dB Fractional Bandwidth (GHz;%) | Design Complexity | Modelling Technique |
|---|---|---|---|---|---|---|
| [30] | Metallic superstrate | $2.54 \times 3.6 \times 0.92$ | Single* | $7.7-9.7;23\%$ | (+) | HFSS |
| [31] | Dielectric superstrate | $2.4 \times 2.4 \times 1.2$ | Single | $8.75-11.25;25\%$ | (+) | CST |
| [32] | Parasitic patch above foam | $2.33 \times 3.03 \times 0.79$ | Single* | $7.85-9.25;16.2\%$ | (+) | CST |
| [33] | Dielectric superstrate | $16.6 \times 13 \times 0.62$ | Single* | $9.4-10.8;13.86\%$ | (+) | HFSS |
| [1] | Compact Partially Reflective Surface | $2.2 \times 2.2 \times 0.54$ | Single | $8.8-11.4;25\%$ | (++) | HFSS |
| [2] | AMC ground plane and a FSS superstrate | $3.33 \times 3.33 \times 0.35$ | Single | $7.7-9.5;20\%$ | (++) | NA |
| [4] | Metamaterial substrate | $1.25 \times 0.9 \times 0.04$ | Single* | $9.2-11;17.8\%$ | (++) | NA |
| [34] | Cavity backed structure | $0.46 \times 2.1 \times 0.025$ | Single | $9.4-10.5;11\%$ | (+) | HFSS |
| [14] | Air cavity | $1.25 \times 1.25 \times 0.37$ | Single | $7.7-10;25\%$ | (−) | NA |
| This work | Resonant iris as feeding technique | $1.76 \times 1.65 \times 1.29$ | Single* | $8-10.6;27.9\%$ | (−) | MOM-GEC + HFSS |

Ant: Antenna; W× L×T: Width×Length×Thickness; SIW: Substrate integrated waveguide; Single*: Single with dual-resonance; AMC: Artificial Magnetic Conductor; FSS: Frequency Selective Surface; (++): Very high; (+) High; (-) Low; NA: not mentioned; HFSS: High Frequency Simulation Software; CST: Computer Simulation Technology.

## V. CONCLUSION

In this work, the modelling of dual-resonant antenna with closely spaced resonance frequencies for bandwidth enhancement has been investigated for X-band applications. The antenna consists of a microstrip patch antenna fed by a waveguide using an end-wall iris through ground plane. The antenna has a size of $1.76\lambda_0 \times 1.65\lambda_0 \times 1.29\lambda_0$, and has a fractional bandwidth of 27.9%.

The antenna is modelled by the hybrid MOM-GEC method. Equivalent circuits (GEC) are introduced in the development of the formulation of integral methods in an attempt to transpose field problems into equivalent circuit problems that are generally easier to deal with. Consequently, a reduction in both memory requirements and computation time is achieved. The problem thus formulated, its numerical resolution is done by applying Galerkin's method, which is known for the simplicity of its formulation.

This procedure is, in fact, general and it can be applied to the study of several electromagnetic problems, namely: the uniaxial discontinuity in waveguides, the multiaxial diffraction discontinuities in free space, the antenna radiation, the circuits comprising localized sources, etc. Moreover, the proposed hybrid method can be extended to become a multi-scale method. The techniques for solving each electromagnetic problem essentially differ from each other in the development of the operators involved. Admittedly, the theoretical basis and the approach to be followed remain unchanged. This is due to the fact that the methods used are in all cases integral methods.

## REFERENCES


[1] F. Meng and S. K. Sharma, "A wideband resonant cavity antenna with compact partially reflective surface," *IEEE Trans. Antenn. Propag.*, vol. 68, no. 2, pp. 1155-1160, 2020.

[2] R. Fakhte and I. Aryanian, "Compact Fabry-Perot antenna with wide 3-dB axial ratio bandwidth based on FSS and AMC structures," *IEEE Antennas Wirel. Propag. Lett*, vol. 19, no. 8, pp. 1326-1330, 2020.

[3] H. Hung Tran and N. Nguyen-Trong, "Performance enhancement of MIMO patch antenna using parasitic elements," *IEEE Access*, vol. 9, pp. 30011-30016, 2022.

[4] O. Borazjani, M. Naser-Moghadasi, J. Rashed-Mohassel, and R. A. Sadeghzadeh, "Bandwidth improvement of planar antennas using a single-layer metamaterial substrate for X-band application," *Intern. Journ. Micro. Wirel. Tech.*, vol. 12, no. 9, pp. 906-914, 2020.

[5] X. Zhang, T. Tan, Q. Wu, L. Zhu, S. Zhong, and T. Yuan, "Pin-loaded patch antenna fed with a dual-mode SIW resonator for bandwidth enhancement and stable high gain," *IEEE Antennas Wirel. Propag. Lett.*, vol. 20, no. 2, pp. 279-283, 2021.

[6] X. Liu, W. Hu, S. Gao, L. Wen, Q. Luo, R. Xu, and Y. Liu, "A wideband triple-mode differentially fed microstrip patch antenna," *IEEE Antennas Wirel. Propag. Lett.*," vol. 20, no. 7, pp. 1160-1164, 2021.

[7] M. Kanda, D. Chang, and D. Greenlee, "The characteristics of iris-fed millimeter-wave rectangular microstrip patch antennas," *IEEE Trans. Electro. Compat.*, vol. 27, no. 4, pp. 212–220, 1985.

[8] K. K. Sood, R. Jyoti, and S. B. Sharma, "A waveguide shunt slot-fed microstrip patch antenna—analysis using the method-of-moments," *IEEE Trans. Antenn. Propag.*, vol. 61, no. 1, pp. 5385-5394, 2013.

[9] A. Omar, M. Hussein, I. Rajmohan, and K. Bathich, "Dual-band MIMO coplanar waveguide-fed-slot antenna for 5G communications," *Heliyon*, vol. 7, no. 4, pp. 1-10, 2021.

[10] N. C. Karmakar, "Investigations into a cavity-backed circular-patch antenna," *IEEE Trans. Antenn. Propag.*, vol. 50, no 12, pp 1706-1715, 2002.

[11] M. Martinis, K. Mahdjoubi, R. Sauleau, S. Collardey, and L. Bernard, "Bandwidth behavior and improvement of miniature cavity antennas with broadside radiation pattern using a metasurface," *IEEE Trans. Antenn. Propag.*, vol. 63, no. 5, pp. 1899-1908, 2015.

[12] M. A. K. Khan, M. I. Ullah, R. Kabir, and M. A. Alim, "High-performance graphene patch antenna with superstrate cover for terahertz band application," *Plasmonics*, vol. 15, pp. 1719-1727, 2020.

[13] P. K. Malik, S. Padmanaban, and J. B. Holm-Nielsen, *Microstrip Antenna Design for Wireless Applications*, 1st ed., CRC Press: Boca Raton, USA, 2021.

[14] R. Fakhte and I. Aryanian, "High gain and wideband patch antenna with wide 3-dB axial ratio bandwidth operating at TM01 and TM11 modes," *IET Micro. Antenn. Propag. Journ.*, vol. 15, no. 4, pp. 389-396, 2021.

[15] Y. Zhong, H. Wang, W. Huang, W. Xu, J. Xu, and J. Dai, "A hybrid loop-tree FEBI method for low-frequency well logging of 3-D structures in layered media," *IEEE Trans. Geo. Rem. Sens.*, vol. 60, pp. 1-9, 2021.

[16] J. Ma, S. Gong, X. Wang, Y. Liu, and Y. Xu, "Efficient wide-band analysis of antennas around a conducting platform using MoM-PO hybrid method and asymptotic waveform evaluation technique,"

*IEEE Trans. Antenn. Propag*., vol. 60, no. 12, pp. 6048-6052, 2021.

[17] H. Baudrand, *Introduction au calcul des éléments de circuits passifs en hyperfréquences*, Cépaduès Éditions, Toulouse, 2001.

[18] S. Smirani, M. Aidi, S. Mili, and T. Aguili, "Electromagnetic modeling of rectenna based on the hybrid MoM–GEC combined to the harmonic balance method for wireless power transmission," *Journ. Electro. Wav. App.* , vol. 34, no. 6, pp. 697-714, 2020.

[19] H. Helali, S. Smirani, M. Aidi, and T. Aguili, "Electromagnetic modeling of reconfigurable antenna array for 5G communications. Journal of Electromagnetic Waves and Applications," *Journ. Electro. Wav. App.* , vol. 35, no. 17, pp. 2368-2383, 2021.

[20] K. Minas, L. Nikolaos, and F. George, "Method of auxiliary sources with an excitation source: The auxiliary-current vector norm," *IEEE Micro. Wirel. Comp. Lett.*, vol. 29, no. 10, pp. 1-4, 2021.

[21] K. Minas, L. Nikolaos, and F. George, "Mode analysis by the method of auxiliary sources with an excitation source," *IEEE Trans. Micro. Theory Tech.*, vol. 69, no. 6, pp. 2960-2971, 2021.

[22] T. Aguili, *Modélisation des composants S. H. F planaires par la méthode des circuits équivalents généralisés*, Department of Electrical Engineering, National Engineering School of Tunis ENIT, 2000.

[23] H. Baudrand, "Representation by equivalent circuit of the integral methods in microwave passive elements," *Eur. Micro. Conf.*, Hungary, 9-13 Sep., 1990.

[24] N. Raveu and O. Pigaglio, *Résolution de problèmes hautes fréquences par les schémas équivalents*, Cépaduès Éditions, Toulouse, pp. 127-146, May 2012.

[25] Z. Mekkioui and H. Baudrand, "Bi-dimensional biperiodic centred-fed microstrip leaky-wave antenna analysis by a source modal decomposition in spectral domain," *IET Micro. Antenn. Propag. Journ.*, vol. 3, no. 7, pp. 1141-149, 2009.

[26] H. Baudrand and D. Bajon, "Equivalent circuit representation for integral formulations of electromagnetic problems," *Int. Journ. Num. Model.-Elect. Net. Dev. Fields*, vol. 15, no. 1, pp. 23-57, 2002.

[27] H. Helali, M. Aidi, and T. Aguili, "Electromagnetic modelling of multiband frequency reconfigurable antenna for wireless communications," *Journ. Electro. Wav. App.*, vol. 34, no. 5, pp. 634-654, 2020.

[28] Z. Chen, C. Wang, and W. Hoefer, "A unified view of computational electromagnetics," *IEEE Trans. Micro. Theory Tech.*, vol. 70, no. 2, pp. 955-969, 2022.

[29] Agilent Technologies 8510C Network Analyzer System: Operating and Programming Manual, Editions 3, USA, 2001.

[30] R. Fakhte and H. Ghorbaninejad, "High gain and improved waveguide slot antenna using a metallic superstrate as main radiator," *IET Micro. Antenn. Propag.*, vol. 11, no. 8, pp. 563-557, 2016.

[31] T. Rahim and J. Xu, "Design of high gain and wide band EBG resonator antenna with dual layers of same dielectric superstrate at X-bands," *Journ. Micro., Opto. Electro. App.* , vol. 15, no. 2, pp. 93-104, Jun. 2016.

[32] R. Fakhte and H. Ghorbaninejad, "High-gain waveguide slot antenna using simple parasitic patch's cover," *Int. Journ. RF Micro. Comp. Aid. Eng.*, vol. 28, no. 2, 1-8, 2017.

[33] F. Scattone, M. Ettorre, B. Eddo, R. Sauleau, and N. Fonseca, "Truncated leaky-wave antenna with Cosecant-squared radiation pattern," *IEEE Antennas Wirel. Propag. Lett.*, vol. 17, no. 5, pp. 841-844, 2018.

[34] D. El Khamlichi, N. A. Touhami, T. Elhamadi, and M. A. Ennasar, "High-gain and broadband SIW cavity-backed slots antenna for X-band applications," *Int. Journ. Micro. Wirel. Tech.*, vol. 13, no. 10, pp. 1078-1085, 2021.

**Mariem Abdi** is an electronical engineer and obtained a master's degree in Communication Systems from the National School of Engineering of Tunis (ENIT). She is currently a PhD student in Telecommunications at the National Engineering School of Tunis (ENIT). Her research interests are in full-wave numerical methods in electromagnetics and high frequency electronics.

**Taoufik Aguili** is currently Professor at the National Engineering School of Tunis (ENIT), Tunis El Manar University, and the Director of the Communications Systems Laboratory (Sys'Com). He is also responsible for research and master's degree in the Communications and Information's Technology Department. His research interests include modeling of microwave systems and nano-devices, full-wave numerical methods in electromagnetics, electromagnetic wave phenomena in multilayered media, integrated transmission lines, and leaky wave phenomena, waveguides, and antennas.

# A Low-profile Wideband PIFA with Co-design of Ground Plane for WLAN Applications

**Xiao Yu Li, Zu Ang Liu, and Mei Song Tong**

Department of Electronic Science and Technology
Tongji University, Shanghai 201804, China
mstong@tongji.edu.cn

***Abstract* –** In this paper, a novel low-profile wideband planar inverted-F antenna (PIFA) with co-design of the ground plane for WLAN applications and IoV applications is proposed. This antenna consists of three parts: a slotted radiating patch, a vertical shorting plate and a ground plane with a cross-shaped slot. The influence and the parameter of the slot are discussed. The antenna is fed by a 50 Ω coaxial line and a shorting pin is also used in this design. The overall size of the antenna is $30 \times 44 \times 3.5$ mm$^3$. The whole structure is simulated in ANSYS Electronics Desktop 2018.0 and several prototypes are made to verify the simulation results. The bandwidth of the antenna can reach 3.96 GHz (−10 dB) and cover the frequency range of $5.64 - 9.6$ GHz. The max gain of the antenna is 5.4 dBi.

***Index Terms* –** low-profile, multi-resonant modes, planar inverted-F antenna, wideband.

## I. INTRODUCTION

The planar inverted-F antenna (PIFA) has been widely used in many sub-areas of the modern wireless communication systems because of its high gain and small size, and slots on the radiating patch make it easy to achieve multiband feature. However, due to the single resonant mode, typical PIFA has the disadvantage of a narrow impedance bandwidth, which restricts its application in many wideband-required situations. So, for the PIFA, the enhancement of impedance bandwidth to cover the range of $5 - 6$ GHz or even more is important for the current communication technology such as 5G wireless applications and 6G wireless systems in the future [1, 2].

A number of papers on the expanding bandwidth of the PIFA have been published. Traditional methods to improve the bandwidth include introducing parasitic patches near the radiating patch [3, 4], enlarging the size of the ground plane [5], and increasing the height of the whole structure. In [3], a vertical parasitic element is loaded and the impedance bandwidth is enhanced to about 48%, while the overall size is increased and the fabrication becomes more difficult. In [6], the influence of the ground plane on the impedance bandwidth is studied and then four different PIFA designs are evaluated. The results show that altering the slots on the ground plane can effectively change the bandwidth and the slots must be perpendicular to the dominant current direction, which provides some design guides in this paper.

Furthermore, adjusting the resonant frequencies to combine the bandwidth of two or more resonant frequencies has become a prevalent method in recent years. By combining $TM_{10}$ and $TM_{12}$ modes, the bandwidth of the antenna in [7] increases to about 10%. In [8], the bandwidth increases to 11.8% through a similar method. A pair of shorting pins are loaded and a slot is etched in [9], and $TM_{0,1/2}$ and $TM_{0,3/2}$ modes are combined. The bandwidth increased to 18% and could meet the requirements for 5G WLAN applications. In [10], a small rectangular strip is loaded on the top of the feeding probe and $TM_{1/2,2}$ and $TM_{3/2,0}$ modes are combined, and the impedance bandwidth is enhanced to about 33% (from 5 to 7 GHz). However, the position of the strip might bring challenges for the fabrication, and the height of the substrate (0.254 mm) is hard to control during manufacturing.

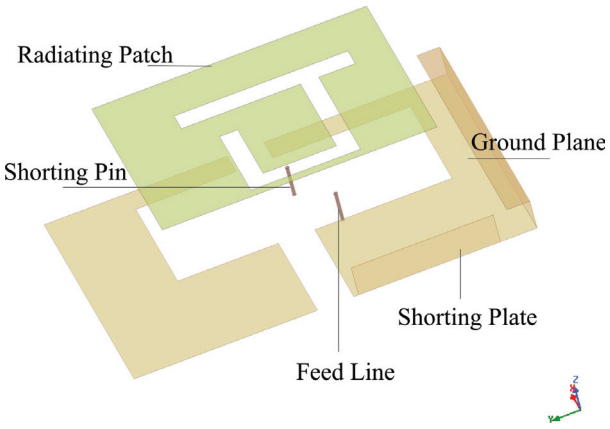


Fig. 1. Components of the proposed antenna.

In this paper, a novel low-profile wideband planar inverted-F antenna with co-design of the ground plane is

*Submitted On: April 24, 2022*
*Accepted On: February 6, 2023*



https://doi.org/10.13052/2023.ACES.J.380209

proposed as shown in Fig. 1. The design process is introduced and some important parameters are studied. A cross-shaped slot is loaded on the ground plane and the size and position of the slot are studied to enhance the impedance bandwidth. The results show that the slot that parallels to the dominant current direction on the ground plane can change the bandwidth of the antenna effectively. The data from the simulation and the measurement of the proposed antenna show that the bandwidth ($S_{11} < -10$ dB) can be expanded to 51%, covering the range of 5.64 GHz to 9.6 GHz. The max gain can be 5.4 dBi and the vertical omnidirectional performance is also better than typical PIFAs.

## II. GEOMETRY AND FABRICATION

The proposed antenna is shown in Fig. 2, consisting of a radiating patch, a shorting plate, a ground plane, a shorting pin and a 50 Ω coaxial feed line. The slot on the radiating patch is designed to excite multiple radiation modes. The positions of the shorting pin and the feed point are well-chosen to realize the wideband feature, and the details will be shown in the next section. The ground plane is etched with a cross-shaped slot to combine the radiation modes and the influence of the width is studied. The values of the design properties are shown in Table 1. The entire structure is simulated using ANSYS Electronic Desktop 2018.0.

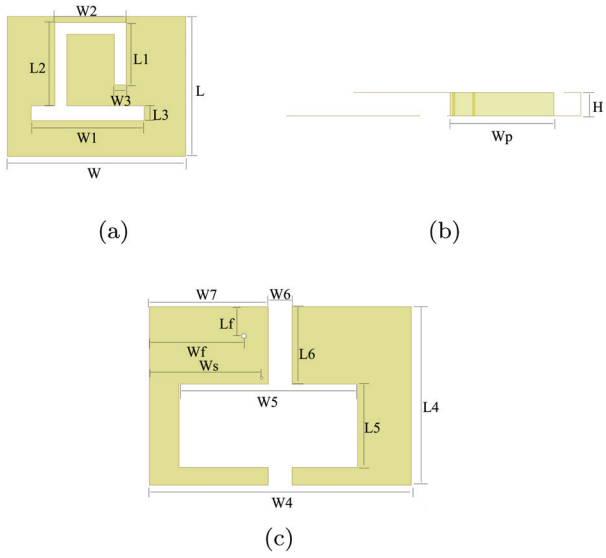


Fig. 2. Design parameters of components. (a) Patch. (b) Shorting plate. (c) Ground plane.

## III. DESIGN APPROACH AND PARAMETRIC STUDIES

### A. Design approach

Figure 3 shows the design approach of the proposed antenna. In Fig. 3 (a), a traditional single mode PIFA with narrow bandwidth is shown and its resonant frequency is 2.75 GHz. A winding slot similar to U-shape is loaded in Fig. 3 (b) to excite multiple resonant frequencies. The antenna becomes a tri-band PIFA with the slot. The basic principle for the expanding of bandwidth is to pull these resonant frequencies closer and combine those receptive frequency ranges. In Fig. 3 (c), a narrow slot parallel to $x$-axis on the ground plane is loaded to widen the bandwidth of each frequencies. Finally, a wide slot vertical to the narrow one is loaded to combine these resonant frequencies further as shown in Fig. 3 (d) and the effect will be discussed later. The positions of the feed point and shorting pin are well-chosen to achieve a better bandwidth, and the sizes of the patch and the ground plane have been adjusted during the design process.

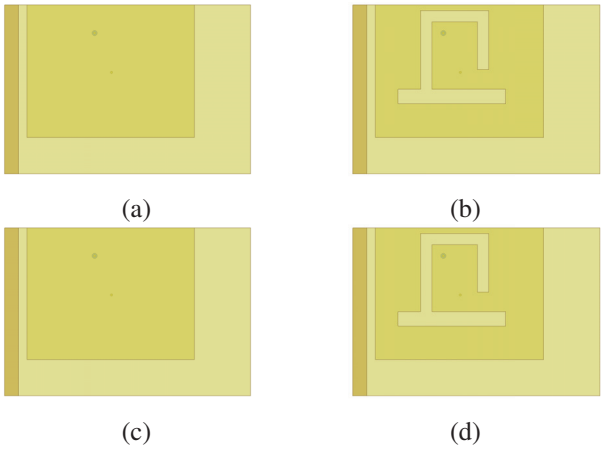


Fig. 3. Design process. (a) Original PIFA. (b) Slot on the patch. (c) Slot on the ground plane. (d) Wide slot.

Table 1: Design parameters

| Parameters | Dimension | Parameters | Dimension | Parameters | Dimension |
|---|---|---|---|---|---|
| $L$ | 23.5 mm | $L_f$ | 5 mm | $W_6$ | 4 mm |
| $L_1$ | 10.5 mm | $W$ | 30 mm | $W_7$ | 20 mm |
| $L_2$ | 14 mm | $W_1$ | 19 mm | $W_f$ | 16 mm |
| $L_3$ | 2.5 mm | $W_2$ | 12 mm | $W_s$ | 19 mm |
| $L_4$ | 30 mm | $W_3$ | 2 mm | $W_p$ | 15.5 mm |
| $L_5$ | 14 mm | $W_4$ | 44 mm | $H$ | 3.5 mm |
| $L_6$ | 13 mm | $W_5$ | 30 mm | | |

### B. Parametric studies

In the PIFA, the relative position between feed point and slot can effectively change the radiating performance. Usually, etching a winding slot between the feed point may excite more than one radiating mode and alter the current distribution on the patch. Hence, the parameter $L_f$ is important for the whole radiating feature. Figure 4 shows the results of different values of $L_f$, and it can be seen that as the value increases, the impedance bandwidth ($-10$ dB) decreases significantly and the shape of the curve becomes sharper. This can be attributed to the difference between the two resonant

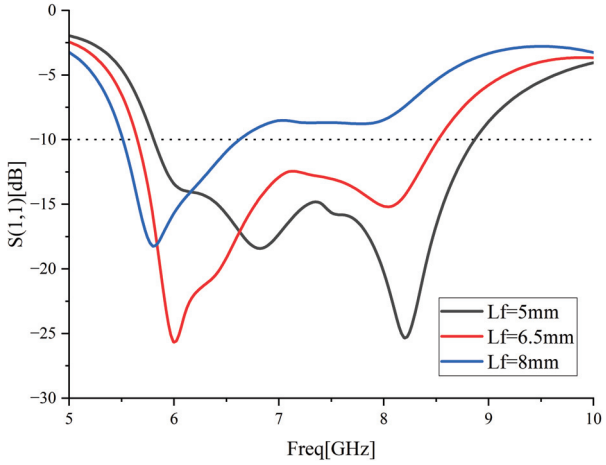


Fig. 4. The influence of $L_f$.

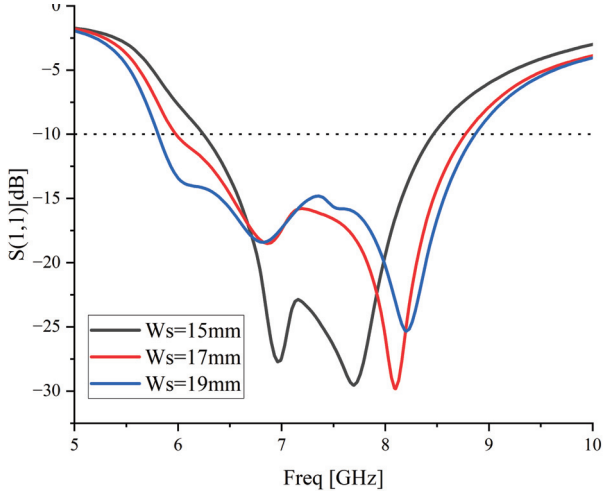


Fig. 5. The influence of $W_s$.

frequencies decreasing as the value of $L_f$ increases. The value of $L_f$ is chosen to be 5 mm to reach a better bandwidth performance.

Additionally, the influence of the shorting pin's position is also studied. The results are shown in Fig. 5. Moving the shorting pin does not change the whole radiating performance as significantly as the feed point. The impedance bandwidth decreases slightly as the value of $W_s$ decreases, while the magnitude of return loss increases. In this case, $W_s = 19$ mm is chosen to expand the $-10$ dB range further.

The design of the ground plane is a convenient way to improve the radiating performance without adding extra components and complicating the whole structure. According to [6], it is found that altering the ground plane using slots can allow for greater bandwidth and the direction of the slots must be perpendicular to the

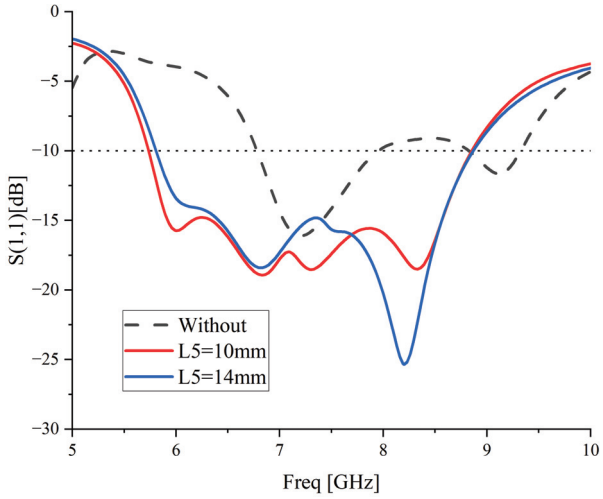


Fig. 6. The influence of $L_5$.

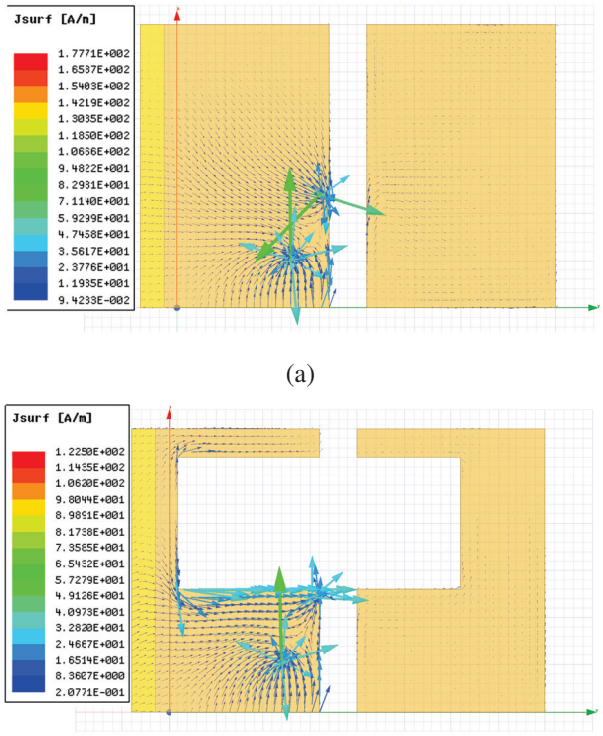


Fig. 7. Current density on the ground plane. (a) Without the wide slot. (b) With the wide slot.

predominant current direction. For the proposed antenna, a perpendicular slot is used on the ground plane. In addition, a wide vertical slot is added and a cross-shaped slot is made. Figure 6 shows the influence of the wide slot and the radiating performance is improved after adding it. The width of the wide slot $L_5$ is chosen to be

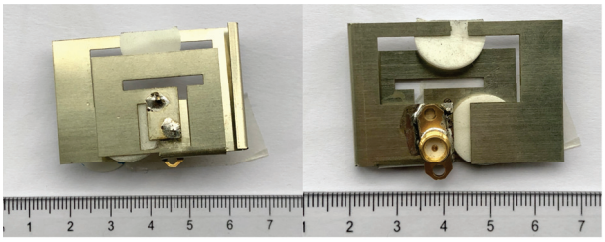

(a) (b)

Fig. 8. Prototype of the proposed antenna. (a) Top view. (b) Bottom view.

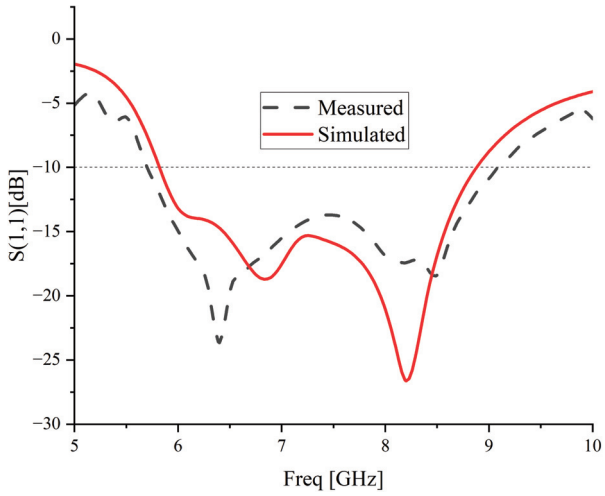


Fig. 9. Return loss of simulation and measurements.

14 mm. Figure 7 shows the current flow distribution on the ground plane with and without the wide slot. It can be seen that the slot does not change the main current concentration points, but the current density does become larger in the slot edge area.

## IV. RESULTS AND DISCUSSION

The prototypes of the antenna are fabricated and measured, in order to verify the results of simulation. A vector network analyzer is used to measure the return loss, and the far-field antenna test system is used to measure the radiation patterns. The pictures of the prototype are shown in Fig. 8, including top and bottom views.

### A. Return loss

The simulated and measured results of return loss are shown in Fig. 9. For simulated results, the impedance bandwidth (−10 dB) covers the range of 5.64 GHz to 8.37 GHz, and the fractional bandwidth is 39.0%. For measured results, 5.64 – 9.60 GHz is covered, and the total bandwidth is 3.96 GHz with a fractional bandwidth of 51%. It can be concluded that the results of

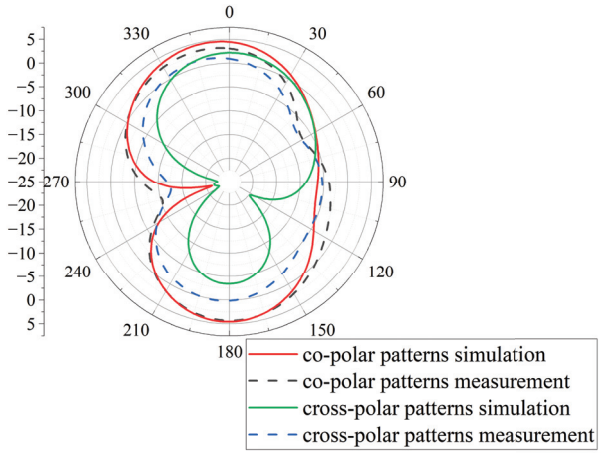


(a)

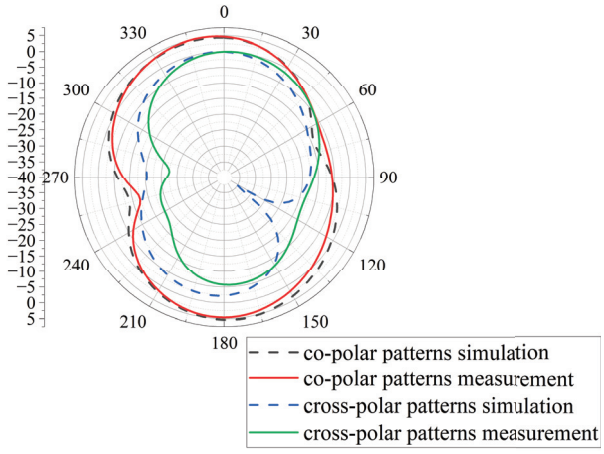


(b)

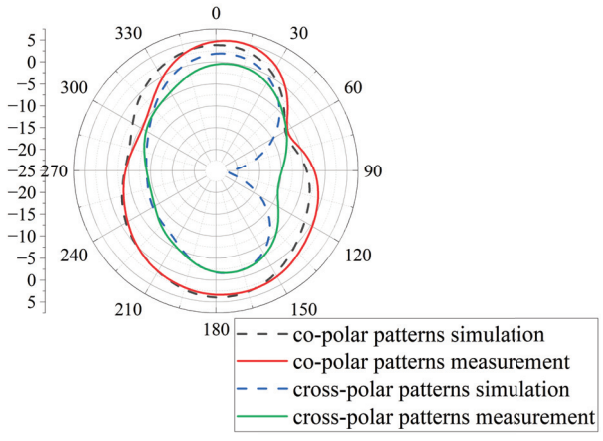


(c)

Fig. 10. Radiation patterns at 5.89 GHz, 6.56 GHz, and 8.14 GHz on the *xoz* plane. (a) 5.89 GHz. (b) 6.56 GHz. (c) 8.14 GHz.

the simulation and the measurement are in quite good agreement. The results of different prototypes are not

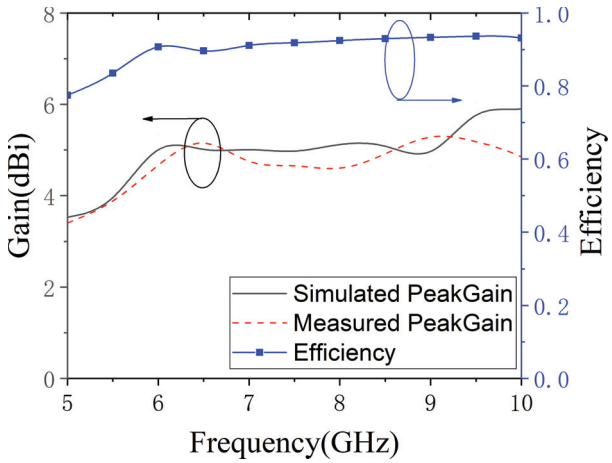


Fig. 11. Gain and efficiency.

the same due to fabrication errors, and a position deviation of only 1.5 mm of the feed point may cause a huge difference in results, as shown in the parameter studies section. The proposed antenna can meet the requirement of 5G and 6G WLAN. The bandwidth has been expanded several times compared to the traditional PIFA.

### B. Radiation patterns

The radiation pattern of the proposed antenna is shown in Fig. 10. The gains at 5.89 GHz, 6.56 GHz, and 8.14 GHz on the *xoz* plane are measured and the peak gain is 5.4 dBi, obtained at 8.14 GHz according to measurement. At high resonant frequency points, the radiation patterns are approximately omnidirectional and the minima of gain is more than −10 dBi, which achieves a better vertical omnidirectional performance compared to traditional PIFAs. That might be attributed to the folded ground plane and is about to study in the future.

### C. Peak gain and efficiency

The gain and simulated efficiency are shown in Fig. 11. The results show that the peak gain of the proposed antenna remains stable in this wide bandwidth. The simulated efficiency remains about 90% in the entire frequency range.

Table 2: Comparisons of the proposed antenna to other PIFAs

| Ref. | Area ($mm^2$) | Profile (mm) | $f_0$ (GHz) | BW (GHz) | Peak Gain (dBi) | Size Comparison |
|---|---|---|---|---|---|---|
| [9] | 46×36 | 5.5 | 5.5 | 0.94(18%) | 5.90 | 197.1% |
| [10] | 53×41.4 | 1.754 | 6 | 2(33.33%) | 10.82 | 83.3% |
| [11] | 42×28 | 4 | 5.5 | 0.94(17.09%) | 6.70 | 101.8% |
| This work | 44×30 | 3.5 | 7.62 | 3.96(51%) | 5.40 | 100% |

## V. CONCLUSION

A low-profile wideband planar inverted-F antenna is proposed in this paper. A cross-shaped slot is used on the ground plane to combine three resonant modes and achieve the wide bandwidth feature. Several prototypes are fabricated to verify the simulation results. The proposed antenna has a measured −10 dB bandwidth of 3.96 GHz and the fractional bandwidth is 51%. A peak gain of 5.4 dBi is measured and the gain remains stable in the bandwidth. The proposed antenna can meet the requirements for wireless local area networks (5725 – 5825 MHz), and IoV applications (5905 – 5925 MHz). The latest 6G-band of WiFi 6E (5946 – 7105 MHz) is also covered. The comparisons between the proposed antenna and other PIFAs are shown in Table 2.

## ACKNOWLEDGEMENTS

This work was supported by the National Natural Science Foundation of China with the Project No. 62071331.

## REFERENCES

[1] Y. Zhang, L. Gao, and X. Y. Zhang, "Compact quad-band bandpass filter for DCS/WLAN/WiMAX/5G Wi-Fi application," *IEEE Microw. Wirel. Components Lett.*, vol. 25, no. 10, pp. 645-647, Oct. 2015.

[2] N. H. Mahmood, H. Alves, O. A. López, M. Shehab, D. P. M. Osorio, and M. Latva-Aho, "Six key features of machine type communication in 6G," *2020 2nd 6G Wireless Summit*, Levi, Finland, Mar. 2020.

[3] K. L. Lau, P. Li, and K. M. Luk, "A wideband and dual-frequency shorted-patch antenna with compact size," *IEEE Antennas and Propagation Society Symposium*, vol. 1, pp. 249-252, Monterey, CA, Jul. 2004.

[4] S. J. Lin and J. S. Row, "Bandwidth enhancement for dual-frequency microstrip antenna with conical radiation," *Electron. Lett.*, vol. 44, no. 1, pp. 2–3, Feb. 2008.

[5] M. C. Huynhand and W. Stutzman, "Ground plane effects on planar inverted-F antenna (PIFA) performance," *IEE Proc. Microw. Antennas Propag.*, vol. 150, no. 4, pp. 209–213, Aug. 2003.

[6] N. L. Bohannon and J. T. Bernhard, "Design guidelines using characteristic mode theory for improving the bandwidth of PIFAs," *IEEE Trans. Antennas Propag.*, vol. 63, no. 2, pp. 459-465, Feb. 2015.

[7] N. Liu, L. Zhu, W. Choi, and X. Zhang, "A low-profile differential-fed patch antenna with bandwidth enhancement and sidelobe reduction under operation of $TM_{10}$ and $TM_{12}$ modes," *IEEE Trans. Antennas Propag.*, vol. 66, no. 9, pp. 4854–4859, Sep. 2018.

[8] N. W. Liu, L. Zhu, W. W. Choi, and X. Zhang, "Wideband shorted patch antenna under radiation of dual-resonant modes," *IEEE Trans. Antennas Propag.*, vol. 65, no. 6, pp. 2789–2796, Jun. 2017.

[9] G. Gao, C. Yang, B. Hu, R. Zhang, and S. Wang, "A wide-bandwidth wearable all-textile PIFA with dual resonance modes for 5GHz WLAN applications," *IEEE Trans. Antennas Propag.*, vol. 67, no. 6, pp. 4206–4211, Jun. 2019.

[10] R. Jian, Y. Chen, and T. Chen, "A low-profile wideband PIFA based on radiation of multiresonant modes," *IEEE Antennas Wirel. Propag. Lett.* , vol. 19, no. 4, pp. 685-689, Apr. 2020.

[11] G. Gao, C. Yang, B. Hu, R. Zhang, and S. Wang, "A wearable PIFA with an all-textile metasurface for 5 GHz WBAN applications," *IEEE Antennas Wirel. Propag. Lett.*, vol. 18, no. 2, pp. 288-292, Feb. 2019.

**Xiao Yu Li** received the B.S. degree in Communication and Information Engineering and the M.S. degree in Electronic and Information Engineering from University of Electronic Science and Technology of China, Chengdu, China, in 2017 and 2020, respectively. He is currently pursuing the Ph.D. degree in Control Science and Engineering with Tongji University, Shanghai, China, and his current research interests include reconfigurable antennas and computational electromagnetics.

**Zu Ang Liu** received the B.S. degree of Electronic Science and Technology and the M.S. degree of Microelectronic Science and Engineering from Tongji University, Shanghai, China, in July 2019 and June 2022, respectively. Currently, he is an engineer in a high-tech company, Beijing, China.

**Mei Song Tong** received the B.S. and M.S. Degrees from Huazhong University of Science and Technology, Wuhan, China, respectively, and Ph.D. degree from Arizona State University, Tempe, Arizona, USA, all in electrical engineering. Currently, he is the Distinguished/Permanent Professor, Head of Department of Electronic Science and Technology, and Vice Dean of College of Microelectronics, Tongji University, Shanghai, China. He has also held an adjunct professorship at the University of Illinois at Urbana-Champaign, Urbana, Illinois, USA, and an honorary professorship at the University of Hong Kong, Hong Kong, China. He has published more than 500 papers in refereed journals and conference proceedings and co-authored six books or book chapters. His research interests include electromagnetic field theory, antenna theory and technique, modeling and simulation of RF/microwave circuits and devices, interconnect and packaging analysis, inverse electromagnetic scattering for imaging, and computational electromagnetics.

Prof. Tong is a Fellow of the Electromagnetics Academy, Fellow of the Japan Society for the Promotion of Science (JSPS), and Full Member (Commission B) of the USNC/URSI. He has been the chair of Shanghai Chapter since 2014 and the chair of SIGHT committee in 2018, respectively, in IEEE Antennas and Propagation Society. He has served as an associate editor or guest editor for some well-known international journals, including IEEE Antennas and Propagation Magazine, IEEE Transactions on Antennas and Propagation, IEEE Transactions on Components, Packaging and Manufacturing Technology, International Journal of Numerical Modeling: Electronic Networks, Devices and Fields, Progress in Electromagnetics Research, and Journal of Electromagnetic Waves and Applications, etc. He also frequently served as a session organizer/chair, technical program committee member/chair, and general chair for some prestigious international conferences. He was the recipient of a Visiting Professorship Award from Kyoto University, Japan, in 2012, and from University of Hong Kong, China, 2013. He advised and coauthored 12 papers that received the Best Student Paper Award from different international conferences. He was the recipient of the Travel Fellowship Award of USNC/URSI for the 31th General Assembly and Scientific Symposium (GASS) in 2014, Advance Award of Science and Technology of Shanghai Municipal Government in 2015, Fellowship Award of JSPS in 2016, Innovation Award of Universities' Achievements of Ministry of Education of China in 2017, Innovation Achievement Award of Industry-Academia-Research Collaboration of China in 2019, Chapters Award of IEEE New Jersey Section, USA, in 2019, "Jinqiao" Award of Technology Market Association of China in 2020, and Baosteel Education Award of China in 2021. In 2018, he was selected as the Distinguished Lecturer (DL) of IEEE Antennas and Propagation Society for 2019-2022.

# Phase-shifter-less Vortex Electromagnetic Wave Generation Technology with Tunable Topological Charge/Steering Angle under Random Initial Phase Condition of Phase-locked Source

**Yuliang Zhou[1], Kaiyuan Yao[1], Xiaona Li[1], Yong Mao Huang[2], and Haiyan Jin[1]**

[1]School of Aeronautics and Astronautics
University of Electronic Science and Technology of China, Chengdu, 611731, China
uestcjhy@uestc.edu.cn

[2]School of Electrical and Electronic Information
Xihua University, Chengdu, 610097, China

***Abstract –*** This paper demonstrates how to implement a vortex electromagnetic wave generation system with beam steering using only delay lines as phase-shifting elements. The system is based on uniform circular array and phased array technology. A detailed theoretical derivation is presented, which yields an input frequency matrix corresponding to each target case. Furthermore, considering the random initial phase problem of the actual phase-locked source, the above scheme is further improved in this paper. By cleverly setting the circuit structure, the influence of the initial phase inconsistency on the phase control system is filtered out. The performance is verified by analytical calculations and full-wave electromagnetic simulations, which are in good agreement with the proposed theory. The scheme proposed in this paper can completely get rid of the phase shifter and realize the free adjustment of the topological charge number/beam steering angle. The adjustment accuracy depends on the tuning accuracy of the phase-locked source, which can achieved an accuracy over 1Hz at a cost of less than six dollars, which makes it an interesting and flexible low-cost vortex electromagnetic wave generation scheme.

***Index Terms –*** OAM (orbital angular momentum) wave, phase-shifter-less, random initial phase, tunable steering angle, tunable topological charge.

## I. INTRODUCTION

Over the past decades, investigations have shown that electromagnetic waves not only have spin angular momentum, but also orbital angular momentum [1]. Some subsequent studies have stated clearly that electromagnetic waves carrying orbital angular momentum, called vortex electromagnetic waves, have a helical phase structure, whose wavefront rotates along the beam axis in space [2]. The vortex electromagnetic waves of different OAM modes have different phase structures, and the integer modes are orthogonal to each other [3], which means that the orbital angular momentum can provide rotational degrees of freedom for the electromagnetic field and this is beneficial for novel multiplexing applications [4, 5]. Orbital angular momentum has been discovered in optical research [1], and vortex electromagnetic waves have been used in radar imaging [6], quantum state manipulation [7], identification of scatterer characteristics [8], 2D underwater imaging [9] and other fields.

The state-of-the-art OAM generation architectures can be mainly divided into four types, namely transmission helical structure [10], transmission grating structure [11], helical reflector structure [12] and array antenna [13, 14]. When vortex electromagnetic waves were first proposed, the proponents described how to feed a uniform circular array to generate orbital angular momentum in the radio frequency band [15]. A uniform circular phased array has the advantages of simple processing and easy operation, so it is a good vortex electromagnetic wave generator [16]. As one of the commonly used methods of generating vortex electromagnetic waves [17, 18], the uniform circular array antenna usually needs to be used with phase shifters [19–21]. Due to the high cost of phase shifters, many authors try to replace the phase shifter with other structures in the design of the OAM generator [22–24]. However, none of these solutions have good reconfigurability.

In this work, an effective OAM phased array implementation method based on the uniform circular array antenna is proposed to achieve system reconfigurability at low cost. In some schemes, delay lines are used instead of phase shifters to generate vortex electromagnetic waves with different topological charges, which simplifies the system. However, if the beam pointing control of OAM is to be further realized without chang-

*Submitted On: August 13, 2022*
*Accepted On: February 20, 2023*



https://doi.org/10.13052/2023.ACES.J.380210

ing the length of the delay line, the phase shifter is still required. In contrast, the proposed technique can be performed without other phase-shifting units. By adjusting the frequency of each local oscillator signal, a vortex electromagnetic wave generation system with arbitrary topology charge and beam pointing angle is designed without the need for phase shifters.

## II. LOW-COST OAM PHASED ARRAY SYSTEM

### A. Low-cost OAM phased array circuit-level implementation technology

The uniform circular array used to generate vortex electromagnetic waves is shown in Fig. 1 (a).

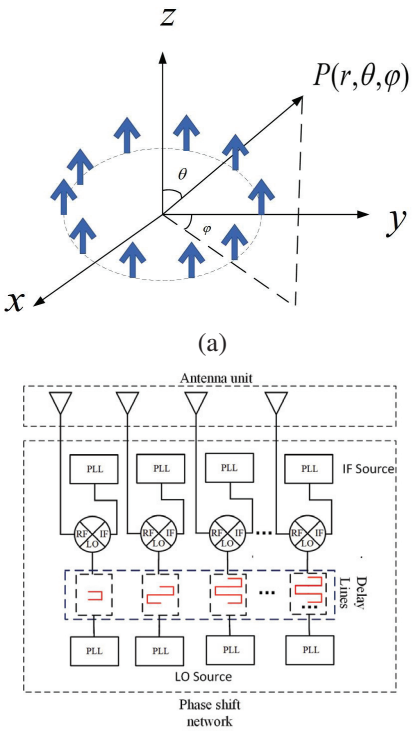


Fig. 1. (a) Diagram of the circular array configuration, and (b) low-cost OAM phased array system schematic diagram.

The far-field radiation pattern for a uniform circular array is [25]:

$$G(A,\theta,\varphi)=\sum_{m=1}^{M}A_m e^{i[ka\sin\theta\cos(\varphi-\varphi_m)+\alpha_m]}, \quad (1)$$

where $\varphi_m=2\pi m/M$, $A_m$ is the amplitude of the excitation signal for each antenna element, and $\alpha_m$ is the phase relationship of them. When $\alpha_m=2\pi ml/M$ ($l\varphi_m$), the directional pattern function of the array is [7]:

$$G(\theta,\varphi)=\sum_{m=1}^{M}\mathrm{e}^{il\varphi_m}\cdot e^{ika\sin\theta\cos(\varphi-\varphi_m)}$$
$$=M\mathrm{e}^{il\varphi}i^{-1}J_l(sin\theta). \quad (2)$$

It carries a phase factor $\mathrm{e}^{il\varphi}$, so it can generate vortex electromagnetic waves, where $l$ is the mode of OAM. On this basis, the beam pointing control factor is added. If the preset pointing angle is $(\theta_0,\varphi_0)$, the phase excitation vector of each array element can be given by the following equation [26]:

$$S=\left\{ka\sin\theta_0\cos\left(\varphi_0-\frac{2\pi m}{M}\right)\right\}. \quad (3)$$

Therefore, to generate a vortex electromagnetic wave with a topological charge of $l$, and a beam pointing angle of $(\theta_0,\varphi_0)$, the phase shift should be [15]:

$$S=\left\{l\varphi_m+ka\sin\theta_0\cos\left(\varphi_0-\frac{2\pi m}{M}\right)\right\}. \quad (4)$$

By plugging Eq. 4, the radiation pattern is reobtained as [27]:

$$G(\theta,\varphi)=\sum_{m=1}^{M}\mathrm{e}^{il\varphi_m}e^{ika(\sin\theta\cos(\varphi-\varphi_m)-\sin\theta_0\cos(\varphi_0-\varphi_m))}$$
$$=M\mathrm{e}^{il\xi}\cdot e^{il\frac{\pi}{2}}J_l(ka\rho), \quad (5)$$

where $\rho=\sqrt{\mathrm{u}^2+v^2}$, $\cos\xi=\frac{u}{\sqrt{\mathrm{u}^2+v^2}}$, $\mathrm{u}=\sin\theta\cos\varphi-\sin\theta_0\cos\varphi_0$, $\mathrm{v}=sin\theta\sin\varphi-\sin\theta_0\sin\varphi_0$. It can be seen that after adding beam pointing control, the array factor function still carries the azimuth component, which proves that it also has the characteristics of vortex electromagnetic waves.

The system schematic diagram is shown in Fig. 1 (b). Beam steering is performed by simply changing the radiation frequency, since the necessary phase shifts are provided by the delay lines [28]. The phase-modulated signal is sent by M channels of local oscillator signal sources, and the phase is adjusted through the fixed-length delay line. After that, the signals are mixed with the M channels of intermediate frequency signal sources through the heterodyne mixer, which form the TX chains and then send the mixed signal into the antenna array through a filter. In this way, the purpose of adjusting the phase of each antenna unit without changing its finally radio frequency is achieved.

Let the IF signal be $S_{IF}=A\cos(\omega_{IF}t+\varphi_1)$, and the local oscillator signal be $S_{LO}=B\cos(\omega_{LO}t+\varphi_2)$. After mixing the two and filtering:

$$S_{RF}=C\cos((\omega_{IF}+\omega_{LO})t+(\varphi_1+\varphi_2)). \quad (6)$$

When the frequency of the local oscillator signal increases $\Delta\omega$, the frequency of the intermediate frequency signal decreases $\Delta\omega$. Let the delay line act on the local oscillator signal source, the local oscillator signal will add a phase shift $\Delta\varphi$ generated by passing through

them, and at this time the local oscillator signal is:

$$S_{LO} = B\cos\left(\left(\omega_{LO}+\Delta\omega\right)t+\varphi_2+\Delta\varphi\right). \quad (7)$$

If the phase shift constant of the delay line is $\beta = \omega\sqrt{\varepsilon\mu}$, let the length of the delay line be $l'$, and the corresponding phase shift $\Delta\varphi$ is $l'\beta$. By plugging it into Eq. 7, and assuming that the initial phase of the signal source is 0, we obtain:

$$S_{RF} = C\sin\left(\left(\omega_{IF}+\omega_{LO}\right)t+l'\left(\omega_{LO}+\Delta\omega\right)\sqrt{\varepsilon\mu}\right). \quad (8)$$

In order to obtain the vortex electromagnetic wave, the phase offset required for the $m$th array element is $\Delta\varphi_m = 2\pi ml/M$. Then, the length of the delay line corresponding to the $m$th array element is calculated as:

$$l'_m = \frac{\Delta\varphi_m}{\omega_m\sqrt{\varepsilon\mu}} = \frac{2\pi ml}{M\omega_m\sqrt{\varepsilon\mu}}, \quad (9)$$

where $\omega_m$ is the input frequency of the delay line corresponding to the $m$th element. Set $l = 1$, $\Omega_M = (\omega_1, \omega_2, ..., \omega_M)^T = (\omega', \omega', ..., \omega')^T$, and substitute into Eq. 9 to obtain:

$$l'_m = \frac{2\pi m}{M\omega'\sqrt{\varepsilon\mu}}. \quad (10)$$

To determine the length of the delay line corresponding to each array element by Eq. 10, let it be $L'_M = (l'_1, l'_2, ..., l'_M)^T$, and set $L = (1, 2, ..., M/2-1)^T$. By plugging Eq. 10 into Eq. 9 it, we obtain: $\omega_m = \omega' l$, and then we can obtain the frequency matrix as:

$$\Omega_{(l,m)} = \begin{pmatrix} \omega' & \omega' & \cdots & \omega' \\ 2\omega' & 2\omega' & \cdots & 2\omega' \\ \vdots & \vdots & \ddots & \vdots \\ \left(\frac{M}{2}-1\right)\omega' & \left(\frac{M}{2}-1\right)\omega' & \cdots & \left(\frac{M}{2}-1\right)\omega' \end{pmatrix}. \quad (11)$$

This is a matrix with $M/2-1$ rows and $M$ columns, (the rows and columns correspond to the topological charge and the array element serial number respectively), and its value is the frequency value that the local oscillator signal source needs to output.

It can be seen that if the delay line-based system is used to generate vortex electromagnetic waves, when the length of the delay line is determined and control beam pointing is not considered, there is a linear relationship between the frequency and the topological charge. The frequency of the input signal required by the time line is the same. Therefore, only two signal sources are required to output eight local oscillator signals and eight intermediate frequency signals, respectively, through the power divider.

If the beam is deflected with an angle of $(\theta_0, \varphi_0)$, the phase offset required by the $m$th array element is given by Eq. 4. At this time, the output frequency of the local oscillator signal source corresponding to the $m$th array element is:

$$\omega_m = \frac{2\pi ml - kaM\sin\theta_0\cos\left(\varphi_0 - \frac{2\pi m}{M}\right)}{Ml'_m\sqrt{\varepsilon\mu}}. \quad (12)$$

Let the length of the delay line still be $L'_M = (l'_1, l'_2, ..., l'_M)^T$, to make the beam pointing angle $(\theta, \varphi)$=$(\theta_1, \varphi_1)$, let $(\theta_1, \varphi_1)$=$\nu_1$, and set: $\psi_{\nu_1}(m) = -\omega' kaM\sin\theta_1\cos\left(\varphi_1 - 2\pi m/M\right)/2\pi m$. Then Eq. 12 can be written as: $\omega_m = \omega' l + \psi_{\nu_1}(m)$. Finally, the frequency matrix is written as:

$$\overline{\Omega} = \begin{pmatrix} \omega'+\psi(1) & \cdots & \omega'+\psi(M) \\ 2\omega'+\psi(1) & \cdots & 2\omega'+\psi(M) \\ \vdots & \ddots & \vdots \\ \left(\frac{M}{2}-1\right)\omega'+\psi(1) & \cdots & \left(\frac{M}{2}-1\right)\omega'+\psi(M) \end{pmatrix}. \quad (13)$$

Eq. 13 is the frequency matrix corresponding to the local oscillator signal. It can be seen from Eq. 13 that after adding beam pointing control, the input frequencies required for the corresponding delay lines of different array elements under the same topology load and beam pointing angle are no longer the same, so one signal source cannot be used to provide all entries. If the final RF signal frequency is $\omega_{RF}$, the frequency matrix corresponding to the intermediate frequency signal is $\omega_{RF} - \overline{\Omega}_{(l,m)}$.

To sum up, without changing the length of the delay line, the system needs 2 M signal sources, including M local oscillator signal sources and M intermediate frequency signal sources. In practical applications, two groups of one-way constant temperature crystal oscillators plus M-way phase-locked loops can be used to realize this function.

### B. Electromagnetic simulation

Select a uniform circular antenna array with eight elements, select the X-band (10GHz) as the RF frequency, and simulate the system in Systemvue. When the beam pointing angle is (0, 0) and the OAM mode is 1, select 500MHz as the M-channel local oscillator signal source output frequency. On this basis, according to Eq. 13, the frequency value of the output signal of each signal source is regulated to generate different forms of vortex electromagnetic waves. The system block diagram is shown in Fig. 2.

In this paper's simulation, the beam pointing angle is uniformly specified in the direction of the lowest amplitude value in the zero-depth region. As shown in Fig. 3, when the topological charge is both 1 and the pointing angle is (15, 15) and (30, 30) respectively, (a) and (b) reveal the relationship curves between the amplitude value and the pitch angle $\theta$ on the azimuth pointing plane. The angle corresponding to the minimum amplitude value is the beam deflection angle. Panels (c) and (d) in Fig. 3 indicate the situation when the pointing angles are same but the topological charge generated is changed to 2. Therefore we can conclude that when the 30dB deviation is used as the standard, under the same topological charge condition, the angle

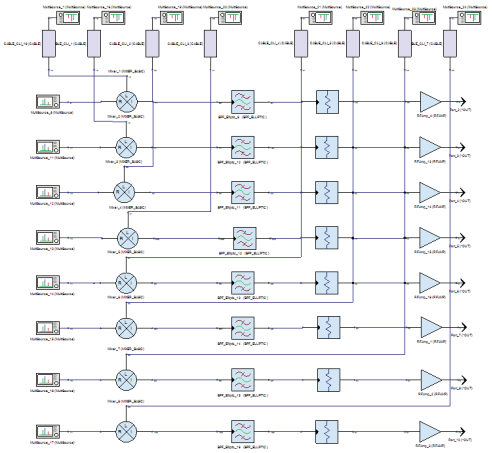

Fig. 2. System block diagram.

occupied by the zero-depth area is proportional to the beam deflection angle value. When the influence of the deflection angle is not considered, the zero-depth area will follow the OAM mode and increased significantly. In the lower right corner of each picture in Fig. 3, there is a complete array pattern. It can be seen that the system has achieved splendid results in the control of azimuth and pitch angles, and can maintain the structure of vortex electromagnetic waves at the same time.

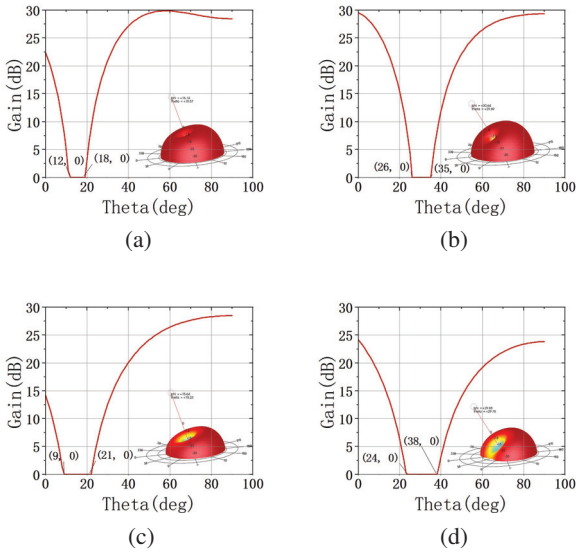


Fig. 3. Array pattern. (a) Charge1 (15,15). (b) Charge1 (30,30). (c) Charge2 (15,15). (d) Charge2 (30,30).

Multiple phase-locked loops in a system can maintain the same initial phase when outputting the same frequency signal, but different phase-locked loops in this paper need to output different frequencies, so the initial phase of each signal becomes random. This will cause the phase relationship between the signals that are finally fed to the antenna elements of the array to no longer be as preset, and the impact will be devastating. A random initial phase of 0°-360° is assigned to a certain number of signal sources in Fig. 2. Set the topological load is a 1, and the pitch angle deflection is 20°, the generated pattern and phase diagram are shown in Figs. 4 (a) and (b), respectively.

It can be seen that the phased structure of the vortex electromagnetic wave was damaged, and if the system is executed a second time, another unordered result will be randomly obtained, so it needs to be improved.

## III. RANDOM INITIAL PHASE CONDITIONS SYSTEM

### A. Improved scheme of phase-locked source under random initial phase conditions

According to Section II A, the premise that the system can successfully achieve the expected effect requires that the initial phases of the M channels of local oscillator signal sources are consistent, and the same is true of the M channels of IF signal sources. If there is an initial phase difference between the signal sources, the difference will remain until the final signal input to the antenna array, which will eventually destroy the phase control structure of the vortex electromagnetic wave generation system, as in Fig. 4. However, because of the system's constant temperature crystal oscillator and M-channel phase-locked loop, it cannot guarantee that the initial phase is still consistent after random frequency modulation. In contrast to the instantaneous phase, the initial phase has no practical significance and an accurate and effective measurement method, so it is difficult to realize in practice.

According to equation, when the topological charge is $l$, and the control beam angle is $v_0 = (\theta_0, \varphi_0)$, the required output frequency of each local oscillator signal is $l\omega' + \psi_{v_0}(m)$, and each IF signal is $(\omega_{RF} - l\omega') - \psi_{v_0}(m)$. If the frequency of one LO signal source is preset as $l\omega'$, and the frequency of one IF signal source is

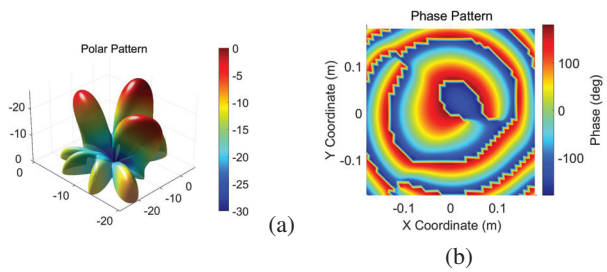


Fig. 4. After adding random initial phase: (a) Pattern, and (b) Phase diagram.

set as $\omega_{RF} - l\omega'$, then each of them needs to be added or subtracted $\psi_{v_0}(m)$, which is the required frequency. Therefore, we can mix these two signals with M signals of frequency $\psi_{v_0}(m)$ (here called weighted signals), and then filter out the interference frequency, and the output signal frequency is the required value.

The schematic diagram of the improved system is shown in Fig. 5, and in this way, the primary phase interference can be eliminated.

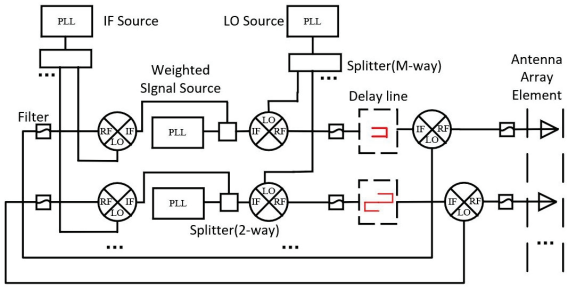


Fig. 5. Random initial phase condition system schematic diagram.

Let the IF signal be $S_{IF} = A\cos(\omega_{IF}t + \varphi_1)$, the local oscillator signal be $S_{LO} = B\cos(\omega_{LO}t + \varphi_2)$, and the m-way weighted signal be:

$$S_C = B\cos\left(\psi_{v_0}(m)t + \varphi'_m\right), \tag{14}$$

where $\varphi_1$, $\varphi_2$, $\varphi'_m$ are all random phases from 0 to 360°. After mixing and filtering with the m-way weighted signals, the intermediate frequency signal and the local oscillator signal become:

$$S_{IF} = A\cos\left(\left(\omega_{IF} - \psi_{v_0}(m)\right)t + \varphi_1 - \varphi'_m\right), \tag{15}$$

$$S_{LO} = B\cos\left(\left(\omega_{LO} + \psi_{v_0}(m)\right)t + \varphi_2 + \varphi'_m\right). \tag{16}$$

After that, the local oscillator signals of each channel pass through the delay line to obtain:

$$S_{LO} = B\cos\left(\left(\omega_{LO} + \psi_{v_0}(m)\right)t + \varphi_2 + \varphi'_m + \Delta\varphi_m\right), \tag{17}$$

where $\Delta\varphi_m$ is the desired phase difference relationship. The M channels of local oscillator signals are mixed with the intermediate frequency and filtered, and the final signal is obtained as:

$$S_{RF} = C\cos\left(\left(\omega_{LO} + \omega_{IF}\right)t + \varphi_2 + \varphi_1 + \Delta\varphi_m\right), \tag{18}$$

where $\varphi_1$ and $\varphi_2$ are independent of the array element number $m$, except for $\Delta\varphi_m$, there is no additional phase difference between the signals input to each antenna unit, and the structure of vortex electromagnetic wave and beam pointing control remains intact.

### B. Electromagnetic simulation

The system block diagram in Systemvue is shown in Fig. 6. The uniform circular antenna array with eight elements and the X band radio frequency are still selected. A random initial phase of 0-360° is added to each signal source in Fig. 6.

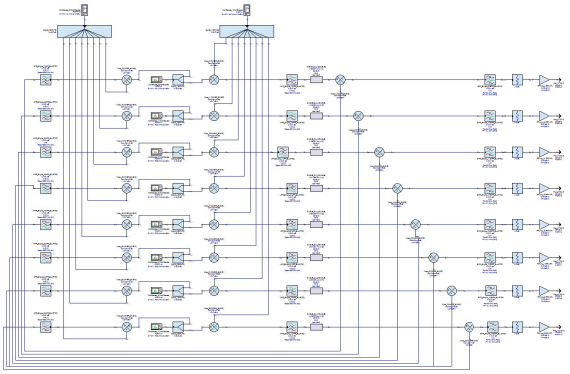

Fig. 6. Random initial phase condition system block diagram.

The system is simulated and the results obtained are shown in Fig. 7. When the topological load is set to 1

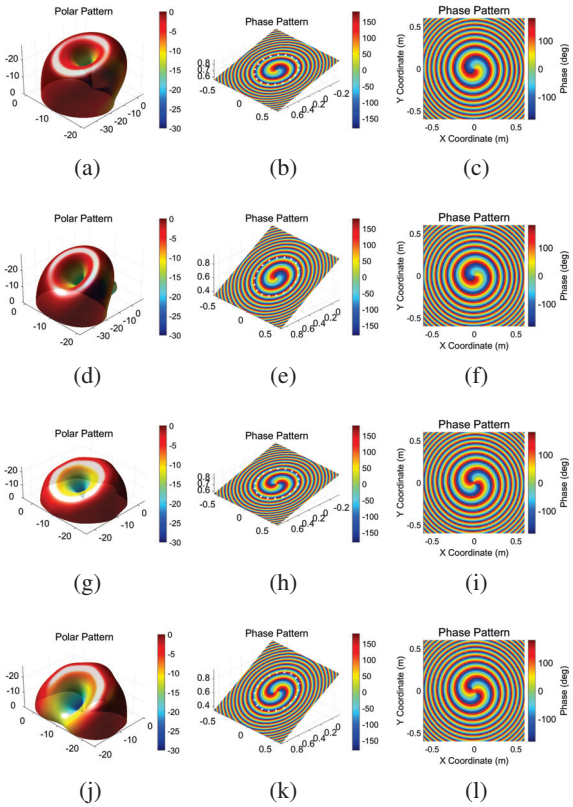


Fig. 7. Charge1 (15,0). (a) Pattern. (b) Phase diagram with pointing. (c) Phase diagram Charge1 (30,0). (d) Pattern. (e) Phase diagram with pointing. (f) Phase diagram Charge2 (15,0). (h) Pattern. (h) Phase diagram with pointing. (i) Phase diagram Charge2 (30,0). (j) Pattern. (k) Phase diagram with pointing. (l) Phase diagram.

and the beam pointing is set to (15, 0), (a) is the pattern of the array, and it can be seen that the pitch angle $\theta$ is shifted by a certain degree. As shown in (b), the plane is intercepted with the pointing axis of (a) as the normal and the phase diagram is drawn when the condition of the circular field is satisfied. (c) is the front view of the phase map. (j) (k) (l) show the same situation when the OAM mode is 2 and the beam pointing is (30, 0). As can be seen from Fig. 7, even if the initial phases of the various signal sources are inconsistent, the system can still offset the effects and obtain ideal results. In order to further verify the system's effect, the OAM spectrum is drawn here. It can be seen that there is a circle of white lines on the phase diagram of the three-dimensional space in Figs. 7 (b) and (d), which is the ring current selected as the reference for the OAM spectrum drawing. As shown in Fig. 8, (a) and (b) are histograms of the purity of each OAM mode with the topological charge set to 1 and the pitch angle $\theta$ pointing set to 15° and 30° respectively, (c) and (d) are for the same case but the topological charge is set to 2.

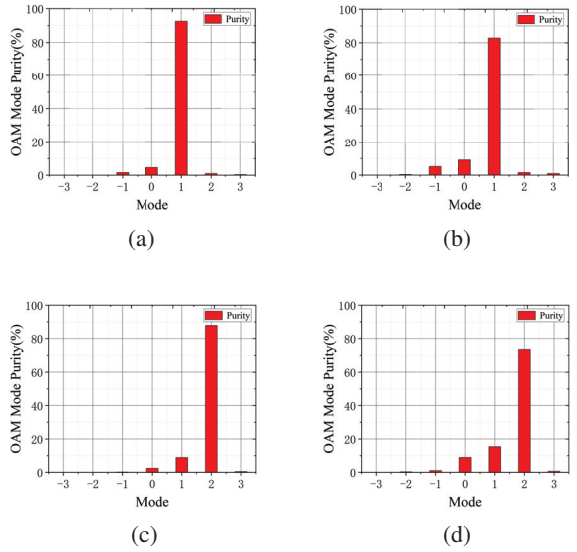


Fig. 8. OAM mode purity. (a) Charge1 (15,0). (b) Charge1 (30,0). (c) Charge2 (15,0). (d) Charge2 (30,0).

It can be seen from Fig. 7 that the OAM generated by the system has good purity, and, under the same topological charge, when the angular deflection increases, the OAM purity has a relatively obvious decline. When the angular orientation control is not considered, the closer the topological charge is to $M/2-1$, and the purity also decreases to a certain extent.

## IV. CONCLUSION

In this work, a vortex electromagnetic wave generation system with beam steering function is designed based on the delay line. The system is improved by rearranging the phase-locked loop and the signal source, so that it cannot be affected by the phase noise to a certain extent. At the same time, the phase interference which cannot be handled by the initial phase random structure can be compensated by modifying the frequency matrix, Eq. 13, which increases the robustness of the system. The two systems were separately modeled in Systemvue for electromagnetic simulation and structure analyses of the generated vortex electromagnetic wave, which subsequently demonstrates that the proposed system has achieved quite good results. It can generate vortex electromagnetic waves of various modes in the range of $l \leq N/2-1$, and control the beam pointing with high precision. Future work is expected to focus on achieving sidelobe suppression, and further optimization of the system structure.

## DECLARATION OF COMPETING INTEREST

The authors declare that they have no known competing financial interests or personal relationships that could have appeared to influence the work reported in this paper.

## REFERENCES

[1] L. Allen, M. W. Beijersbergen, R. Spreeuw, and J. Woerdman, "Orbital angular momentum of light and the transformation of laguerre-gaussian laser modes," *Phys. Rev. A* vol. 45, no. 11, 8185, 1992. doi:10.1103/PhysRevA.45.8185.

[2] S. M. Mohammadi, L. K. Daldorff, J. E. Bergman, R. L. Karlsson, B. Thidé, K. Forozesh, T. D. Carozzi, and B. Isham, "Orbital angular momentum in radio—A system study," *IEEE Trans. Antennas and Propag.*, vol. 58, no. 2, pp. 565-572, 2009. doi:10.1109/TAP.2009.2037701.

[3] F. Tamburini, E. Mari, A. Sponselli, B. Thidé, A. Bianchini, and F. Romanato, "Encoding many channels on the same frequency through radio vorticity: first experimental test," *New J. Phys.*, vol. 14, no. 3, 033001, 2012. doi:10.1088/1367-2630/14/3/033001.

[4] B. Thidé, F. Tamburini, H. Then, C. Someda, and R. Ravanelli, "The physics of angular momentum radio," arXiv:1410.4268, 2014. doi:10.1109/ursi-at-rasc.2015.7302908.

[5] L. Li and F. Li, "Beating the rayleigh limit: Orbital-angular-momentum-based super-resolution

diffraction tomography," *Phys. Rev. E*, vol. 88, no. 3, 033205, 2013. doi:10.1103/physreve.88.033205.

[6] K. Liu, Y. Cheng, Z. Yang, H. Wang, Y. Qin, and X. Li, "Orbital-angular-momentum-based electromagnetic vortex imaging," *IEEE Antennas Wirel. Propag. Lett.*, vol. 14, pp. 711-714, 2014. doi:10.1109/LAWP.2014.2376970.

[7] A. Vaziri, G. Weihs, and A. Zeilinger, "Superpositions of the orbital angular momentum for applications in quantum experiments," *J. Opt. B: Quantum Semiclass. Opt.*, vol. 4, no. 2, S47, 2002. doi:10.1088/1464-4266/4/2/367.

[8] H.-T. Chen, Z.-Q. Zhang, and J. Yu, "Near-field scattering of typical targets illuminated by vortex electromagnetic waves," *Applied Computational Electromagnetics Society Journal (ACES)*, pp. 129-134, 2020.

[9] Y. Yang, G. Liu, F. Shen, J. Sun, K. Guo, Z. Guo, Q. Zhou, H. Jiang, Z. Wu, B. Zeng, "Generating and detecting broad-band underwater multiple oams based on water-immersed array," *IEEE Access*, vol. 8, pp. 149586-149594, 2020. doi:10.1109/ACCESS.2020.3016389.

[10] Y. Jiang, Y. He, and F. Li, "Wireless communications using millimeter-wave beams carrying orbital angular momentum," *2009 WRI Int. Conf. Commum. Mobile Comput.*, vol. 1, pp. 495-500, 2009. doi:10.1109/CMC.2009.315.

[11] V. Vaishnavi, V. Priya, M. Kumar, S. Venkatesh, G. A. S. Sundaram "Simulation of helical modulation in a focal plane array," *2014 Int. Conf. Commun. Signal Process.,* Melmaruvathur, India, 2014, pp. 1414-1418. doi:10.1109/ICCSP.2014.6950082.

[12] F. E. Mahmouli and S. D. Walker, "4-gbps uncompressed video transmission over a 60-ghz orbital angular momentum wireless channel," *IEEE Wirel. Commun. Lett.*, vol. 2, no. 2, pp. 223-226, 2013. doi:10.1109/WCL.2013.012513.120686.

[13] H.-T. Chen, R. Pan, W.-Z. Sun, and S.-Y. He, "Microstrip reflectarray for generation of electromagnetic waves with beam vorticity," *Applied Computational Electromagnetics Society Journal (ACES)*, vol. 33, no. 5, pp. 488-493, 2018.

[14] Q. Feng, Y. Lin, Y. Zheng, and L. Li, "Vortex beam optimization design of concentric uniform circular array antenna with improved array factor," *Applied Computational Electromagnetics Society Journal (ACES)*, vol. 36, no. 7, pp. 830-837, 2021.

[15] B. Thidé, H. Then, J. Sjöholm, K. Palmer, J. Bergman, T. Carozzi, Y. N. Istomin, N. Ibragimov, and R. Khamitova, "Utilization of photon orbital angular momentum in the low-frequency radio domain," *Phys. Rev. lett.*, vol. 99, no. 8, 087701, 2007. doi:10.1103/physrevlett.99.087701.

[16] J. D. Jackson, *Classical Electrodynamics*, John Wiley & Sons, New York, 1999.

[17] Q. Bai, A. Tennant, B. Allen, and M. U. Rehman, "Generation of orbital angular momentum (oam) radio beams with phased patch array," *2013 Loughborough Antennas Propag. Conf. (LAPC)*, pp. 410-413, 2013.

[18] Q. Bai, A. Tennant, E. Cano, and B. Allen, "An experimental phased array for oam generation," *2014 Loughborough Antennas Propag. Conf. (LAPC)*, Loughborough, 2014, pp. 165-168. doi:10.1109/LAPC.2014.6996347.

[19] K. Liu, H. Liu, Y. Qin, Y. Cheng, S. Wang, X. Li, and H. Wang, "Generation of oam beams using phased array in the microwave band," *IEEE Trans. Antennas Propag.*, vol. 64, no. 9, pp. 3850-3857, 2016. doi:10.1109/TAP.2016.2589960.

[20] M. Klemes, H. Boutayeb, and F. Hyjazie, "Orbital angular momentum (oam) modes for 2-d beam-steering of circular arrays," *2016 IEEE Can. Conf. Electr. Comput. Eng. (CCECE)*, Vancouver, BC, Canada, pp. 1-5, 2016. doi:10.1109/CCECE.2016.7726746.

[21] T. Yuan, Y. Cheng, H. Wang, and Y. Qin, "Beam steering for electromagnetic vortex imaging using uniform circular arrays," *IEEE Antennas Wirel. Propag. Lett.*, vol. 16, pp. 704-707, 2016. doi:10.1109/LAWP.2016.2600404.

[22] P. Mao and C. Gao, "Design and simulation of a hexagonal microstrip array antenna with oam," *2019 Int. Conf. Intell. Comput., Automat. Sys. (ICICAS),* Chongqing, China, pp. 100-104, 2019.

[23] Y. Wang, J. Liu, D. Yang, and W. Jie, "Generation of multiple oam modes using time-modulated concentric circular arrays," *2019 Int. Symp. Antennas Propag. (ISAP)*, Xi'an, China, pp. 1-2, 2019.

[24] S. Tan, J. Dong, M. Wang, Z. Jiang, X. Zhuang, and L. Deng, "New circular array configurations for generating orbital angular momentum (oam) beams," *2018 Int. Appl. Comput. Electromagn. Soc. Symp.-China (ACES)*, Beijing, China, pp. 1-2, 2018.

[25] D. G. Grier, "A revolution in optical manipulation," *Nature*, vol. 424, no. 6950, pp. 810-816, 2003. doi:10.1038/nature01935.

[26] K. Liu, Y. Cheng, H. Wang, X. Li, and Y. Qin, "Radiation pattern synthesis for the generation of vortex electromagnetic wave," *IET Microw. Antennas Propag.,* vol. 11, no. 5, pp. 685-694, 2017. doi:10.1049/iet-map.2016.0681.

[27] K. Liu, Y. Cheng, X. Li, H. Wang, Y. Qin, and Y. Jiang, "Study on the theory and method of vortex-electromagnetic-wave-based radar

imaging," *IET Microw. Antennas Propag.*, vol. 10, no. 9, pp. 961-968, 2016. doi:10.1049/iet-map.2015.0842.

[28] T. Nishio, H. Xin, Y. Wang, and T. Itoh, "A frequency-controlled active phased array," *IEEE Microw. Wirel. Compon. Lett.*, vol. 14, no. 3, pp. 115-117, 2004. doi:10.1109/LMWC.2004.825188.

**Yuliang Zhou** received a B.S. degree in Applied Physics and the Ph.D. degree in Communication and Information Systems from the University of Electronic Science and Technology of China, Chengdu, China, in 2012 and 2020, respectively. Now he is a Post-Doctoral Researcher with the School of Aeronautics and Astronautics, University of Electronic Science and Technology of China.

From 2017 to 2018, he was with the Microwave Laboratory, University of Pavia, Pavia, Italy. His current research interests include substrate integrated circuits, leaky-wave antennas, and systems for wireless communication.

**Kaiyuan Yao** was born in Dengzhou, Henan, China in 2000 and obtained the degree certificate of Communication Engineering from Southwest Minzu University in 2021. He is currently working toward a master's degree in Traffic and Transportation from the University of Electronic Science and Technology of China, Chengdu, China. His research interests include antennas, and radio frequency circuits.

**Xiaona Li** was born in Xinzhou, Shanxi, China, in 1999. She is currently working toward a master's degree in Electronic Information from the University of Electronic Science and Technology of China, Chengdu, China. Her research interests include antennas, and radio frequency circuits.

**Yong M. Huang** Yong Mao Huang received the B.S. degree in Communication Engineering and the Ph.D. degree in Communication and Information Systems from the University of Electronic Science and Technology of China, Chengdu, China, in 2010 and 2017, respectively.

From 2014 to 2015, he was with the Department of Electrical Engineering, University of South Carolina, Columbia, SC, USA. He is currently an Assistant Professor with the School of Electrical Engineering and Electronic Information, Xihua University, Chengdu. He has authored or coauthored over 40 refereed articles. His current research interests include RF/microwave/millimeter-wave circuits and systems for wireless communication, radar and sensing applications, substrate integrated circuits, and reconfigurable components.

**Haiyan Jin** received a B.S. degree in Electronic Information Technology and M.S. and Ph.D. degrees in Electrical Engineering from the University of Electronic Science and Technology of China (UESTC), Chengdu, China, in 2001, 2006, and 2010, respectively.

From 2013 to 2014, he was a Post-Doctoral Researcher with the Poly-Grames Research Center, École Polytechnique de Montreal, University of Montreal, Montreal, QC, Canada, where he focused on beam forming antennas. Since 2010, he has been with the School of Information and Communication Engineering, UESTC, where he is currently an Associate Professor. He has authored or coauthored over 50 publications in referred journals and international conferences/symposia. His current research interests include antenna array designs and substrate integrated techniques for microwave and millimeterwave communication systems.